

https://dspace.org/

The geology of the southwestern part of the Uitloop Farm, northern limb of the Bushveld Complex, Limpopo, South Africa

Mapiloko, Mabatho

2020

https://hdl.handle.net/10539/32745

Downloaded from a DSpace repository. https://dspace.org/



The geology of the southwestern part of the Uitloop Farm, northern limb of the Bushveld Complex, Limpopo, South Africa

By

'Mabatho Mapiloko

604450

A research report submitted to the Faculty of Science, University of the Witwatersrand, Johannesburg, in partial fulfilment of the requirements for the degree of Master of Science.

University of the Witwatersrand, Johannesburg.

2020

DECLARATION

I declare that this thesis is my own, except where referenced or specific acknowledgements have been made to the work of others. It is being submitted for degree of Master of Science in the University of the Witwatersrand, Johannesburg. It has not been submitted before for any degree or examination in any other University.



……

Signature of candidate

Date: ……..02/10/2020…….

ABSTRACT

The research area is based on the southwestern portion of the Uitloop farm, which is located in the northern limb about 9 km northeast of Mokopane in the Limpopo province. The study involves the stratigraphic, petrological and geochemical investigation of the magmatic and metasedimentary rocks within two boreholes: Z19 and Z20, from the Uitloop farm. The main aim of this study was to utilise whole rock geochemical and mineral chemical characteristics to substantiate stratigraphic correlation with known units (the Lower Zone or the Platreef) of the northern limb, with the long-term goal to establish the Ni-Cu-PGE potential of the study area.

The outcomes of the study have demonstrated that the stratigraphy at the southwestern portion of the Uitloop farm consists of magmatic rocks dominated by feldspathic pyroxenite intercalated with feldspathic harzburgite, pyroxenite, norite, gabbro, gabbronorite, leuconorite and parapyroxenite while calcsilicate and a variety of hornfels with angular inclusions form the footwall lithologies. A few lenses of orthopyroxenite are also observed within the hornfels units in borehole Z20, they consist entirely of granular orthopyroxene and can potentially be assigned to the Marginal Zone sills. Several stratigraphical and petrological similarities exist between the studied area of the Uitloop farm and the Platreef, however, unlike the Platreef which has the Main Zone lithologies forming the hanging wall, the magmatic rocks at Uitloop farm are bound by metasedimentary rocks of the Duitschland Formation.

The chromite mineralisation on the southwestern part of the Uitloop farm occurs mainly as disturbed seams and patches of densely disseminated grains and accessory disseminations as well as a thin chromitite stringer at the top of the sequence in borehole Z20 hosted by feldspathic pyroxenites and feldspathic harzburgite units, similar to the Upper Chromite Zone in the Platreef as observed by Yudovskaya and Kinnaird (2010). The sulphide mineralisation, which generally increases with increasing depth towards the footwall contact, is dominated by pyrrhotite with subordinate pentlandite, chalcopyrite and pyrite. Like the Platreef, PGE mineralisation at Uitloop farm is associated with feldspathic pyroxenites, feldspathic harzburgites as well as hybrid rocks (e.g. parapyroxenite). Two styles of PGE mineralisation are noted: 1) the reef-style horizon that is associated with irregular or disturbed chromitites at the top of the intersection in borehole Z20 and 2) contact-style mineralisation rich in sulphides with modest PGE that is confined to the lower part of borehole Z19 sequence and to the footwall.

The whole-rock geochemical analysis of the magmatic rocks revealed high MgO (12.2 – 27.9 wt.%) and high Cr_2O_3 (up to 7.7 wt.%) in ultramafic cumulates whereas low MgO (6.21 – 22.9 wt.%) and high Na_2O (up to 2 wt.%) correspond to plagioclase-richer lithologies that crystallised from differentiated

melts. Graphite-bearing pyroxenite and parapyroxenite in the footwall sequences show an increase in Al_2O_3 (9.7 and 10.4 wt.%), CaO (6.1 and 18.48 wt.%) and Fe_2O_3 (18.5 and 14.68 wt.%) contents that also indicate magma contamination, which may have influenced the development of the predominantly bottom-loaded PGE mineralisation in borehole Z19. The majority of the mafic/ultramafic samples from the studied area of the Uitloop farm recorded Cr/MgO >100 suggesting Critical Zone affinity. The REE content and distribution patterns are also consistent with the Platreef/Critical Zone melt signature. This study thus concludes that the geology of the southwestern portion of the Uitloop farm resembles the Platreef more than the Lower Zone, the studied sequence represents an offshoot formed by multiple sills or injections of melts of the Critical/Platreef type.

ACKNOWLEDGEMENTS

Firstly, I would like to express my utmost gratitude to the management at Umbono Capital for allowing me an opportunity to work on this research project. I would also like to thank Prof. Judith Kinnaird and my supervisors Prof. Paul Nex and Dr Marina Yudovskaya whose expertise and knowledge have guided me through this project. A special thanks to Marina for continuous guidance, critical comments and for taking time out to ensure that I understood all aspects of this project as well as the Bushveld Complex as a whole.

I would also like to thank Innes Buurman and Dr Matthew McCreesh from Umbono Capital for providing with all the necessary historical literature on the Zebediela project and for allowing me to tag along to Mokopane on many occasions as well as for sharing their insights on the project.

I am very grateful to the University of the Witwatersrand EarthLabs for allowing me to use their facilities as well as Dr. Christian Reinke of SPECTRAU labs at the University of Johannesburg for his help with the microprobe analysis.

To all my friends, particularly; Onesimo, Botle, Saby, Makani and Mothae, thank you for your ceaseless support during trying times. My sincere gratitude goes out to my parents Mathabiso and Mojalefa for their unconditional love, financial support and encouraging me to further my studies.

Finally, I would like to thank the Almighty God for daily protection and guidance.

CONTENTS

1. CHAPTER 1: ZEBEDIELA PROJECT 2
   1.1 STUDY AREA 2
   1.2 PREVIOUS WORK DONE ON UITLOOP FARM 6
   1.3 MOTIVATION FOR PRESENT STUDY 9
   1.4 OBJECTIVES OF THE PROJECT 10
   1.5 ENVISAGED OUTCOMES OF THE RESEARCH 10
   1.6 DISCUSSION 11
2. CHAPTER 2: GENERAL GEOLOGY OF THE BUSHVELD COMPLEX 12
   2.1 STRATIGRAPHY OF THE RUSTENBERG LAYERED SUITE 12
   2.2 MINERALISATION IN THE BUSHVELD COMPLEX 16
      2.2.1 CHROMITE 16
      2.2.2 PLATINUM GROUP ELEMENTS 17
   2.3 DISCUSSION 19
3. CHAPTER 3: THE NORTHERN LIMB 20
   3.1 INTRODUCTION 20
   3.2 THE STRATIGRAPHY OF THE NORTHERN LIMB 22
   3.3 THE PLATREEF 27
      3.3.1 HANGING WALL LITHOLOGIES 27
      3.3.2 FOOTWALL LITHOLOGIES 27
      3.3.3 PLATREEF LITHOLOGIES 28
      3.3.4 PLATREEF SECTORS 29
      3.3.5 MINERALISATION IN THE PLATREEF 33
   3.4 CHROMITE MINERALISATION IN THE NORTHERN LIMB 36
      3.4.1 CHROMITE MINERALIZATION IN THE LOWER ZONE 36
      3.4.2 CHROMITE MINERALISATION IN THE PLATREEF 36
   3.5 DISCUSSION 38
4. CHAPTER 4: STRATIGRAPHY OF THE ZEBEDIELA PROJECT AREA 40
   4.1 HANGING WALL LITHOLOGIES 41
   4.2 THE MAGMATIC LITHOLOGIES ON UITLOOP FARM 42
      4.2.1 PYROXENITE 42
      4.2.2 FELDSPATHIC PYROXENITE 42
      4.2.3 FELDSPATHIC HARZBURGITE 43
      4.2.4 NORITE 44

4.2.5 GABBRO AND GABBRONORITE 45
4.2.6 PARAPYROXENITE 46
4.3 FOOTWALL LITHOLOGIES 46
4.3.1 BOREHOLE Z19 FOOTWALL LITHOLOGY 46
4.3.2 BOREHOLE Z20 FOOTWALL LITHOLOGY 47
5. CHAPTER 5: PETROGRAPHY OF THE ZEBEDIELA PROJECT ROCKS 52
5.1 FELDSPATHIC PYROXENITE 52
5.2 ORTHOPYROXENITE 54
5.3 FELDSPATHIC HARZBURGITE 54
5.4 NORITE 56
5.5 GABBRO 57
5.6 PARAPYROXENITE 58
5.7 HORNFELS 59
5.8 CALCSILICATE 60
5.9 DISCUSSION 61
6. CHAPTER 6: MINERALISATION ON THE SOUTHWESTERN PORTION OF UITLOOP FARM 63
6.1 CHROMITE 63
6.1.1 CHROMITE OCCURRENCE IN UITLOOP LITHOLOGIES 63
6.2 BASE METAL SULPHIDES 66
6.2.1 THE DISTRIBUTION OF SULPHIDES WITHIN UITLOOP LITHOLOGIES 66
6.2.2 SULPHIDE MINERALOGY 68
6.2.3 PGE MINERALISATION 71
6.3 DISCUSSION 72
7. CHAPTER 7: GEOCHEMISTRY OF THE ZEBEDIELA PROJECT ROCKS 73
7.1 INTRODUCTION 73
7.2 MAJOR ELEMENT VARIATIONS IN ROCK TYPES 73
7.3 TRACE ELEMENT VARIATIONS IN ROCK TYPES 80
7.4 DISTRIBUTION OF RARE EARTH ELEMENTS 91
7.5 DISCUSSION 93
7.5.1 MAJOR ELEMENT CHEMISTRY 93
7.5.2 TRACE ELEMENT CHEMISTRY 95
8. CHAPTER 8: MINERAL CHEMISTRY OF CHROMITE AND OLIVINE IN MAGMATIC LITHOLOGIES ON THE SOUTHWESTERN PART OF THE UITLOOP FARM 98
8.1 INTRODUCTION 98

8.2 CHROMITE DISTRIBUTION 100
8.3 CHROMITE MORPHOLOGY 102
8.4 CHROMITE CHEMISTRY 105
8.4.1 CHROMITE COMPOSITIONS IN DIFFERENT LITHOLOGIES 105
8.4.2 CHROMITE COMPOSITION IN RELATION TO DIFFERENT MINERAL HOSTS 111
8.5 COMPARISON TO OTHER BUSHVELD COMPLEX CHROMITE COMPOSITIONS 117
8.5.1 COMPARISON TO PLATREEF CHROMITE COMPOSITIONS 117
8.5.2 COMPARISON TO LOWER ZONE (GRASVALLY) CHROMITE COMPOSITIONS 120
8.5.3 COMPARISON TO CRITICAL ZONE CHROMITE COMPOSITIONS 122
8.6 OLIVINE CHEMISTRY 124
8.7 MINERAL CHEMISTRY SUMMARY 128
8.7.1 CHROMITE 128
8.7.2 OLIVINE 130
9. CHAPTER 9: DISCUSSION AND CONCLUSION 132
9.1 DISCUSSION 132
9.1.1 STRATIGRAPHY 132
9.1.2 BASE METAL SULPHIDE OCCURRENCE 134
9.1.3 CHROMITE MINERALISATION 135
9.2 CONCLUSION 136
10. REFERENCES 138
11. APPENDICES 148
APPENDIX A: METHODOLOGY 149
1. SAMPLE COLLECTION 149
2. PETROGRAPHIC ANALYSIS 150
3. GEOCHEMISTRY 150
3.1 SAMPLE PREPARATION FOR XRF AND ICP-MS 150
3.2 X-RAY FLUORESCENCE (XRF) ANALYSIS 151
3.2.1 FUNCTION OF THE WD-XRF MACHINE 151
3.3 ICP-MS ANALYSIS 151
3.3.1 SAMPLE ANALYSIS 152
4. ELECTRON PROBE MICROANALYSIS (EPMA) 152
4.1 SAMPLE ANALYSIS 152
APPENDIX B: PETROLOGICAL ANALYSIS 154
1. GEOLOGY LOG SHEETS 154

2. SAMPLE PHOTOGRAPHS 159
3. PETROGRAPHIC DESCRIPTIONS OF POLISHED THIN SECTIONS 172
4. SAMPLE LIST 184
5. REFLECTED LIGHT MICROPHOTOGRAPHS 185
APPENDIX C: GEOCHEMICAL DATA 202
1. REFERENCE MATERIALS 202
2. GEOCHEMICAL RESULTS 204
APPENDIX D: MINERAL CHEMISTRY DATA 211
1. CHROMITE CHEMISTRY 211
2. OLIVINE CHEMISTRY 221

LIST OF FIGURES

Figure 1-1: Geological map of the northern limb of the Bushveld Complex indicating the northern, central and southern sectors (Modified by Nex and Kinnaird, 2004 after van der Merwe, 1978). The red line indicates the outline of the farm Uitloop 3KS while the red circle shows the location of the studied area on the farm. 3
Figure 1-2: Location of the study area in the Uitloop farm indicating position of the boreholes use on this study A) & B) simplified geological map of the Uitloop farm (study area) (After van der Merwe, 1978), indicating the licenced area. C) Google earth image of Figure B. 5
Figure 1-3: SouthernEra soil geochemical contour map indicating Copper (Cu) anomalies on the Uitloop farm (Lowman, 2007). 7
Figure 1-4: Southern Era soil geochemical contour maps indicating nickel (Ni) anomalies on the Uitloop farm (Lowman, 2007) 7
Figure 1-5: Map showing the historical boreholes across the Uitloop II body. (Croll et al., 2012). 8
Figure 1-6: Location and orientation of conduit-type intrusions in the Bushveld Complex. Up=Uitloop, Ap= Apiesdooringdraai, Uk=Uitkomst (Modified after Clarke et al., 2009a). 11
Figure 2-1: Geological map indicating different segments of the Rustenburg Layered Suite of the Bushveld Complex (Yudovskaya et al., 2013). 13
Figure 2-2: A north-south cross section through the Rustenburg Layered Suite of the Bushveld Complex (Kruger, 2005). 13
Figure 2-3: The stratigraphy of the Rustenburg layered suit of the Bushveld Complex (After Eales & Cawthorn, 1996). 15
Figure 2-4: The stratigraphic positions of the chromitite layers within the Critical Zone (Naldrett et al., 2009). 17
Figure 3-1: Geological map of the northern limb of the Bushveld Complex (Kinnaird & McDonald, 2018). 21
Figure 3-2: A simplified stratigraphy of the Waterberg project area showing the position of the mineralised intervals, F-zone and T-zone, PGE grades are also presented in the form of histograms (Kinnaird et al., 2017) 25
Figure 3-3: The stratigraphy of the northern limb indicating the occurrence of economic mineralisation within different Zones (McDonald et al., 2005) 26
Figure 3-4: A schematic cross-section through the entire strike length of the Platreef (Kinnaird et al., 2005). 28
Figure 3-5: A NE-SW cross-section across the Flatreef and its down-dip extension on Turfspruit farm (Grobler et al., 2018). 30
Figure 3-6: The stratigraphical correlation between the Platreef/Flatreef and the Upper Critical Zone of the western limb of the Bushveld Complex (Grobler et al., 2018). 32
Figure 3-7: Stratigraphic logs showing persistent chromite-bearing horizons; termed the Upper Chromite Zones (UCR) and Lower Chromite Zone (LCR), within the Platreef along strike on Overysel (OY), Zwartfontein (ZN), Vaalkop (VK), Sandsloot (SS) and Tweefontein (TN) farms (Yudovskaya & Kinnaird, 2010). 37
Figure 4-1: In borehole Z20, a 2.5 m thick assimilation zone (parapyroxenite) separates the dolomite hanging wall from the underlying feldspathic pyroxenite of the Bushveld Complex. 41
Figure 4-2: A photograph of borehole core sample showing fine-grained orthopyroxenite, sample Z20-195.7. 42

Figure 4-3: A photograph of borehole core sample showing medium to coarse-grained feldspathic pyroxenite (Sample Z19-137.7) with fine-grained chromite disseminations. 43
Figure 4-4: A photograph of borehole core sample showing medium to coarse-grained feldspathic pyroxenite (sample Z20-173.7) with net-textured base metal sulphide mineralisation. 43
Figure 4-5: A photograph of borehole core sample showing coarse-grained serpentinised harzburgite (sample Z20-53.7). 43
Figure 4-6: A photograph of borehole core sample showing medium to coarse-grained harzburgite (sample Z20-54.25) with a chromite stringer. 44
Figure 4-7: A photograph of borehole core sample showing coarse-grained feldspathic harzburgite (sample Z20-57.5) with chromite disseminations. 44
Figure 4-8: A photograph of borehole core sample showing coarse-grained highly serpentinised feldspathic harzburgite (sample Z20-66.5). 44
Figure 4-9: A photograph of borehole core sample showing medium-grained melanorites (sample Z19-78.3) with finely disseminated base metal sulphides. 45
Figure 4-10: A photograph of borehole core sample showing coarse-grained leuconorite (sample Z20-153.5). 45
Figure 4-11: A photograph of borehole core sample showing coarse grained gabbro (sample Z20-140.1) with base metal sulphide blebs. 45
Figure 4-12: A photograph of borehole core sample showing fine-grained parapyroxenite (sample Z19-175.1). 46
Figure 4-13: A photograph of borehole core sample showing fine-grained mica-rich hornfels (sample Z19-178.6). 47
Figure 4-14: A photograph of borehole core sample showing fine-grained hornfels (sample Z19-203.2) with quartz-cordierite hornfels fragments (sedimentary breccia). 47
Figure 4-15: A photograph of borehole core sample showing a sharp contact between the Feldspathic pyroxenite and the metasedimentary footwall lithologies (mica-rich hornfels) of the Transvaal Supergroup at a depth of 176.1m in borehole Z20. 48
Figure 4-16: A photograph of borehole core sample showing hornfels (Sedimentary breccia) (sample Z20183.5) with various quartz-cordierite hornfels fragments rimmed by base metal sulphides. 48
Figure 4-17: A photograph of borehole core samples showing a sharp contact between the hornfels and the underlying dolomitic unit at a depth of 196 m below surface. 49
Figure 4-18: A photograph of borehole core sample showing dolomite with bands of magnetite and minor base metal sulphides as well as calcite veins. 49
Figure 4-19: Simplified geological log of borehole Z19 indicating major stratigraphic positions; HW = hanging wall, Cr = chromite mineralisation, FW = footwall, E.O.H = end of hole, a graph displaying the down-hole 4E grade profile is also included. 50
Figure 4-20: Simplified geological log of borehole Z20 indicating major stratigraphic positions; HW = hanging wall, Cr = chromite mineralisation, FW = footwall, E.O.H = end of hole, a graph displaying the down-hole 4E grade profile is also included. 51
Figure 5-1: Photomicrographs (taken under XPL) of feldspathic pyroxenites under XPL from the southwestern portion of the Uitloop farm. (A) Cumulus orthopyroxene laths, sample Z19–100.35, (B) Cumulus orthopyroxene with intercumulus plagioclase, sample Z20–134.8, (C) Twinned clinopyroxene (D) Clinopyroxene oikocryst enclosing orthopyroxene, sample Z20–121.9, (E) Zoned and twinned intercumulus plagioclase, sample Z20–121.9 and (F) Granophyric quartz, sample Z20–120.75. 53

Figure 5-2: Photomicrographs (taken under XPL) of orthopyroxenite from the local magmatic lithologies at the southwestern portion of the Uitloop farm. (A) Fine-grained cumulus orthopyroxene crystals, sample Z19–174.9. (B) Coarse-grained cumulus orthopyroxene crystals, sample Z19–199. . 54
Figure 5-3: Photomicrographs (taken under XPL) of feldspathic harzburgite from the magmatic lithologies at the southwestern portion of the Uitloop farm. (A) Serpentinised olivine with characteristic fractures filled with magnetite, sample Z20 – 54.25, (B) Cumulus olivine and interstitial twinned plagioclase, sample Z20 – 66.5, (C) Clinopyroxene oikocryst enclosing olivine and orthopyroxene, sample Z20–111, (D) Orthopyroxene phenocryst with orthopyroxene inclusions, sample Z20–111, and (E) Olivine with characteristic fractures filled by magnetite, altered orthopyroxene crystals, phlogopite with chromite inclusions, sample Z20-53.7. 55
Figure 5-4: Photomicrographs (taken under XPL) of norite from the local magmatic stratigraphy at the southwestern portion of the Uitloop farm. (A) Fine-grained cumulus plagioclase, sample Z20-164.5. (B) Clinopyroxene exsolution lamellae in orthopyroxene, sample Z20-164.5. (C) Twinned K-feldspar and orthopyroxene with clinopyroxene exsolution lamellae and orthopyroxene inclusions, sample Z19-78.3. (D) Twinned plagioclase enclosed by clinopyroxene oikocryst with orthopyroxene exsolution lamellae, sample Z19-78.3. (E) Cumulus plagioclase laths, sample Z20-164.5. (F) Clinopyroxene with orthopyroxene inclusions, sample Z20-164.5. 57
Figure 5-5: Photomicrographs (under XPL) of Gabbro, sample Z20-140.1, from the local magmatic stratigraphy in borehole Z20 at the southwestern portion of the Uitloop farm. (A) Altered clinopyroxene phenocryst. (B) Altered clinopyroxene and sericitized twinned plagioclase. (C) Interstitial quartz with a granophyric texture. 58
Figure 5-6: Photomicrographs (taken under XPL) of parapyroxenite (sample Z19-170.5) from footwall lithologies at the southwestern portion of the Uitloop farm in borehole Z19. (A & B) Granular pyroxene crystals. 59
Figure 5-7: Photomicrographs (taken under XPL) of pyroxene hornfels from the footwall lithologies at the southwestern-portion of the Uitloop farm. (A) Quartz and cordierite clusters as well as amphibole clusters set in a fine-grained pyroxene-rich groundmass in pyroxene hornfels, sample Z20-183.5. (B) Quartz and cordierite clusters in pyroxene hornfels, sample Z19-203.2. 59
Figure 5-8: Photomicrographs, under XPL, of phlogopite hornfels from footwall lithologies at the southwestern portion of the Uitloop farm. (A) Fine-grained phlogopite hornfels, sample Z19-177.9. (B) Randomly orientated biotite laths associated with quartz grains in biotite hornfels, sample Z20-194.4. 60
Figure 5-9: Photomicrographs, taken under XPL in transmitted light (A-B) and taken in reflected light (C), of calcsilicate with magnetite bands, sample Z20-212.5, from footwall lithologies at the southwestern portion of the Uitloop farm. (A) Magnetite grains in an altered calcsilicate. (B) Clinopyroxene crystals within altered brown crystal mush. (C) Magnetite and Base Metal Sulphides. 61
Figure 6-1: A photograph of borehole core samples showing chromite disseminations in feldspathic pyroxenite (sample Z19-137.7). 64
Figure 6-2: A photograph of borehole core samples showing a chromite stringer in harzburgite and fine-grained chromite disseminations in feldspathic harzburgite at a depth of 54.25 m and 57.5 m respectively in borehole Z20. 64
Figure 6-3: Photomicrographs of chromite under XPL in transmitted light (A, B & C) and reflected light (D, C & F). (A)Chromite disseminations within cumulus pyroxene, (B) plagioclase (B) and mica in feldspathic pyroxenite. (C) Chromite inclusions within olivine in feldspathic harzburgite and (D)

feldspathic pyroxenite. (E) Annealing chromite crystals. (F) Chromite crystals in close association with pyrrhotite. 65
Figure 6-4: A photograph of borehole core samples showing finely disseminated base metal sulphides in feldspathic pyroxenite lithologies at a depth of 107.7 m in borehole Z20. 66
Figure 6-5: A photograph of borehole core samples showing net-textured base metal sulphides, dominated by pyrrhotite, in feldspathic pyroxenite lithologies adjacent to the footwall contact at a depth of ~173.7 m in borehole Z20. 67
Figure 6-6: A photograph of borehole core samples showing parapyroxenite with sulphide blebs, sample Z19-170.5. 67
Figure 6-7: A photograph of borehole core sample showing mica-rich hornfels (Sample Z20-183.5), with quartz-cordierite clasts rimmed by pyrrhotite. 67
Figure 6-8: A photograph of borehole core sample showing base metal sulphides orientated along bedding structures in calcsilicate lithologies in borehole Z20, where they are associated with magnetite bands. 67
Figure 6-9: Photomicrographs under reflected light, of base metal sulphides observed within magmatic rocks at the southwestern portion of the Uitloop farm. (A & B) Sulphides associated with chromite grains. (C) Pyrrhotite rims around plagioclase and orthopyroxene. (D &E) Evidence of sulphide liquid fractionation. (F) Chalcopyrite remobilization into inclusions in plagioclase. (Chr = chromite, Mgt= magnetite, Po= pyrrhotite, Pn = pentlandite, Ccp = chalcopyrite). 69
Figure 6-10: Photomicrographs under reflected light, of base metal sulphides observed within the magmatic rocks at the southwestern portion of the Uitloop farm. (A) Pentlandite exsolution in pyrrhotite. (B & C) Pyrrhotite replaced by needle-like amphibole (tremolite). (D) Pyrrhotite vein truncating orthopyroxene crystals. (Mgt= magnetite, Po= pyrrhotite, Pn = pentlandite, Ccp = chalcopyrite). 69
Figure 6-11: Photomicrographs under reflected light, of base metal sulphides in the footwall lithologies at the southwestern portion of the Uitloop farm; (A & B) parapyroxenite, (C) hornfels and (D) magnetite-rich calcsilicate. (Mgt= magnetite, Po= pyrrhotite, Py = Pyrite). 70
Figure 6-12: Photomicrographs under reflected light (A) and BSE (B), of base metal sulphides associated with feldspathic harzburgite, sample Z20-66.5. (A) Pyrrhotite and pentlandite rimmed by secondary magnetite. (B) Platinum group minerals (PGM) associated with secondary magnetite. (Mgt= magnetite, Po= pyrrhotite, Pn = pentlandite). 71
Figure 7-7-1: Variation in major element concentrations with stratigraphic height in borehole Z19. (FPXNT = feldspathic pyroxene, PXNT = pyroxenite, NOR = norite, PARAPXNT = parapyroxenite). 75
Figure 7-2: Variation in major element concentrations with stratigraphic height in borehole Z20. (FHRZ = feldspathic harzburgite, FPXNT = Feldspathic pyroxene, NOR = norite, GAB = gabbro). 76
Figure 7-3: Binary variation diagrams showing selected major elements concentrations (wt.%) versus MgO content (wt.%) in borehole Z19 lithologies. (FHRZ = Feldspathic harzburgite, FPXNT = Feldspathic pyroxene, NOR = Norite, PXNT = Pyroxenite, PARAPXNT =Parapyroxenite). 78
Figure 7-4: Binary variation diagrams showing major elements concentrations (wt. %) versus MgO content (wt. %) in borehole Z20 lithologies. (FHRZ = Feldspathic harzburgite, FPXNT = Feldspathic pyroxene, NOR = Norite, GAB =Gabbro). 79
Figure 7-5: Variation in selected trace element concentrations (ppm) with stratigraphic height in borehole Z19 from the Uitloop farm. (FHRZ = Feldspathic harzburgite, FPXNT = Feldspathic pyroxene, NOR = Norite, PXNT = Pyroxenite, PARAPXNT =Parapyroxenite). 82

Figure 7-6: Variation in selected trace element concentrations (ppm) with stratigraphic height in borehole Z20 from the Uitloop farm. (FHRZ = Feldspathic harzburgite, FPXNT = Feldspathic pyroxene, NOR = Norite, GAB =Gabbro). 84
Figure 7-7: Binary variation diagrams showing selected trace elements (Rb, Sr, Ba, Sc, V, Cr, Co, Ni, Cu, Zn, Y, Zr & Ga) concentrations (ppm) versus MgO content (wt.%) in borehole Z19 lithologies. ... 88
Figure 7-8: Binary variation diagrams showing selected trace elements (Rb, Sr, Ba, Sc, V, Cr, Co, Ni, Cu, Zn, Y & Zr) concentrations (ppm) versus MgO content (wt.%) in borehole Z20 lithologies. 90
Figure 7-9: Cr/MgO vs depth for boreholes Z19 (A) and Z20 (B) showing that majority of the mafic/ultramafic rocks from the southwestern part of the Uitloop farm have Cr/MgO >80 and thus are of Critical Zone affinity. (MZ = Main Zone, CZ = Critical Zone). 91
Figure 7-10: Primitive mantle normalized REE graphs (normalised to data by Hoffman (1988)) of the feldspathic pyroxenite (FPXNT) and pyroxenite (PXNT) + parapyroxenites (PARAPXNT) from borehole Z19 of the southwestern portion of Uitloop farm. 92
Figure 7-11: Primitive mantle normalized REE graphs (normalised to data by Hoffman (1988)) of the feldspathic pyroxenite (FPXNT) and feldspathic harzburgite (FHRZ) and Norite (NOR) + gabbro (GAB) from borehole Z20 of the southwestern portion of Uitloop farm. 92
Figure 7-12: Primitive mantle normalized REE graphs (normalised to data by Hoffman (1988)) of the ultramafic rocks from the southwestern part of the Uitloop farm compared to the Lower Zone data from Turfspruit and Sandsloot and Platreef data from Turfspruit and Akanani (data supplied by Dr M. Yudovskaya). 97
Figure 8-1: A photograph of borehole core sample showing chromite disseminations in feldspathic pyroxenite, sample Z19-137.7. 100
Figure 8-2: A photograph of borehole core sample showing a chromite stringer and chromite disseminations in feldspathic harzburgite at depths of 54.25 m and 57.5 m respectively in borehole Z20. 100
Figure 8-3: Photomicrographs of cumulus chromite in feldspathic pyroxenite (A-C & E) and feldspathic harzburgite (D). (A) Z20-101, under XPL; chromite in orthopyroxene and clinopyroxene, (B) Z20-101, under XPL in transmitted light; chromite in phlogopite and altered plagioclase, (C) Z20-137.5, in reflected light; chromite in Base Metal Sulphides (pyrrhotite), (D) Z20-66.5-4_39, BSE; chromite in olivine with characteristic fractures filled by magnetite and serpentine. (E) Z19-100.35-1_17, BSE; euhedral and rounded chromite and apatite crystals hosted by a quartz-phlogopite-plagioclase interstitial assemblage, (F) Z19-100.35-2, BSE; euhedral chromite hosted by orthopyroxene and plagioclase in close association with zircon and a uranium-rich mineral phase. (Chr= chromite, Opx= orthopyroxene, Ol = olivine, Cpx = clinopyroxene, Plag = plagioclase, Apt = apatite, Qrtz = quartz, Ph = phlogopite, Po = pyrrhotite, Mgnt = magnetite, U-rich = uranium-rich). 102
Figure 8-4: The morphology of chromite crystals from the southwestern part of the Uitloop farm. (A) Z20-100.35-3_9, subrounded chromite crystals enclosed by sulphides with needle-like amphibole intergrowths. (B) Z19-101.4_29, cumulus euhedral chromite with rutile exsolutions in plagioclase. (C) Z20-66.5_23, BSE; Cr-Spinel with secondary magnetite along crystals boundaries enclosed by sulphide minerals. (D) Z20-66.5_26, BSE; chromite crystals rimmed by magnetite hosted by olivine. (Chr= chromite, Opx= orthopyroxene, Amph = Amphibole, Plag = plagioclase, Phl = phlogopite, Po = pyrrhotite, Pn = pentlandite, Mgnt = magnetite, Cr-Spi = Chromium-spinel, Rut = rutile). 103
Figure 8-5: The morphology of the chromite crystals from the southwestern part of the Uitloop farm. (A) Z20-111-1_46, BSE; coarse interstitial anhedral chromite crystals with fish-hook, magnetite along

crystals boundaries and silicate inclusions. B) Z20-111-1_47, BSE; fish-hook chromite set between orthopyroxene and corroded by phlogopite, this chromite crystal also has silica inclusions. (C) Z20-111-2_48, BSE; amoeboidal chromite corroded by phlogopite, with sulphides and secondary magnetite (a fine-grained spinel phase) along crystals boundaries. (D) Z20-111-2_49, BSE; corroded sieve-textured chromite replaced by phlogopite and magnetite, (E) Z20-111-2_50, BSE; chromite relic within secondary phlogopite. (F) Z20-111-1_45, BSE; sieve textured chromite relic within secondary phlogopite. (Chr= chromite, Opx= orthopyroxene, Plag = plagioclase, Sulph = sulphide, Phl = phlogopite). 104
Figure 8-6: Geochemical graphs of chromite composition from feldspathic pyroxenite lithologies from the southwestern portion of the Uitloop farm; (A) Cr_2O_3 vs MgO (B) Al_2O_3vs MgO (C) FeO vs MgO (D) Fe_2O_3 vs MgO. 106
Figure 8-7: Geochemical graphs of chromite composition from feldspathic pyroxenite lithologies from the southwestern portion of the Uitloop farm; (A) Cr_2O_3 vs Al_2O_3 (B) Cr_2O_3 vs TiO_2 (C) Cr_2O_3 vs TiO_2. 107
Figure 8-8: Geochemical graphs of chromite composition from feldspathic harzburgite lithologies from the southwestern portion of the Uitloop farm; (A) Cr_2O_3vs MgO (B) Al_2O_3 vs MgO (C) FeO vs MgO (D) Fe_2O_3 vs MgO 108
Figure 8-9: Geochemical graphs of chromite composition from feldspathic harzburgite lithologies from the southwestern portion of the Uitloop farm; (A) Cr_2O_3 vs Al_2O_3 (B) Cr_2O_3 vs Ti02 (C) Al_2O_3 vs TiO_2. 109
Figure 8-10: Cr# vs Mg# graphs for chromites hosted by magmatic lithologies from the southwestern portion of the Uitloop farm. Feldspathic pyroxenite (blue, marron, green and purple s) and feldspathic harzburgites (blue and orange), showing the proximity of chromite crystals to their original cumulus compositions. 110
Figure 8-11: Geochemical graphs of chromite composition from feldspathic pyroxenite lithologies from the southwestern portion of the Uitloop farm; (A) Cr_2O_3 vs MgO (Blue: Z19-100.35, Orange: Z19-101.4) (B) Cr_2O_3 vs MgO (Red: Z19-101.6, Purple: Z19-137.5). 112
Figure 8-12: Geochemical plots of chromite composition from feldspathic pyroxenite lithologies from the southwestern portion of the Uitloop farm; (A) Cr_2O_3 vs Al_2O_3 (Blue: Z19-100.35, Orange; Z19-101.4) (B) Cr_2O_3 vs Al_2O_3. (Red: Z19-101.6, Purple: Z19-137.5). 112
Figure 8-13: Geochemical graphs of chromite composition from feldspathic pyroxenite lithologies from the southwestern portion of the Uitloop farm; (A) Al_2O_3 vs MgO (Blue: Z19-100.35, Orange: Z19-101.4) (B) Al_2O_3 vs MgO Red: Z19-101.6, Purple: Z19-137.5). 113
Figure 8-14: Geochemical graphs of chromite composition from feldspathic pyroxenite lithologies from the southwestern portion of the Uitloop farm; (A) Cr_2O_3 vs MgO (Blue: Z19-100.35, Orange: Z19-101.4) (B) Cr_2O_3 vs MgO (Red: Z19-101.6, Purple: Z19-137.5). 114
Figure 8-15: Geochemical plots of chromite composition from feldspathic pyroxenite lithologies from the southwestern portion of the Uitloop farm; (A) Al_2O_3 vs TiO_2 (Blue: Z19-100.35, Orange: Z19-101.4) (B) Al_2O_3 vs TiO_2 (Red: Z19-101.6, Purple: Z19-137.5). 114
Figure 8-16: Geochemical graphs of chromite composition from feldspathic harzburgite (Yellow: Z20-66.5 & Green: Z20-111) lithologies from the southwestern portion of the Uitloop farm; (a) Cr_2O_3 vs MgO (b) Cr_2O_3vs Al_2O_3 c) Al_2O_3 vs MgO D) Cr_2O_3 vs $Ti0_2$ E) Al_2O_3 vs TiO_2. 116
Figure 8-17: Cr# vs Mg# variation diagrams for chromites from the southwestern portion of the Uitloop farm magmatic lithologies. 117

Figure 8-18: Compositional variation diagrams comparing the compositions of chromites from the southwestern portion of the Uitloop farm magmatic lithologies to those from different parts of the Platreef (Yudovskaya & Kinnaird, 2010) in the northern limb. (UIT = Uitloop, AMK = Macalacaskop, ATS = Turfspruit, SS = Sandsloot, VK = Vaalkop, ZN = Zwartfontein and OY = Overysel). 119
Figure 8-19: Compositional variation diagrams comparing the compositions of chromites from the southwestern portion of the Uitloop farm magmatic lithologies to those from the Lower Zone lithologies south of Mokopane (Hulbert, 1983) in the northern limb. (UIT FPXT = Uitloop feldspathic pyroxenite, UIT FHRZ = Uitloop feldspathic harzburgite, LZ =Lower Zone). 121
Figure 8-20: Compositional variation diagrams comparing the compositions of chromites from the southwestern portion of the Uitloop farm to those of the Merensky Reef (Li et al., 2005) and the UG-2 chromitite layer (Mondal & Mathez, 2007). (UIT FPXT = Uitloop feldspathic pyroxenite, UIT FHRZ = Uitloop feldspathic harzburgite, MR = Merensky Reef, UG-2 = UG-2 = Chromitite layer). 123
Figure 8-21: Photomicrographs of olivine crystals under XPL (A) and BSE (B). (A) Z20-66.5, transmitted cross polarized light; chromite and clinopyroxene lamellae in olivine. (B) Z20-66.5-3_44, BSE; chromite and clinopyroxene lamellae in olivine. (Ol = Olivine, Serp = Serpentine, Chr = Chromite, Cpx =Clinopyroxene). 124
Figure 8-22: Compositional variation diagrams comparing the compositions of olivine crystals from the southwestern portion of the Uitloop farm magmatic lithologies to the Lower Zone olivine crystals from Turfspruit, Sandsloot (Yudovskaya & Kinnaird, 2010), Grasvally farms (Hulbert, 1983) and the Merensky Reef (Naldrett et al., 2009). (UIT = Uitloop, LZ = Lower Zone, PR = Platreef, GV = Grasvally, UMT = Turfspruit, SS = Sandsloot, MR = Merensky Reef). 126
Figure 8-23: Compositional variation diagrams comparing the compositions of olivine crystals from the southwestern portion of the Uitloop farm (UIT) magmatic lithologies to those of the Lower Zone (LZ) and Platreef (PR) olivine crystals from Turfspruit (UMT), Sandsloot (SS) (Yudovskaya & Kinnaird, 2013), Grasvally farms (GV) (Hulbert, 1983) and Merensky Reef (MR) (Naldrett et al., 2009). 127
Figure 11-1: Drill core laid out at Umbono storage facility in Mokopane. Limpopo province. 149
Figure 11-2: A Photograph of sample Z19-78.3 (norite). 159
Figure 11-3: A photograph of sample Z19-100.35 (feldspathic pyroxenite). 159
Figure 11-4: A photograph of sample Z19-101. 4 (feldspathic pyroxenite). 159
Figure 11-5: A photograph of sample Z19-101.6 (feldspathic pyroxenite). 160
Figure 11-6: A photograph of sample Z19-123.2 (feldspathic pyroxenite). 160
Figure 11-7: A photograph of sample Z19-137.7 (feldspathic pyroxenite). 160
Figure 11-8: A photograph of sample Z19-150.6 (feldspathic pyroxenite). 161
Figure 11-9: A photograph of sample Z19-167.1 (feldspathic pyroxenite). 161
Figure 11-10: A photograph of sample Z19-169.2 (feldspathic pyroxenite). 161
Figure 11-11: A photograph of sample Z19-170.5 (pyroxenite). 162
Figure 11-12: A photograph of sample Z19-174.9 (parapyroxenite). 162
Figure 11-13: A photograph of sample Z19-177.9 (hornfels). 162
Figure 11-14: A photograph of sample Z19-178.6 (hornfels). 163
Figure 11-15: A photograph of sample Z19-195.7 (pyroxenite). 163
Figure 11-16: A photograph of sample Z19-199 (parapyroxenite). 163
Figure 11-17: A photograph of sample Z19-203.2 (hornfels with calcsilicate inclusions (metasedimentary breccia)). 164
Figure 11-18: A photograph of sample Z20-53.7 (harzburgite). 164
Figure 11-19: A photograph of sample Z20-54.25 (harzburgite with a thin chromite stringer). 164

Figure 11-20: A photograph of sample Z20-57.5 (feldspathic harzburgite with chromite disseminations). 164
Figure 11-21: A photograph of sample Z20-59.5 (feldspathic pyroxenite)..... 165
Figure 11-22: A photograph of sample Z20-62.7 (feldspathic pyroxenite)..... 165
Figure 11-23: A photograph of sample Z20-66.5 (feldspathic harzburgite). 165
Figure 11-24: A photograph of sample Z20-83 (feldspathic pyroxenite)..... 165
Figure 11-25: A photograph of sample Z20-107.7 (feldspathic pyroxenite)..... 166
Figure 11-26: A photograph of sample Z20-111 (feldspathic harzburgite). 166
Figure 11-27: A photograph of sample Z20-119 (feldspathic pyroxenite)..... 166
Figure 11-28: A photograph of sample Z20-120.1 (feldspathic pyroxenite)..... 166
Figure 11-29: A photograph of sample Z20-120.75 (feldspathic pyroxenite)..... 167
Figure 11-30: A photograph of sample Z20-121.9 (feldspathic pyroxenite)..... 167
Figure 11-31: A photograph of sample Z20-124.8 (feldspathic pyroxenite)..... 167
Figure 11-32: A photograph of sample Z20-131.8 (feldspathic pyroxenite)..... 167
Figure 11-33: A photograph of sample Z20-134.8 (feldspathic pyroxenite)..... 168
Figure 11-34: A photograph of sample Z20-140.1 (gabbro). 168
Figure 11-35: A photograph of sample Z20-149.3 (feldspathic pyroxenite)..... 168
Figure 11-36: A photograph of sample Z20-153.5 (leuconorite). 168
Figure 11-37: A photograph of sample Z20-164.5 (norite with a silica vein). 169
Figure 11-38: A photograph of sample Z20-173. 7 (feldspathic pyroxenite). 169
Figure 11-39: A photograph of sample Z20-175.5 (feldspathic pyroxenite)..... 169
Figure 11-40: A photograph showing a sharp contact between the Rustenburg Layered Suite (RLS) (feldspathic pyroxenite) and the metasedimentary footwall lithologies (hornfels) at a depth of ~176.1m in borehole Z20. A transitional contact is observed between sample Z20-175.9 (feldspathic pyroxenite) and sample Z20- 176 (feldspathic pyroxenite). 169
Figure 11-41: A photograph of sample Z20-183.5, hornfels with inclusions of quartz-cordierite hornfels rimmed by base metal sulphides. 170
Figure 11-42: A photograph of sample Z20-184.4, hornfels with inclusions of quartz-cordierite hornfels associated with base metal sulphides. 170
Figure 11-43: A photograph of sample Z20-186, hornfels with inclusions of quartz-cordierite hornfels. 170
Figure 11-44: A photograph of sample Z20-194.4, hornfels with silica veins..... 170
Figure 11-45: A photograph of sample Z20-212.5, dolomite with magnetite bands. 171
Figure 11-46: Modal mineralogy estimation bar chart for borehole Z19 thin sections. 182
Figure 11-47: Modal mineralogy estimation bar chart for borehole Z20 thin sections. 183
Figure 11-48: Photomicrographs, under reflected light, of sample Z19-78.3 (feldspathic pyroxenite) from the southwestern part of Uitloop farm..... 185
Figure 11-49: Photomicrographs, under reflected light, of sample Z19-100.35 (feldspathic pyroxenite) from the southwestern part of Uitloop farm. 185
Figure 11-50: Photomicrographs, under reflected light, of sample Z19-101 (feldspathic pyroxenite) from the southwestern part of Uitloop farm..... 186
Figure 11-51: Photomicrographs, under reflected light, of sample Z19- 101.4 (feldspathic pyroxenite) from the southwestern part of Uitloop farm..... 186
Figure 11-52: Photomicrographs, under reflected light, of sample Z19-101.6 (feldspathic pyroxenite) from the southwestern part of Uitloop farm..... 186

Figure 11-53: Photomicrographs, under reflected light, of sample Z19-123.2 (feldspathic pyroxenite) from the southwestern part of Uitloop farm. 187
Figure 11-54: Photomicrographs, under reflected light, of sample Z19-150.6 (feldspathic pyroxenite) from the southwestern part of Uitloop farm. 187
Figure 11-55: Photomicrographs, under reflected light, of sample Z19-169.2 (feldspathic pyroxenite) from the southwestern part of Uitloop farm. 188
Figure 11-56: Photomicrographs, under reflected light, of sample Z19-170.5 (parapyroxenite) from the southwestern part of Uitloop farm. 188
Figure 11-57: Photomicrographs, under reflected light, of sample Z19-174.9 (parapyroxenite) from the southwestern part of Uitloop farm. 189
Figure 11-58: Photomicrographs, under reflected light, of sample Z19-195.5 (orthopyroxenite) from the southwestern part of Uitloop farm. 189
Figure 11-59: Photomicrographs, under reflected light, of sample Z20-53.7 (harzburgite) from the southwestern part of Uitloop farm. 190
Figure 11-60: Photomicrographs, under reflected light, of sample Z20-54.25 (harzburgite) from the southwestern part of Uitloop farm. 191
Figure 11-61: Photomicrographs, under reflected light, of sample Z20-57.5 (feldspathic harzburgite) from the southwestern part of the Uitloop farm. 192
Figure 11-62: Photomicrographs, under reflected light, of sample Z20-57.9 (feldspathic pyroxenite) from the southwestern part of the Uitloop farm. 192
Figure 11-63: Photomicrographs, under reflected light, of sample Z20-62.7 (feldspathic pyroxenite) from the southwestern part of the Uitloop farm. 193
Figure 11-64: Photomicrographs, under reflected light, of sample Z20-66.5 (feldspathic harzburgite) from the southwestern part of the Uitloop farm. 193
Figure 11-65: Photomicrographs, under reflected light, of sample Z20-83.2 (feldspathic pyroxenite) from the southwestern part of the Uitloop farm. 193
Figure 11-66: Photomicrographs, under reflected light, of sample Z20-107.7 (feldspathic pyroxenite) from the southwestern part of the Uitloop farm. 194
Figure 11-67: Photomicrographs, under reflected light, of sample Z20-111 (feldspathic harzburgite) from the southwestern part of the Uitloop farm. 194
Figure 11-68: Photomicrographs, under reflected light, of sample Z20-120.75 (feldspathic pyroxenite) from the southwestern part of the Uitloop farm. 194
Figure 11-69: Photomicrographs, under reflected light, of Sample Z20-121.9 (feldspathic pyroxenite) from the southwestern part of the Uitloop farm. 195
Figure 11-70: Photomicrographs, under reflected light, of feldspathic pyroxenite (Sample Z20-124.8) from the southwestern part of the Uitloop farm. 195
Figure 11-71: Photomicrographs, under reflected light, of feldspathic pyroxenite (Sample Z20-134.8) from the southwestern part of the Uitloop farm. 196
Figure 11-72: Photomicrographs, under reflected light, of gabbro (sample Z20-140.1) from the southwestern part of the Uitloop farm. 196
Figure 11-73: Photomicrographs, under reflected light, of feldspathic pyroxenite (sample Z20-149.3) from the southwestern part of the Uitloop farm. 197
Figure 11-74: Photomicrographs, under reflected light, of feldspathic pyroxenite (sample Z20-155.7) from the southwestern part of the Uitloop farm. 197

Figure 11-75: Photomicrographs, under reflected light, of norite (sample Z20-153.5) from the southwestern part of the Uitloop farm. 198
Figure 11-76: Photomicrographs, under reflected light, of feldspathic pyroxenite (sample Z20-173.7) from southwestern part of the Uitloop farm. 198
Figure 11-77: Photomicrographs, under reflected light, of feldspathic pyroxenite (sample Z20-175.5) from the southwestern part of the Uitloop farm. 198
Figure 11-78: Photomicrographs, under reflected light, of feldspathic pyroxenite (sample Z20-175.9) from the southwestern part of the Uitloop farm. 199
Figure 11-79: Photomicrographs, under reflected light, of feldspathic pyroxenite (sample Z20-176) from the southwestern part of the Uitloop farm. 199
Figure 11-80: Photomicrographs, under reflected light, of feldspathic pyroxenite (sample Z2-176.1) from the southwestern part of the Uitloop farm. 200
Figure 11-81: Photomicrographs, under reflected light, of mica-rich hornfels (sample Z20-183.5) from footwall rocks to the southwestern part of the Uitloop farm. 200
Figure 11-82: Photomicrographs, under reflected light, of mica-rich hornfels (sample Z20-184.4) from footwall rocks to the southwestern part of the Uitloop farm. 201
Figure 11-83: Photomicrographs, under reflected light, of mica-rich hornfels (Sample Z20-194.4) from footwall rocks to the southwestern part of the Uitloop farm under reflected light. A & B show a close relationship between pyrrhotite and pyrite. 201
Figure 11-84: Photomicrographs, under reflected light, of dolomite with alternating magnetite bands (sample Z20-212.5) from footwall rocks southwestern part of the Uitloop farm. 201

LIST OF TABLES

Table 7-1: The comparison of major element concentrations between different rock types in boreholes Z19 and Z20. 74
Table 7-2: The comparison of trace element concentrations between different rock types in boreholes Z19 and Z20. 81
Table 8-1: Spinel group minerals (Deer et al., 1992). 98
Table 8-2: Summary of selected major element concentrations in chromite crystals from the southwestern part of the Uitloop farm lithologies. 105
Table 11-1: Borehole Z19 geological core log sheet. 154
Table 11-2: Borehole Z20 geological log sheet. 155
Table 11-3: Petrographic analysis of borehole Z19 samples. 172
Table 11-4: Petrographic analysis of borehole Z20 samples. 176
Table 11-5: Samples list 184
Table 11-6: Reference Materials used for calibration in major element analysis. 202
Table 11-7: Reference Materials used for calibration in minor and trace element analysis. 203
Table 11-8: Major oxide data from boreholes Z19 and Z20 lithologies at the southwestern part of the Uitloop farm by XRF. 204
Table 11-9: Trace element data for borehole Z19 samples by ICP-MS 206
Table 11-10: Trace element data for borehole Z20 samples by ICP-MS 208
Table 11-11: Cr/MgO ratios for borehole Z19 lithologies. 210
Table 11-12:Cr/MgO ratios for borehole Z20 lithologies. 210
Table 11-13: Analysis of the chromite Standard Reference Material. 211
Table 11-14: The initial results of major oxide compositions by microprobe analysis. 212
Table 11-15: Recalculated EMPA oxide results according to the spinel stoichiometry calculation template - latest version Dec 21 2004 developed by S.J. Barnes with correction from C-J De Hoog. 215
Table 11-16: Cation proportions recalculated according to the to the spinel stoichiometry calculation template - latest version Dec 21 2004 developed by S.J. Barnes with correction from C-J De Hoog. 217
Table 11-17: The initial EMPA oxide results of olivine 221

CHAPTER 1

ZEBEDIELA PROJECT

1.1 STUDY AREA

Umbono Capital's Zebediela project is located on the northern limb of the Bushveld Complex. The company has prospecting rights over the Uitloop 3KS farm located about 9 km northeast of Mokopane in the Limpopo province (24°06'43.64"S (Latitude) and 29°0'09.34"E (Longitude)) (Fig 1-1). The Ivanplats' Platreef project is located directly north of the Zebediela project. The farm encompasses the Uitloop body which outcrops as two separate offshoot intrusions of Lower Zone affinity; Uitloop I and Uitloop II. These LZ bodies intruded through the metasedimentary rocks of the Transvaal Supergroup and the Archaean basement granites (van der Merwe, 1978) (Fig 1-1). These bodies strike north-west and dip 30° to 45° south-west, although their three-dimensional form remains unknown (Van der Merwe, 1976).

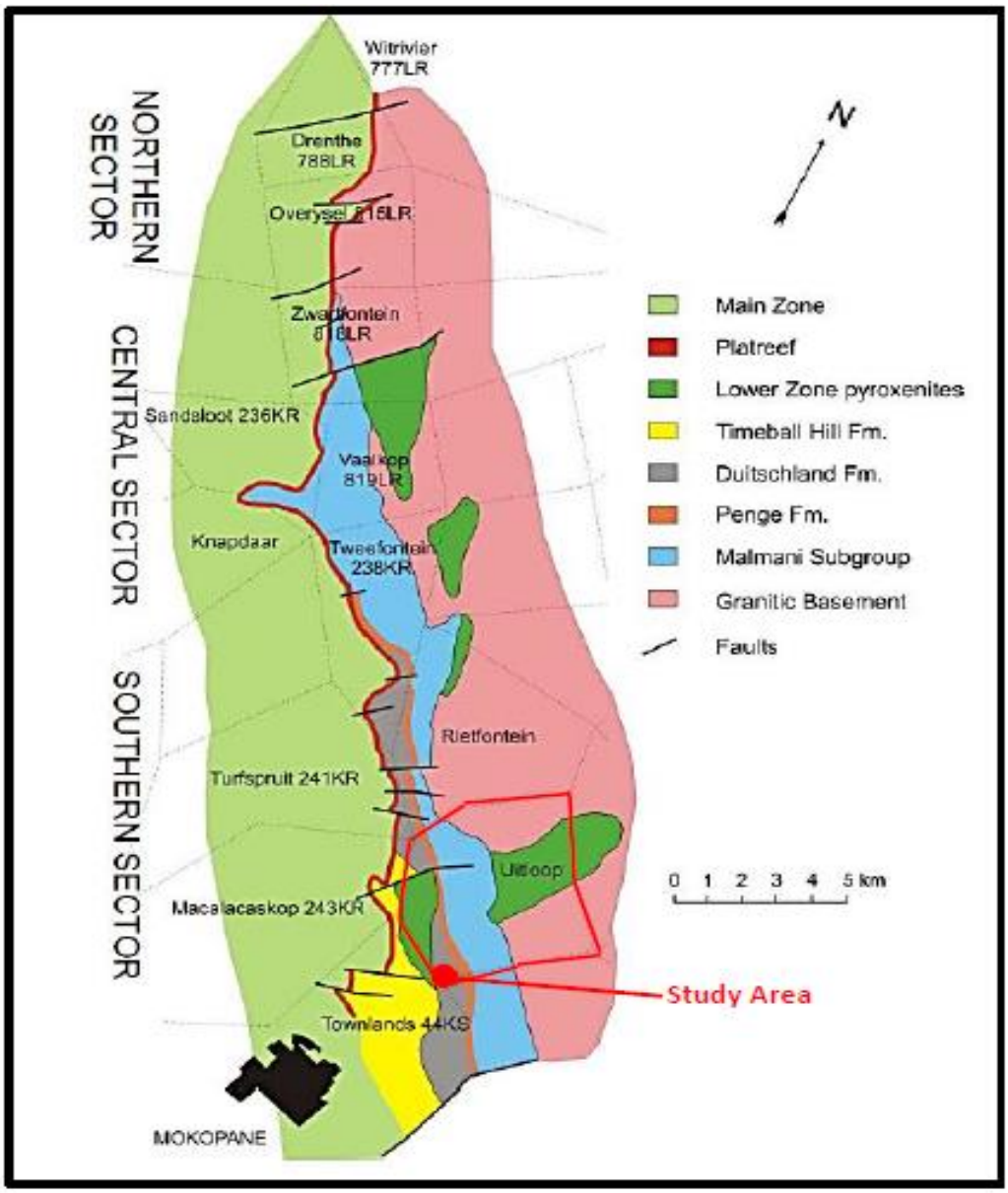


Figure 1-1: Geological map of the northern limb of the Bushveld Complex indicating the northern, central and southern sectors (Modified by Nex and Kinnaird, 2004 after van der Merwe, 1978). The red line indicates the outline of the farm Uitloop 3KS while the red circle shows the location of the studied area on the farm.

This study focuses on a small area located southeast of the Uitloop II offshoot intrusion (Fig 1-2) which outcrops over an area of about 12 km^2. van der Merwe (1978) established the maximum thickness of the Uitloop II body to be about 630 m, however, studies done by the MSA Geoservices suggest that its thickness may range between 800 – 1300 m (Lawman, 2007). Outcrops mapped at surface dip between 10° and 60° to the southwest which is generally steeper than the 10° to 20° southwestwards dip of the BC lithologies in the area. The Uitloop II body is overlain and underlain by carbonate metasedimentary rocks of the Pretoria Group and consists of predominantly serpentinised dunite, harzburgite and pyroxenite units underlain by a fine-grained norite layer containing an abundance of

altered metasedimentary xenoliths (e.g. calcareous xenoliths) (assimilation zone) (van der Merwe, 1978). Other rock types recognised in the area include olivine bearing norites and gabbronorites (Lowman, 2007). No chromitite seams were traced out in this Lower Zone body, however, several chromitite lenses were found close to the base. The stratigraphy of the Uitloop II body has not yet been fully established using historical data as there is considerable lithological variation between adjacent boreholes. Nevertheless, it has been observed that high Ni grades in the body are associated with ultramafic rocks than the olivine-bearing mafic rocks (Lowman, 2007).

Two major structural trends are observed in the study area (Fig 1-2): north-northwestern-southeast and northeast-southwest. Dykes are however not as common as in the rest of the Bushveld Complex (Lowman, 2007). The genesis of the Uitloop satellite intrusions is debatable, however, it is clearly syn-Bushveld and shares geochemical affinities with the Lower Zone. The Platreef is inferred to overlie the Uitloop II intrusion along the southwestern margin of the licence area, where a thin selvedge of metasediments separates the Uitloop II intrusion from the overlying RLS that contains the Platreef mineralisation in the contact zone (Lawman, 2007; Croll, 2012).

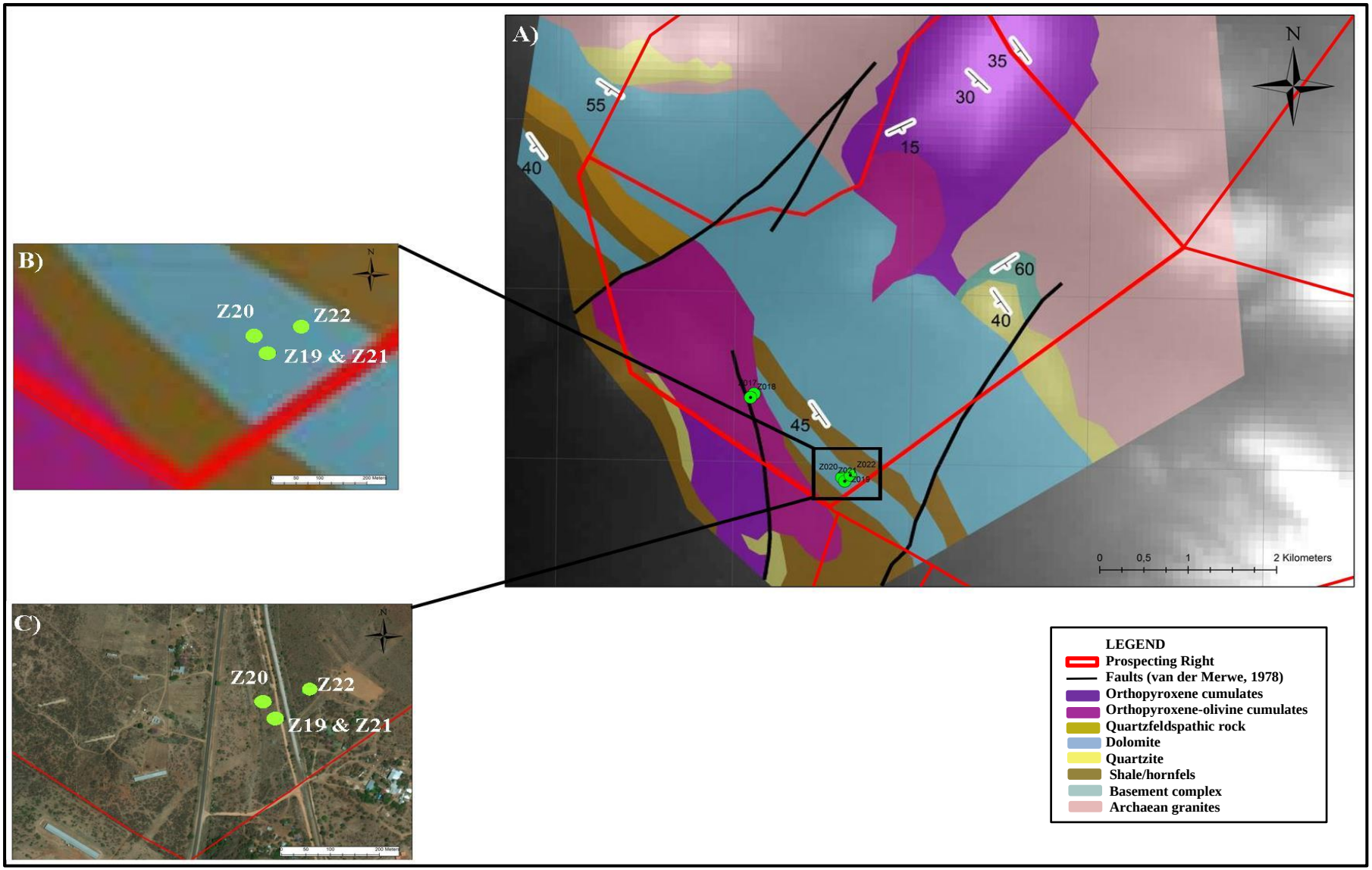


Figure 1-2: Location of the study area in the Uitloop farm indicating position of the boreholes use on this study A) & B) simplified geological map of the Uitloop farm (study area) (After van der Merwe, 1978), indicating the licenced area. C) Google earth image of Figure B.

1.2 PREVIOUS WORK DONE ON UITLOOP FARM

The literature on the historical work done on Uitloop farm is based on two unpublished reports compiled by the MSA Geoservices (Pty) Ltd. on behalf of Lesego Platinum Mining (Pty) Ltd. (Lawman, 2007) and Umnex Minerals Limpopo (Pty) Ltd. (Croll et al., 2012). The Uitloop satellite intrusions have been previously explored, unsuccessfully, for massive Ni-Cu and Platreef style PGE-mineralisation, by various companies which include; Rand Mines (1967 – 1971), SouthernEra Resources (Pty) Ltd. (1998 – 1999) and Falcon Bridge Ventures of Africa (FVA) (2000 – 2001). Rand Mines explored for massive nickel sulphide mineralisation, they conducted a Ni-Cu soil sampling programme, reconnaissance ground magnetic survey and Induced Polarization (IP) survey over the entire Uitloop 3KS farm. Through these exploration methods an anomaly within the dolomitic Transvaal rocks as well as four other anomalous horizons located in the Bushveld Complex lithologies were identified, a total of fourteen boreholes (UL 1 – 14) (Fig 1-5) were then drilled based on their results. The downhole geophysical work done on the farm did not produce any positive mineralised ore body, perhaps because the boreholes were not drilled deep enough to prove the existence of a massive Ni-deposit (Lawman, 2007; Croll et al., 2012).

In 1998, Minex identified the potential for Uitloop farm to host Platreef style mineralisation and approached SouthernEra Resources to develop the project further. Soil geochemical analysis undertaken by SouthernEra revealed a low-level Cu anomaly as well as a very strong Cu-Ni anomaly in the northern and southern portion respectively (Fig 1-3 & 1-4). Upon further investigation, the anomaly in the northern portion proved to be a result of agricultural use of $CuSO_4$. During this time; FVA had also initiated a project called the Lion's Den in search of massive Ni-mineralisation on Townlands 44KS, Amatava 43KS and Uitloop 3KS farms and were particularly interested in obtaining a prospecting licence for Uitloop. In 2000, SouthernEra entered into a Joint Venture (JV) with FVA to explore for massive Ni-mineralisation on Uitloop farm. MSA Geoservices (Pty) Ltd was then appointed in 2001 to conduct fieldwork which included detailed geological mapping, diamond core drilling, core logging, sampling and geophysical work on the western portion of the farm (under supervision of FVA). In 2001; five boreholes (UIT 1-1 – UIT 1-5) (Fig 1-5) were drilled and Platreef-style mineralisation was intersected in boreholes UIT 1-3 and UIT 1-4 instead of the expected massive Ni-mineralisation (Lawman, 2007; Croll et al., 2012).

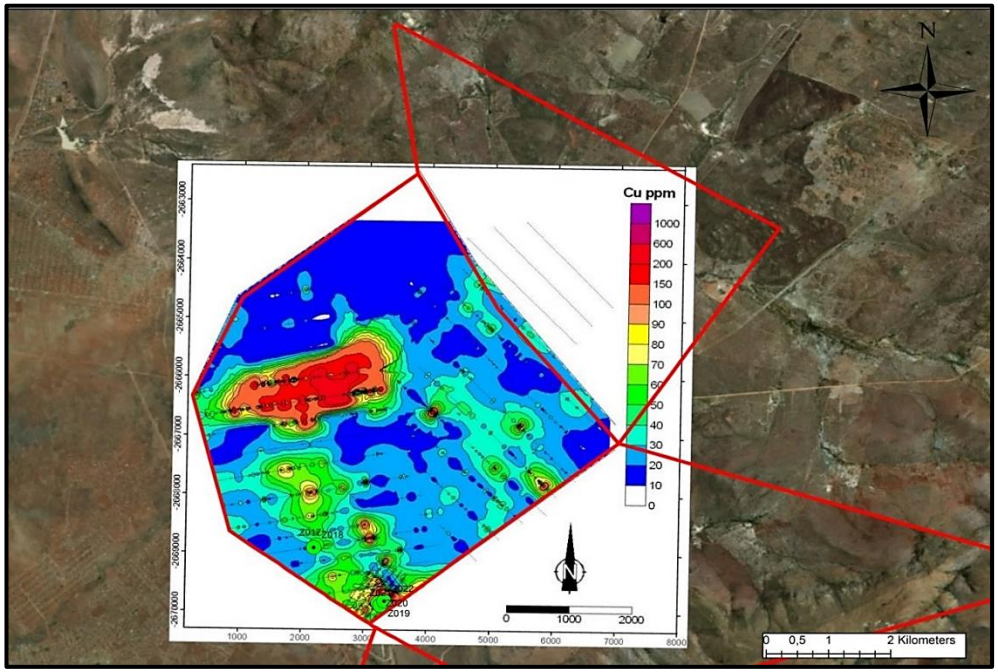


Figure 1-3: SouthernEra soil geochemical contour map indicating Copper (Cu) anomalies on the Uitloop farm (Lowman, 2007).

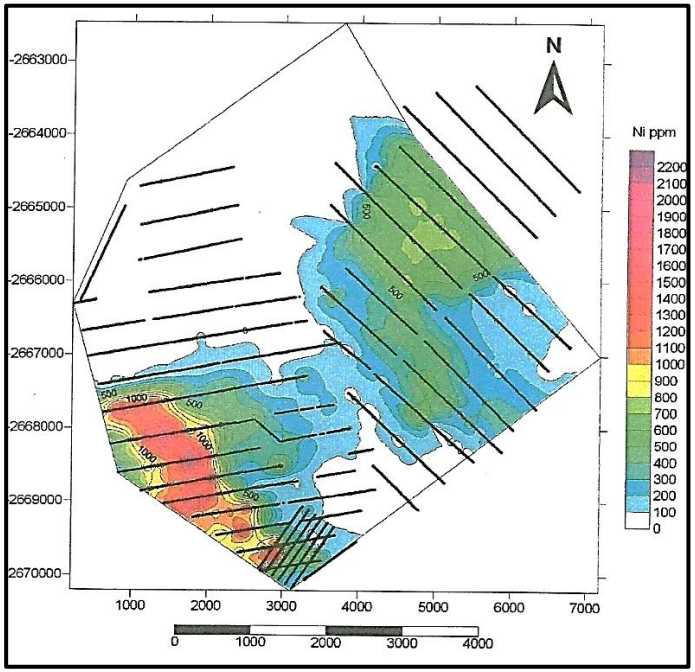


Figure 1-4: Southern Era soil geochemical contour maps indicating nickel (Ni) anomalies on the Uitloop farm (Lowman, 2007)

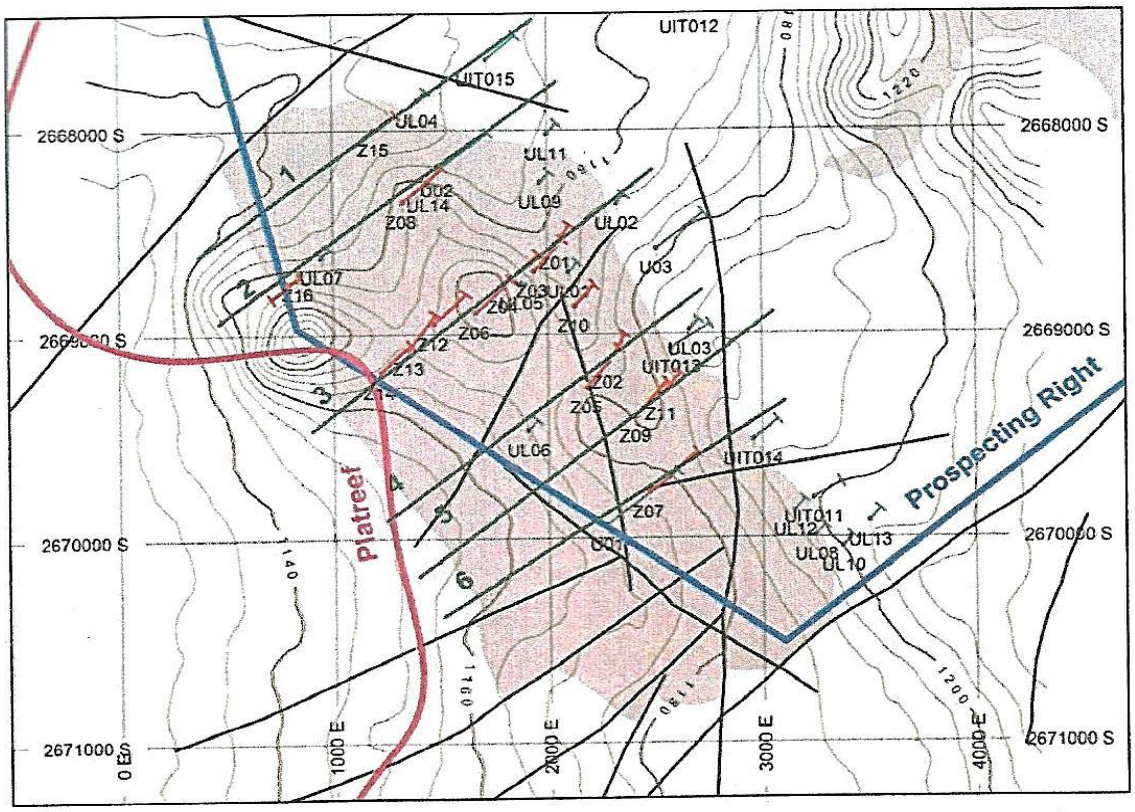


Figure 1-5: Map showing the historical boreholes across the Uitloop II body. (Croll et al., 2012).

In 2007; MSA Geoservices continued exploration activities on the Uitloop farm for Lesego Platinum Mining (Pty) Ltd., this time to investigate and delineate possible platinum and base metal sulphide mineralisation. Fieldwork included further soil geochemical analyses which pointed out a strong Ni anomaly along the southwestern portion of the Uitloop farm. Three additional boreholes, U 1, U2 and U3 were drilled up to depths of 662.03 m, 461.63 m and 438.16 m respectively, samples were taken and assayed for Cu, Ni, Pt, Pd and Au. MSA Geoservices concluded that the elevated Ni values in boreholes U1 and U2 allude to potentially exploitable Ni-mineralisation. Platreef style mineralisation was identified in borehole U3 at four stratigraphic intervals with variable thicknesses. MSA Geoservices also concluded that the strong Ni-Cu anomalies observed are an indication that the Uitloop farm hosts Platreef-style mineralisation which is attributed to sulphur contamination resulting from the assimilation of Bushveld Complex magmas with sedimentary country rocks (Lawman, 2007; Croll et al., 2012).

In 2010, an application in terms of Section 11 of the Mineral and Petroleum Resources Development Act (MPRDA), No, 28 of 2002, was granted for the transfer of prospecting rights for the Uitloop farm from SouthernEra Mining and Exploration (Pty) Ltd. to Lesego Platinum Mining (Pty) Ltd. A further application in terms of Section 11 of the MPRDA was launched in 2010 for the transfer of the prospecting right from Lesego Platinum Mining (Pty) Ltd. to Lesego Platinum Uitloop (Pty) Ltd. Umnex

Minerals Limpopo (Pty) Ltd. holds 100 % interest in Lesego Platinum Uitloop which now has prospecting rights for chrome, cobalt, copper, nickel and Platinum Group Minerals (PGMs) in the Uitloop farm. In 2011; Umnex appointed MSA Geoservices to provide a Preliminary Economic Assessment (PEA) on the Zebediela project (Croll et al., 2012).

Umnex drilled a total of sixteen boreholes (Z01 – 16) across the Uitloop II offshoot intrusion from October 2011 to January 2012, with a drilling programme aimed at the disseminated, potentially opencastable Ni-mineralisation in the Uitloop II intrusion. The depth of these boreholes ranged from 168.05 to 474.20 m. Work done on the boreholes included; downhole magnetic survey at 3 m intervals (7 m in altered zones), core logging, sampling and assaying at 2 m intervals as well as petrographic investigations, geochemical analysis (e.g. XRF, XRD, ICP-OES, SEM, EMPA) (Croll et al., 2012). Umnex drilled six additional boreholes (Z17 – 22) in 2017; two (Z19 and Z20) of which are used in this study.

1.3 MOTIVATION FOR PRESENT STUDY

The northern limb has previously received less attention from geologists as compared to the eastern and western limbs. Exploration activity has increased dramatically over the years as mining companies invested in academic research to have a better understanding of the development of the limb. However, very little published literature on some parts of the northern limb is available, particularly on the Uitloop farm.

The majority of the recent studies in the northern limb stem from the work done by Mauritz van der Merwe in the 1970s, as he was the first author to produce comprehensive geological maps of the entire limb as well as detailed mineralogical investigations of the seven Lower Zone offshoot intrusions (Kinnaird and McDonald, 2005). In the early 1980s, Hulbert and von Gruenewald were the first authors to conduct the first in depth whole rock geochemical investigations of the Lower and Critical Zones in the northern limb.

The stratigraphic positions, parental magmas well as the age of the Uitloop offshoot intrusions are not entirely clear, their emplacement mechanisms and crystallization history are also unknown. It is believed that the Lower Zone units in contact with dolomitic footwall rocks on the western portion of the Uitloop farm have potential to generate Platreef-style mineralisation, a few geochemical soil analyses and diamond core drilling programmes were commissioned to investigate the validity of this theory. Historical work done in the 1990s and early 2000s has identified the occurrence of disseminated mineralisation throughout the ultramafic sequence in the western portion of the Uitloop farm, with few higher-grade zones and no strong lithological affiliation observed.

1.4 OBJECTIVES OF THE PROJECT

The objectives of this research project include:

1) To understand the local geology of the study area as well as to aid sampling.
2) To provide complete information on the rock types, their mineral constituents and textural characteristics.
3) To compare the sulphide mineralisation on the Uitloop farm to the mineralisation in the Platreef and Critical Zone in the eastern and western limbs of the Bushveld Complex.
4) Further definition of the lithologies leading to an understanding of petrogenetic and mineralisation processes in the research area using whole-rock major and trace element geochemical data.
5) Identify major chemical and textural similarities and contrasts of Uitloop chromite with respect to Platreef chromite (from Turfspruit to Sandsloot and Overysel) as well as chromite from the Lower Zone, Merensky Reef and UG-2 of the main Bushveld Complex.

1.5 ENVISAGED OUTCOMES OF THE RESEARCH

1) Acquisition of modal mineralogy, composition, rock types and mineral textures.
2) Whole-rock geochemical and mineral chemical characteristics to substantiate stratigraphic correlation with the known units (either of the Lower Zone or the Platreef) of the northern limb.
3) Evaluation of igneous-country rock interactions *(*Substantial magma-country rock interaction expected changing magma composition triggering sulphide immiscibility).*
4) Emplacement and crystallization history of the intrusive lithologies.
5) Assessment of the PGE-Ni-Cu exploration potential?

1.6 DISCUSSION

The age as well as the three-dimensional form of the Uitloop body are unknown (Van der Merwe, 1976). Similar to the Uitkomst Complex (Fig 1-6); this Lower Zone body may have been emplaced as a conduit-type intrusion that stems from the TML located to the south, as a result the Uitloop intrusion could also be interpreted as a magma feeder conduit (to the main BC) that distributed the Lower Zone magmas from the centrally disposed TML main feeder Zone (Clarke et al., 2009a; Croll et al., 2012). The Uitkomst Complex is a Ni-Cu-PGE-Cr deposit, it is actively mined at Nkomati mine specifically for nickel as well as by-product PGE's. Mineralisation in the Uitkomst Complex is associated with disseminated and net-textured sulphides hosted by mafic/ultramafic as well as massive sulphides within the Archaean granite-gneisses which form the footwall to the Uitkomst complex (Maier et al., 2017). The Uitkomst Complex together with a similar intrusion named the Apiesdooringdraai peridotite body are orientated orthogonal to the Uitloop offshoot intrusions (Fig 1-6) (Clarke et al., 2009b).

This research study will determine whether the southwestern part of the Uitloop farm is of Lower Zone affinity or can be considered as an unrecognised extension of the Platreef, by identifying and comparing the type of mineralisation present in this area to better understood parts (Critical Zone, Lower Zone and the Platreef) of the Bushveld Complex.

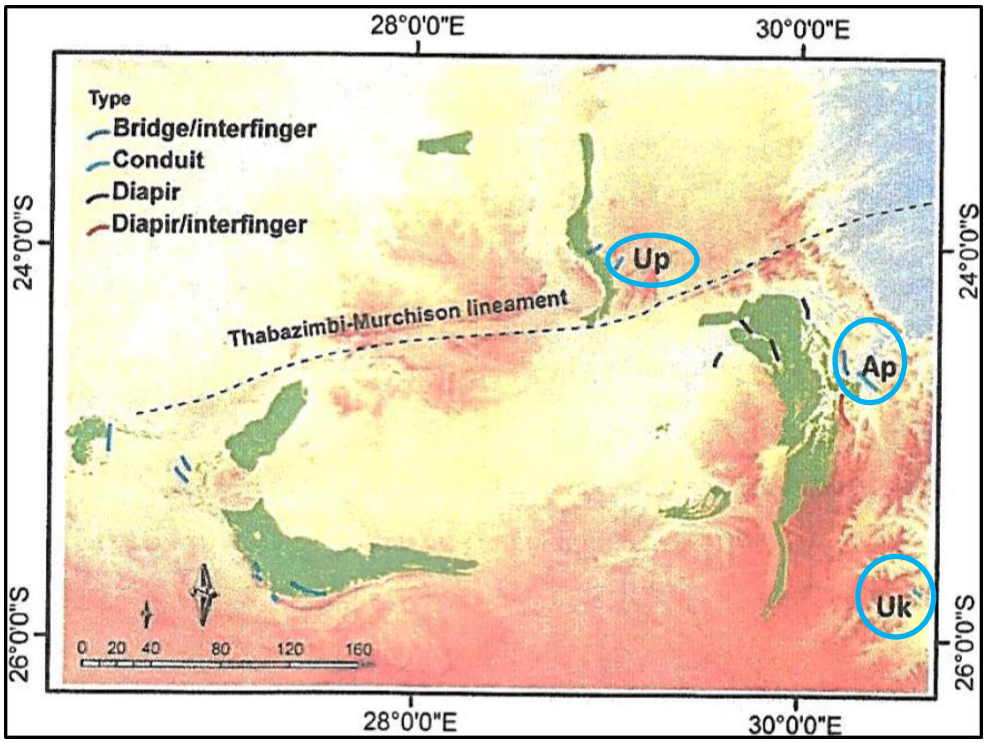


Figure 1-6: Location and orientation of conduit-type intrusions in the Bushveld Complex. Up=Uitloop, Ap= Apiesdooringdraai, Uk=Uitkomst (Modified after Clarke et al., 2009a).

CHAPTER 2

GENERAL GEOLOGY OF THE BUSHVELD COMPLEX

The Archaean Kaapvaal craton in southern Africa hosts the world's largest layered intrusion known as the Bushveld Complex (BC), it covers an area of about 90 000 km^2 (Finn et al., 2015). The BC intruded through the Paleoproterozoic sedimentary rocks of the Transvaal Supergroup as well as the Archaean granites around 2055.91 Ma (Zeh et al., 2015). This intrusion is also the world's largest repository of platinum group elements (PGEs), chromium and vanadium. The BC consists of four intrusive entities; the Rooiberg Group, Rustenburg Layered Suite and Bushveld granites (Rashoop Granophyre Suite and Lebowa Granite suite) (Kinnaird, 2005; Zeh et al., 2015). The Rustenburg Layered Suite is the most economically important entity as it hosts three principal platiniferous units of the BC; the UG-2 chromitite layer, the Merensky Reef and the Platreef ore bodies.

2.1 STRATIGRAPHY OF THE RUSTENBERG LAYERED SUITE

The Rustenburg Layered Suite (RLS) of the Bushveld Complex is divided into five limbs; the eastern limb, western limb, far western limb and the northern limb as well as the southeastern limb (Bethal limb) which is buried under younger sediments (Fig 2-1) (Eales et al., 1993). These limbs dip towards the geographical centre of the complex at approximately 15° (Du Toit, 1926). The eastern and western limbs are the most widespread and intensively studied outcrops of the RLS. Also, their stratigraphic sequences are similar (Eales et al., 1993) and can be correlated over about 300 km (Viljoen, 2016).

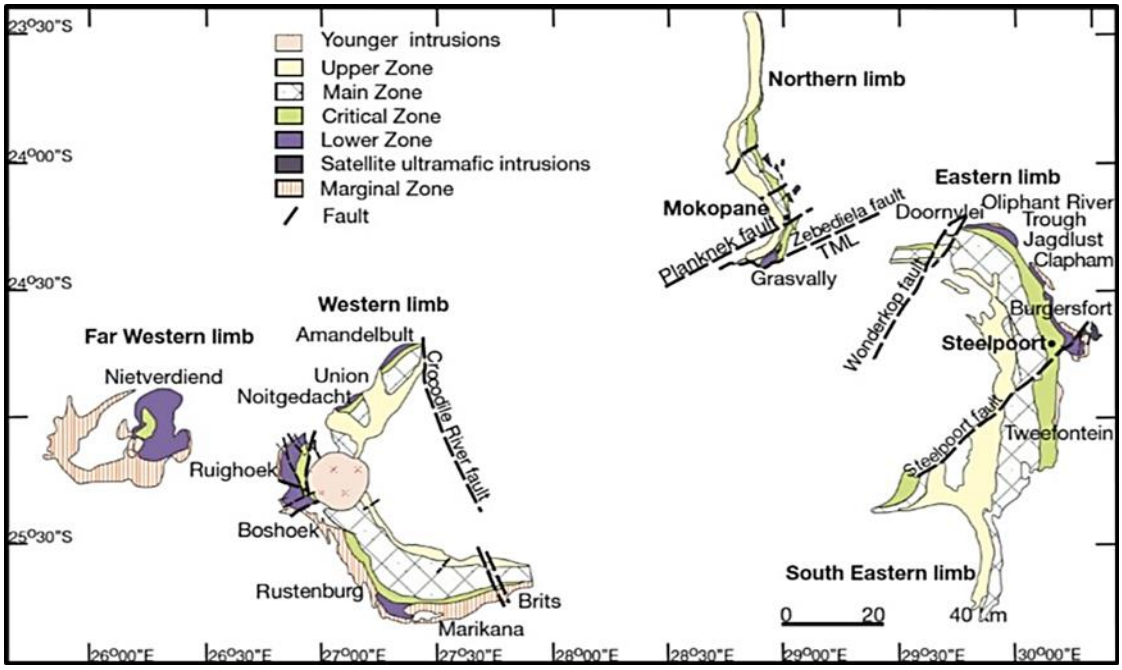


Figure 2-1: Geological map indicating different segments of the Rustenburg Layered Suite of the Bushveld Complex (Yudovskaya et al., 2013).

The mafic/ultramafic RLS in the eastern and western limbs attains a thickness of 7500 – 9000 m. The stratigraphy of the RLS is subdivided into five zones (Fig 2-2 & 2-3); the Marginal Zone (MRZ) at the base, Lower Zone (LZ), Critical Zone (CZ), Main Zone (MZ) and the Upper Zone (UZ) at the top (Cawthorn & Walraven, 1998). The Marginal Zone consists of pyroxenites and norites with variable thickness of up to 800 m, these mafic/ultramafic rocks host copious amounts of country rock xenoliths (Eales et al., 1993; Cawthorn & Walraven, 1998).

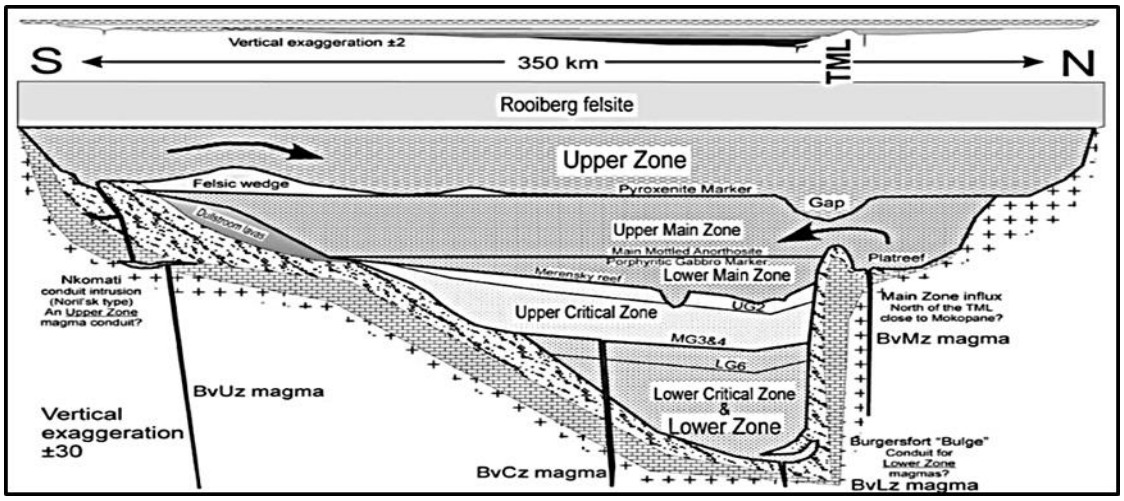


Figure 2-2: A north-south cross section through the Rustenburg Layered Suite of the Bushveld Complex (Kruger, 2005).

The Lower Zone overlies the Marginal Zone; it consists of alternating layers of dunite, orthopyroxenite and harzburgite (Eales et al., 1993). This ultramafic sequence does not have consistent exposure throughout the entire BC (Eales & Cawthorn, 1996), however it is best developed in the eastern limb where it has a maximum thickness of 1700 m (von Gruenewaldt et al., 1985). Cameron (1978) subdivided the LZ of the eastern limb, specifically in the Olifants river trough area, into the basal, lower orthopyroxenite, harzburgite as well as the upper orthopyroxenite subzones. Although the Lower Zone in the eastern and western limbs lacks economic mineralisation, trace amounts of chromite were observed in association with olivine and pyroxene within LZ sequences (Cameron, 1978).

The contact between the Lower Zone and the Critical Zone (CZ) is marked by an increase in plagioclase towards the top of the LZ sequence (Cameron, 1978) and an appearance of the lowest chromitite seam (Cawthorn et al., 1996). The lithology of the CZ is well-defined with recurring rock layers (Cameron, 1978; Eales et al., 1993). This 1500 – 1800 m thick mafic/ultramafic unit is divided into two different subzones; the lower Critical Zone (lCZ) and upper Critical Zone (uCZ). The lCZ consists of predominantly pyroxenites with minor peridotites (harzburgite & dunite). The uCZ starts at the appearance of first cumulus plagioclase layer and has more plagioclase than lCZ and is composed of norites, gabbronorites, pyroxenites and anorthosites (Cameron, 1982; Naldrett et al., 2009). The lCZ and uCZ both host chromitite layers which are enriched with PGEs (Cawthorn et al., 2002). The lCZ contains seven Lower Group (LG 1-7) and two Middle Group (MG 1-2) chromitite layers whereas the uCZ hosts two Middle Group (MG 3-4) and two Upper Group (UG 1-2) (as well as the UG-3 in the Eastern Limb) chromitite layers. The topmost portion of the uCZ is also characterised by presence of the Merensky and Bastard Reefs (Eales and Cawthorn, 1996). The Merensky Reef is a laterally persistent thin layer strongly enriched in PGEs with respect to underlying and overlying rocks. The Bastard Reef belongs to the Bastard Reef unit, which overlies the Merensky Reef unit. It is composed of noritic rocks with lesser PGEs and chromite content than the UG-2 chromitite layer and Merensky Reef (Eales & Cawthorn, 1996). The UG-2 chromitite layer and the Merensky Reef are the most economically important entities of the CZ as they are renowned for their world class chromium and PGE deposits (von Gruenewaldt et al., 1986).

The boundary between the Critical Zone and the overlying Main Zone (MZ) is marked by the top of the Bastard mottled anorthosite (Kruger, 1990). The MZ not only lacks chromite and olivine cumulates (Eales and Cawthorn, 1996) but also has coarser and less distinct layering as compared to the fine-scale layering of the CZ (Eales et al., 1993). It is the thickest zone of the RLS with a maximum thickness of approximately 3000 – 3400 m (von Gruenewaldt, 1973; Naldrett et al., 2009). This zone consists of predominantly norites and gabbronorites (von Gruenewaldt, 1973) as well as unique marker layers such as spotted anorthosite markers, porphyritic gabbro marker as well as pyroxenite markers

(Viljoen, 2016). The MZ lacks important mineralisation (Harney & von Gruenewaldt, 1995), however, it is mined for dimension stone (Kinnaird, 2005).

The Upper Zone (UZ) is a 2000 m thick mafic unit that overlies the MZ, with the boundary between the two marked by a sudden appearance of cumulus magnetite above the MZ pyroxenite Marker (Kruger 1990). The UZ consists of well-layered leucogabbro and anorthosite to gabbro and gabbrodiorite associated with a total of twenty-five magnetite layers (Eales & Cawthorn, 1996). The UZ is exploited for its vanadium content within some magnetite layers, this zone hosts about half of the world's vanadium ore deposits (Kinnaird, 2005).

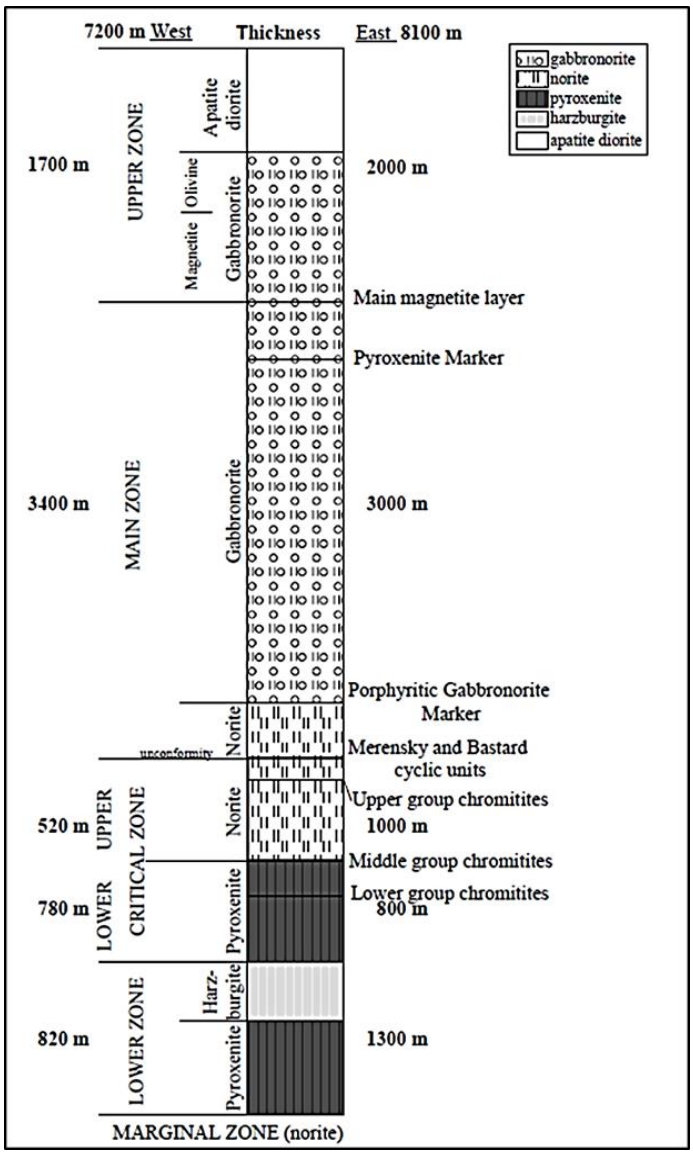


Figure 2-3: The stratigraphy of the Rustenburg layered suit of the Bushveld Complex (After Eales & Cawthorn, 1996).

2.2 MINERALISATION IN THE BUSHVELD COMPLEX

The Bushveld Complex is well known for its Cr and Ni-Cu-PGE mineralisation. The chromitites in the Bushveld Complex occur mainly in the Critical Zone of the eastern and western limbs, they account for over 80% of the world's chromium resources (Viljoen, 2016). The BC also hosts three of the most important PGE deposits in the world; the Merensky Reef, UG-2 chromitite layer and the Platreef orebodies (McLaren & DeVilliers, 1982; Cawthorn, 1999; Schouwstra, Kinloch & Lee, 2000). More recently a major deposit has been found on the Waterberg project in the north of the northern limb (Kinnaird et al., 2017).

2.2.1 CHROMITE

The chromitites in the Critical Zone of the eastern and western limbs are divided into three stratigraphical groupings; the Lower Group (LG), the Middle Group (MG) and the Upper Group (UG) (Fig 2-4) (Cousins & Feringa, 1964). The Merensky Reef in the uCZ is also associated with very thin (1 – 2 cm) discontinuous chromitite seams at the top and bottom of the Reef. These CZ chromitites are enriched with important PGE mineralisation, the UG-2 chromitite layer is a major economic PGE resource.

The Lower Group consists of seven major layers (LG 1–7) hosted by feldspathic pyroxenite while the Middle Group is composed of four layers (MG 1–4) hosted by feldspathic pyroxenite or norite. The Upper Group comprises of two chromitite units (UG 1–2) which are hosted by pyroxenite, norite or anorthosite, however a UG-3 chromitite layer is also observed in the eastern limb (Schurmann et al., 1998; Kinnaird et al., 2002). These chromitite layers may also consist of single or multiple seams (Fig 2-4). The boundary between the lCZ and the uCZ is marked by an appearance of an anorthosite layer just above the MG-3 chromitite layer (Cawthorn and Walraven, 1998; Kinnaird et al., 2002).

Most of these chromitite layers can be traced along-strike for distances of up to 300 km in both the eastern and western limbs, with thicknesses ranging between 0.15 – 2 m in thickness (Hatton & von Gruenewaldt, 1987; Scoon & Teigler, 1994; Schurmann et al., 1998). The chromium content (Cr_2O_3) of chromite in these chromitite layers in the CZ stratigraphy decreases upwards from 46 – 47% Cr_2O_3 in the LG-6 chromitites to 44 – 46% Cr_2O_3 in the MG chromitites and eventually 43% Cr_2O_3 in the UG-2 chromitites (Schurmann et al., 1998). This is reflected in the upward decrease in the Cr/Fe ratio; which ranges between 1.56 – 1.60 in the LG-6 chromitites, 1.35 – 1.50 in the MG chromitites and 1.26 – 1.40 in the UG-2 chromitites (Kinnaird et al., 2002). The dominant intercumulus phase within these chromitites also changes from orthopyroxene in the LG chromitites, to orthopyroxene and plagioclase in the MG chromitites and lastly plagioclase in the UG chromitites. Chromite is mainly mined from the

LG-6, MG-1 and MG-4 chromitite layers (Kinnaird et al., 2002). The Critical Zone is not as well developed in the northern limb; however, chromitites are observed in the Lower Zone and the Platreef lithologies which will be discussed in chapter 3.

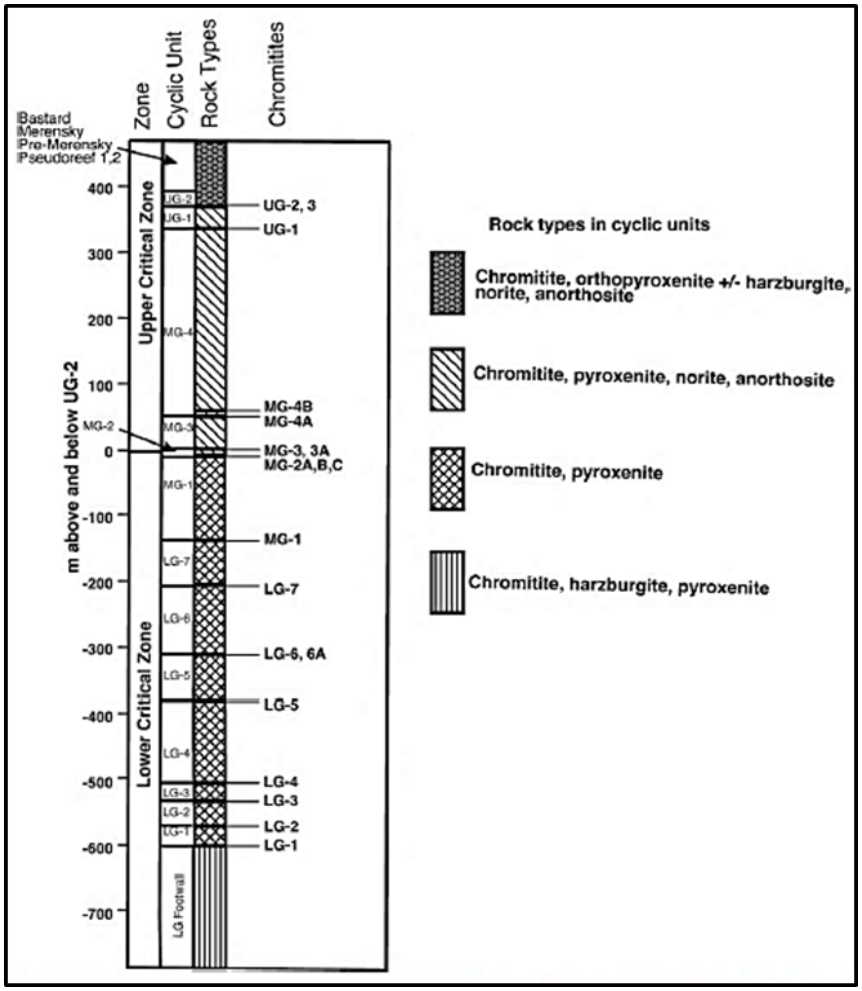


Figure 2-4: The stratigraphic positions of the chromitite layers within the Critical Zone (Naldrett et al., 2009).

2.2.2 PLATINUM GROUP ELEMENTS

Platinum group elements (PGE) refers to six transition metals; ruthenium (Ru), rhodium (Rh), palladium (Pd), osmium (Os), iridium (Ir) and platinum (Pt), these elements have similar physical and chemical properties, and tend to occur together in the same mineral deposits. PGE reefs are a type of deposit that form laterally persistent layers within layered intrusions (Yudovskaya et al., 2017). PGE are chalcophile elements and therefore strongly partition into immiscible sulphide liquids, as a result PGE are frequently associated with base metal sulphides such as pyrrhotite, pentlandite and chalcopyrite (Naldrett, 2004). However, in some chromitite reefs PGE and Platinum Group Minerals (PGMs) are also associated with chromite. PGEs in association with sulphides are present as solid

solutions in sulphide and as discrete PGMs whereas chromite does not incorporate significant PGE in its structure (Naldrett, 2004; Barnes & Ripley, 2016).

The UG-2 chromitite layer and the Merensky Reef in the eastern and western limbs as well as the Platreef at the base of the BC in the northern limb are no exception as they are hosted within the Archaean Kaapvaal craton (Maier & Groves, 2011). The MR and UG-2 contain PGEs as solid solution in sulphides (mainly in pentlandite) as well as discrete PGMs. The Platreef, which hosts PGE orebodies in the northern limb, will be discussed further in the next chapter.

The UG-2 chromitite layer (0.4 – 2.5 m thick) is located 15 – 400 m below the Merensky Reef (Lee, 1996; Schouwstra, Kinloch & Lee, 2000). The UG-2 is commonly underlain by a pegmatoidal feldspathic pyroxenite or melanorite, though in places anorthosite forms the footwall (Viljoen, 2016). A few low grade thin chromitites (<10 cm thickness) occur in the feldspathic pyroxenite hanging wall (Lee, 1996). The UG-2 consists of 60 – 90 % chromite, with minor plagioclase as well as sulphide minerals dominated by pentlandite and chalcopyrite with minor pyrite, pyrrhotite, arsenopyrite, bornite, chalcocite, covellite, galena and millerite (Vermaak, 1985). Although the UG-2 contains very low sulphide contents, these sulphides have a very high metal tenor (Maier & Barnes, 2008). The PGM assemblage is dominated by PtPd sulphides (35 %), the Ru sulphide laurite (30 %), with other PGMs including Pt-Fe alloys and intergrowths (21 %), Rh sulphides (11 %) and palladium alloys (3 %). The PGMs are also largely interstitial to the chromite grains and are associated with sulphide minerals (McLaren and DeVilliers, 1982). The PGE mineralisation in the UG-2 is top- and bottom-loaded (Schouwstra, Kinloch & Lee, 2000) with grades reaching up to 10 ppm (3.6 ppm Pt, 3.81 ppm Pd, 0.3 ppm Rh) (Lee, 1996).

The Merensky Reef generally has a thickness of about 1 m and has been traced for about 300 km across the eastern and western limbs, its dip ranges between 8 ° – 27 °, sometimes reaching up to 65° in the northeastern part of the eastern limb (Kinnaird, 2005). The Merensky Reef is a predominantly feldspathic pyroxenite and/or feldspathic pegmatoidal pyroxenite unit containing base metal sulphides (BMS) and PGMs. It is typically bound by thin (1 – 2 cm) discontinuous chromitite stringers that are associated with the highest PGE grades (top- and bottom-loaded). The hanging wall consists of feldspathic pyroxenite while the footwall consists of either anorthosites and/or norites (Viljoen, 2016).

2.3 DISCUSSION

Ni-Cu and PGE enriched deposits are formed from primitive, relatively magnesian, mantle-derived magmas or their differentiates, as a result, their deposits are commonly located in similar environments (i.e. mafic/ultramafic rocks) (Naldrett, 2004; Cawthorn et al., 2006). Many of the PGE deposits are generally located within stable cratons, where they are emplaced as stratabound or stratiform reefs within large layered intrusions (such as the Merensky Reef, UG-2 chromitite layer and the Platreef in the Bushveld Complex) (Maier & Groves, 2011). The Bushveld Complex is the largest known preserved layered intrusion in the world, it extends over an area of about 90 000 km^2 (Finn et al., 2015).

CHAPTER 3

THE NORTHERN LIMB

3.1 INTRODUCTION

The northern limb, on which this study is based, is in the Limpopo province in South Africa. It is exposed over an area of about 2000 km^2 as a north-south orientated 110 km long sinuous outcrop with a width of about 15 km (Fig 3-1) (van der Merwe, 1976; van der Merwe, 2008). The northern limb intruded through a succession of the Paleoproterozoic metasedimentary rocks of the Transvaal Supergroup in the south and rests upon the Archaean granite-gneiss towards the north. This is structurally detached from the eastern and western limbs by the ENE-WSW trending Thabazimbi-Murchison Lineament (TML), the Ysterberg-Planknek and Zebediela faults north of Mokopane are major branches of the TML (Fig 1-1). The northern limb is renowned for its platinum-bearing Platreef as well as the Lower Zone lithology associated with chromite and Ni-Cu-PGE mineralisation especially in the Grasvally area.

The northern limb outcrop is divided into three sectors at surface; the southern, central and northern sectors (Fig 3-1) (van der Merwe, 2008). The northern sector consists of predominantly the Upper Zone magnetite bearing rocks with a thin layer of Main Zone gabbronorites as well as the mineralised Platreef at the base of the sequence. The central sector on the other hand displays a complete RLS mafic rock sequence. Lastly, the southern sector is dominated by Main and Upper Zone sequences along with the Lower Zone and the upper units of the Critical Zone (van der Merwe, 2008).

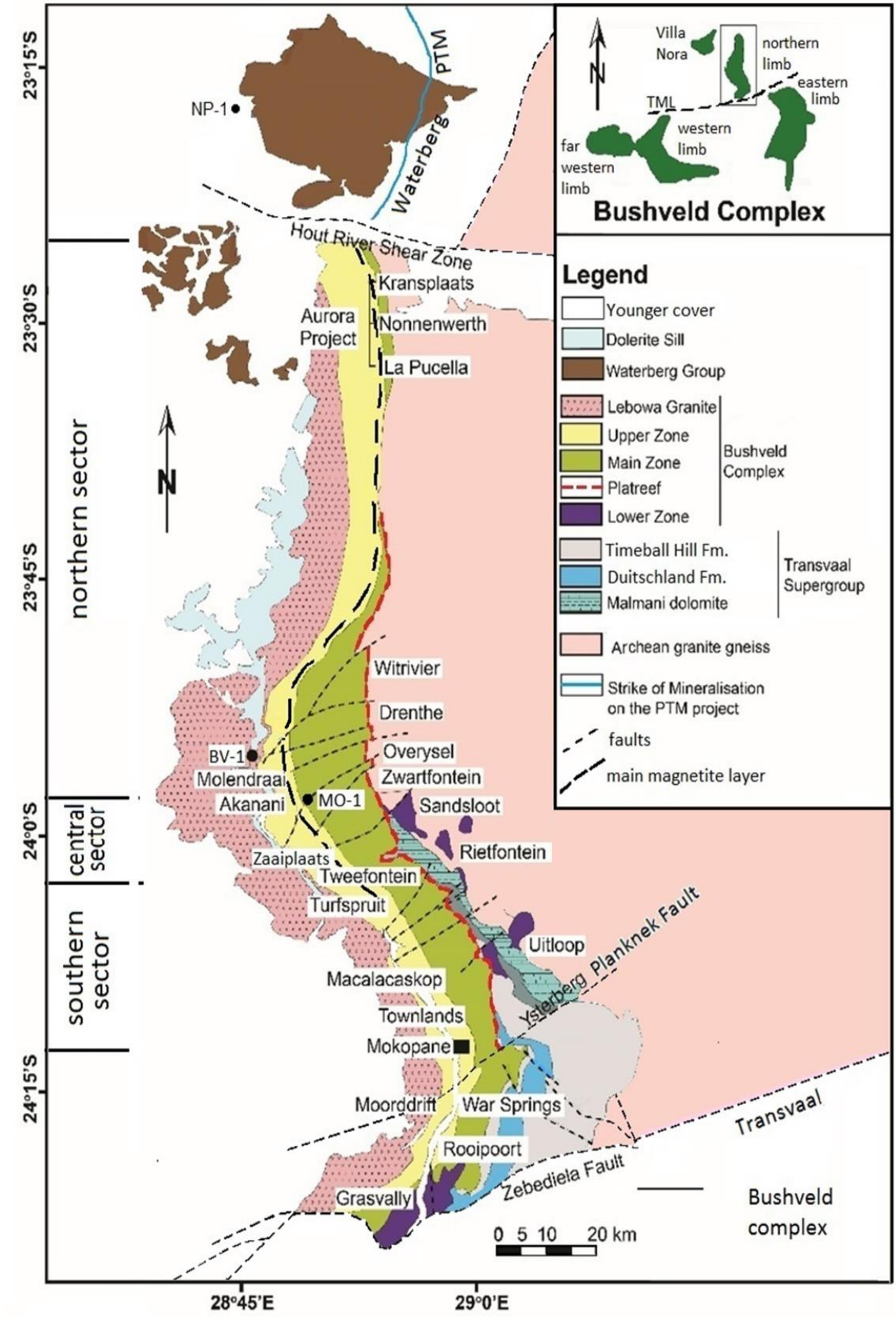


Figure 3-1: Geological map of the northern limb of the Bushveld Complex (Kinnaird & McDonald, 2018).

3.2 THE STRATIGRAPHY OF THE NORTHERN LIMB

The stratigraphy of the northern limb does not completely correlate with that of the eastern and western limbs; not only is the Marginal Zone notably absent in some parts of the limb (van der Merwe, 2008) but also the Lower Zone is not continuous (Fig 3-1). Moreover, the northern limb lacks extensive outcrops of the Critical Zone (van der Merwe, 1976).

The Marginal Zone (MRZ) in the northern limb is of very minute extent; with variable thickness of up to tens of meters (van der Merwe, 2008). The MRZ in the northern limb appears to be an intrusive layer and is composed of gabbronorite where it occurs in contact with the Critical and Main Zones as well as noritic rocks where it is in contact with the Lower Zone (van der Merwe, 1976; Maier et al, 2013). Xenoliths of granite, hornfels and quartzite as well as carbonate rocks have been observed within this zone. The MRZ has been traced out in the Grasvally, Rooipoort, Uitloop, Sandsloot and Zwartfontein farms (van der Merwe, 1978), where there is an interaction between the underlying floor rocks and main Bushveld intrusion (van der Merwe, 2008). A thick MRZ was also traced out beneath Turfspruit and Sandsloot (Yudovskaya et al., 2013).

The LZ is well developed south of Mokopane in Vaalkop 325 KR, Volspruit 326 KR and Grasvally 293 KR farms (Fig 3-1) (Hulbert and von Gruenewaldt; 1982), with a maximum thickness of 1700 m documented on Grasvally (Hulbert, 1983). This ultramafic sequence is termed the Grasvally body (Van der Merwe, 1976). It consists of 37 cyclic units; each cyclic unit is composed of olivine-chromite cumulates overlain by olivine-orthopyroxene-chromite and orthopyroxene cumulates (Hulbert and von Gruenewaldt; 1982). The LZ in the south is divided into three segments; the sulphide and PGE mineralised Volspruit and Drummondlea subgroups as well as the Moordrift subzone (Fig 3-3) (Hulbert, 1983). There are two economically important chromitite layers located at 620 m and 690 m depths in the Drummondlea subgroup as well as a Ni-PGE mineralised horizon in the Volspruit subgroup known as the Volspruit PGE Zone (Fig 3-3) (Hulbert & von Gruenewaldt, 1982; Hulbert & von Gruenewaldt, 1985).

Historically; the LZ north of Mokopane was thought to be emplaced only as pyroxenite dominated offshoot intrusions beneath the Platreef; the Uitloop I, Uitloop II, Rietfontein, Bultongfontein I, Bultongfontein II and Zwartfontein bodies in the central sector (Fig 3-1) (van der Merwe, 1976; Yudovskaya et al., 2013). These offshoot intrusions occur as discrete sheet-like bodies arranged in a semi-circle around the position of the northern limb feeder inferred by gravity data west of Mokopane, the rocks here also appear to have been subjected to metamorphism induced by emplacement of the main Bushveld intrusion (van der Merwe, 1978; van der Merwe, 2008). The RLS in the central sector is fully developed (van der Merwe, 2008); this means that although the Marginal

Zone is not well developed throughout the northern limb (van der Merwe, 1976); it could possibly underlie the LZ offshoot intrusions in the central sector as per the stratigraphy of the RLS. In areas where the Marginal Zone is not developed, the LZ is underlain by sediments of the Transvaal Supergroup and the Archaean granite-gneisses (van der Merwe, 1976). To investigate whether the LZ north of Mokopane was only emplaced as offshoot intrusions, a recent study by Yudovskaya et al. (2013) discovered the presence of an 800 m thick LZ sequence beneath the Platreef in Sandsloot and Turfspruit. The LZ in these areas is composed of cyclic sequences dunite, harzburgite and pyroxenite whereas the footwall rocks consist of hornfels and calcsilicate of the Duitschland Formation. Some of these LZ satellite intrusions (Uitloop and Zwartfontein bodies) host chromitite layers and lenses as well as Ni-Cu-PGE mineralisation (van der Merwe, 1978). The Lower Zone in the northern limb is different from the rest of the Bushveld Complex because of its extreme thickness, high grade chromite ore as well as the silicate mineral compositions (e.g. higher Mg content in orthopyroxene and olivine) (van der Merwe, 1976).

The Critical Zone is poorly developed in the northern limb in comparison to the eastern and western limbs (van der Merwe, 1976). The Grasvally-Norite-Pyroxenite-Anorthosite (GNPA) member and the Platreef in the northern limb have been equated to the Upper Critical Zone found elsewhere in the BC (Hulbert 1983; van der Merwe 2008; Maier et al., 2008a). The GNPA member is located south of the Ysterberg–Planknek fault; it is a 350 m thick sequence that consists of cyclic units of norite, pyroxenite and anorthosite (Hulbert & von Gruenewaldt, 1983). This mafic unit hosts a PGE-bearing chromitite seam that has similar characteristics to the UG-2 chromitite layer in the eastern and western limbs; this layer has been labelled the 'UG2-like chromitite layer' (Hulbert, 1983). Although there are similarities between the two, chromite of the 'UG2-like chromitite' has elevated TiO_2 and Al_2O_3 concentrations (Hulbert, 1983; Hulbert & von Gruenewaldt, 1986). Also, the PGE pattern in the GNPA member is quite different from that of the UG-2 chromitite layer in the eastern and western limbs (von Gruenewaldt et al., 1989). The GNPA member has the same stratigraphic position as the Platreef, it is overlain by the Main Zone with the Lower Zone and the Pretoria Group sediments as the footwall (Hulbert, 1983; von Gruenewaldt & Hulbert, 1985; Smith, 2014).

North of the Ysterberg–Planknek fault, the NW/N striking Platreef is emplaced as multiple sill-like intrusions located at the base of the northern limb (Figs 3-1) (Kinnaird et al., 2005; van der Merwe, 2008). It consists of pyroxenites, peridotites, serpentinites, norites, gabbronorites as well as a variety of hybrid lithologies (Holwell et al., 2006). There are also various country rock xenoliths incorporated within the Platreef. South of Mokopane the xenoliths consist of shales, siltstones, mudstones and

hornfelsed banded ironstones whereas in the north the Platreef contains dolomite and calcsilicate xenoliths (van der Merwe, 1976; Kinnaird et al., 2005). The Platreef is discussed further in section 3.3.

The MZ in the northern limb is also characterised by rhythmic and cryptic layering of gabbro, anorthosite, pyroxenite as well as peridotitic rocks such as harzburgite and lherzolite (van der Merwe, 1976). This stratigraphic unit is not only thinner (1700 m) (von Gruenewaldt et al., 1989) but also lacks pyroxenite markers present in the eastern and western limbs (van der Merwe, 1976). The MZ in the northern limb however has a unique appearance of a troctolitic unit north west of Mokopane (Fig 3-3) (von Gruenewaldt et al., 1989). These troctolitic rocks have somewhat similar mineral compositions to that of the uCZ in the eastern and western limbs (Roelofse, 2010).

The MZ in the northern limb has also been proven to be highly prospective for PGE mineralisation. More recently, a major PGE deposit hosted by a >3.5 by 24 km lobate intrusion was discovered by Platinum Group Metals (PTM) on their Waterberg project which is located north of the Hout River Shear Zone (HRSZ) (Fig 3-1) (McCreesh, 2013; Kinnaird et al., 2017). The Archaean gneisses that are commonly interfingered with pyroxenite form the footwall to the Waterberg intrusion while the Waterberg Group sediments and a thin layer of Karoo sediments constitute the hanging wall lithologies (McCreesh, 2013). The U/Pb zircon dating indicated the ages for the Waterberg intrusion to be 2059 ± 3 and 2053 ± 5 Ma, thus the intrusion is coeval with the intrusion of the Bushveld Complex (Huthmann et al, 2016).

According to Kinnaird et al. (2017) and McCreesh et al. (2018), the Main Zone at the Waterberg Project (Fig 3-2) consists of the basal ultramafic sequence (UmS), it varies in thickness from 2.5 – 100 m and consists of olivine pyroxenite, orthopyroxenite, feldspathic pyroxenite and feldspathic harzburgite. The UmS is then overlain by a 400 – 800 m thick troctolite-gabbronorite-anorthosite sequence (TGA) which is composed of troctolite, olivine gabbronorite and norite with minor feldspathic pyroxenite and anorthosite. The UmS and TGA host two PGE reefs, the lower F-zone which extends over a strike length of 17 km and the upper T-zone which is restricted to the southern portion of the Waterberg project area. The F-zone is hosted within the UmS (Fig 3-2), where it attains a thickness of <10 m in the southern portion of the Waterberg Project area but thickens to about 60 m in the central portion (termed the “super F-zone”) (Kinnaird et al., 2017). The T-zone is situated at the contact between the TGA and the Upper Zone (Fig 3-2). The T-zone is subdivided into the upper T1 and lower T2, in some areas these two units are separated by a 20 – 35 m thick middling unit which consists of olivine-bearing feldspathic pyroxenites, pegmatoidal leucogabbro or a vari-textured pegmatoidal anorthosite. T1 attains a maximum thickness of about 20 m and is hosted by feldspar-rich pegmatoid, feldspathic

pyroxenite, troctolite/harzburgite and gabbronorite. In contrast, T2 ranges in thickness from 2 – 15 m and is associated with gabbronorite and gabbro (Kinnaird et al., 2017).

The PGE mineralization in the T-reef and F-reef is associated with sulphides, particularly pyrrhotite, pentlandite, chalcopyrite and pyrite. This mineralization is Pd-dominated, with unusual amounts of Au in the T-reef. The Pt + Pd + Au grades range between 1 – 7 g/t (reaching up to 14 g/t) in the T-zone and while the highest grade in the F-zone can be up to 10 g/t (McCreesh et al., 2018).

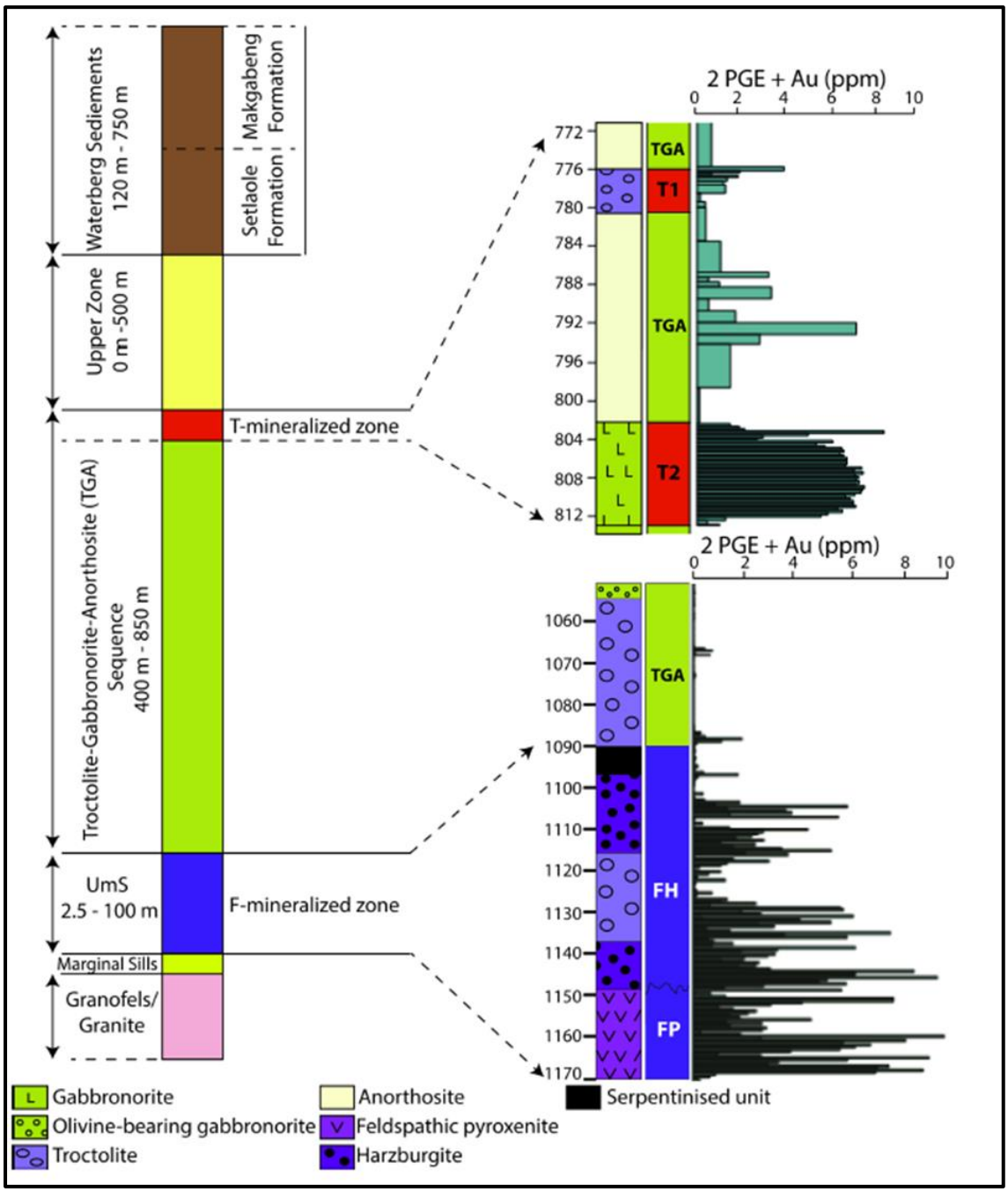


Figure 3-2: A simplified stratigraphy of the Waterberg project area showing the position of the mineralised intervals, F-zone and T-zone, PGE grades are also presented in the form of histograms (Kinnaird et al., 2017).

The Upper Zone in the northern limb has a thickness of about 1100 m and is composed of alternating units of gabbro, magnetitite gabbro, magnetite and spotted anorthosite (van der Merwe, 2008). The UZ is identified by the presence of twenty cumulus magnetite layers with elevated vanadium and titanium (van der Merwe, 1976). However, the UZ in the Waterberg project area is characterised by a 120 m thick sequence of gabbronorite, anorthosite, feldspathic pyroxenite, feldspathic harzburgite and troctolite (McCreesh et al., 2018). The in the Waterberg project also lacks the distinctive magnetite layers, rather very fine-grained magnetite disseminations were identified using a magnetic susceptibility meter (Huthmann et al., 2016; Kinnaird et al., 2017).

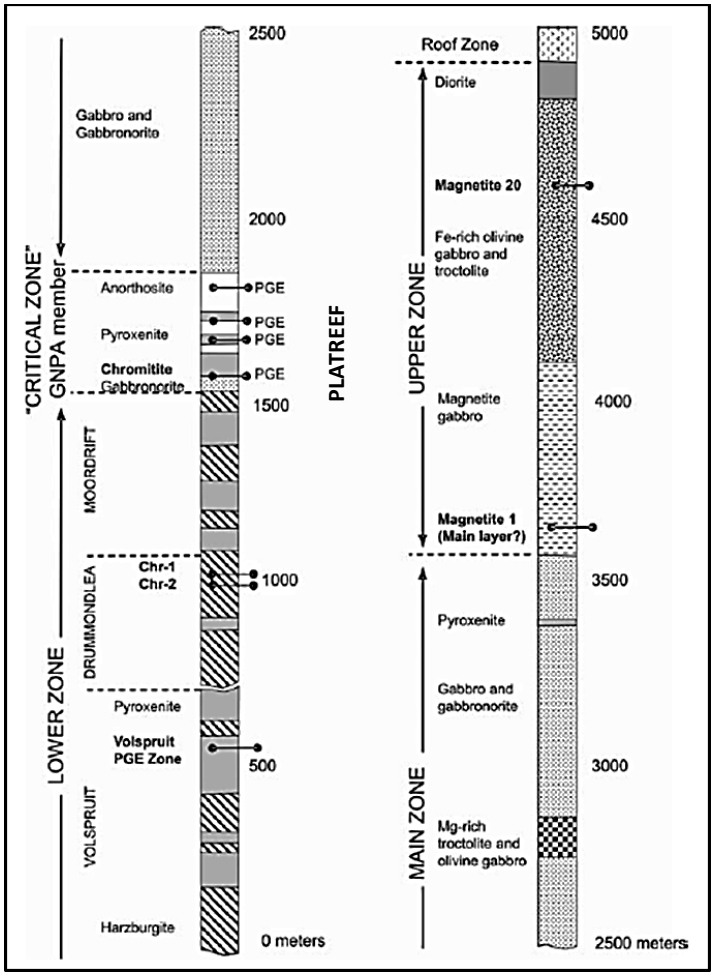


Figure 3-3: The stratigraphy of the northern limb indicating the occurrence of economic mineralisation within different Zones (McDonald et al., 2005).

3.3 THE PLATREEF

The Platreef is a unit or package that is composed of intercalated igneous mafic/ultramafic, hybrid and contact metamorphic rocks located north of the Ysterberg–Planknek fault in the northern limb, it extends for over 35 km northwards from Mokopane and dips 40° – 60° to the west. This package is emplaced as multiple, chemically distinctive, sill-like intrusions between the Paleoproterozoic Transvaal Supergroup to Archaean granites-gneisses and Main Zone lithologies, where it attains a thickness of 10 – 400 m (van der Merwe, 1978; Kinnaird et al., 2005). The internal structure and lithologies of the Platreef are highly variable and depend on the changing footwall composition. The mineralisation is hosted by feldspathic pyroxenites, feldspathic harzburgites and by different hybrid rocks and exoskarns (Yudovskaya et al., 2017). The Platreef is increasingly recognised as a stratigraphic equivalent of the Upper Critical Zone (Maier et al., 2008) or the Critical Zone (Yudovskaya et al., 2017; Grobler et al., 2018). Grobler et al. (2018) discovered a down-dip extension of the Platreef with a more layered sequence on Turfspruit farm, known as the Flatreef. This discovery has enabled a better correlation between the Platreef in the northern limb and the Critical Zone in the eastern and western limbs.

3.3.1 HANGING WALL LITHOLOGIES

The Main Zone is made up of mainly medium-grained norites and gabbronorites composed of cumulus plagioclase with cumulus orthopyroxene and oikocrystic clinopyroxenes. A thin layer of fine-grained poikilitic leuconorite, containing up to 90% plagioclase and pyroxene oikocrysts, is observed at the base of the sequence. Pyroxenites of Platreef affinity are also encountered in the Main Zone as well as sporadic calcsilicate xenoliths like those of the footwall (Fig 3-4) (Holwell et al., 2005). Later Main Zone norites/ gabbronorites also intruded the Platreef pyroxenitic packages as sills (inter-fingering) (Kinnaird, 2005).

3.3.2 FOOTWALL LITHOLOGIES

From south to north; the Platreef displays a downward transgression into different footwall lithologies (van der Merwe, 1978). Kinnaird et al. (2005) divided the Platreef into Southern, Central and Northern Sectors based on the variation of footwall lithologies (Fig 3-4). The Southern Sector extends from Townlands to Tweefontein Hill, where the Silverton, Timeball Hill and Duitschland Formations form the footwall whereas the Central Sector on northern Tweefontein, Sandsloot and Zwartfontein is characterised by Penge banded iron formations and Malmani dolomite footwall rocks. Lastly, the Archaean granite-gneiss footwall on Overysel and northwards constitute the Northern Sector.

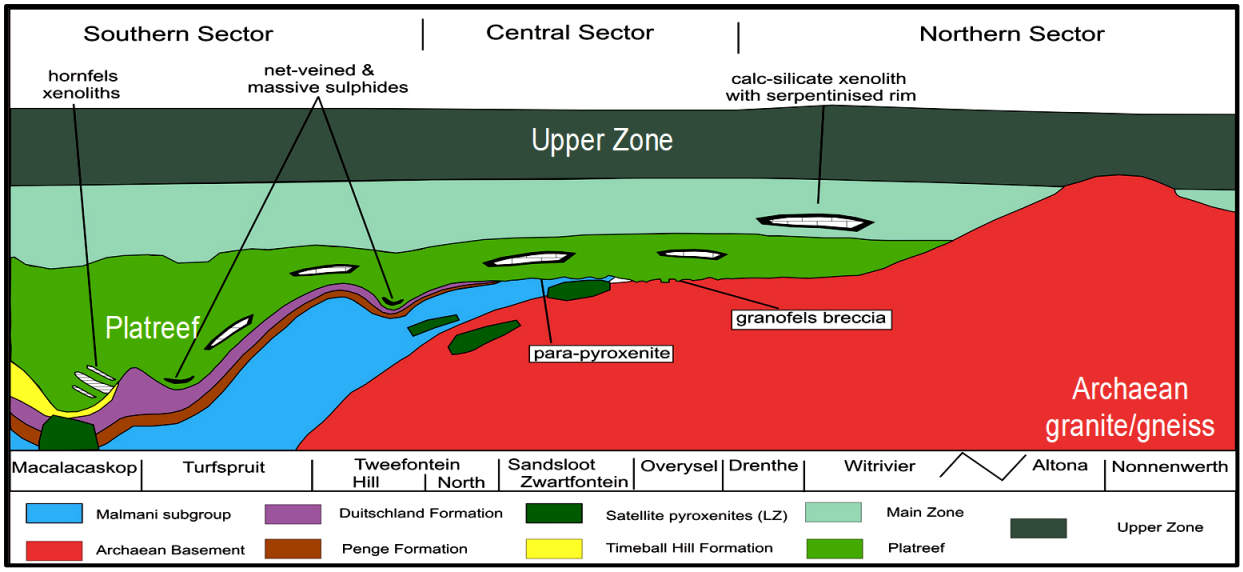


Figure 3-4: A schematic cross-section through the entire strike length of the Platreef (Kinnaird et al., 2005).

3.3.3 PLATREEF LITHOLOGIES

The Platreef sequence thins out from south to north, attaining a maximum thickness of 400 m on Turfspruit to <50 m on Drenthe (Fig 3-4) (Kinnaird et al., 2005). This discrepancy in thickness is thought to be partially controlled by structures in the footwall rocks (Friese and Chunnett, 2004; Nex, 2005). According to Holwell et al. (2005), the Platreef consists of predominantly feldspathic pyroxenite rocks made up of cumulus orthopyroxene with minor intercumulus plagioclase and clinopyroxene as well as accessory interstitial BMS. Other magmatic rock types noted in the Platreef stratigraphy include pyroxenites, peridotites, serpentinites, norites and gabbronorites (Kinnaird et al., 2005). Discontinuous chromite-rich horizons (chromitite stringers and chromite disseminations) are also associated with Platreef lithologies (Holwell & McDonald, 2006; Yudovskaya & Kinnaird, 2010; Grobler et al., 2018). The Platreef also comprises a variety of hybrid rocks along strike, whose composition is attributed to interaction of the Platreef magma with the changing footwall composition. For example; parapyroxenites and granofels result from the assimilation of dolomitic and granite-gneiss respectively. The type of country rock xenoliths within the Platreef also differ along strike, xenoliths consist of metamorphosed shales, siltstones, mudstones and banded ironstones in the Southern Sector while serpentinised calcsilicate xenoliths are more abundant in the Central Sector (van der Merwe, 1976; Buchanan et al., 1981, Kinnaird et al., 2005, Kinnaird, 2005; Holwell et al., 2005).

3.3.4 PLATREEF SECTORS

3.3.4.1 SOUTHERN SECTOR

Manyeruke et al. (2005) described the Platreef on Townlands farm as a 150 m thick package of gabbronorites and feldspathic pyroxenites underlain by quartzites and shales of the Timeball Hill Formation. Three distinct Platreef sills (lower, middle and upper) that are separated by layers of hornfels were identified based on their mineralogical and geochemical characteristics. The Platreef sequence on Macalacaskop and Turfspruit farms is much thicker (up to 400 m) than elsewhere (Yudovskaya & Kinnaird, 2010) and consists of diverse rock types which include feldspathic pyroxenites, peridotites, norite, gabbro and occasionally anorthosites (Kinnaird et al., 2005). The Platreef on the two farms is underlain by hornfelses and calcsilicates of the Duitschland Formation (Kinnaird et al., 2005; Hutchinson & Kinnaird, 2005). Recent studies have shown that footwall lithologies on Turfspruit differ from south to north; the Platreef on southern Turfspruit is separated from the underlying Lower Zone by a 300 m thick hornfels layer intercalated with the norite and feldspathic pyroxenite of Marginal Zone affinity. In the central and northern parts of Turfspruit farm, the Platreef is underlain by dolomitic and evaporitic rocks of the Duitschland Formation (Kinnaird et al., 2005; Yudovskaya et al., 2013; Kekana, 2014). At Turfspruit, the persistent PGE reefs are located at the top of the Platreef close to the contact with the overlying Main Zone and they are thought to be equivalent of the Merensky Reef (Yudovskaya et al., 2017; Grobler et al., 2018). In addition, contact-style sulphide-rich mineralisation occurs in the lower part of the Platreef at Turfspruit.

A recent study by Grobler et al. (2018) on Turfspruit revealed an area known as the Flatreef, where the Platreef temporarily transitions from a 40° – 60° westerly dip to gently dipping/subhorizontal (15°), down-dip the Platreef resumes its normal westerly part of the farm (deep Flatreef extension) (Fig 3-5). The Flatreef is located at 600 – 1100 m depth and extends over an area of about 15 km^2; it consists of primary magmatic layering, cyclic sequences as well as 20 – 30 m thick mineralised horizons (Grobler et al., 2018).

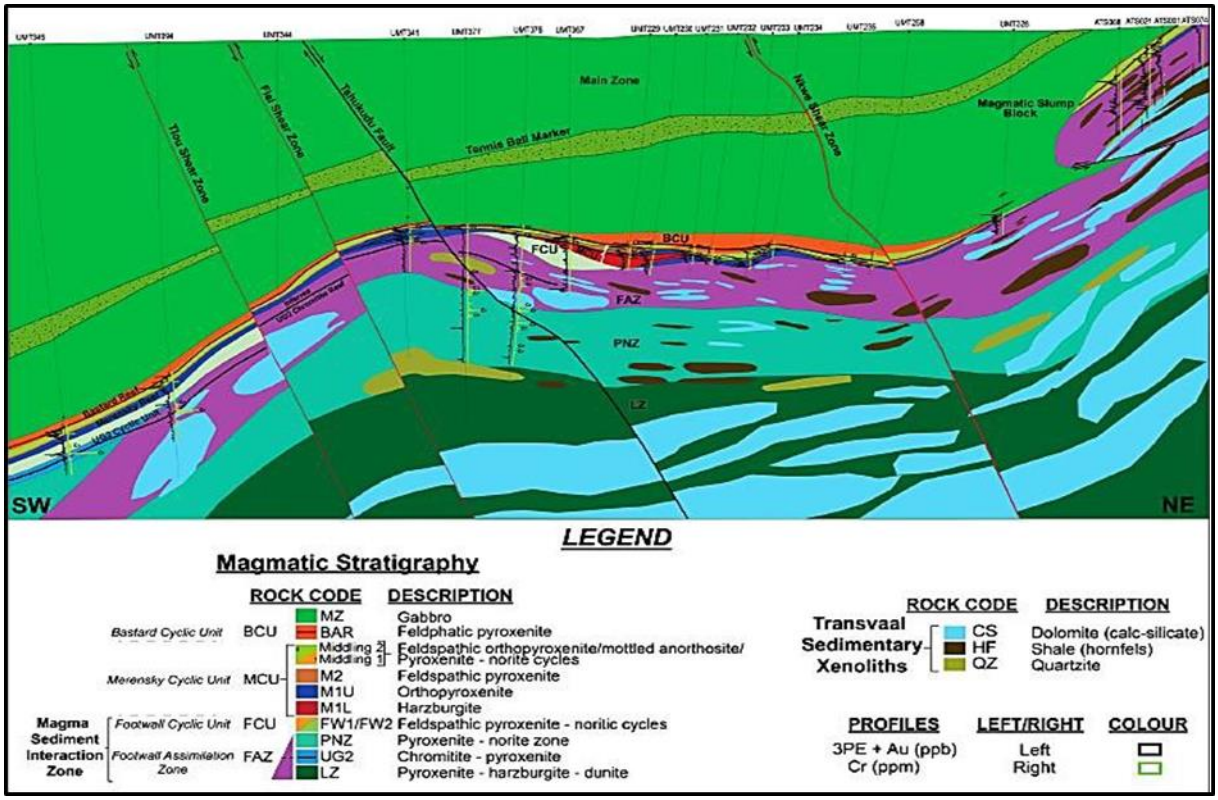


Figure 3-5: A NE-SW cross-section across the Flatreef and its down-dip extension on Turfspruit farm (Grobler et al., 2018).

According to Grobler et al. (2018), the Flatreef is underlain by sedimentary rocks of the Duitschland Formation (shale and dolomite metamorphosed to hornfels and calcsilicate) in the east and 800 m thick cyclical units of pyroxenite, dunite and harzburgite of Lower Zone affinity in the central to southwestern part of Turfspruit farm (Fig 3-5). The Lower Zone and the Duitschland Formation are then overlain by a 570 m thick Pyroxenite-Norite Zone (PNZ) (Fig 3-5) which is composed of poorly differentiated, fine- to medium-grained pyroxenites and norites with abundant hornfels xenoliths and poorly developed bands, stringers and disseminated chromitite zones are also observed towards the top. PNZ is overlain by the Footwall Assimilation Zone (FAZ) which consists of norite with shale-hornfels xenoliths as well as parapyroxenite/paraharzburgite units with abundant xenoliths and large bodies (up to >100 m in width and thickness) of calcsilicate and hornfels of the Duitschland Formation (Grobler et al., 2018). The FAZ is then overlain by a 45 – 100 m thick sequence of alternating pyroxenite-norite-anorthosite sub-units known as the Footwall cyclic unit (FCU). Most of the contacts between pyroxenite and anorthosite are associated with thin chromitite stringers, also; the pyroxenite layers, mainly those at the base of the FCU, are associated with disseminated sulphides (Grobler et al., 2018).

The Main Reef is represented by a lower 15 m (can be up to 60 m) thick pegmatoidal ultramafic layer which consists of orthopyroxene and/or harzburgite with a basal chromitite stringer and an overlying 2.5 – 10 m thick orthopyroxenite layer bound by chromitite stringers. The Middling Unit above the

Main Reef comprises a 14 – 100 m interval of interlayered pyroxenite-norite-anorthosite in the deep western and south-central parts of the Turfspruit farm and feldspathic orthopyroxenite in the shallow central and eastern parts of the farm. The pyroxenitic Upper Reef attains a thickness of 5 – 10 m and hosts a thin poorly developed basal chromite stringer and sulphide mineralisation Grobler et al., 2018). The upper part of the Flatreef is subdivided into a hanging wall unit 2 (HW2) which consists of mottled anorthosite (0.3 – 30 m thick) and an underlying hanging wall unit 1 (HW1) composed of interlayered mela- and leucogabbronorite with thicknesses of up to 20 m (Fig 3-6) (Grobler et al., 2018).

Grobler et al. (2018) deduced that the PNZ not only has similar lithologies to the Lower Critical Zone but also holds the same stratigraphic position above the Lower Zone (Fig 3-6). The thick chromitite layers at the base of the FCU at Turfspruit resemble the UG-2 chromitite layer in the eastern and western limbs, thus the two mineralized horizons have been correlated (Grobler et al., 2018). The harzburgite and orthopyroxenite within the pegmatoidal ultramafic unit are correlated with the lower portion of the Merensky Reef as M1 lower and M1 upper respectively, whereas the overlying pyroxenite layer along with the upper and basal chromitite stringers have been equated to the upper portion of the Merensky Reef (M2). The Middling Unit is linked to the Merensky Cyclical Unit (MCU). The pyroxenitic Upper Reef with a basal chromite stringer has been correlated to the Bastard Reef (BAR) while the mottled anorthosites of the HW1 together with the mela- and leucogabbronorite rocks of the HW2 have been assigned to the Bastard Cyclic Unit (BCU) (Fig 3-6) (Grobler et al., 2018).

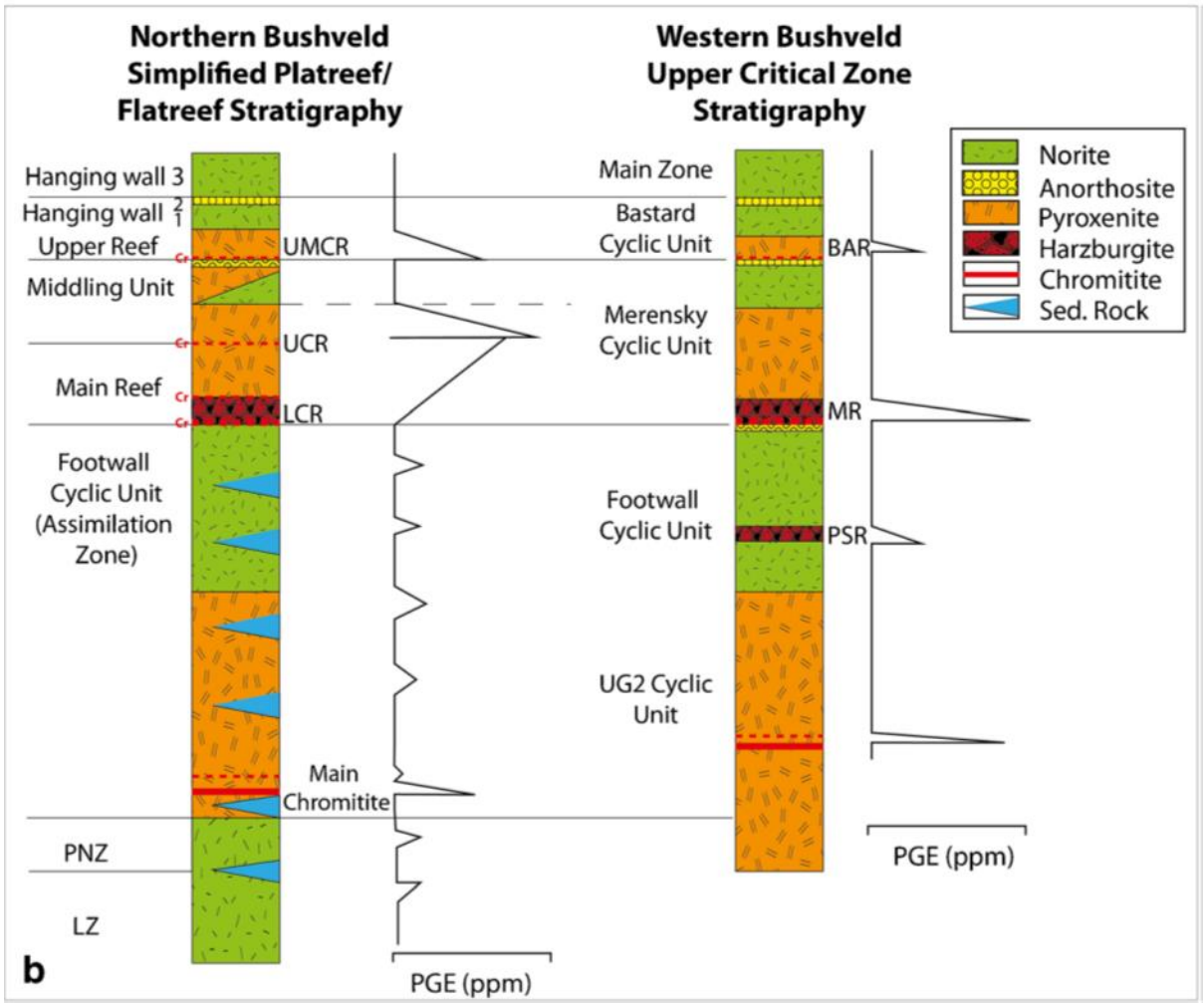


Figure 3-6: The stratigraphical correlation between the Platreef/Flatreef and the Upper Critical Zone of the western limb of the Bushveld Complex (Grobler et al., 2018).

3.3.4.2 CENTRAL SECTOR

The Platreef on Tweefontein Hill and Tweefontein north are underlain by hornfels and calcsilicate rocks of the Duitschland Formation as well as banded ironstones of the Penge Formation (metamorphosed to magnetite-bearing hornfels) (Viljoen & Schurmann, 1998; Nex, 2005; McCutcheon, 2012) (Fig 3-4). The Platreef on Tweefontein North is 220 m thick; it is composed mainly of pyroxenites with minor norites and basal micronorites (Nyama et al., 2005). The Platreef on Sandsloot is underlain by Malmani dolomites; it has a maximum thickness of >400 m (Harris & Chaumba, 2001; Armitage et al., 2002; McDonald et al., 2005) and consists of predominantly pegmatoidal feldspathic pyroxenites with minor gabbros, clinopyroxenites, peridotites, serpentinites and calcsilicate xenoliths. Parapyroxenites and serpentinised calcsilicates form at the boundary between the Platreef lithologies and the footwall.

The southern portion of Zwartfontein farm has similar footwall lithologies (Malmani dolomites) as Sandsloot, however the Platreef sequence is a lot thicker here and contains a greater proportion of

serpentinised calcsilicate xenoliths (Holwell & Jordaan, 2006). Further north, the Platreef on Zwartfontein is underlain by Archaean granite-gneisses. In Lonmin's Akanani Project area on Zwartfontein farm, the Platreef has a thickness ranging between 80 – 300 m and extends down-dip to the west of the surface outcrop. Deep drilling in the area intersected Platreef containing calc-silicate xenoliths on a footwall composed of gneiss and Lower Zone pyroxenites and harzburgites; thick chromitiferous horizons are also encountered (Spies, 2005). The Platreef on Overysel is underlain by Archaean granite-gneisses, assimilation between Platreef magma and these footwall rocks lead to formation of granofels. Cawthorn et al. (1985) described the Platreef as a 200 m thick package often having a thin basal medium grained norite which grades into a coarse grained pyroxenite. Holwell and McDonald (2006) studied two boreholes from Overysel consisting of feldspathic pyroxenites and intrusive norites with serpentinised calcsilicate and chromitite xenoliths. A basal hybrid zone of quartzo-feldspathic pyroxenite also formed because of invasion of a felsic melt derived from partial melting of the footwall granite-gneisses.

3.3.4.3 NORTHERN SECTOR

The Platreef on Drenthe is also underlain by Archaean granite-gneisses; it attains a thickness of up to 250 m with a 40 – 80 m thick basal feldspathic pyroxenite chilled at its base against footwall granites (Gain & Mostert, 1982). PGE and BMS mineralisation within the Platreef are associated both with igneous lithologies and calcsilicate xenoliths and extend into the Main Zone hanging wall (Kinnaird et al., 2005). North of Drenthe, the Platreef disappears, the Main Zone and Upper Zone lithologies sit directly onto footwall rocks (van der Merwe, 1978).

3.3.5 MINERALISATION IN THE PLATREEF

The Platreef is irregularly mineralised with platinum group elements (PGEs), copper (Cu), nickel (Ni), and gold (Au), and contains a higher percentage of base metal sulphides (BMS) than the Merensky Reef (Sharman-Harris et al., 2005). Three styles of mineralisation are recognised in the Platreef: magmatic PGE reefs, contact-style disseminated sulphides and massive to semi-massive sulphide bodies (Yudovskaya et al., 2017). The origin and nature of the disseminated and massive mineralisation is completely different from that of the Merensky Reef and UG-2 chromitite layer in the eastern and western limbs, syn- and post-magmatic fluid alteration also occurred on a much greater scale. In the Platreef, the PGEs and BMS are interstitial to the silicate constituents of the host rocks (Holwell et al., 2005). The contact-style mineralisation in the Platreef is thought to have formed as a result of the assimilation of country rocks which also led to important regional variations in the

igneous rock types, hybrid rocks, sulphide content, and grade of the Platreef along strike (von Gruenewaldt et al., 1985; Hutchinson and Kinnaird, 2005; Holwell & McDonald, 2007; Penniston-Dorland et al., 2008).

3.3.5.1 BASE METAL SULPHIDES

The Platreef is highly enriched in base metal sulphides (BMS) in comparison to the rest of the Bushveld Complex. The sulphides in the Platreef are dominated by pyrrhotite, pentlandite, chalcopyrite and occasionally pyrite. These sulphides are unevenly distributed throughout the Platreef succession and occur as massive, net-textured or disseminated (Viljoen & Schurmann, 1998; Hutchinson & Kinnaird, 2005; Sharman-Harris et al., 2005). The metamorphic footwall lithologies to the Platreef also host sulphides, particularly pyrite and pyrrhotite (Sharman-Harris et al., 2005).

Sulphides in Ni-Cu-PGE deposits can be of primary or secondary origin, the primary sulphide assemblages consist of pentlandite, pyrrhotite and chalcopyrite while secondary sulphide assemblages consists of pyrite, chalcopyrite and pentlandite, with or without pyrrhotite and millerite. Primary sulphides are direct cooling products of a fractionating sulphide liquid, the first phase to crystallise is an Fe-rich high temperature (1000 °C) monosulphide solid solution (MSS) while the second phase to crystallise from the remaining Cu-rich liquid is intermediate solid solution (ISS) at temperatures below 900 °C (Li et al., 1996; Naldrett, 2004; Barnes & Ripley, 2016). High-temperature polymorphs and precursors of pyrrhotite and pentlandite exsolve from MSS while Cu sulphides (e.g. chalcopyrite) form from ISS. Later, at decreasing temperature, the high-temperature phases are transformed into low-temperature assemblages (Naldrett, 2004; Barnes & Ripley, 2016). On the other hand, secondary sulphides are due to replacement (alteration) of primary sulphides at low temperatures (Holwell & McDonald, 2010; Barnes & Ripley, 2016).

Primary magmatic sulphides are simple in composition, disseminated or net-textured ranging from a few microns to centimetre-sized grains of mainly pyrrhotite with minor pentlandite (Kinnaird et al., 2005). Chalcopyrite and pentlandite typically occur either at the margins or inclusions within pyrrhotite grains, flame exsolution of pentlandite are also observed within pyrrhotite grains. Secondary magmatic sulphides are more complex and are associated with intergranular plagioclase, quartz and quartz-feldspar symplectites. Chalcopyrite and pentlandite are more common with minor pyrrhotite and traces of galena and sphalerite (Kinnaird et al., 2005).

3.3.5.2 PLATINUM GROUP ELEMENTS

Platinum Group Element (PGE) reefs are a type of deposit that form laterally persistent layers within layered intrusions and are commonly associated with sulphides (Yudovskaya et al., 2017). The Platreef is the third largest PGE deposit in the world after the Merensky Reef and UG-2 which occur in the eastern and western limbs of the Bushveld Complex (Naldrett et al., 2011).

In the Southern Sector at Macalacaskop, where the footwall consists of dolomite and shales of the Duitschland and Timeball Hill Formations, the PGE mineralisation is located adjacent to the footwall contact (i.e. bottom-loaded) in serpentinised peridotite, feldspathic pyroxenite, serpentinised dolomite xenoliths of footwall dolomite. However, a minor mineralized zone also occurs towards the top of the Platreef (Yudovskaya & Kinnaird, 2010). With increasing depth towards the west, the Platreef sequence becomes more similar to the Critical Zone and persistent high-grade PGE reefs occur at the top of the unit, in the stratigraphic position identical to the position of the Merensky Reef (Grobler at al., 2018). In the Central sector, on Tweefontein north and Sandsloot, PGE mineralisation is top-loaded. In the Northern Sector; the PGE grade is top-loaded (White, 1994; Kinnaird, 2005; Kinnaird et.al., 2005; Hutchinson & Kinnaird, 2005). Where the footwall consists of Malmani dolomites (i.e. on Sandsloot), the Platreef typically contains >4g/t PGE, whereas elsewhere the PGE grades are typically 1-2 g/t with intersections sometimes attaining >10 g/t (Hutchinson &Kinnaird, 2005).

The PGEs in the Platreef occur as sulphides (cooperite and braggite), tellurides (e.g. moncheite), bismuthides (e.g. froodite), antimonides (e.g. genkinite) as well as arsenides of Pd, Pt and Rh (e.g. sperrylite) (Armitage et al., 2002; Hutchinson, Kinnaird & Schurmann, 2004). However, there appears to be a strong link between the host rock types and the type of PGMs; serpentinites are characterised by a relative enrichment of sperrylite, whereas the upper pyroxenites are highly associated with PGE sulphides and alloys (Schouwstra, Kinloch & Lee, 2000). The Bi-Te-dominant assemblages were believed to have been prevalent in unaltered pristine feldspathic pyroxenite and represent the primary style of mineralisation. At shallow depths of Turfspruit, the abundance of Sb- and As-bearing PGM was explained by the contribution of devolatilized Duitschland sediments (Hutchinson & Kinnaird, 2005). Later, however, it was found that the uppermost part of the Platreef sequence, bounded by discontinuous upper chromitite seams on Turfspruit, Tweefontein, Sandsloot, Zwartfontein and Overysel, carries a PGM assemblage by Pt-Pd sulphides along with Pt-Pd bismuthotellurides and subordinate Pt alloys (Yudovskaya et al., 2017).

3.4 CHROMITE MINERALISATION IN THE NORTHERN LIMB

Although the mineralisation of chromite in the northern limb is not as well developed as in the eastern and western limbs, occurrences are observed in the Grasvally body south of Mokopane as well as in some of the Lower Zone offshoot intrusions and in the Platreef.

3.4.1 CHROMITE MINERALIZATION IN THE LOWER ZONE

The Grasvally body hosts two massive chromitites; the Lower and Upper chromitite layers, located at 620 m and 690 m depths in the Drummondlea subgroup (Hulbert & von Gruenewald, 1982). The lower chromitite layer is about 60 cm thick, it is overlain by an orthopyroxene-olivine-chromite cumulate and underlain by an olivine-chromite cumulate (Hulbert & von Gruenewald, 1982). The upper chromitite layer has an average thickness of 41 cm with olivine-chromite cumulates forming the footwall and hanging wall. The Lower and Upper chromitite layers have Cr_2O_3 contents of 57.88 % and 57.11 % with Cr/Fe ratios of 2.99 and 2.69 respectively, these values are the highest reported for chromitites in the Bushveld Complex (van der Merwe, 1978; Hulbert & von Gruenewaldt, 1985).

The Lower Zone offshoot intrusions (Uitloop and Zwartfontein bodies) in the eastern and north-eastern flank of the northern limb also host minor chromite mineralisation. Chromitite lenses are observed adjacent to the footwall contact in the Uitloop II body and about 170 m above the base of the Uitloop I body. The Zwartfontein body hosts two chromitite layers that are separated by orthopyroxene and olivine cumulates. The Lower chromitite layer consists of about 32 cm of massive chromitite with 6 cm of disseminated ore forming the base while the Upper chromitite layer is about 60 cm thick with the lower half consisting of disseminated ore whereas the upper half is massive. van der Merwe (1978) indicated that the Lower chromitites are composed of 52.43 % Cr_2O_3 with the Cr/Fe ratio of 2.22, values for the Upper chromitites are not presented. Chromitite lenses are also observed at 200 m and 445 m above the base of the Zwartfontein body (van der Merwe, 1978). The distribution of chromite mineralisation in the Platreef is sporadic and this is discussed below.

3.4.2 CHROMITE MINERALISATION IN THE PLATREEF

The Platreef in the northern limb lacks the thick, massive and continuous chromitite layers as observed in the Critical Zone of the eastern and western limbs, however; Yudovskaya & Kinnaird (2010) identified two chromite-bearing horizons (Fig 3-7) which are traceable along strike; 1) the Upper Chromitite Zone (UCR) on Sandsloot, Vaalkop and Zwartfontein farms and 2) the Lower Chromitite Zone (LCR) on Overysel, Zwartfontein, Sandsloot, Tweefontein, Vaalkop and Macalacaskop farms.

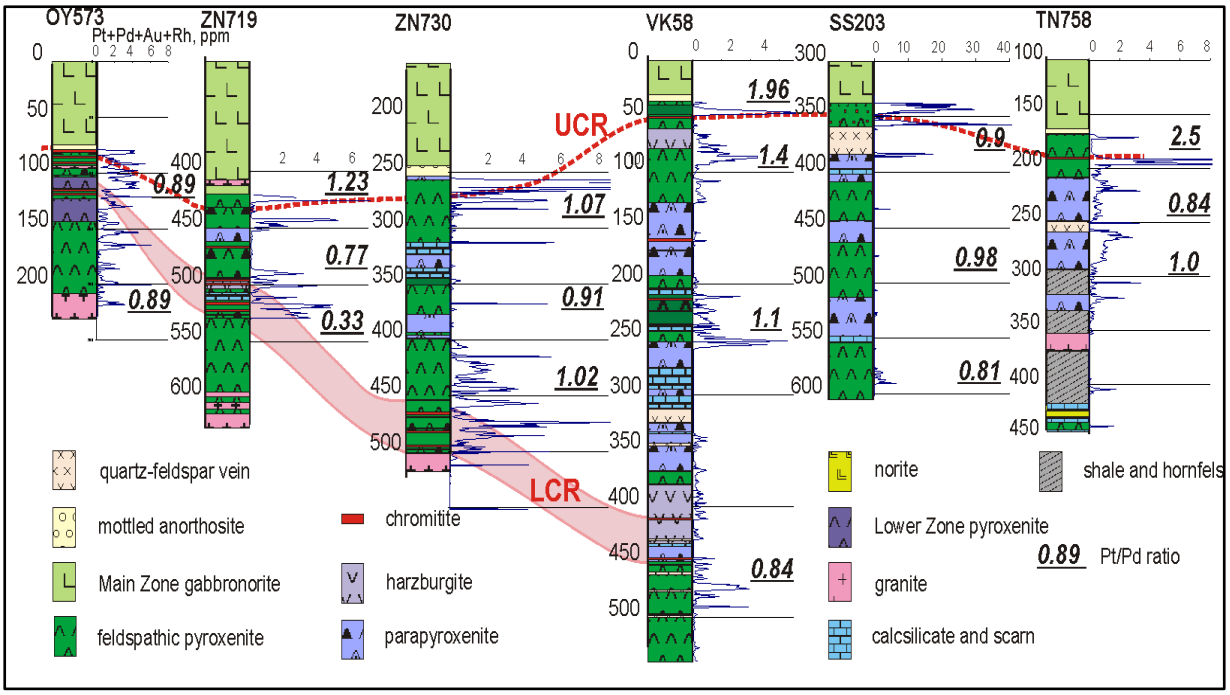


Figure 3-7: Stratigraphic logs showing persistent chromite-bearing horizons; termed the Upper Chromite Zones (UCR) and Lower Chromite Zone (LCR), within the Platreef along strike on Overysel (OY), Zwartfontein (ZN), Vaalkop (VK), Sandsloot (SS) and Tweefontein (TN) farms (Yudovskaya & Kinnaird, 2010).

3.4.2.1 THE UPPER CHROMITITE ZONE (UCR)

The chromitites in the UCR are located towards the top contact of the Platreef (Fig 3-7), where they occur as discontinuous chromite seams and stringers hosted by mainly feldspathic pyroxenite or restricted to boundaries between feldspathic pyroxenite and olivine-bearing lithologies. The UCR can be traced along strike in the Southern Sector on Tweefontein farm, Central Sector on Sandsloot, Zwartfontein and Vaalkop as well as in the Northern Sector on Overysel. The chromitites on Tweefontein farm occur as two to three massive seams composed of up to 80 vol.% chromite, these seams are 5 – 20 cm thick (up to 1 m in parts) (Yudovskaya & Kinnaird, 2010). In the central sector; particularly on Vaalkop, the UCR is characterised by six chromitite horizons which comprise two massive chromitite seams and heavily disseminated chromite. Further north; on Overysel, the UCR occurs directly on or adjacent to the top Platreef contact (Yudovskaya et al., 2010). Holwell and McDonald (2006) also observed chromitite xenoliths within the Platreef on Overysel.

According to Yudovskaya et al. (2010), the chromite crystals in the UCR are large (0.2 – 1 mm) and commonly associated with pyroxenes rather than olivine. The UCR chromite crystals display skeletal/atoll-like, chain-textured atoll, interstitial skeletal or reticulated and less commonly angular euhedral or rounded morphological types. The euhedral chromites commonly host silicate, sulphides, rutile and PGM inclusions, thus creating atoll-like shapes. Chains of chromite crystals occur along silicate grain boundaries, post-cumulus recrystallization and annealing of these crystals form

interstitial skeletal and reticulated chromite textures. Angular euhedral chromite crystals are smaller in size relative to the atoll-like chromites, these crystals tend to anneal when in contact with each other and commonly lack inclusions.

3.4.2.2 LOWER CHROMITITE ZONE (LCR)

The LCR is composed of multiple chromitite seams in the Southern Sector on Macalacaskop as well as in the Central Sector on Tweefontein, Vaalkop, Sandsloot, Zwartfontein and Overysel are located at the base of the Platreef. The chromitite seams on Vaalkop, Sandsloot and Zwartfontein are observed at the contact between pyroxenite and harzburgite lithologies as well as within feldspathic pyroxenites and norites 20 – 50 m above the basal contact. On Sandsloot, thin chromitite stringers also occur at the contact between calcsilicate xenoliths and underlying serpentinised harzburgite. The chromitite horizons on Overysel occur adjacent to the base of the Platreef (Yudovskaya et al., 2010).

The LCR chromite crystals have smaller size than those of the UCR, these crystals display euhedral and angular shapes that tend to form annealed textures. The LCR chromite crystals also occur as chadacrysts (cumulus phases) within orthopyroxene and olivine oikocrysts and sometimes as interstitial (intercumulus) phases. These crystals are commonly fractured and truncated by serpentine-magnetite veinlets, at times altered and replaced by biotite and sulphides. Chains of chromite crystals are usually associated with intercumulus plagioclase and occasionally orthopyroxene oikocrysts. Silicate inclusions are not observed within the LCR chromites (Yudovskaya et al., 2010).

3.5 DISCUSSION

There have been attempts to correlate the stratigraphy of the Platreef to the Critical Zone of the eastern and western limbs based on similarities in stratigraphic position below the Main Zone, silicate compositions and the occurrence of the PGE mineralisation (e.g. Merensky, 1926; Wagner, 1929; van der Merwe, 1978; White, 1994). For a long time, the link between the Platreef and the Critical Zone remained uncertain, with some authors suggesting that perhaps the Platreef represents an event unique to the northern limb (McDonald et al., 2005) or rather of Main Zone affinity (Kruger et al., 2005). Recent exploration by Ivanhoe mines on Turfspruit farm revealed an area, termed the Flatreef, where the Platreef temporarily transitions from a 40° to 60° westerly dip to gently dipping/sub-horizontal (15°). Grobler et al. (2018) successfully correlated the Flatreef at Turfspruit farm to the Critical Zone of eastern and western limbs of the Bushveld Complex despite obvious thickness variations (Fig 3-6).

The formation of Ni-Cu-PGE deposits require for mantle magmas to be saturated with sulphur during cooling. Primitive magmas are S-undersaturated because of the inverse relationship between sulphur solubility and pressure, as a result sulphur saturation can be achieved through three mechanisms: 1) magma differentiation, 2) magma mixing and 3) magma-country rock interaction (Barnes et al., 2017).

It is thought that a higher sulphide content of the mineralised Platreef is a result of liberation of sulphur from country rock xenoliths (Buchanan et al., 1981; Kinloch, 1982; von Gruenewaldt et al., 1985; Harris & Chaumba, 2001; McDonald & Holwell, 2011; Ripley & Li, 2013). The sulphide mineralisation is characterised by a high crustal component expressed by highly enriched and variable incompatible trace element composition, radiogenic Sr-isotope compositions, S-and O-isotope compositions and S/Se ratios (Buchanan et al., 1981; Harris & Chaumba, 2001; Penniston-Dorland et al., 2008). Studies on Akanani and Turfspruit indicate that Platreef contamination decreases with increasing depth, therefore the Platreef sequence becomes a more typical cyclic sequence with PGE reefs at the top (Yudovskaya et al., 2017; Grobler et al., 2018).

CHAPTER 4

STRATIGRAPHY OF THE ZEBEDIELA PROJECT AREA

The Zebediela project is located on the central sector of the northern limb, about 9 km north of Mokopane in the Limpopo province. The magmatic lithologies at Uitloop farm are dominated by feldspathic pyroxenites and pyroxenites with minor norites (melanorites and leuconorites). Internationally recognised nomenclature by the International Union of Geological Sciences (IUGS) for igneous rocks is used to classify the magmatic lithologies based on the modal mineral abundances. Additionally, local Bushveld nomenclature is applied to identify the cumulus or intercumulus nature of plagioclase in feldspathic pyroxenite and norite, respectively, as discussed by Kinnaird et al. (2005).

This chapter provides descriptions of lithologies encountered in boreholes Z19 and Z20; detailed logging of the two boreholes was conducted at the Umbono Capital's core yard in Mokopane. The primary magmatic rocks encountered in the studied boreholes include pyroxenites, peridotites, gabbros and norites. Hybrid rocks (parapyroxenites) as well as metasedimentary lithologies such as dolomite and hornfels were also intersected.

A total of forty-eight samples were selected from the studied boreholes, these were then photographed (Appendix B) and packaged in well labelled plastic bags. Thin sections were prepared and an overview of the mineralogical composition as well as textural information of the different rock types is detailed in Chapter 5. The chromite and base metal sulphide mineralisation in boreholes Z19 and Z20 are also discussed in Chapter 6. Modal mineralogy estimations of the samples are provided in Appendix B.

4.1 HANGING WALL LITHOLOGIES

The hanging wall lithologies in boreholes Z19 (Fig 4-19) and Z20 (Fig 4-20) consist of dolomite belonging to the Duitschland Formation of the Transvaal Supergroup (Fig 4-1). The dolomitic rocks consist of >90 % dolomite and <10 % calcite minerals, other constituents also include various clay minerals. In borehole Z20 the dolomite hanging wall forms a sharp contact with the underlying parapyroxenite unit at 50 m below surface (Fig 4-1). The feldspathic pyroxenite layer beneath the parapyroxenite is highly tectonised at a depth of 52.5 m to 52.9 m; this creates a fractured contact between the two lithologies (Fig 4-1). In borehole Z19, the dolomite hanging wall extends to a depth of approximately 65.6 m below surface, a sharp contact separates this dolomite unit from the underlying melanorites.

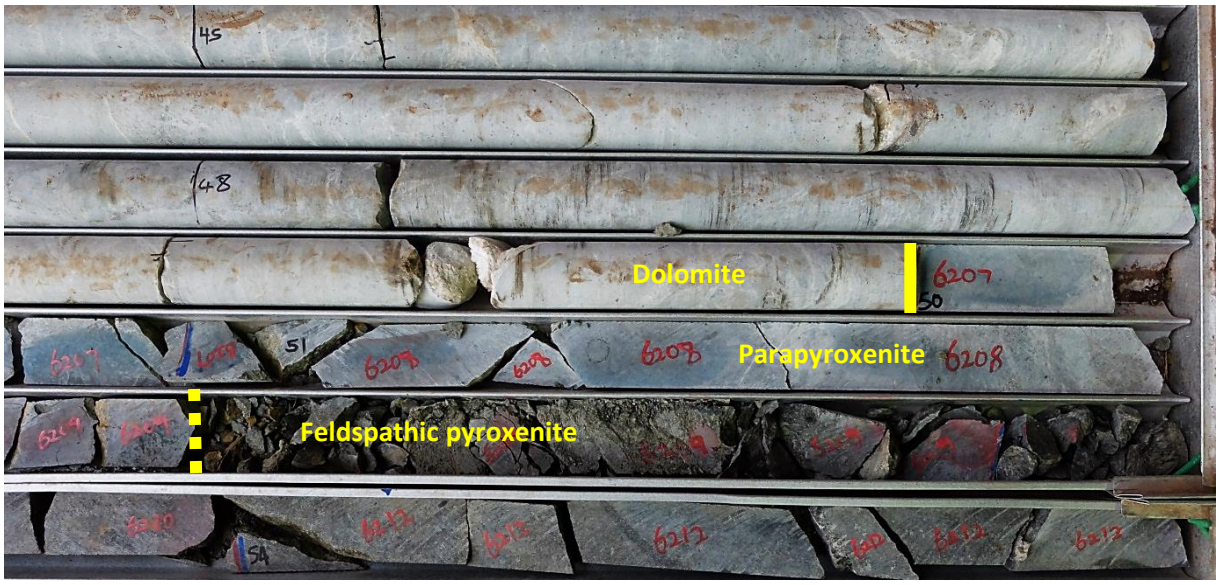


Figure 4-1: In borehole Z20, a 2.5 m thick assimilation zone (parapyroxenite) separates the dolomite hanging wall from the underlying feldspathic pyroxenite of the Bushveld Complex.

4.2 THE MAGMATIC LITHOLOGIES ON UITLOOP FARM

4.2.1 PYROXENITE

Pyroxenites are ultramafic rocks that consist of more than 90% pyroxene minerals (i.e. orthopyroxenes and clinopyroxenes), they can be further subdivided into orthopyroxenite and clinopyroxenite based on the most abundant type of pyroxene within the rock. In borehole Z20, there are thin layers of orthopyroxenite within the footwall lithology; these could be small finger-like intrusions within the footwall rocks (Fig 4-2). These orthopyroxenite units consist of mainly cumulus orthopyroxene (80-100 %) as well as clinopyroxene (0-10 %). Minor accessory minerals that were observed include BMS and phlogopite.



Figure 4-2: A photograph of borehole core sample showing fine-grained orthopyroxenite, sample Z20-195.7.

4.2.2 FELDSPATHIC PYROXENITE

The feldspathic pyroxenites at Uitloop farm are generally medium- to coarse grained, of mainly cumulus orthopyroxene (50 – 80 %) with minor amounts of clinopyroxene (0 – 15 %) and intercumulus plagioclase (10 – 20 %) as well as accessory phlogopite, biotite, quartz and secondary minerals. These rocks also contain up to 15 % disseminated (Fig 4-3) and net-textured base metal sulphides (Fig 4-4). Chromitite lenses and irregular blebs are observed in the feldspathic pyroxenite layers positioned towards the top of the borehole Z19 succession (Fig 4-4).

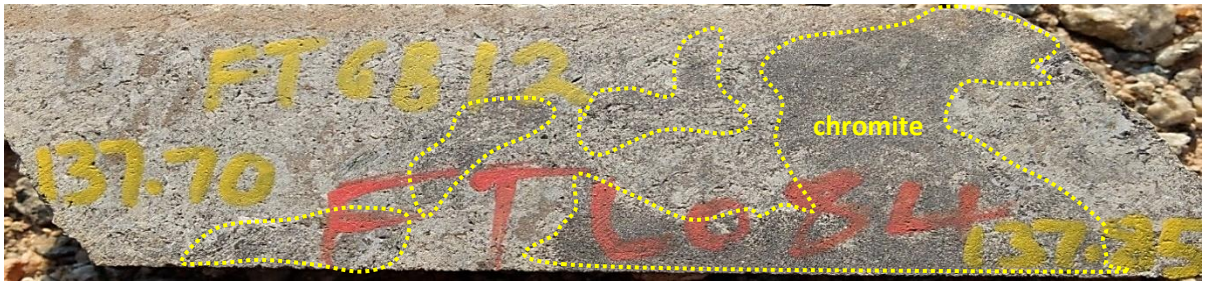


Figure 4-3: A photograph of borehole core sample showing medium to coarse-grained feldspathic pyroxenite (Sample Z19-137.7) with fine-grained chromite disseminations.



Figure 4-4: A photograph of borehole core sample showing medium to coarse-grained feldspathic pyroxenite (sample Z20-173.7) with net-textured base metal sulphide mineralisation.

4.2.3 FELDSPATHIC HARZBURGITE

The feldspathic harzburgite units in borehole Z19 are medium-grained and consist of predominantly serpentinised olivine (15-45 %) and orthopyroxene (25-45 %) cumulates as well as intercumulus plagioclase (10-15 %) and occasionally clinopyroxene (0-5 %). The feldspathic harzburgites in borehole Z20 (Fig 4-5 – 4-8), consist of mainly serpentinised olivine (40-45 %) and orthopyroxene (25-35 %) cumulates with minor amounts of clinopyroxene (<5 %). In both boreholes, these feldspathic harzburgite layers host finely disseminated base metal sulphides. However, in Z20; a thin (0.5 cm) chromite stringer is observed at a depth of approximately 54.25 m (Fig 4-6).



Figure 4-5: A photograph of borehole core sample showing coarse-grained serpentinised harzburgite (sample Z20-53.7).



Figure 4-6: A photograph of borehole core sample showing medium to coarse-grained harzburgite (sample Z20-54.25) with a chromite stringer.

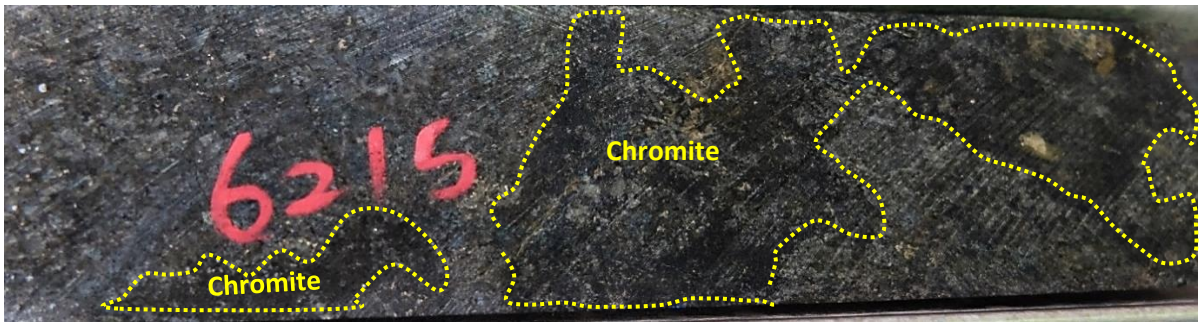


Figure 4-7: A photograph of borehole core sample showing coarse-grained feldspathic harzburgite (sample Z20-57.5) with chromite disseminations.



Figure 4-8: A photograph of borehole core sample showing coarse-grained highly serpentinised feldspathic harzburgite (sample Z20-66.5).

4.2.4 NORITE

The prefixes mela- and leuconorite are used to distinguish between more plagioclase-rich and plagioclase-poor varieties of norite respectively. The melanorites in the studied boreholes are medium-grained to coarse-grained and consist of predominantly cumulus plagioclase (20 – 30 %) and orthopyroxene (35 – 40 %) as well as minor clinopyroxene (5 – 30 %) (Fig 4-9). The leuconorites are composed of more plagioclase than orthopyroxene with 30 – 45 % plagioclase and 15 – 30 % orthopyroxene (Fig 4-10). These norite varieties also contains interstitial base metal sulphides, however, in Z20, the sulphides in melanorites are larger and more sporadic rather than disseminated while the leuconorites are barren.



Figure 4-9: A photograph of borehole core sample showing medium-grained melanorites (sample Z19-78.3) with finely disseminated base metal sulphides.



Figure 4-10: A photograph of borehole core sample showing coarse-grained leuconorite (sample Z20-153.5).

4.2.5 GABBRO AND GABBRONORITE

Gabbro consists of predominantly cumulus clinopyroxene and plagioclase with less than 5 % orthopyroxene. In this study these rocks are medium- to coarse-grained and consist of 70 – 80 % clinopyroxenes with 10 – 35 % cumulus plagioclase (Fig 4-11). Gabbronorite consists of cumulus plagioclase (10 – 30 %) as well as equal amounts of clinopyroxene and orthopyroxene (35 – 45 %).

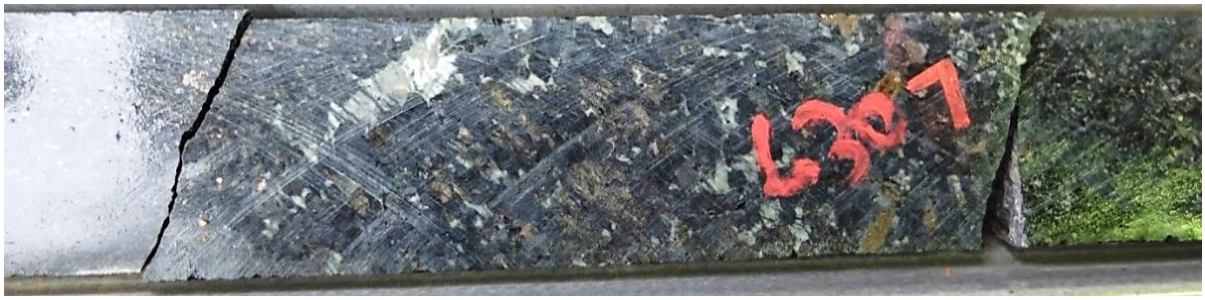


Figure 4-11: A photograph of borehole core sample showing coarse grained gabbro (sample Z20-140.1) with base metal sulphide blebs.

4.2.6 PARAPYROXENITE

On the Uitloop farm parapyroxenites are fine-grained (Fig 4-12). They formed as a result of assimilation of footwall dolomite by ultramafic magma, and they separate the dolomitic unit from the underlying fine-grained brown (mica-rich) hornfels.



Figure 4-12: A photograph of borehole core sample showing fine-grained parapyroxenite (sample Z19-175.1).

4.3 FOOTWALL LITHOLOGIES

The footwall lithologies at Uitloop farm consist of a variety of fine-grained hornfels and dolomite of the Duitschland Formation.

4.3.1 BOREHOLE Z19 FOOTWALL LITHOLOGY

There is a sharp contact between the feldspathic pyroxenite of the Bushveld Complex and the underlying fine-grained dolomitic unit of the Transvaal Supergroup at a depth of ~170.8 m. Calcsilicate veins as well as traces of sulphide disseminations are observed within these dolomitic units. Thin layers of fine-grained parapyroxenite alternate with a variety of hornfelses units in Z19. A reddish-brown (mica-rich) hornfels underlying the parapyroxenite layer has sulphide mineralisation orientated parallel to the bedding (Fig 4-13).

The lowermost intersection in borehole Z19 consists of a greenish-grey hornfels layer containing fragments of quartz-cordierite hornfels (Fig 4-14), this can also be classified as a contact-metamorphosed sedimentary breccia and is separated from the overlying mica-rich hornfels by a thin layer of parapyroxenite.

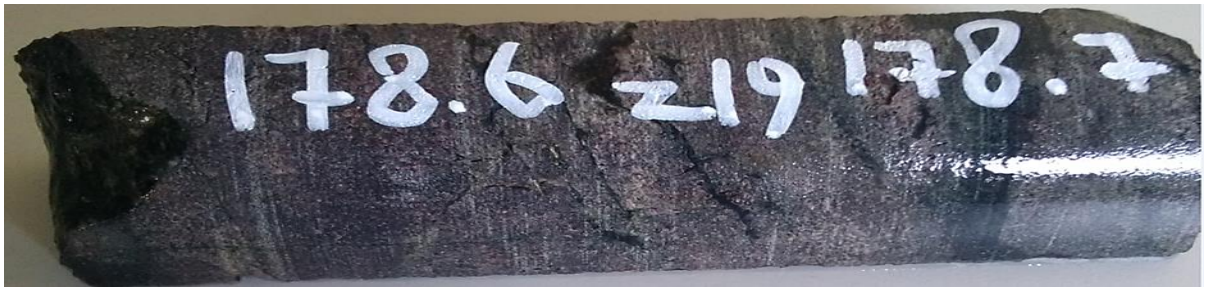


Figure 4-13: A photograph of borehole core sample showing fine-grained mica-rich hornfels (sample Z19-178.6).



Figure 4-14: A photograph of borehole core sample showing fine-grained hornfels (sample Z19-203.2) with quartz-cordierite hornfels fragments (sedimentary breccia).

4.3.2 BOREHOLE Z20 FOOTWALL LITHOLOGY

There is a sharp contact between the magmatic rocks of the Bushveld Complex and the underlying fine-grained mica-rich hornfels of the Transvaal Supergroup at a depth of ~176.2 m (Fig 4-15). The bedding within this hornfels unit is preserved and the layered cycles have thicknesses ranging between 2 cm to 5 cm. There is an increase in calcsilicate veins as well as various hornfels fragments which are surrounded by base metal sulphide disseminations (Fig 4-19 & 4-20) towards the base of this thick hornfels succession. Although this hornfels unit is fairly homogenous, interlayers are occasionally observed. The hornfels layer has a sharp contact with the underlying dolomite unit (Fig 4-17) which extends from ~196 m to ~215 m (end of hole). The dolomite unit includes alternating magnetite bands and minor amounts of base metal sulphides (Fig 4-18).

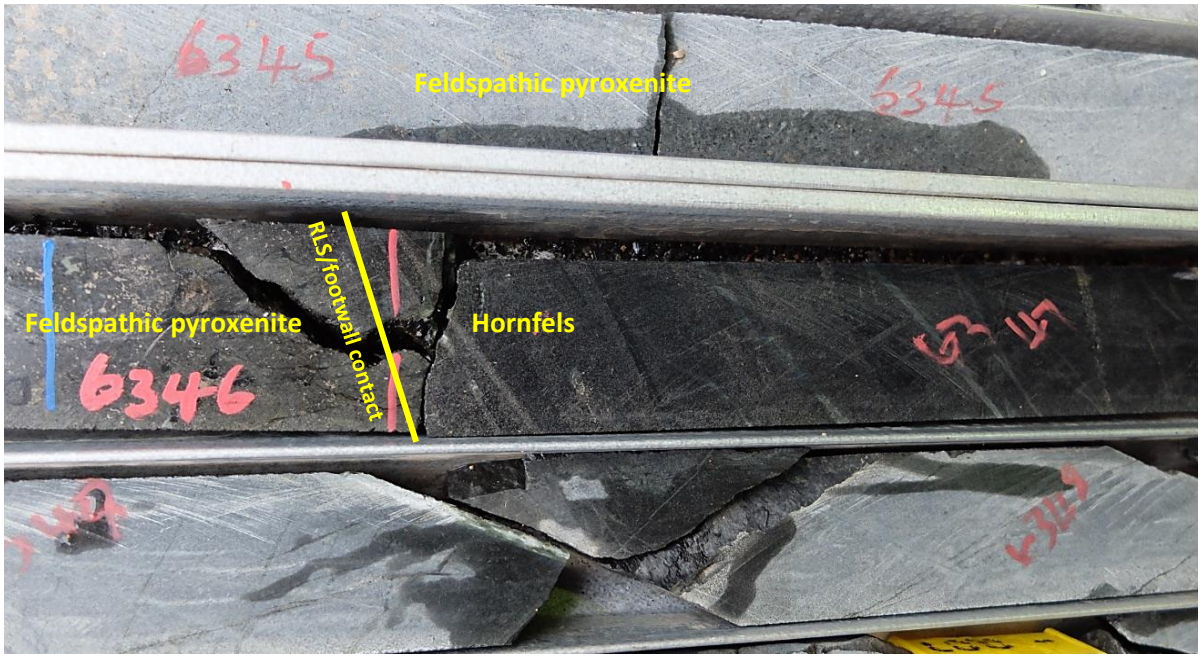


Figure 4-15: A photograph of borehole core sample showing a sharp contact between the Feldspathic pyroxenite and the metasedimentary footwall lithologies (mica-rich hornfels) of the Transvaal Supergroup at a depth of 176.1m in borehole Z20.

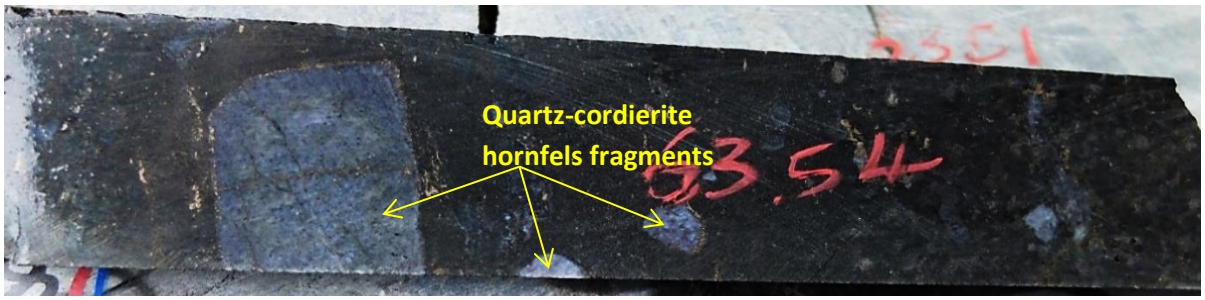


Figure 4-16: A photograph of borehole core sample showing hornfels (Sedimentary breccia) (sample Z20183.5) with various quartz-cordierite hornfels fragments rimmed by base metal sulphides.

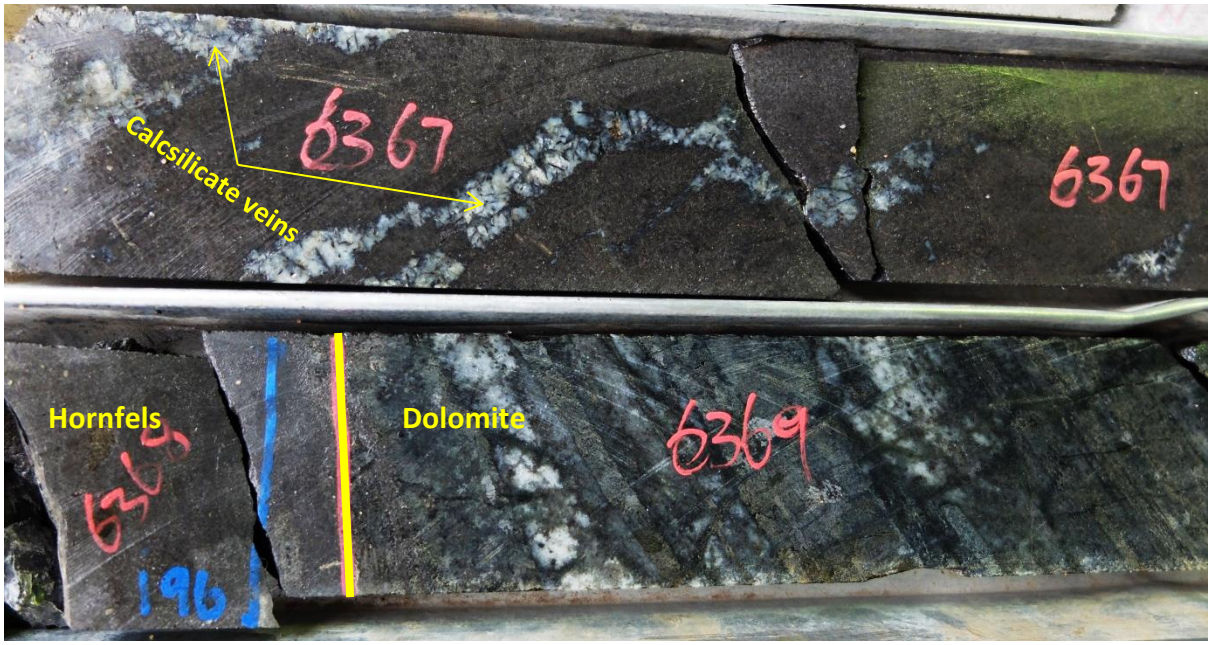


Figure 4-17: A photograph of borehole core samples showing a sharp contact between the hornfels and the underlying dolomitic unit at a depth of 196 m below surface.

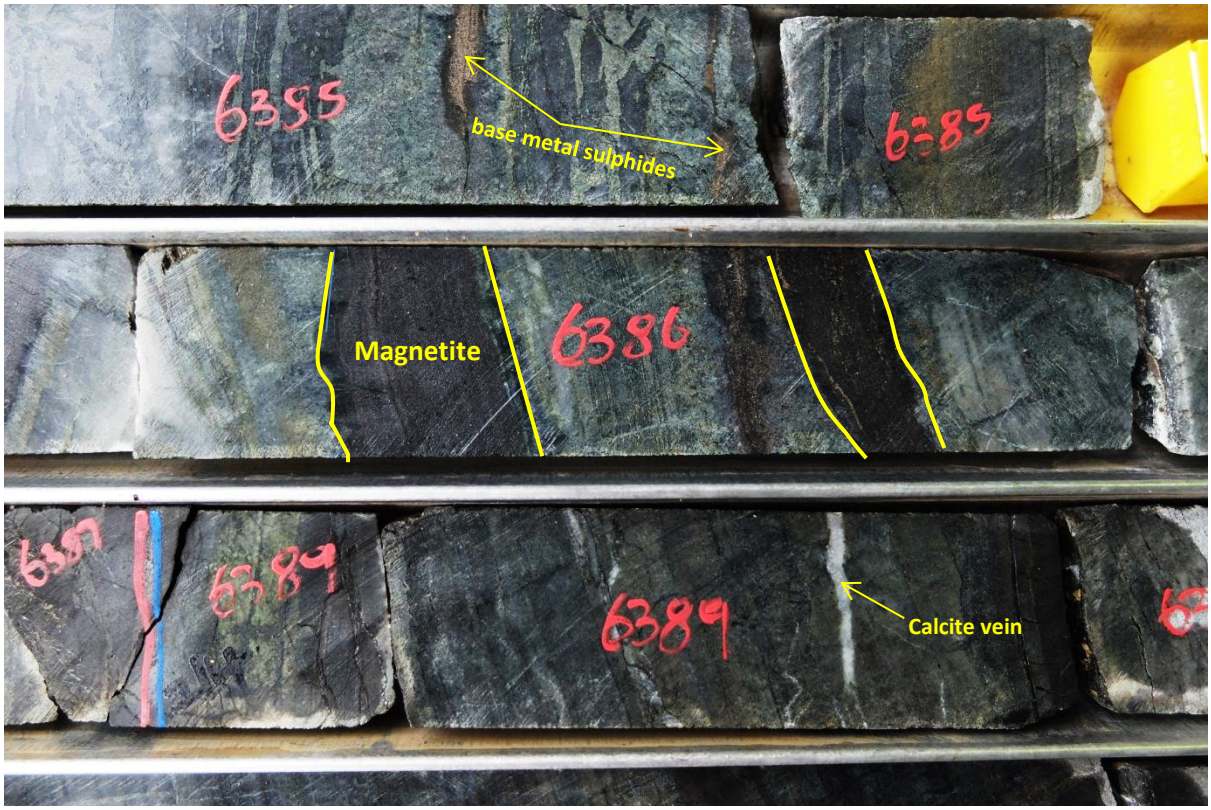


Figure 4-18: A photograph of borehole core sample showing dolomite with bands of magnetite and minor base metal sulphides as well as calcite veins.

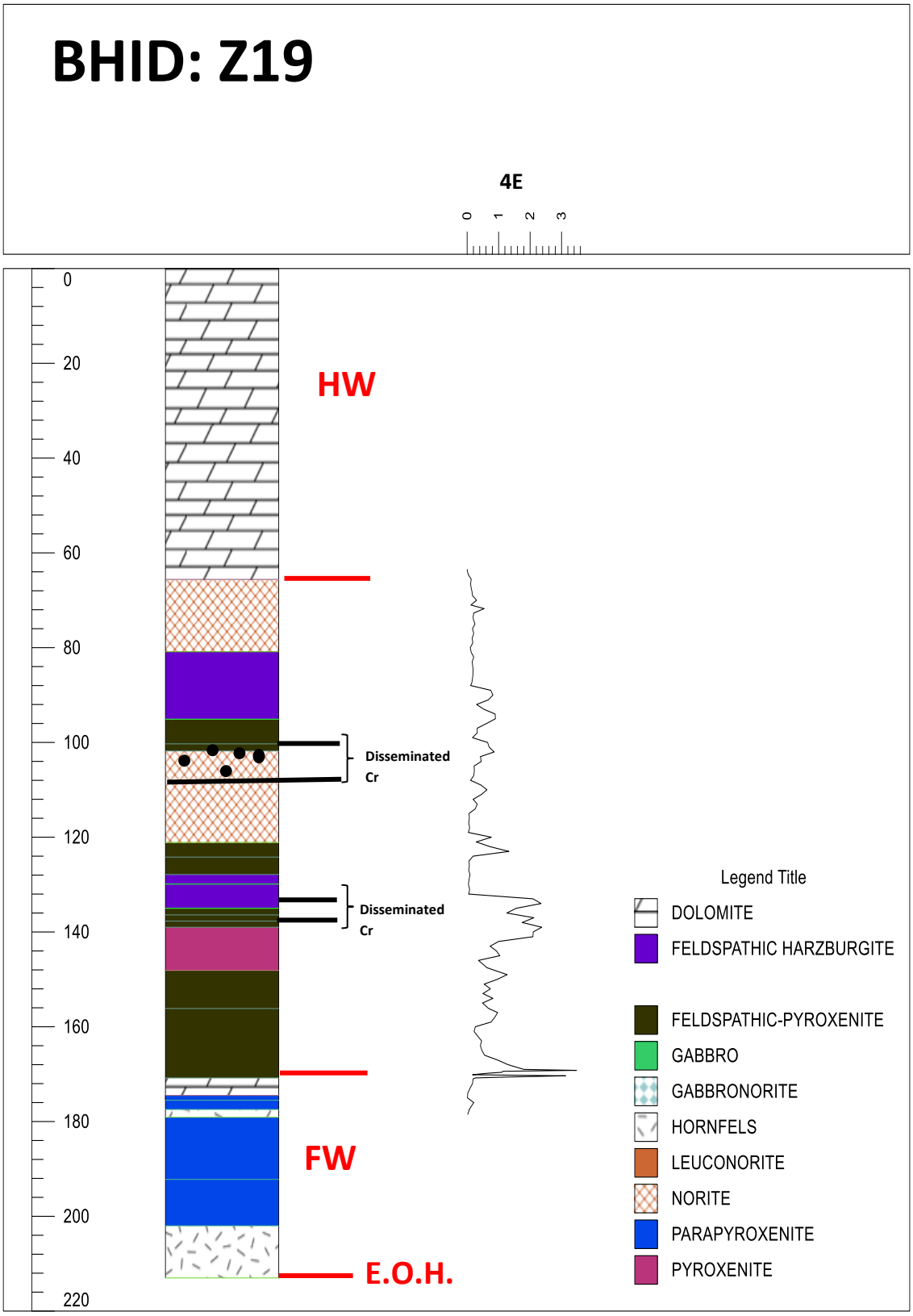


Figure 4-19: Simplified geological log of borehole Z19 indicating major stratigraphic positions; HW = hanging wall, Cr = chromite mineralisation, FW = footwall, E.O.H = end of hole, a graph displaying the down-hole 4E grade profile is also included.

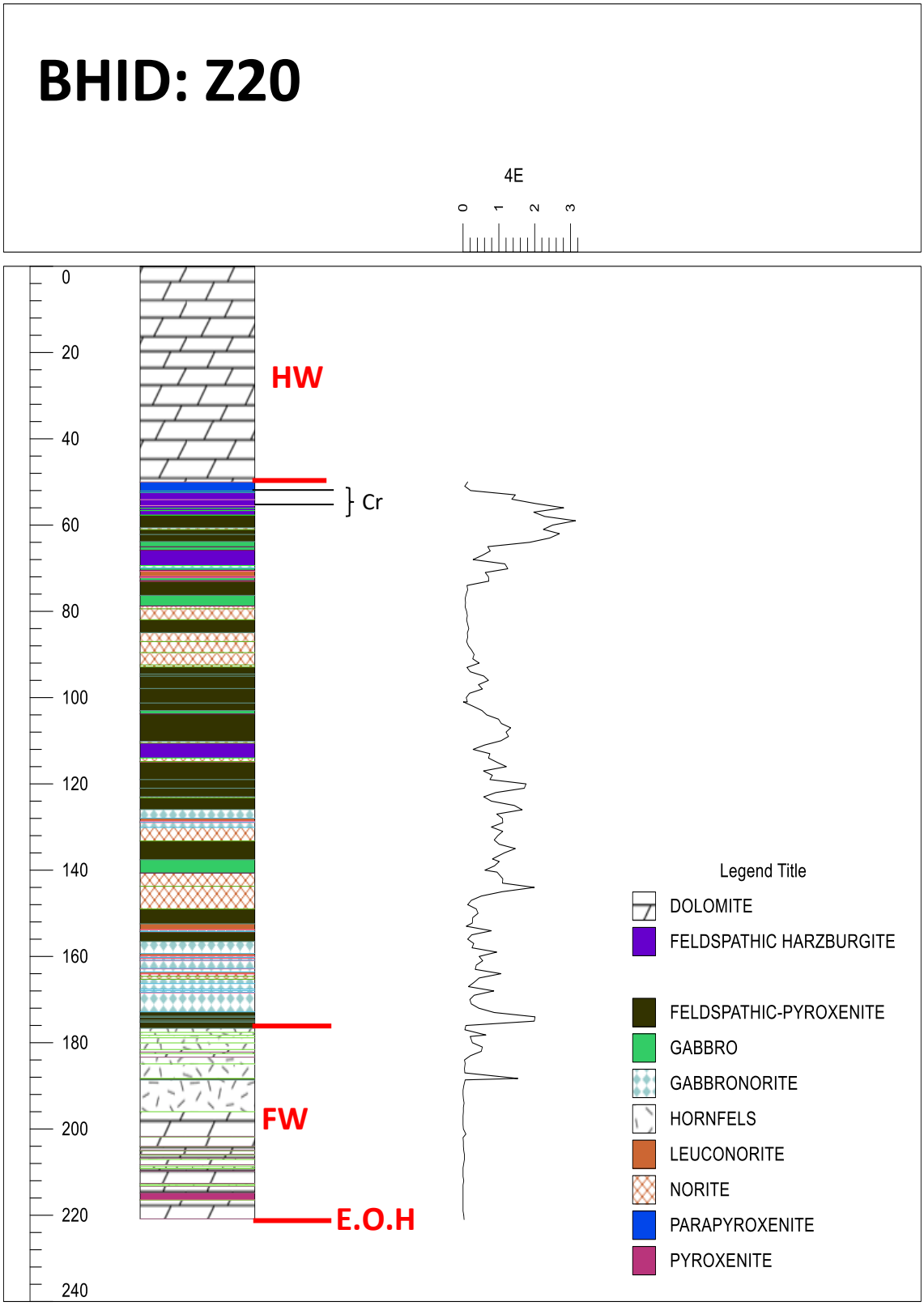


Figure 4-20: Simplified geological log of borehole Z20 indicating major stratigraphic positions; HW = hanging wall, Cr = chromite mineralisation, FW = footwall, E.O.H = end of hole, a graph displaying the down-hole 4E grade profile is also included.

CHAPTER 5

PETROGRAPHY OF THE ZEBEDIELA PROJECT ROCKS

A total of 41 thin sections were made from Z19 and Z20 samples, which were then studied under a petrographic microscope using transmitted and reflected light. Detailed petrographic descriptions of the thin sections include grain size, mineralogical composition as well as textural information.

5.1 FELDSPATHIC PYROXENITE

The local magmatic stratigraphy at Uitloop farm is dominated by feldspathic pyroxenites which are composed of mainly cumulus orthopyroxene (60 – 85 %), intercumulus plagioclase (10 – 15 %) and occasionally minor clinopyroxene (0 – 20 %). Accessory minerals include phlogopite, quartz, amphibole, base metal sulphides, chromite as well as alteration minerals (sericite, serpentine, magnetite etc.).

Orthopyroxene occurs as medium- to coarse-grained euhedral to anhedral crystals, elongated orthopyroxene laths are also observed in some samples (Fig 5-1). Interstitial plagioclase commonly displays lamellar twinning (Fig 5-1B) and zoning (Fig 5-1E). The plagioclase in the majority of the samples is altered to a brown fine-grained isotropic cluster of clay minerals, in some cases the original plagioclase features are not observed. Clinopyroxene is also encountered in some of the feldspathic pyroxenite samples, where it occurs as anhedral twinned crystals (Fig 5-1C) as well as oikocrysts enclosing orthopyroxene inclusions (Fig 5-1D). A granophyric texture, which is composed of an intergrowth between quartz and feldspar is interstitial to pyroxene crystals (Fig 5-1F). Other accessory minerals include phlogopite and secondary amphibole which is locally a result of alteration of orthopyroxene crystals. In both boreholes Z19 and Z20, feldspathic pyroxenites carry base metal sulphides and occasionally chromite disseminations that will be discussed in Chapter 6.

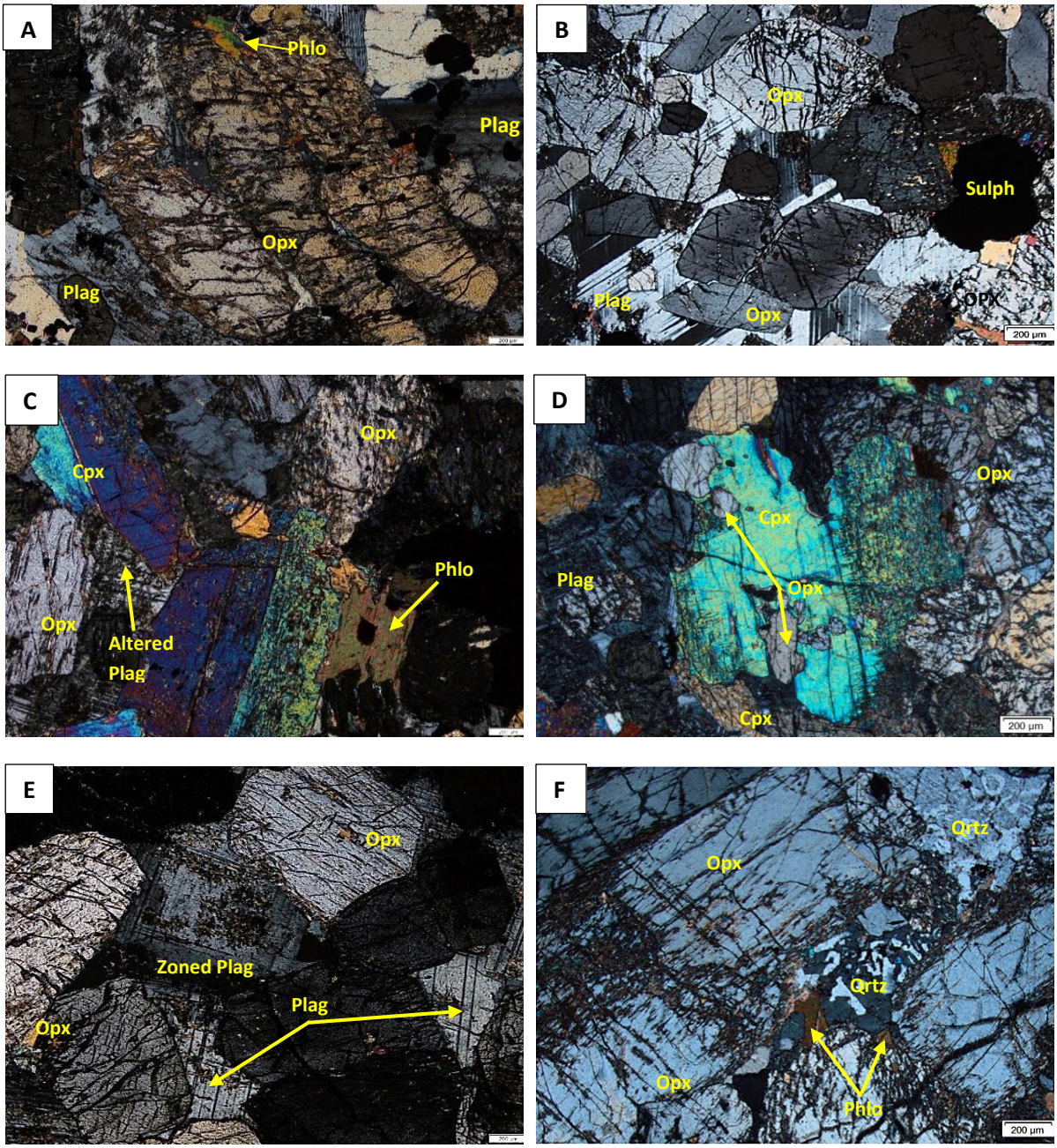


Figure 5-1: Photomicrographs (taken under XPL) of feldspathic pyroxenites under XPL from the southwestern portion of the Uitloop farm. (A) Cumulus orthopyroxene laths, sample Z19–100.35, (B) Cumulus orthopyroxene with intercumulus plagioclase, sample Z20–134.8, (C) Twinned clinopyroxene (D) Clinopyroxene oikocryst enclosing orthopyroxene, sample Z20–121.9, (E) Zoned and twinned intercumulus plagioclase, sample Z20–121.9 and (F) Granophyric quartz, sample Z20–120.75.

5.2 ORTHOPYROXENITE

Orthopyroxenites are pyroxenites, which are composed of >90 % cumulus orthopyroxene crystals displaying a granular to granoblastic texture. Their grain sizes vary from fine to coarse, the orthopyroxene crystals are equigranular and have subhedral to anhedral shapes (Fig 5-2). The accessory minerals are anhedral interstitial quartz and opaque base metal sulphides.

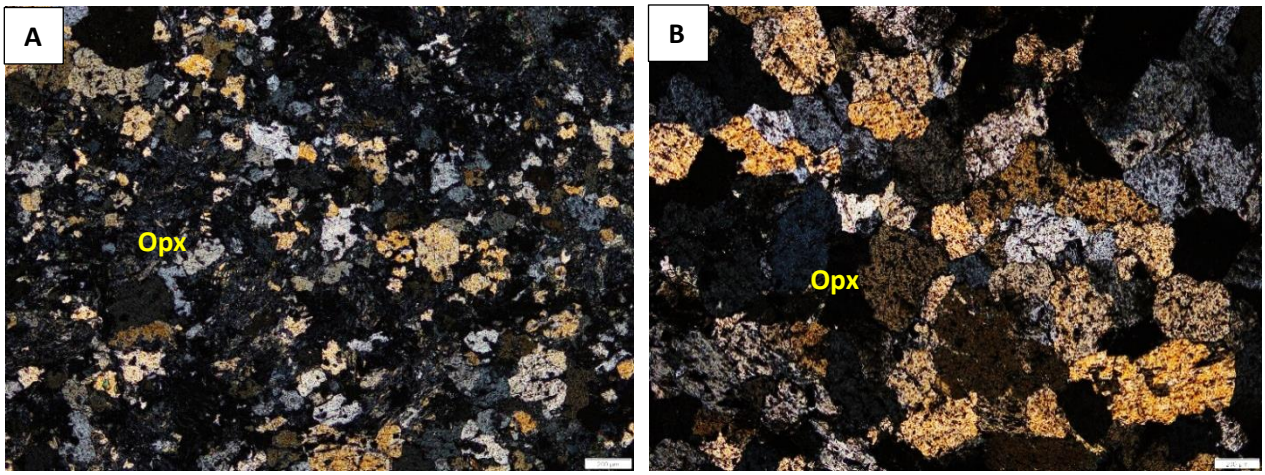


Figure 5-2: Photomicrographs (taken under XPL) of orthopyroxenite from the local magmatic lithologies at the southwestern portion of the Uitloop farm. (A) Fine-grained cumulus orthopyroxene crystals, sample Z19–174.9. (B) Coarse-grained cumulus orthopyroxene crystals, sample Z19–199.

5.3 FELDSPATHIC HARZBURGITE

The feldspathic harzburgite samples are less altered in comparison to the harzburgite lithologies. These feldspathic harzburgites are composed of cumulus olivine (20 – 45 %), orthopyroxene (25 – 45%), oikocrystic to interstitial clinopyroxene (0 – 5 %) and interstitial plagioclase (5 – 15 %). The olivine crystals have euhedral to anhedral shapes; with characteristic fractures filled by magnetite and serpentine although there are some fresh olivine crystals in sample Z20-54.25 (Fig 5-3B). The orthopyroxene and clinopyroxene crystals are generally subhedral to anhedral. The pyroxene crystals are of different generations as shown in Fig 5-3E where an orthopyroxene oikocryst encloses smaller orthopyroxene inclusions. There are also some clinopyroxene oikocrysts which host orthopyroxene and olivine inclusions (Fig 5-3C). The interstitial plagioclase has completely altered to clay minerals (after secondary sericite and saussurite) (Fig 5-3A) while the less altered plagioclase crystals display lamellar twinning (Fig 5-3B). Other accessory minerals associated with the feldspathic harzburgite lithologies include chromite (Fig 5-3B), base metal sulphides and phlogopite.

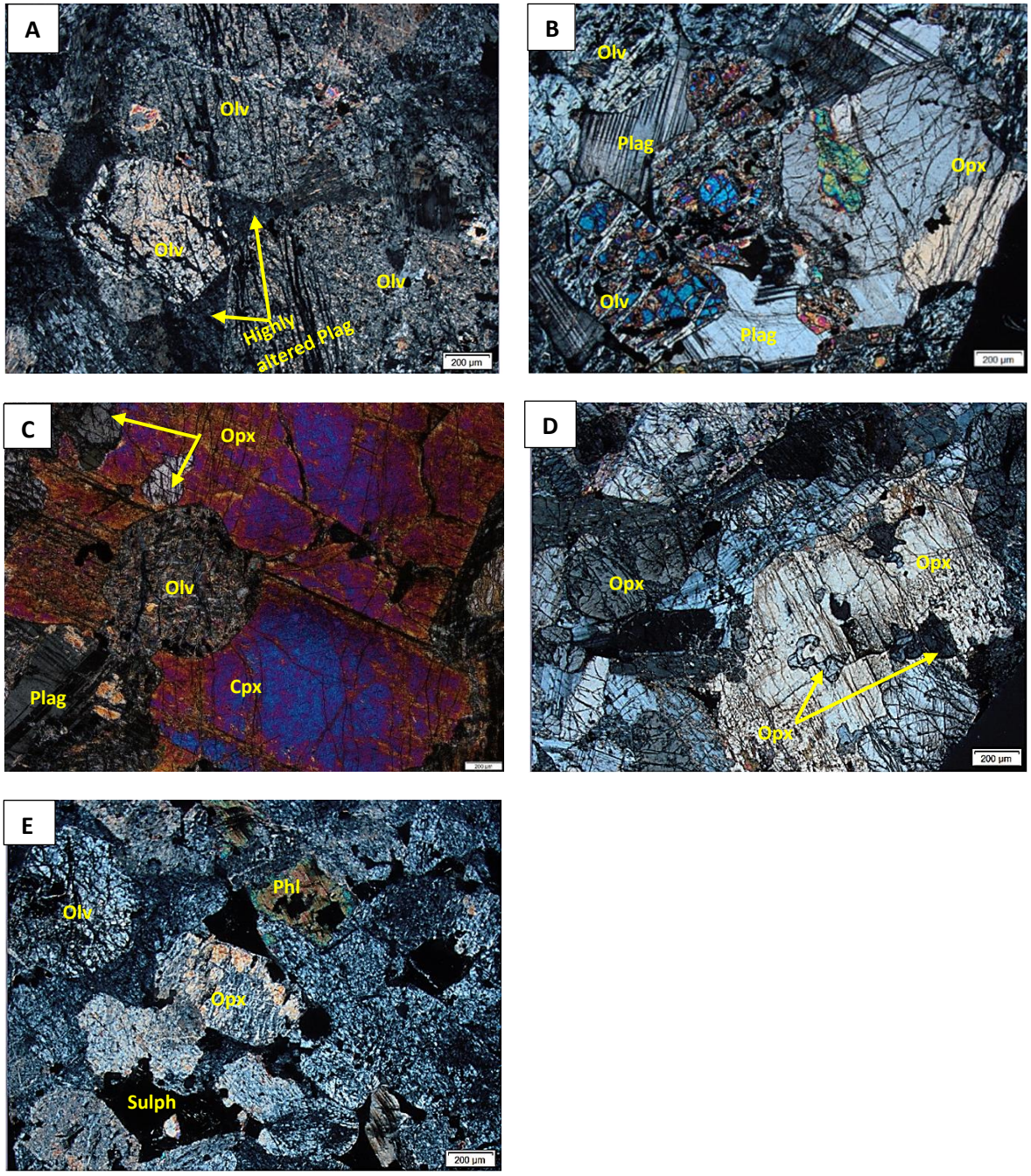
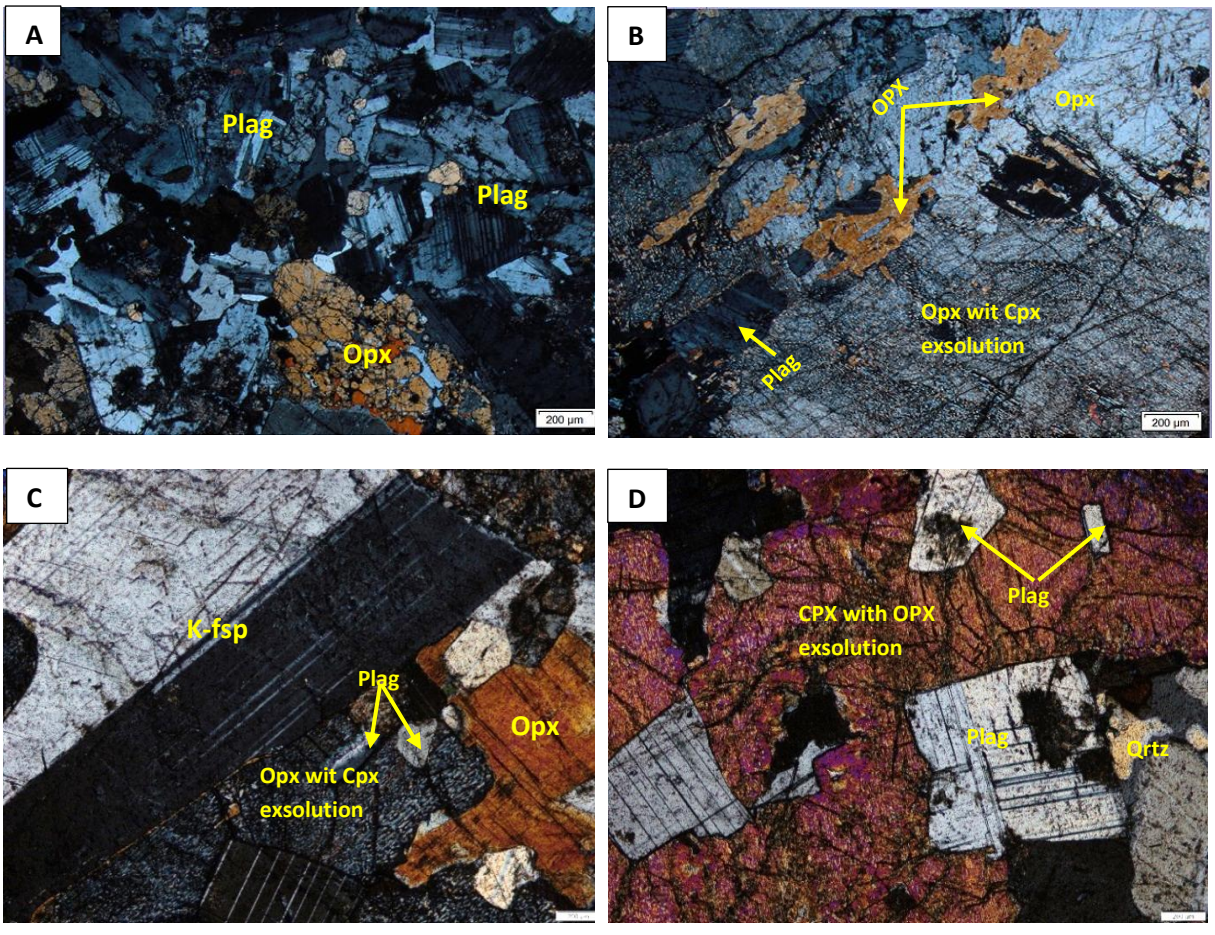


Figure 5-3: Photomicrographs (taken under XPL) of feldspathic harzburgite from the magmatic lithologies at the southwestern portion of the Uitloop farm. (A) Serpentinised olivine with characteristic fractures filled with magnetite, sample Z20 – 54.25, (B) Cumulus olivine and interstitial twinned plagioclase, sample Z20 – 66.5, (C) Clinopyroxene oikocryst enclosing olivine and orthopyroxene, sample Z20–111, (D) Orthopyroxene phenocryst with orthopyroxene inclusions, sample Z20–111, and (E) Olivine with characteristic fractures filled by magnetite, altered orthopyroxene crystals, phlogopite with chromite inclusions, sample Z20-53.7.

5.4 NORITE

The norite lithologies have a similar mineralogical composition as feldspathic pyroxenites; however, the plagioclase crystals in norites are cumulus rather than intercumulus. The norite samples are medium to coarse grained with an inequigranular texture. These rocks consist of predominantly cumulus twinned feldspar, more plagioclase (40 %) than K-feldspar (5 %), with anhedral orthopyroxene (35 %) and clinopyroxene (10 %) crystals. Most of the feldspars have partially altered to saussurite and sericite (Fig 5-4A). There are orthopyroxene crystals which display clinopyroxene exsolution (Fig 5-4B & C). Clinopyroxene oikocrysts which enclose plagioclase (Fig 5-4D) and orthopyroxene inclusions (Fig 5-4F) are also observed. Accessory minerals associated with the norite samples include base metal sulphides, quartz, phlogopite, biotite and alteration minerals (saussurite).



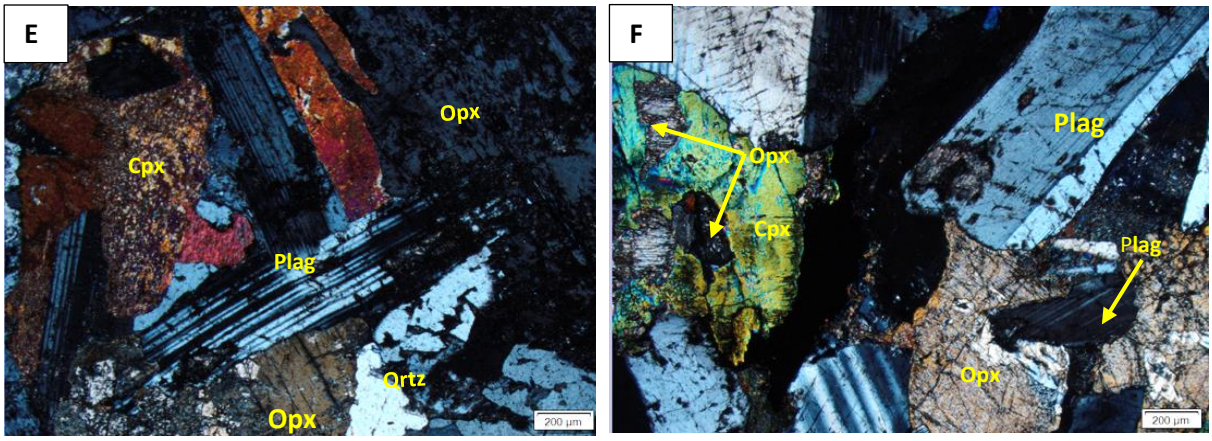


Figure 5-4: Photomicrographs (taken under XPL) of norite from the local magmatic stratigraphy at the southwestern portion of the Uitloop farm. (A) Fine-grained cumulus plagioclase, sample Z20-164.5. (B) Clinopyroxene exsolution lamellae in orthopyroxene, sample Z20-164.5. (C) Twinned K-feldspar and orthopyroxene with clinopyroxene exsolution lamellae and orthopyroxene inclusions, sample Z19-78.3. (D) Twinned plagioclase enclosed by clinopyroxene oikocryst with orthopyroxene exsolution lamellae, sample Z19-78.3. (E) Cumulus plagioclase laths, sample Z20-164.5. (F) Clinopyroxene with orthopyroxene inclusions, sample Z20-164.5.

5.5 GABBRO

The gabbros have a pegmatoidal texture with anhedral crystals and appear to have altered up to 50 %. Unlike norite, gabbroic rocks are principally composed of clinopyroxene (70 %) rather than orthopyroxene (5 %). The clinopyroxene crystals in sample Z20-140.1 are intensely altered to a brownish fine-grained mix of secondary minerals. The twinned plagioclase crystals (15 %) are partially saussuritised (Fig 5-5B). The accessory minerals observed are phlogopite, biotite, opaque sulphides and quartz feldspar granophyric intergrowths (Fig 5-5C).

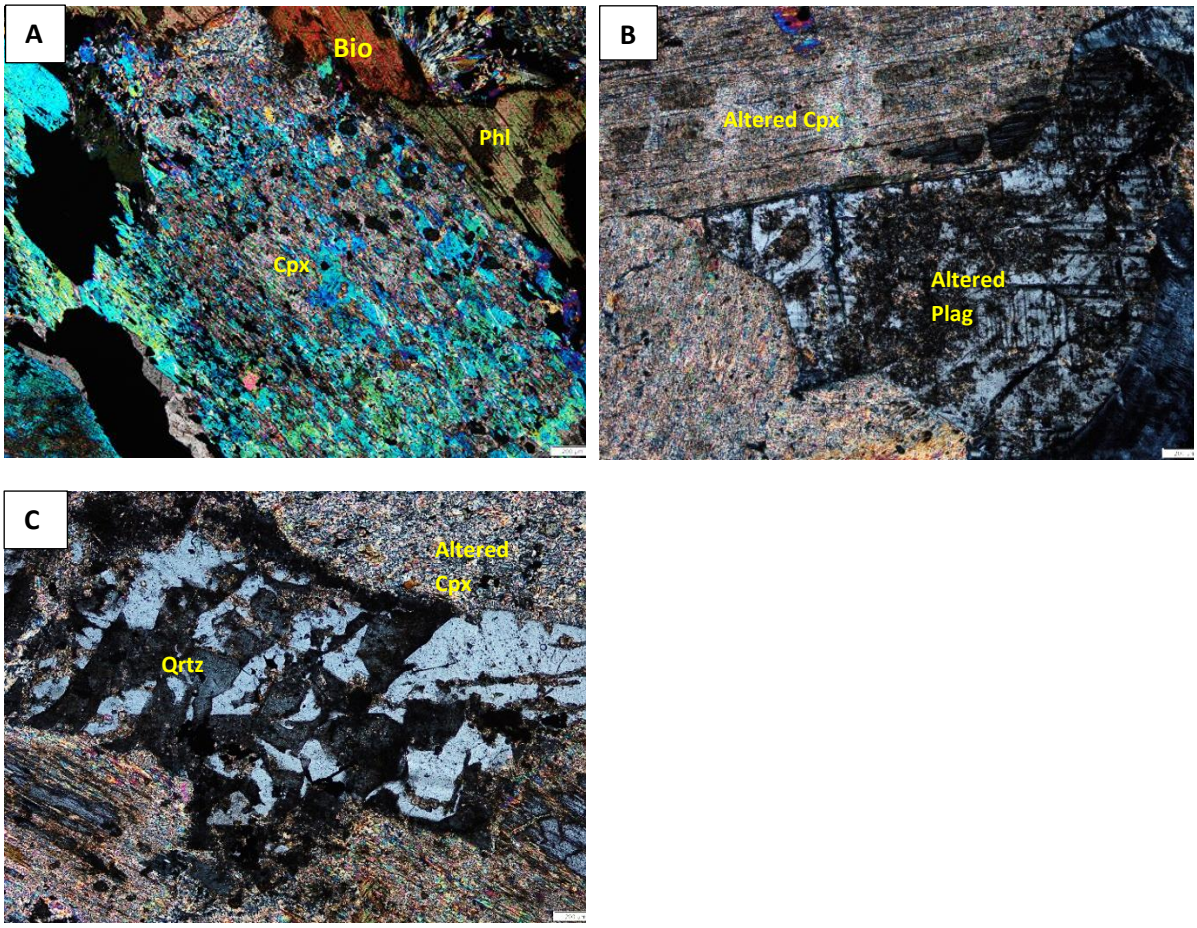


Figure 5-5: Photomicrographs (under XPL) of Gabbro, sample Z20-140.1, from the local magmatic stratigraphy in borehole Z20 at the southwestern portion of the Uitloop farm. (A) Altered clinopyroxene phenocryst. (B) Altered clinopyroxene and sericitized twinned plagioclase. (C) Interstitial quartz with a granophyric texture.

5.6 PARAPYROXENITE

The parapyroxenites from Uitloop are highly altered medium-grained rocks which consist of predominantly anhedral clinopyroxene (>80 %) with minor orthopyroxene (0 – 10 %) and plagioclase (0 – 2 %) (Fig 5-6). Minerals such as sulphides, quartz and carbonate minerals as well as alteration minerals (e.g. saussurite and secondary amphiboles) are also observed in the samples.

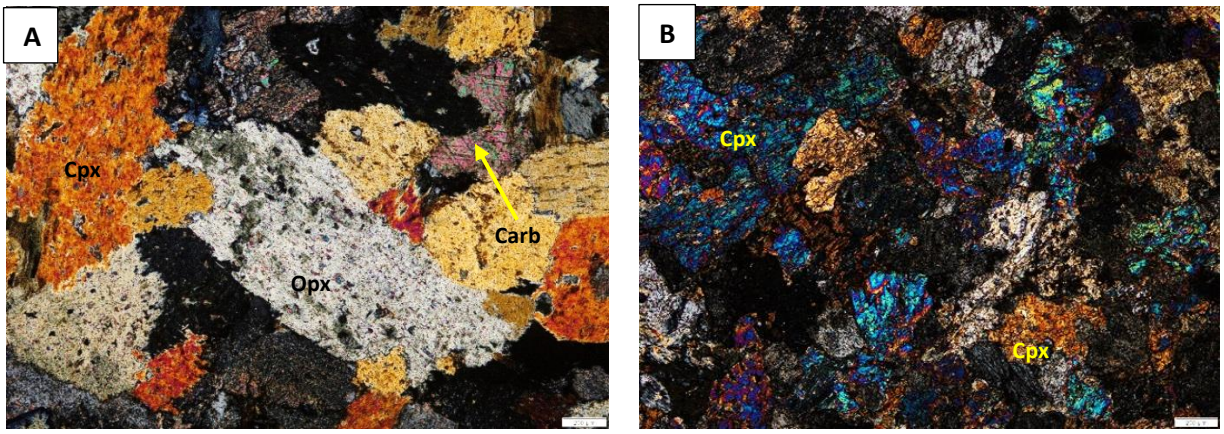


Figure 5-6: Photomicrographs (taken under XPL) of parapyroxenite (sample Z19-170.5) from footwall lithologies at the southwestern portion of the Uitloop farm in borehole Z19. (A & B) Granular pyroxene crystals.

5.7 HORNFELS

A variety of hornfelsed metasedimentary rocks have been intersected in both boreholes Z19 and Z20. Pyroxenite-mica hornfels is fine-grained with a granoblastic texture, the rocks also contain inclusions of quartz and cordierite hornfels which consist of fine-grained granular intergrowths of quartz (30 – 80 %) and cordierite (10 – 60 %) with minor pyroxenes and micas (Fig 5-7). In Sample Z20-183.5, there are also amphibole crystals within the groundmass (Fig 5-7B). Accessory minerals in the pyroxene-mica hornfels include opaque magnetite and base metal sulphides.

Mica-rich hornfels consists predominantly of fine-grained phlogopite (20-40 %) (Fig 5-8A) and/or biotite laths (Fig 5-8B) as well as quartz (30 %). In sample Z20-194.4, large quartz crystals are set within a fine-grained groundmass of biotite, phlogopite and quartz. Other minor minerals observed include clay minerals (chlorite) cordierite, magnetite and sulphides (Fig 5-8B).

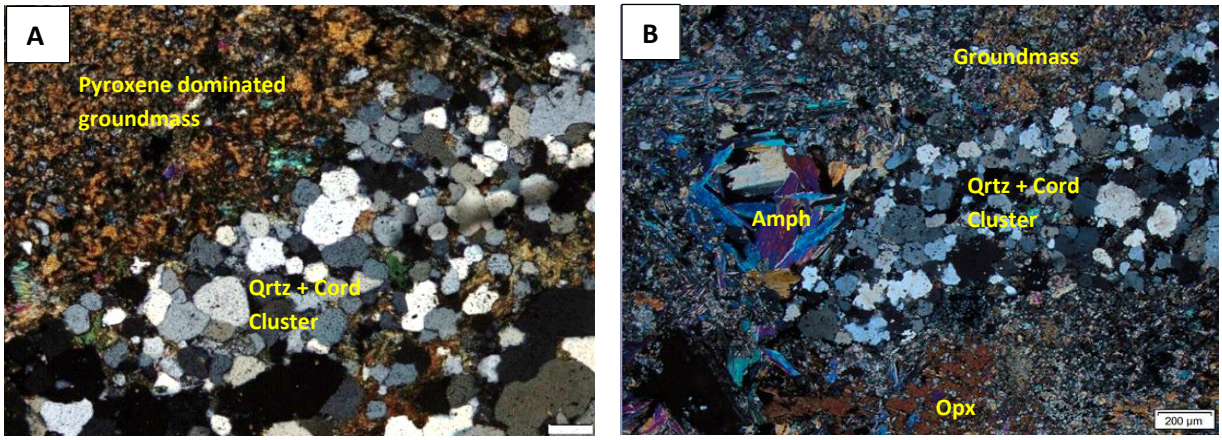


Figure 5-7: Photomicrographs (taken under XPL) of pyroxene hornfels from the footwall lithologies at the southwestern-portion of the Uitloop farm. (A) Quartz and cordierite clusters as well as amphibole clusters set in a fine-grained pyroxene-rich groundmass in pyroxene hornfels, sample Z20-183.5. (B) Quartz and cordierite clusters in pyroxene hornfels, sample Z19-203.2.

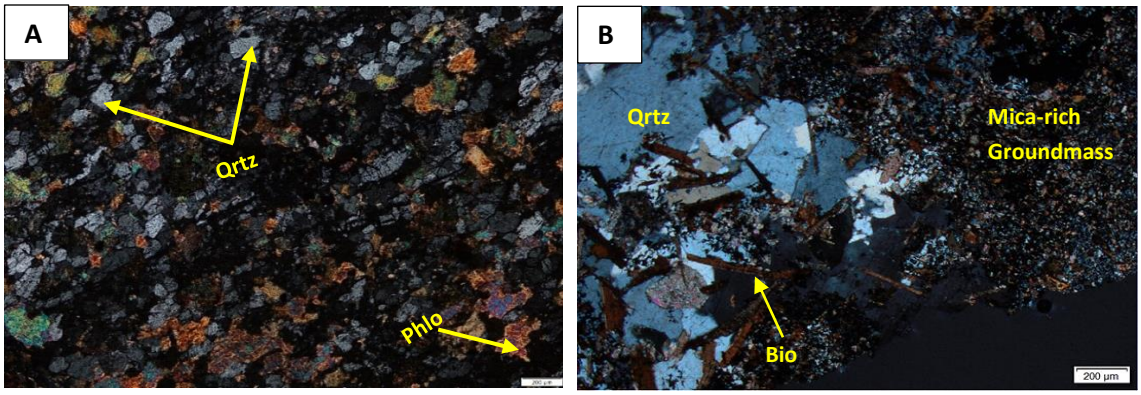


Figure 5-8: Photomicrographs, under XPL, of phlogopite hornfels from footwall lithologies at the southwestern portion of the Uitloop farm. (A) Fine-grained phlogopite hornfels, sample Z19-177.9. (B) Randomly orientated biotite laths associated with quartz grains in biotite hornfels, sample Z20-194.4.

5.8 CALCSILICATE

Calcsilicates at Uitloop consist of consists of minor amounts of re-crystallised clinopyroxene (<15 %) crystals set within the brown crystal mix (50 %) composed of secondary clay minerals, amphiboles and other unidentifiable minerals) (Fig 5-9B). The rocks are highly altered to a mix of very fine-grained brown crystals partly replaced by clay minerals (Fig 5-9A). The sample also contains abundant magnetite (30 %) in close association with the sulphide minerals (5 %) (Fig 5-9C).

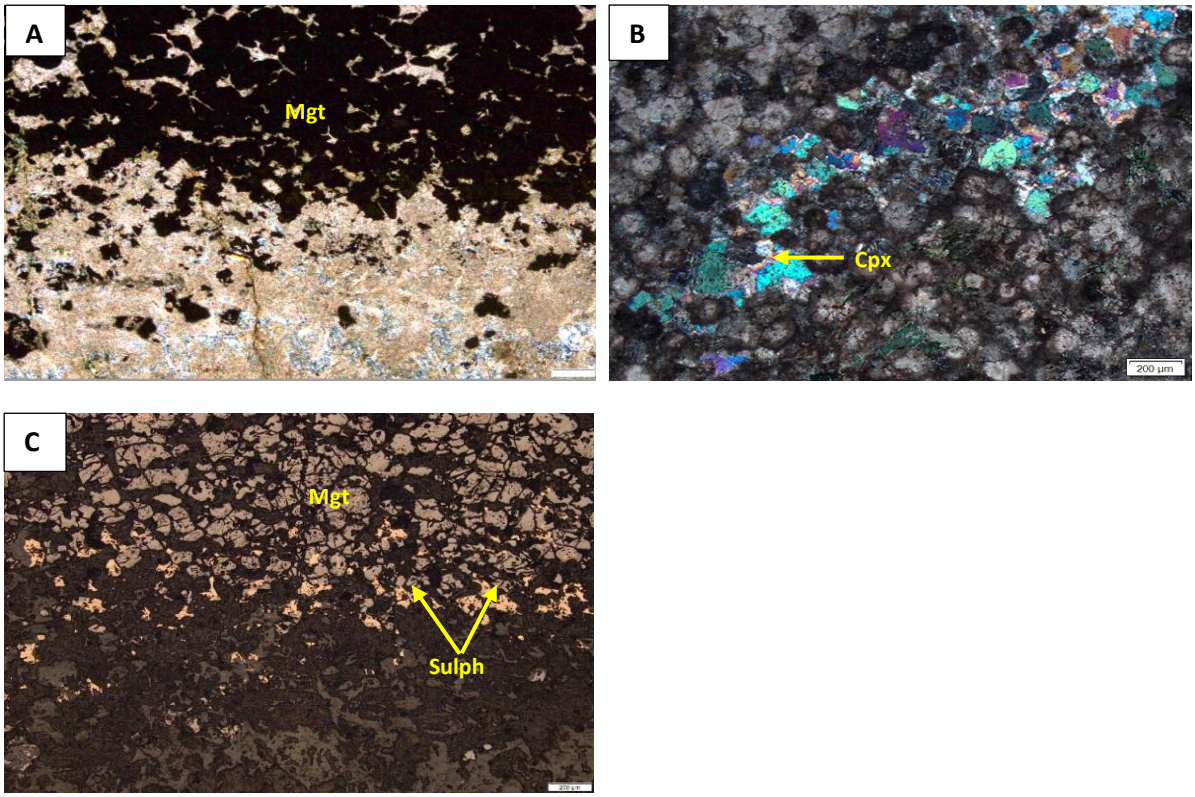


Figure 5-9: Photomicrographs, taken under XPL in transmitted light (A-B) and taken in reflected light (C), of calcsilicate with magnetite bands, sample Z20-212.5, from footwall lithologies at the southwestern portion of the Uitloop farm. (A) Magnetite grains in an altered calcsilicate. (B) Clinopyroxene crystals within altered brown crystal mush. (C) Magnetite and Base Metal Sulphides.

5.9 DISCUSSION

The petrological investigations conducted at the southwestern portion of the Uitloop farm form the foundation for further research in the area. This study is based on two boreholes: Z19 and Z20. The sampling methodology employed in this study tried to capture the different lithologies and styles of sulphide occurrences. The metasedimentary footwall lithologies consist of a variety of hornfels and calcsilicate sequences of the Duitschland Formation. In borehole Z19, there are thin lenses of interfingering sills of orthopyroxenite within the hornfels units, these sills consist entirely of recrystallised orthopyroxene.

The magmatic lithologies intersected in boreholes Z19 and Z20 attain thicknesses of approximately 105.2 m and 124.17 m respectively, they consist of feldspathic pyroxenites, feldspathic harzburgites, norites, orthopyroxenites, gabbros and gabbronorites. In Z20, a thin parapyroxenite layer is observed in the hanging wall, however, in Z19 parapyroxenites are at the base as well as within the footwall. The hanging wall consists of metamorphosed dolomites of the Duitschland Formation while the footwall lithologies are mainly metasedimentary rocks such as hornfelses and calcsilicate after

Duitschland shales and siliceous dolomite. The feldspathic pyroxenite is mainly composed of cumulus orthopyroxene with minor amounts of intercumulus plagioclase and clinopyroxene. The accessory minerals include; phlogopite, biotite, clay minerals (saussurite, sericite, chlorite), secondary amphibole, granophyric intergrowths as well as opaques (sulphides, chromite and magnetite).

The feldspathic harzburgite samples are intensely serpentinised, very few fresh olivine crystals are observed. Other principal minerals in the feldspathic harzburgites are orthopyroxene, plagioclase and clinopyroxene. Accessory minerals also include opaques (chromite, sulphides and magnetite), quartz, phlogopite and secondary clay minerals. The norite, gabbro, gabbronorite and orthopyroxenite lithologies are the least abundant in both boreholes Z19 and Z20.The norite samples are composed of mainly cumulus plagioclase, orthopyroxene with minor clinopyroxene. Gabbros are composed of similar minerals to norites, except that the clinopyroxene content is much higher than that of orthopyroxene. Gabbronorites consist of plagioclase with equal amounts of clinopyroxene and orthopyroxene. Orthopyroxenite samples occurring within the footwall lithologies as thin offshoots or thin sills in borehole Z19 consist entirely of granular orthopyroxene (Fig 5-2) which can potentially be assigned to the Marginal Zone sills.

The parapyroxenite samples are composed of largely clinopyroxene and orthopyroxene crystals displaying a granoblastic texture with minor amounts of opaques (sulphides and magnetite) as well as traces of carbonate minerals. There are two types of hornfels observed at Uitloop farm, namely; pyroxene-plagioclase hornfels and phlogopite-biotite hornfels. The pyroxene hornfels units commonly have angular fragments and veins of quartz-cordierite hornfels. The mineral constituents in the calcsilicate samples from borehole Z20 are difficult to identify in thin section; the sample (Z20-212.5) is dominated by a brown crystal mush of clay minerals (talc and chlorite) and traces of recrystallised clinopyroxene. Magnetite grains also form a large proportion of the calcsilicate samples.

CHAPTER 6

MINERALISATION ON THE SOUTHWESTERN PORTION OF UITLOOP FARM

6.1 CHROMITE

Chromitites in the Bushveld Complex are typically associated with mafic and ultramafic parts of the stratigraphy and usually occur at the base of cyclic units. Several models have been proposed for the formation of massive chromitites, many of which contradict one another, perhaps the formation of the chromitite layers can be attributed to a combination of various models.

Commonly cited models that involve gravity-controlled crystal setting include; 1) magma mixing (e.g. silica contamination induced by the assimilation of country rock into residual melt (Irvine, 1975; Kinnaird et al., 2002) or mixing between resident and new magma (Irvine, 1977; Naldrett et al., 2009; 2012)), 2) pressure changes (Cameron, 1977; Cawthorn, 2005), 3) in-situ growth at the base of the influx (Latypov et al., 2015) and 4) the injection of crystal-rich slurries containing suspended chromite and silicate crystals (orthopyroxene ± olivine) into the magma chamber (Eales, 2000; Mondal & Mathez; 2007; Eales & Costin, 2012). Yudovskaya & Kinnaird (2010) attributed the formation of the Platreef chromitites to the magma mixing model proposed by Irvine (1975; 1977), whereby chromite over-saturation is induced by mixing of two magmas, each near or just at chromite saturation.

6.1.1 CHROMITE OCCURRENCE IN UITLOOP LITHOLOGIES

Chromite is an iron chromium oxide ($FeCr_2O_4$) mineral which belongs to the spinel group. Chromite in borehole Z19 occurs as disseminations within feldspathic pyroxenite lithologies at different stratigraphic levels; e.g. between 100.3 m to 101.8 m and at 137.7 m to 137.85 m depth intervals (Fig 6-1), while in borehole Z20, a thin chromite stringer is observed within the harzburgite layer at a depth of 54.25 m and as fine-grained chromite disseminations in feldspathic harzburgite lithologies at 57.5 m depth (Fig 6-2).



Figure 6-1: A photograph of borehole core samples showing chromite disseminations in feldspathic pyroxenite (sample Z19-137.7).

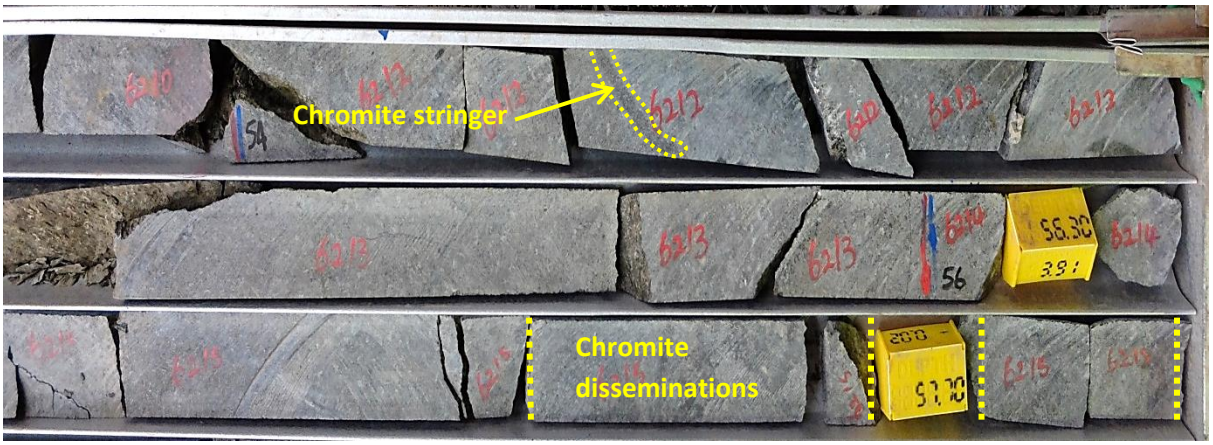


Figure 6-2: A photograph of borehole core samples showing a chromite stringer in harzburgite and fine-grained chromite disseminations in feldspathic harzburgite at a depth of 54.25 m and 57.5 m respectively in borehole Z20.

Chromite crystals in the ultramafic cumulates at Uitloop farm occur as inclusions mainly within pyroxenes, plagioclase, micaceous minerals (phlogopite and biotite) and seldom olivine (Fig 6-3). The majority of these chromite crystals are euhedral. In some samples chromite grains are associated with base metal sulphides (pyrrhotite) (Fig 6-3). The chemistry of the chromite is discussed in Chapter 8.

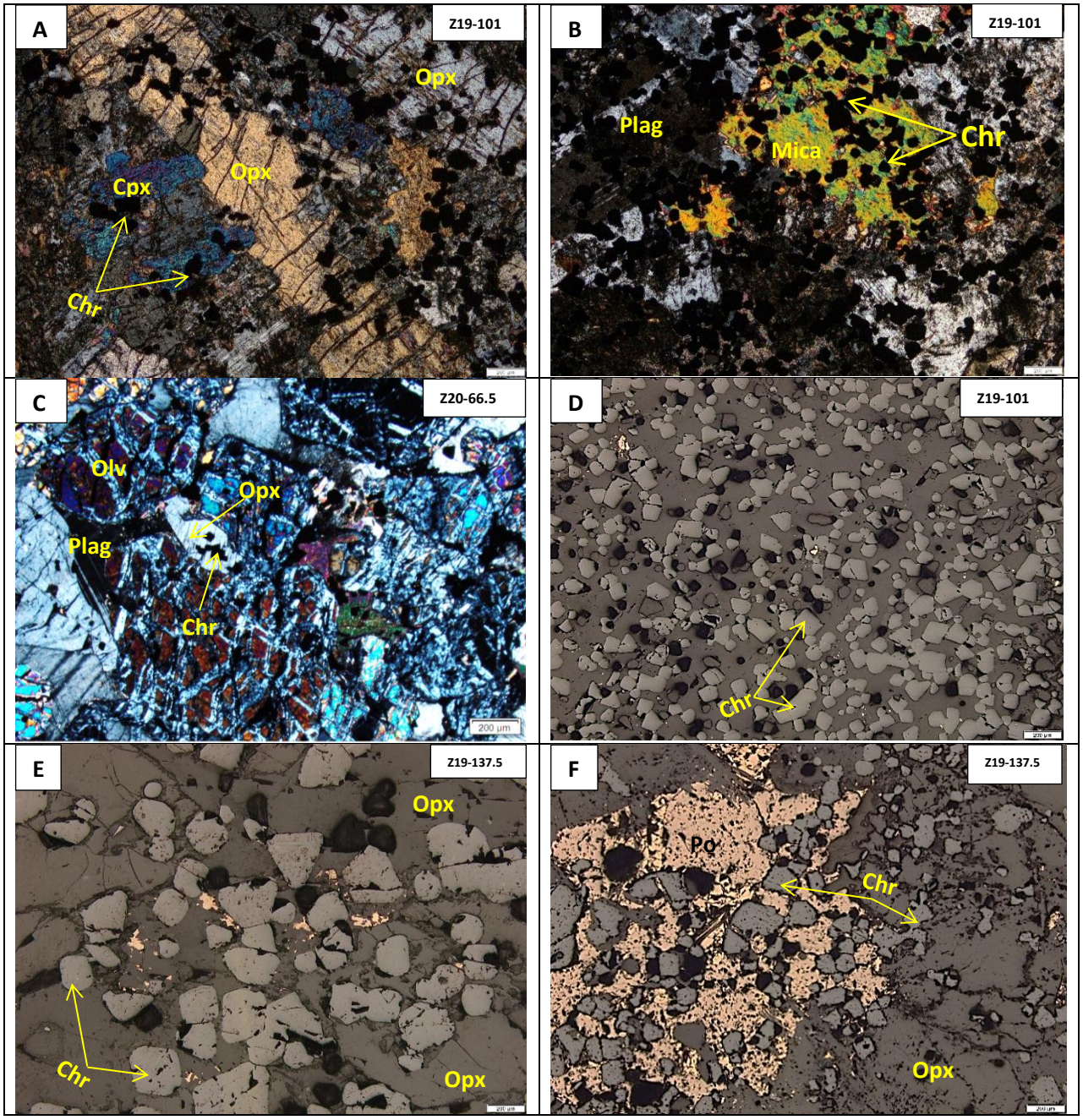


Figure 6-3: Photomicrographs of chromite under XPL in transmitted light (A, B & C) and reflected light (D, C & F). (A)Chromite disseminations within cumulus pyroxene, (B) plagioclase (B) and mica in feldspathic pyroxenite. (C) Chromite inclusions within olivine in feldspathic harzburgite and (D) feldspathic pyroxenite. (E) Annealing chromite crystals. (F) Chromite crystals in close association with pyrrhotite.

6.2 BASE METAL SULPHIDES

6.2.1 THE DISTRIBUTION OF SULPHIDES WITHIN UITLOOP LITHOLOGIES

The base metal sulphides (BMS) are observed in the magmatic lithologies with primary and secondary textures as well as in footwall rocks at Uitloop farm. These sulphides are mainly pyrrhotite ($Fe_{1-X}S$), pentlandite ($(Fe, Ni)_9S_8$) and chalcopyrite ($CuFeS_2$) with minor pyrite (FeS_2). The distribution of sulphides varies with host rock type, however samples with the highest BMS content are feldspathic pyroxenite and feldspathic harzburgites. In both boreholes Z19 and Z20, there is an overall downward increase of sulphides. There is a transition from fine and disseminated sulphides (Fig 6-4) to blebby and net-textured sulphides towards the footwall contact (Fig 6-5).

The primary sulphides in the mafic/ultramafic lithologies of the Uitloop farm consist of finely disseminated pyrrhotite and pentlandite with minor chalcopyrite, with net-textured sulphides occurring in lithologies adjacent to the footwall contact. The footwall lithologies in the studied area also host a significant amount of sulphide mineralisation, dominated by pyrrhotite and pyrite. The sulphides hosted by parapyroxenites are coarsely disseminated and blebby (Fig 6-6), they also form rims around silicate inclusions in the hornfels samples (Fig 6-7). In the calcsilicate units, the sulphides are orientated along the bedding structures, where they alternate with bands of magnetite (Fig 6-8).



Figure 6-4: A photograph of borehole core samples showing finely disseminated base metal sulphides in feldspathic pyroxenite lithologies at a depth of 107.7 m in borehole Z20.

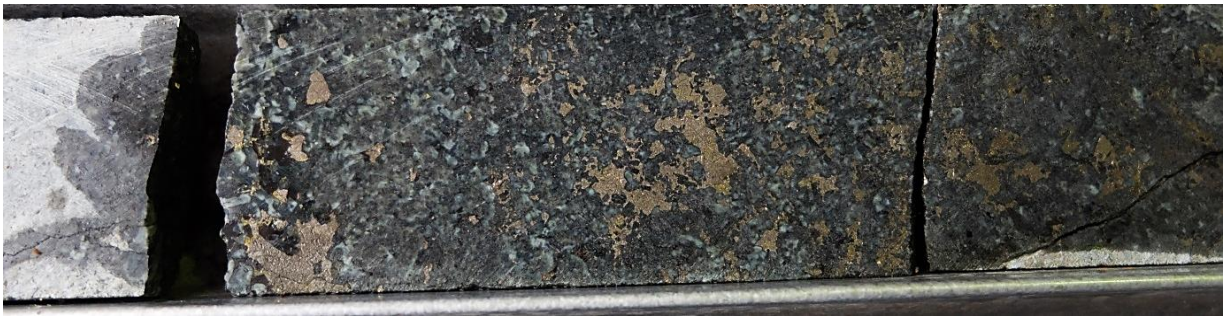


Figure 6-5: A photograph of borehole core samples showing net-textured base metal sulphides, dominated by pyrrhotite, in feldspathic pyroxenite lithologies adjacent to the footwall contact at a depth of ~173.7 m in borehole Z20.



Figure 6-6: A photograph of borehole core samples showing parapyroxenite with sulphide blebs, sample Z19-170.5.



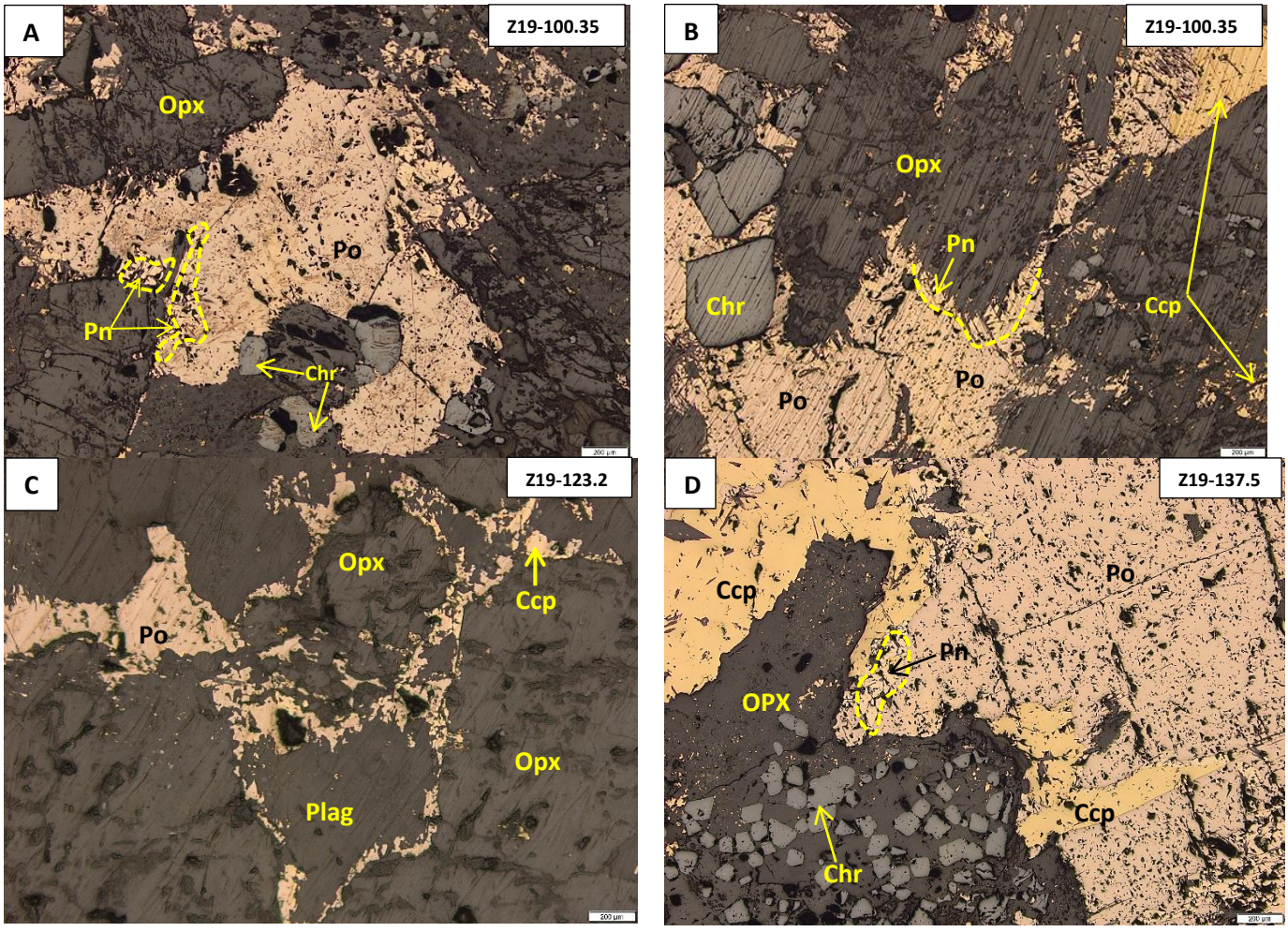
Figure 6-7: A photograph of borehole core sample showing mica-rich hornfels (Sample Z20-183.5), with quartz-cordierite clasts rimmed by pyrrhotite.



Figure 6-8: A photograph of borehole core sample showing base metal sulphides orientated along bedding structures in calcsilicate lithologies in borehole Z20, where they are associated with magnetite bands.

6.2.2 SULPHIDE MINERALOGY

The sulphides in the magmatic lithologies at the southwestern portion of the Uitloop farm are largely interstitial with irregular morphology between the silicate phases (specifically orthopyroxene), Holwell and McDonald (2008) have interpreted these interstitial sulphides as a product of the percolation of a sulphide liquid through a network of intergranular pore spaces. There is evidence of sulphide melt fractionation in the majority of the studied mafic/ultramafic samples, where the sulphide droplets consist of a pyrrhotite core with pentlandite and chalcopyrite generally confined to the margins (Fig 6-9 & 6-10). The BMS also occur in close association with chromite crystals (Fig 6-9 A & B). Flame exsolution of pentlandite in pyrrhotite is also observed (Fig 6-10A). Sulphides (pyrrhotite and chalcopyrite) are commonly replaced by needle-like amphibole (tremolite) intergrowths (Fig 6-10B-C). The secondary sulphides occur as veins (Fig 6-10D) and rims around plagioclase and orthopyroxene crystals (Fig 6-9C); this indicates possible presence of late stage hydrothermal fluid activity.



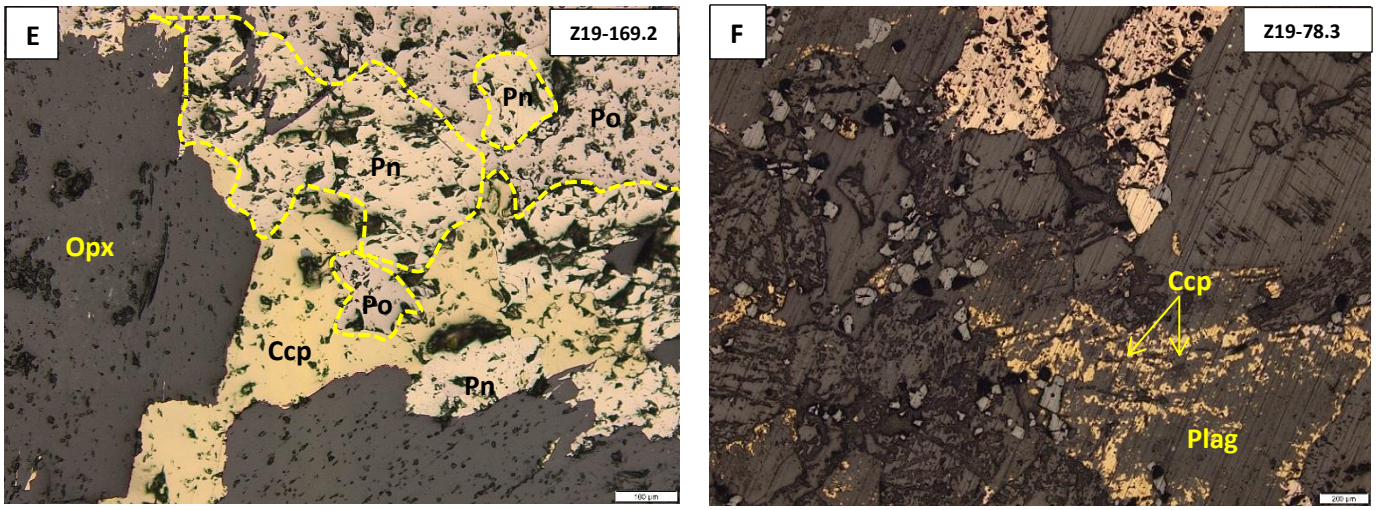


Figure 6-9: Photomicrographs under reflected light, of base metal sulphides observed within magmatic rocks at the southwestern portion of the Uitloop farm. (A & B) Sulphides associated with chromite grains. (C) Pyrrhotite rims around plagioclase and orthopyroxene. (D &E) Evidence of sulphide liquid fractionation. (F) Chalcopyrite remobilization into inclusions in plagioclase. (Chr = chromite, Mgt= magnetite, Po= pyrrhotite, Pn = pentlandite, Ccp = chalcopyrite).

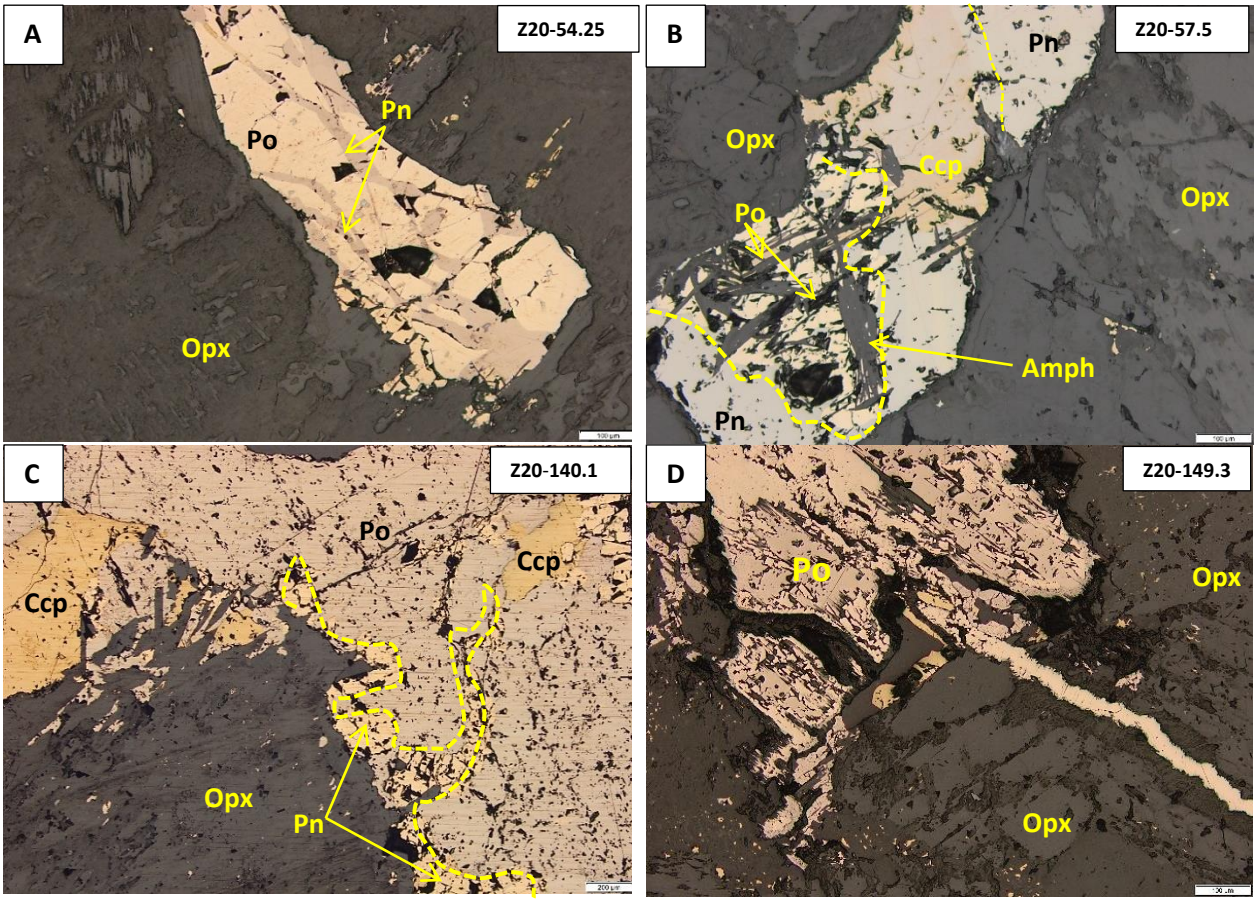


Figure 6-10: Photomicrographs under reflected light, of base metal sulphides observed within the magmatic rocks at the southwestern portion of the Uitloop farm. (A) Pentlandite exsolution in pyrrhotite. (B & C) Pyrrhotite replaced by needle-like amphibole (tremolite). (D) Pyrrhotite vein truncating orthopyroxene crystals. (Mgt= magnetite, Po= pyrrhotite, Pn = pentlandite, Ccp = chalcopyrite).

The sulphides in the footwall lithologies are dominated by pyrrhotite with very little pyrite and chalcopyrite. Pyrrhotite droplets are interstitial to clinopyroxenes in the parapyroxenite samples (Fig 6-11A). The net-textured sulphides within the hornfels samples from borehole Z20 are associated with a fine-grained groundmass of quartz, mica, cordierite and magnetite (Fig 6-11C), while similar rocks in borehole Z19 are barren. Pyrrhotite in the calcsilicate samples occur within interstitial spaces between the fine-grained magnetite (Fig 6-11D). These footwall sulphides are either of low-temperature hydrothermal primary origin or remobilised from adjacent magmatic rocks.

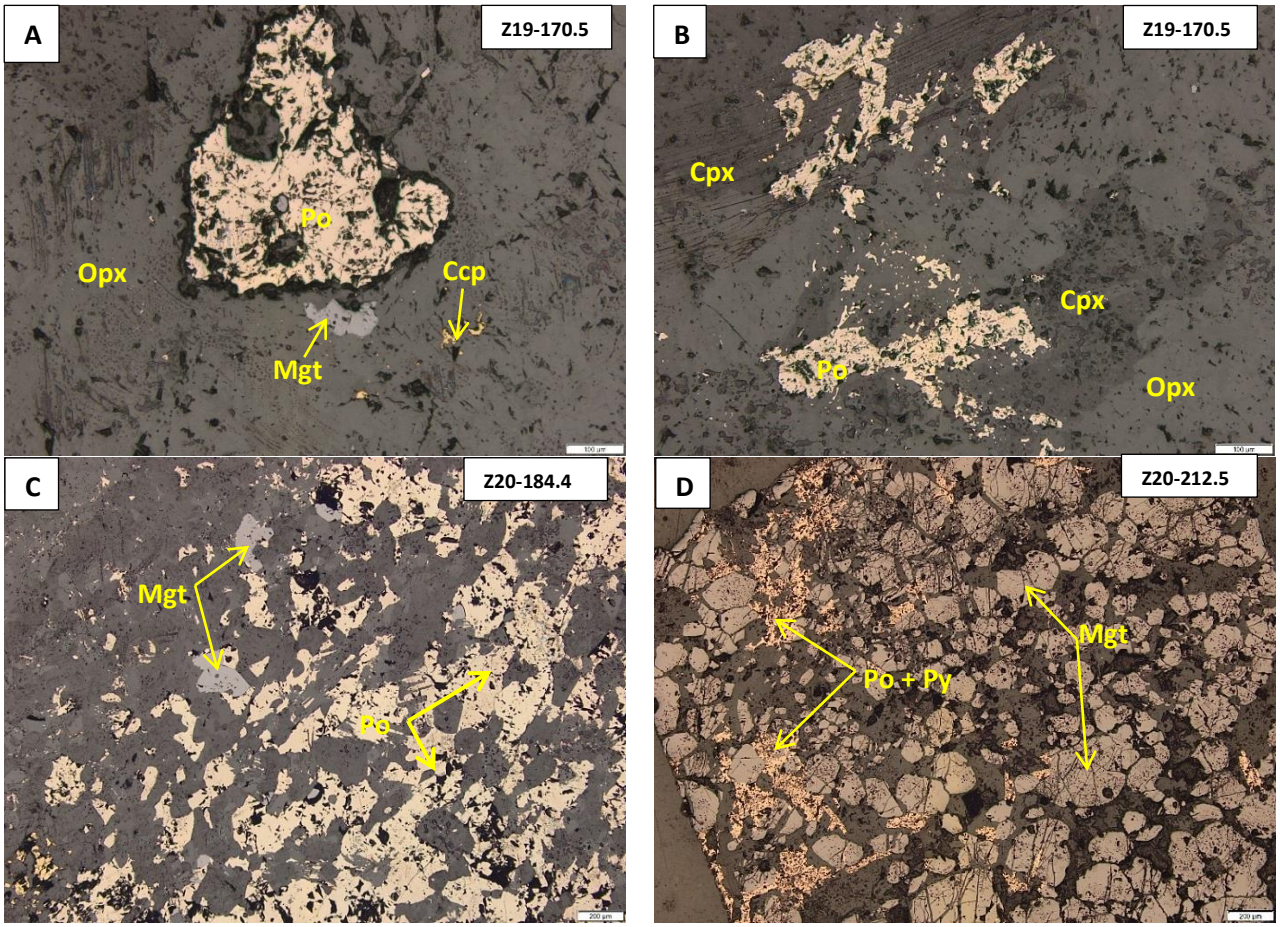


Figure 6-11: Photomicrographs under reflected light, of base metal sulphides in the footwall lithologies at the southwestern portion of the Uitloop farm; (A & B) parapyroxenite, (C) hornfels and (D) magnetite-rich calcsilicate. (Mgt= magnetite, Po= pyrrhotite, Py = Pyrite).

6.2.3 PGE MINERALISATION

The 4E (Au + Pt+ Pd + Rh) grade profile in borehole Z19 (Fig 4-19) illustrates that the PGE grade is middle- and bottom-loaded with major peaks associated with feldspathic pyroxenite lithologies. In borehole Z20; the 4E grade is generally higher than that of borehole Z19, mineralisation is top-loaded with minor mineralisation also occurring at the footwall contact as well as within the hornfels footwall rocks (Fig 4-20). Major mineralisation in Z20 is associated with feldspathic pyroxenite and feldspathic harzburgite as well as with the chromite within these lithologies. The Platinum Group Minerals (PGMs) are extremely difficult to recognize under a petrographic microscope because of their size. However, sulphide hosted PGMs were identified in feldspathic harzburgite (sample Z20-66.5), where they occur within a secondary magnetite rim along margins of large fractionated pyrrhotite and pentlandite bleb (Fig 6-12A), their visibility is accentuated in the BSE image (EPMA) in Figure 6-12B.

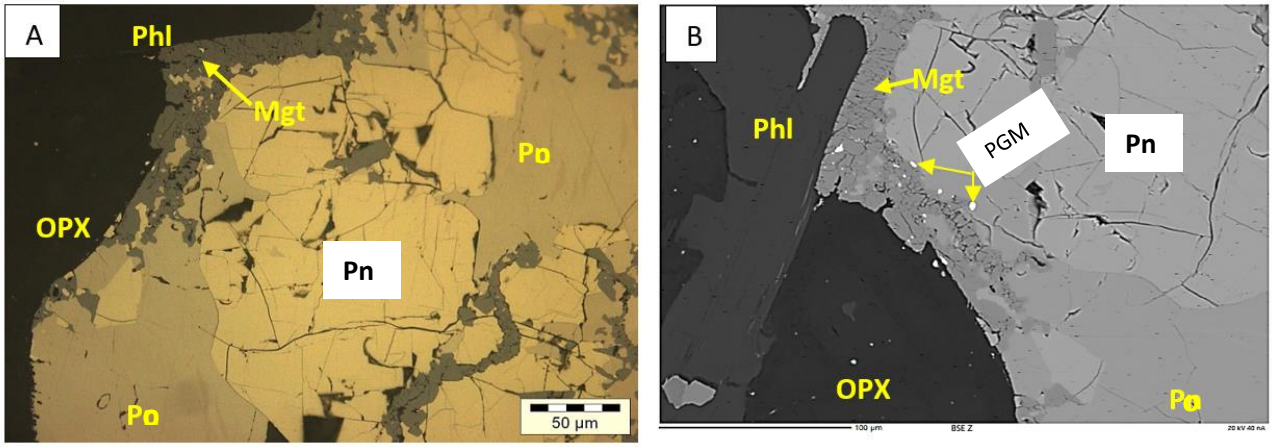


Figure 6-12: Photomicrographs under reflected light (A) and BSE (B), of base metal sulphides associated with feldspathic harzburgite, sample Z20-66.5. (A) Pyrrhotite and pentlandite rimmed by secondary magnetite. (B) Platinum group minerals (PGM) associated with secondary magnetite. (Mgt= magnetite, Po= pyrrhotite, Pn = pentlandite).

6.3 DISCUSSION

The sulphides and chromite at Uitloop farm are associated with the feldspathic pyroxenite and feldspathic harzburgite lithologies. The chromite occurs in the form of disturbed seams and patches of densely disseminated grains and accessory disseminations as well as a very thin chromitite stringer, while sulphides (dominated by pyrrhotite) are net-textured, blebby and disseminated. The chromite is restricted to certain stratigraphic levels, while a general down-hole increase in the sulphides is observed in the magmatic lithologies in both boreholes Z19 and Z20. The sulphides in the norite, gabbro, gabbronorite and orthopyroxenite lithologies are not as prominent, chromite is also absent here. Primary sulphide assemblages in the mafic/ultramafic lithologies consist of pyrrhotite, pentlandite and chalcopyrite, while sulphides in the footwall consist of mainly pyrrhotite with very little pyrite and chalcopyrite in the form of veins or along silicate grain boundaries. These sulphides are potentially a result of remobilization of magmatic sulphides by late stage magmatic fluids. The sulphides within the footwall lithologies are mainly orientated along bedding structures, confined to the lithological contacts, magnetite bands and fragments in breccias. Replacement of sulphides by secondary silicates (i.e. amphiboles) along margins of sulphide blebs is common (Fig 6-10).

Lithologies in borehole Z19 and Z20 show medium to high degrees of alteration, primarily serpentinization and chloritization associated with mainly feldspathic harzburgite sequences. A high degree of alteration is consistent with a high fluid flux derived from contact-metamorphosed sediments above and below the relatively thin intrusion.

The PGE (Au +Pt +Pd + Rh) grade distribution is middle- and bottom-loaded in borehole Z19 where PGE grade is the highest in the net-textured sulphide interval while PGEs in Z20 are top-loaded. In both boreholes, high PGE grades occur in feldspathic pyroxenite and feldspathic harzburgite layers which host sulphide and chromite. Therefore, two styles of PGE mineralisation are noted: the reef-style horizon that is associated with the irregular or disturbed chromitites at the top of the intersection Z20 and contact-style mineralisation rich in sulphides and with modest PGE that is confined to the lower part of the Z19 sequence and to the footwall.

CHAPTER 7

GEOCHEMISTRY OF THE ZEBEDIELA PROJECT ROCKS

7.1 INTRODUCTION

In this chapter, major and trace element compositions of various rock types from the southwestern portion of the Uitloop farm are considered. The element concentrations were determined using X-ray fluorescence (XRF) and Inductively Coupled Plasma-Mass Spectrometry (ICP-MS) techniques. The analyses of thirty-three samples were conducted in the Earth Laboratory in the School of Geosciences at the University of the Witwatersrand. The sample preparation and methodology are provided in Appendix A, while the complete whole rock geochemical dataset is presented in Appendix C. Binary variation diagrams for trace and major elements are presented in this chapter. The major element analysis is useful for the classification of rocks, whereas trace elements are used to understand the conditions under which these rocks formed. As one of the major aims of this study was to establish a correlation between the studied magmatic sequences and either the Lower Zone or Platreef, the least contaminated and altered varieties of most primitive magmatic rock were sampled whereas only a few samples of norite, gabbronorite, parapyroxenite and hornfelses were analysed as their composition cannot help in correlation of magmatic stratigraphy.

7.2 MAJOR ELEMENT VARIATIONS IN ROCK TYPES

Figures 7-1 and 7-2 show the relationship between the major element concentration of Na_2O, K_2O, MgO, CaO, SiO_2, TiO_2, MnO, Al_2O_3, Fe_2O_3 and P_2O_5, with stratigraphic height in boreholes Z19 and Z20 of the Uitloop farm. The Z19 sequence contains a thick interval of chromitiferous feldspathic pyroxenite at the top with minor intervals of feldspathic harzburgite. In borehole Z19, the major element concentrations (except MgO and MnO) within the feldspathic pyroxenites show a decreasing abundance with increasing depth in the borehole (Table 7.1). Figure 7-1 also shows that the feldspathic pyroxenite samples higher in the stratigraphy generally have lower SiO_2 content than those at lower stratigraphic levels.

In contrast, the top part of the Z20 sequences is composed of thick layers of chromitiferous feldspathic harzburgite that intercalate with subordinate feldspathic pyroxenite interlayers. In borehole Z20, CaO, MnO, K_2O and Na_2O in feldspathic harzburgite increase with increasing depth while SiO_2, MgO, TiO_2, Al_2O_3

and Fe_2O_3 show a decreasing abundance with increasing depth in the borehole. The major element concentrations (except MgO) in feldspathic pyroxenite in Z20 generally increase with increasing depth towards the footwall contact (Fig 7-2).

Table 7-1: The comparison of major element concentrations between different rock types in boreholes Z19 and Z20.

		Major elements (wt.%)									
BH	Rock type	MgO	CaO	SiO_2	TiO_2	MnO	Al_2O_3	Fe_2O_3	Na_2O	K_2O	P_2O_5
Z19	FPYX	13.8 – 18.9	3.8 – 9.4	40.0 – 51.5	0.2 – 0.4	0.2	6.8 – 10.4	10.8 – 17.8	0.7 – 1.3	0.32 – 1.0	0.2 – 0.5
Z20	FPYX	7.2 – 27.9	1.7 – 8.4	35.7 – 53.7	0.1 – 0.6	0.1 – 0.2	3.4 – 13.3	8.4 – 36.5	0.1 – 1.5	0.2 – 1.8	0.1
	FHRZ	22.4 – 27.9	1.9 – 3.8	42.8 – 49.6	0.2 – 0.4	0.1 – 0.2	5.3 – 6.0	12.2 – 16.6	0.2 – 0.7	0.2 – 0.4	0.02 – 0.04

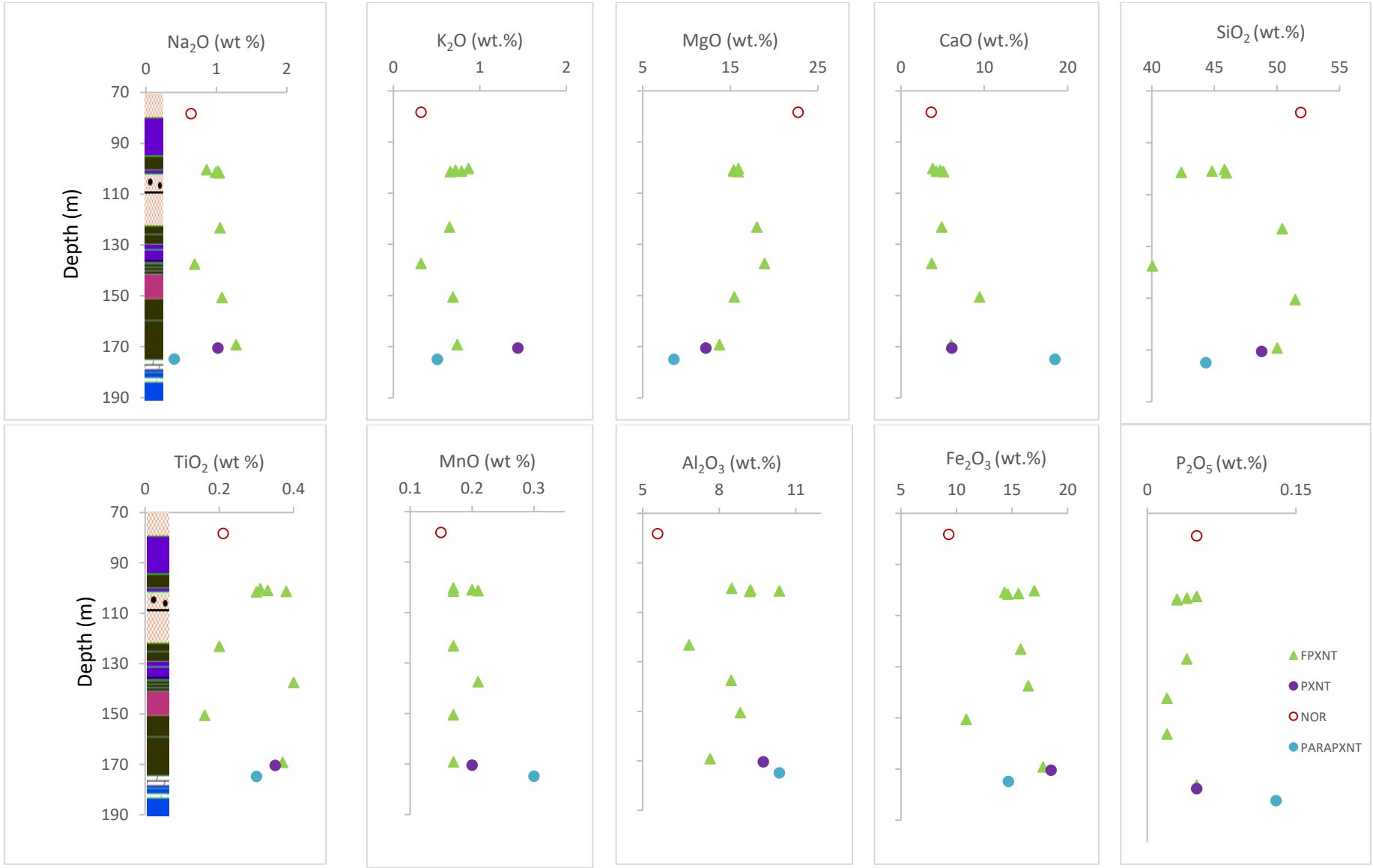


Figure 7-7-1: Variation in major element concentrations with stratigraphic height in borehole Z19. (FPXNT = feldspathic pyroxene, PXNT = pyroxenite, NOR = norite, PARAPXNT = parapyroxenite).

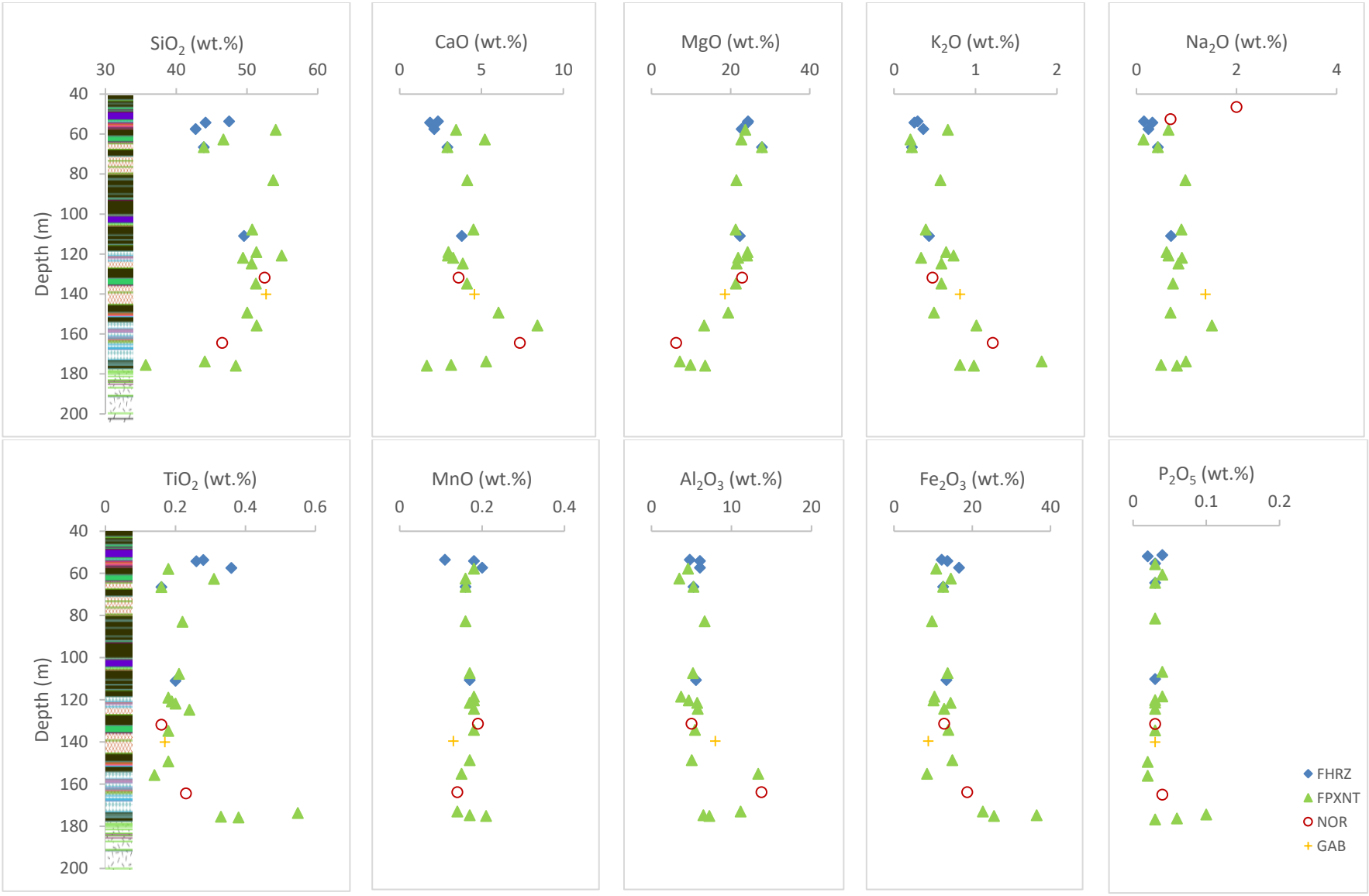


Figure 7-2: Variation in major element concentrations with stratigraphic height in borehole Z20. (FHRZ = feldspathic harzburgite, FPXNT = Feldspathic pyroxene, NOR = norite, GAB = gabbro).

Binary variation diagrams of MgO versus SiO_2, TiO_2, Al_2O_3, Fe_2O_3, MnO, CaO, K_2O and Na_2O are presented in Figures 7-3 and 7-4, this is because MgO has a wide variation and abundance in mafic/ultramafic rocks. The variations in major element compositions represent the proportion of olivine, pyroxene and plagioclase that are present within the samples. The variation in major elements is reflective of the modal mineralogy of individual samples; the Al_2O_3, CaO and Na_2O contents in the samples reflect the modal proportion of feldspar minerals (i.e. plagioclase) while the MgO and FeO values reflect the modal proportions of pyroxene and olivine. At the same time, an occurrence of major chromite in chromitiferous intervals has a great influence on rock chemistry as chromite provides not only significant Cr_2O_3 (that shifts the balance of other major oxides) but also excess Fe, Ti and Al. The presence of sulphides, in particular pyrrhotite, also results in elevated Fe in the compositions of the mineralised rocks.

Although the data points in these diagrams are highly scattered different major element relationships can be distinguished. In borehole Z20 (Fig 7-4); the feldspathic pyroxenite samples generally have higher SiO_2 content with an MgO range that is consistent with a higher proportion of silica-rich orthopyroxene. The MgO in feldspathic pyroxenite samples generally increases with decreasing SiO_2 content. In these feldspathic pyroxenite samples; Al_2O_3, CaO, TiO_2, Na_2O and K_2O show a fairly strong negative linear association with MgO while Fe_2O_3 and MnO show positive correlations with MgO an indication of the increase in plagioclase and decrease in modal pyroxene and olivine.

Figure 7-4 shows the major element variations in samples from borehole Z20, MgO shows some correlation with SiO_2 and MnO in feldspathic pyroxenites. In both rock types; the MgO displays a strong negative association with Al_2O_3, Fe_2O_3, CaO, K_2O and Na_2O. Unlike in borehole Z19, feldspathic pyroxenite and feldspathic harzburgite samples have a similar range of Al_2O_3 content, although a few feldspathic pyroxenite samples have much higher Al_2O_3. The chemistry of ultramafic rocks is controlled by varying proportions of silica-rich orthopyroxene and silica-poor olivine. Plagioclase and chromite are subordinate minerals that provide Cr, Fe, Al, Ti and Ca. The chemical composition of norite and gabbro is rather similar to that of ultramafic rocks in terms of MgO and SiO_2 content, however, elevated CaO and Al_2O_3 indicate a higher proportion of clinopyroxene and plagioclase.

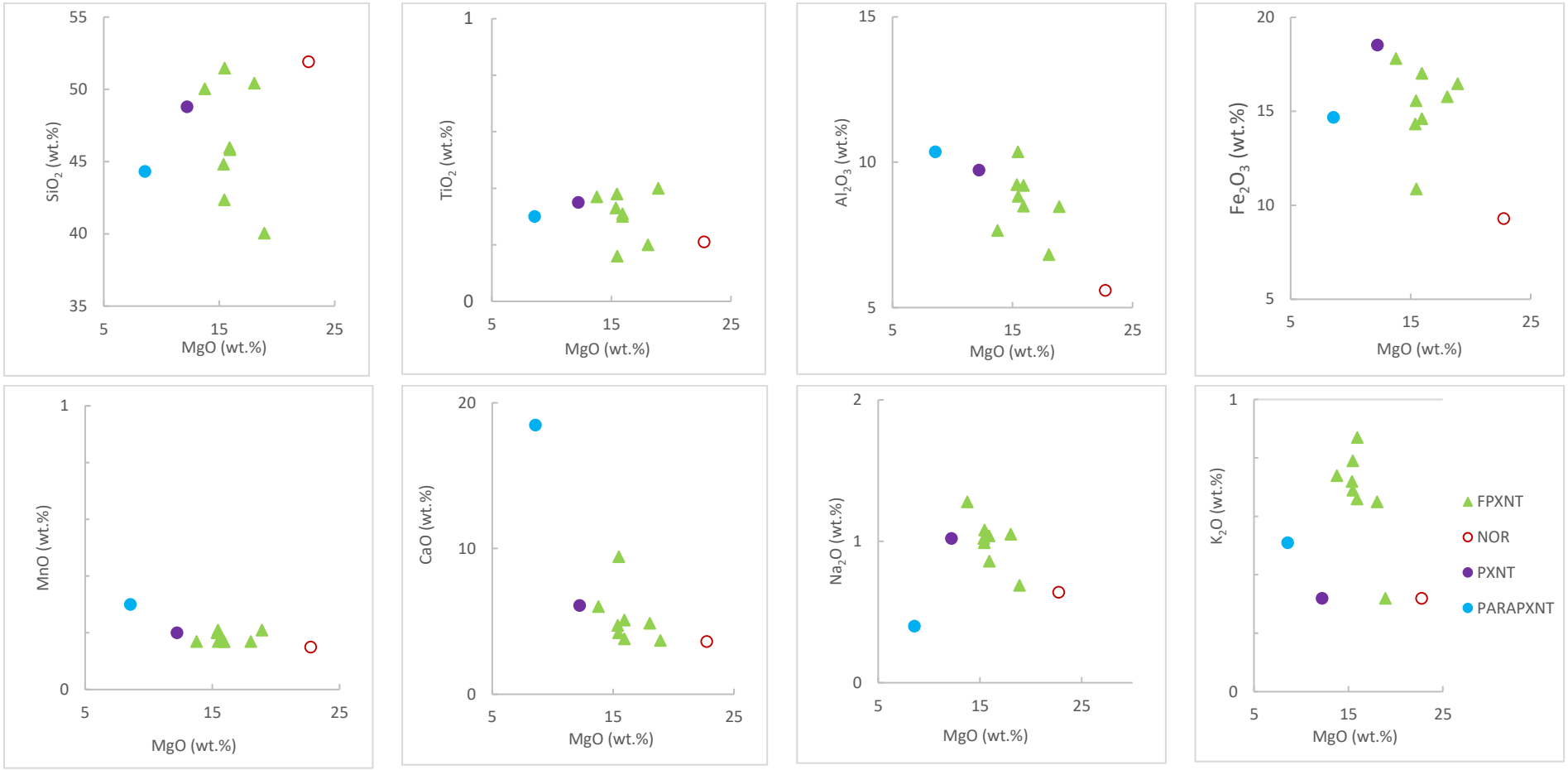


Figure 7-3: Binary variation diagrams showing selected major elements concentrations (wt.%) versus MgO content (wt.%) in borehole Z19 lithologies. (FHRZ = Feldspathic harzburgite, FPXNT = Feldspathic pyroxene, NOR = Norite, PXNT = Pyroxenite, PARAPXNT =Parapyroxenite).

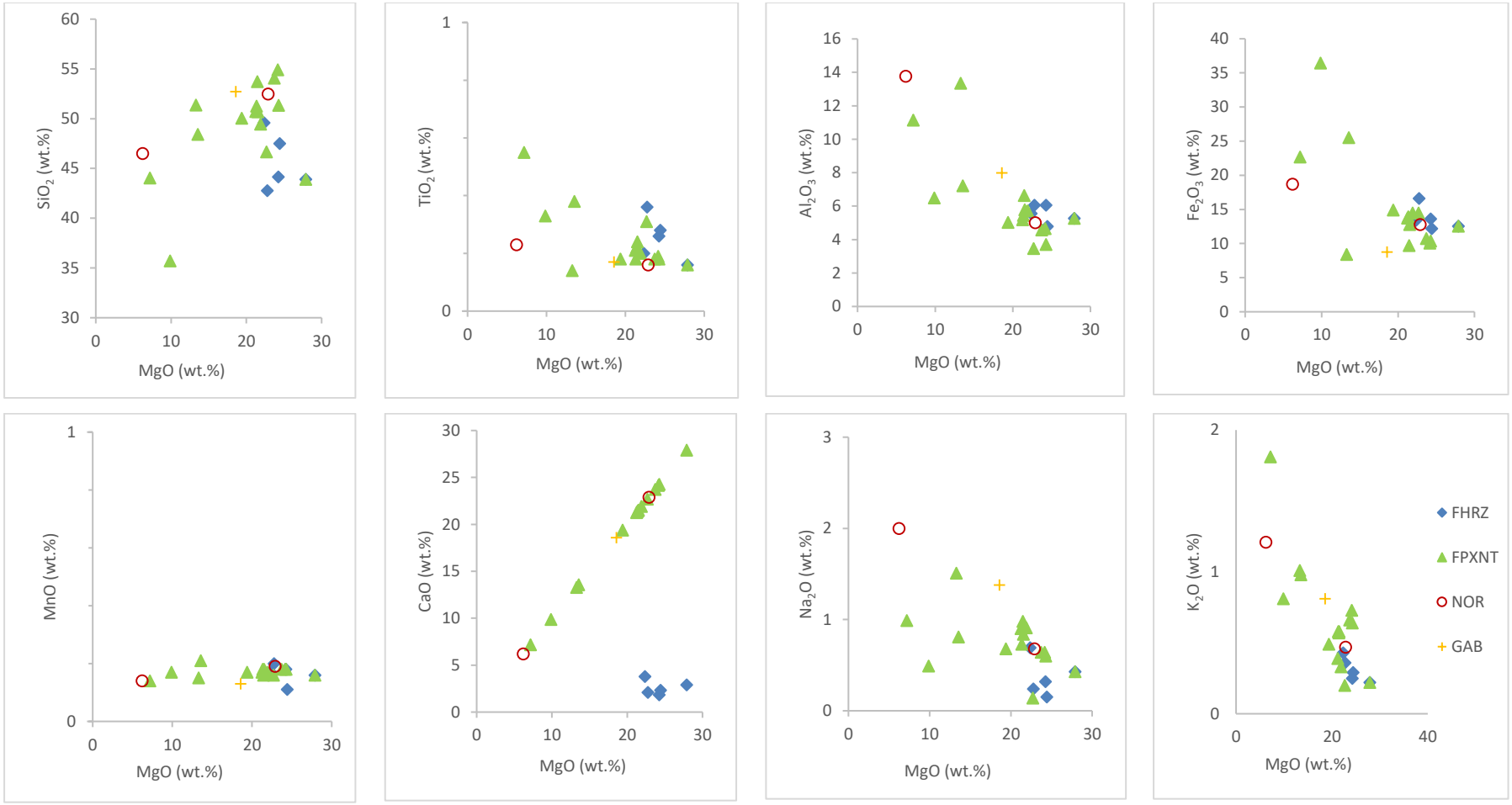


Figure 7-4: Binary variation diagrams showing major elements concentrations (wt. %) versus MgO content (wt. %) in borehole Z20 lithologies. (FHRZ = Feldspathic harzburgite, FPXNT = Feldspathic pyroxene, NOR = Norite, GAB =Gabbro).

7.3 TRACE ELEMENT VARIATIONS IN ROCK TYPES

Trace elements show significant variation related to the formation and modification of rocks. Binary variation diagrams for selected trace elements versus MgO as well as their variation with stratigraphic depth are presented in Figures 7-7 – 7-8 and Figures 7-5 – 7-6 respectively.

The feldspathic pyroxenite in Z19 (Fig 7-5) is characterised by relatively narrow ranges of Ba, Rb (with an outlier of 67 ppm), Sr (with an outlier of 155 ppm), Y, Zn and Ga and wider variations of Co, Cu, Cr, Sc, Ni, Zr and V. The chromitiferous varieties are enriched in Ba, Co, Cr, Ni, Sr, Zr and V with respect to the Cr-poorer rocks (Table 7-2). Norite contains Ba (0.5 ppm), Co (76 ppm), Cu (38 ppm), Sr (42 ppm), Ni (534 ppm) and Ga (4 ppm) that are significantly less than their concentrations in the feldspathic pyroxenite.

The feldspathic pyroxenite in Z20 (Fig 7-6) is characterised by relatively narrow ranges of (in ppm): Ba, Cr, Sc, Rb (with up to 110 ppm in samples adjacent to footwall contact), Sr (with an outlier of 173 ppm), Y, Zr (with an outlier at 105), V and Zn (with an outlier at 591 ppm) and wider variations of Co, Cu and Ni. Feldspathic harzburgite are poor in Co, Rb and Sr and rich in Cr and V compared to feldspathic pyroxenite, however, Ba, Co, Cu, Sc, Ni, Y, Zr, Zn and Ga concentrations fall within the same ranges as those of feldspathic pyroxenite (Table 7-2). Chromitiferous varieties are enriched in Cr and poor in Rb and Sr with respect to the Cr-poorer rocks (Fig 7-6). Norite and gabbro contain somewhat similar ranges of trace element concentrations as ultramafic rocks. In both boreholes Z19 and Z20, as expected, the concentration of chalcophile elements increases with increasing depth as a result of an increase in sulphides towards the base of the core.

Table 7-2: The comparison of trace element concentrations between different rock types in boreholes Z19 and Z20.

		Trace elements (ppm)												
BH	Rock type	Ba	Rb	Sr	Y	Zn	Ga	Co	Cu	Cr	Sc	Ni	Zr	V
Z19	FPYX	0.7 – 1.7	9 – 33	11 – 50	3 – 10	41 – 151	5 –12	106 – 242	108 – 1870	1193 – 59537	13 – 34	671 – 3852	11 – 44	82 – 387
Z20	FPYX	0.4 – 1.0	16 – 25	36 – 173	3 -8	45 – 591		61 – 567	74 – 6612	590 – 4382	12 – 42	610 – 12437	14 – 105	60 – 306
	FHRZ	0.4 – 0.8	10 – 23	6.8 – 60	3 – 11	62 – 2095	4 – 9	81 – 236	260 – 1799	3032 – 100 000	11 – 28	2429 – 5743	8 – 30	68 – 262

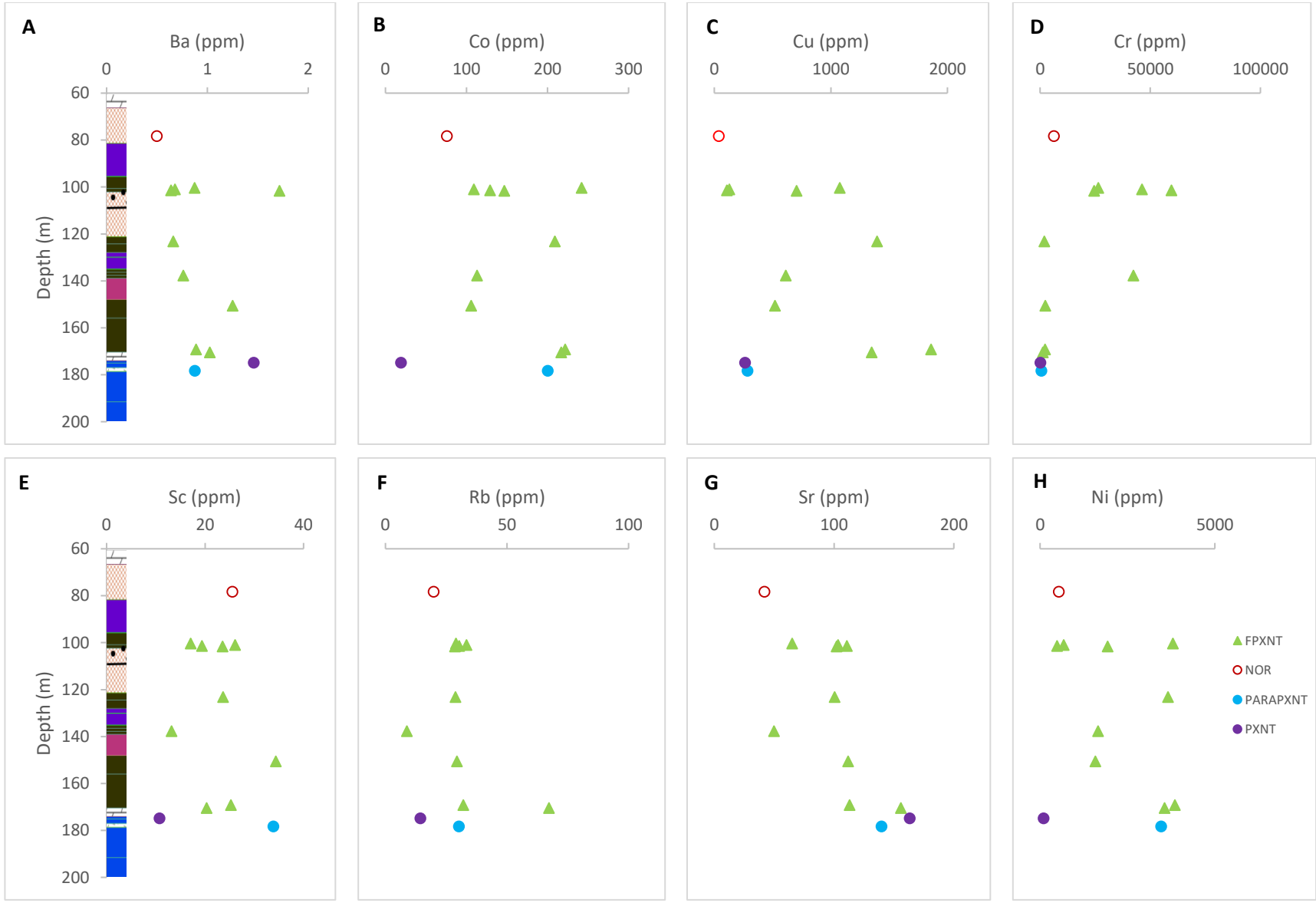
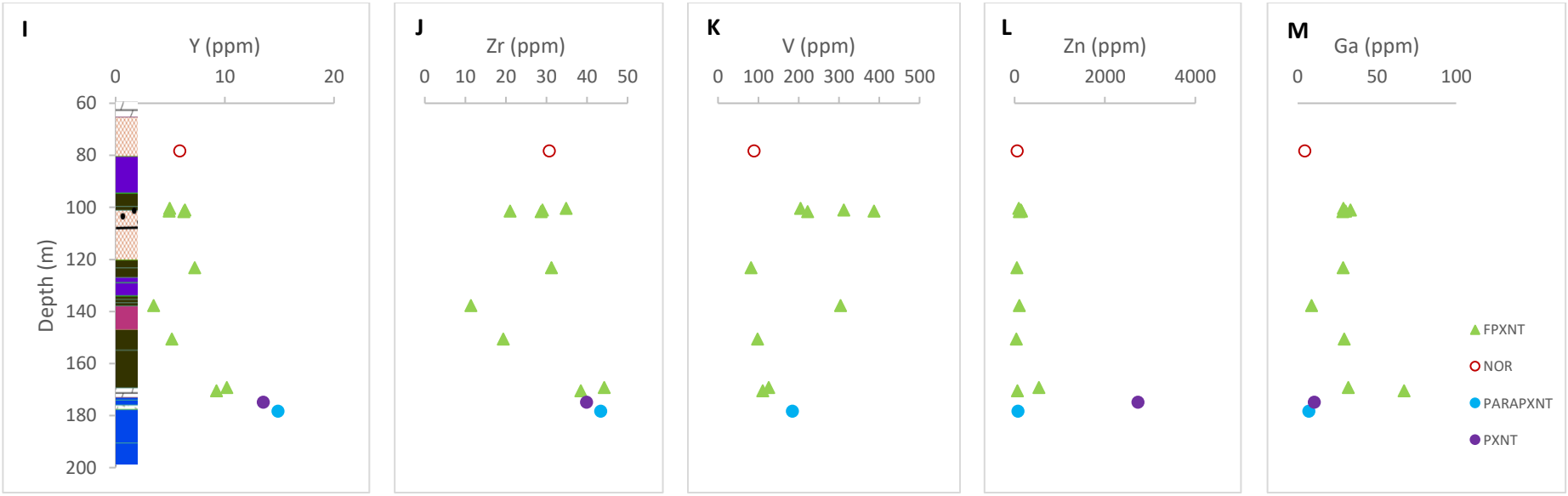


Figure 7-5: Variation in selected trace element concentrations (ppm) with stratigraphic height in borehole Z19 from the Uitloop farm. (FHRZ = Feldspathic harzburgite, FPXNT = Feldspathic pyroxene, NOR = Norite, PXNT = Pyroxenite, PARAPXNT =Parapyroxenite).



(Figure 7-5 cont.) (FHRZ = Feldspathic harzburgite, FPXNT = Feldspathic pyroxene, NOR = Norite, PXNT = Pyroxenite, PARAPXNT =Parapyroxenite).

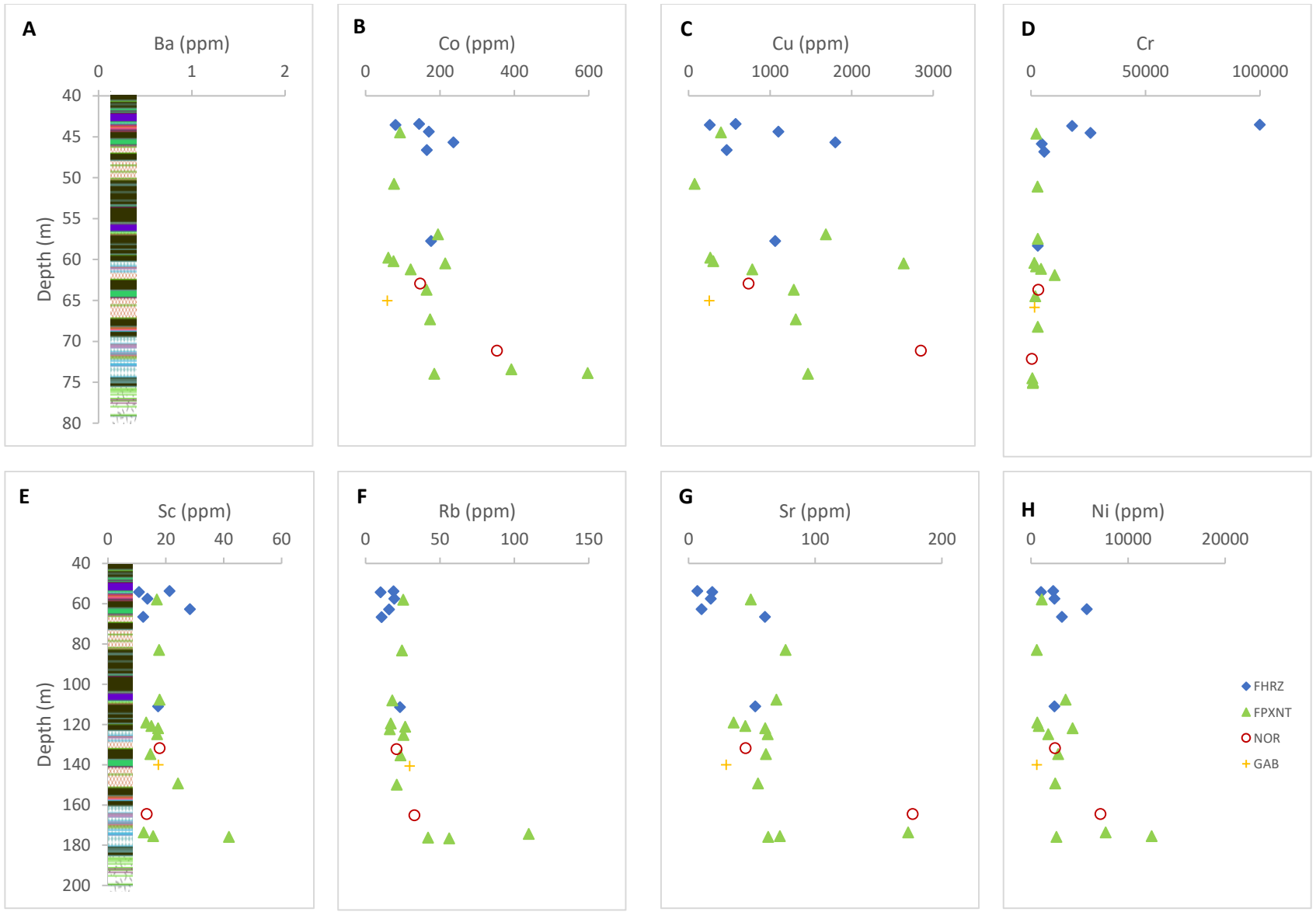


Figure 7-6: Variation in selected trace element concentrations (ppm) with stratigraphic height in borehole Z20 from the Uitloop farm. (FHRZ = Feldspathic harzburgite, FPXNT = Feldspathic pyroxene, NOR = Norite, GAB =Gabbro).

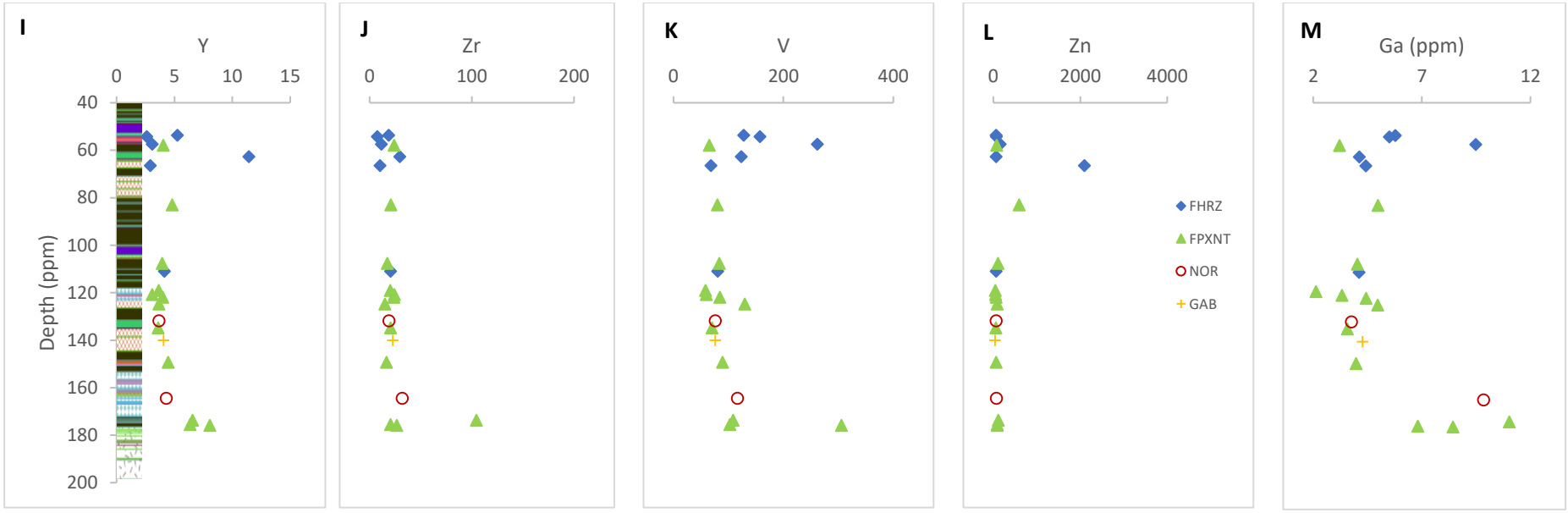
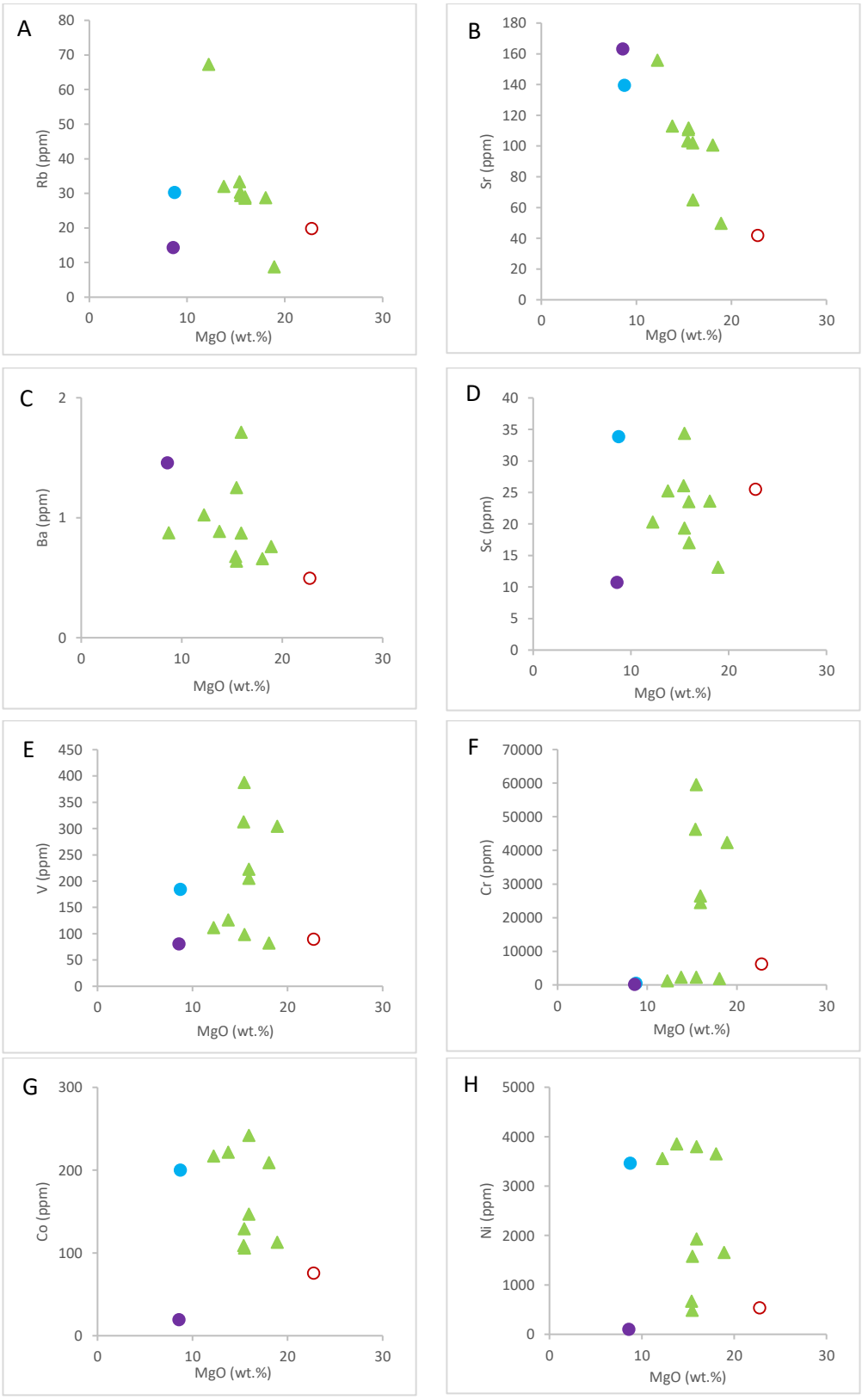


Fig 7-6 cont.) (FHRZ = Feldspathic harzburgite, FPXNT = Feldspathic pyroxene, NOR = Norite, GAB =Gabbro).

Binary variation diagrams for trace elements (ppm) versus MgO (wt.%) are also presented in Figures 7-7 and 7-8. In borehole Z19 (Fig 7-7); the Rb concentrations in feldspathic pyroxenite are less than 35 ppm and show a negative correlation with MgO (Fig 7-7A). Although not enough data is available, the Rb content in the parapyroxenite is much lower than in the mafic/ultramafic rocks in borehole Z19. A strong negative trend is also observed between Sr and MgO in the feldspathic pyroxenites (Fig 7-7B), with concentrations varying between 49.8 – 113 ppm. Much higher Sr (up to ppm 140 ppm) concentrations are recorded for the parapyroxenite sample (Fig 7-7B).

Ba displays a moderately strong correlation with MgO in feldspathic pyroxenites with concentrations not exceeding 2 ppm (Fig 7-7C). Sc shows a negative correlation with MgO, with values ranging between 13 – 34 ppm in feldspathic pyroxenite (Fig 7-7D). V ranges between 82 – 387 ppm and shows a positive correlation with MgO in feldspathic pyroxenite (Fig 7-7E). The Cr content displays a strong positive trend with MgO in feldspathic pyroxenites with concentrations ranging from 1184 –59538 ppm (Fig 7-7F). Co shows a negative correlation with MgO in feldspathic pyroxenites with concentrations varying between 106 –242 ppm (Fig 7-7G). Ni shows a negative correlation with MgO in feldspathic pyroxenite samples (Fig 7-7H), Ni contents range between 484 – 3852 ppm. The feldspathic pyroxenite samples show a strong negative correlation between Cu and MgO with Cu concentrations ranging between 108 – 1860 ppm (Fig 7-7I). Essentially, the high Ni and Cu contents in feldspathic pyroxenite are attributed to a high sulphide content.

A negative correlation is observed between Zn and MgO in feldspathic pyroxenite (Fig 7-7J), with values ranging from 41 – 152 ppm (with an outlier of 539 ppm in a sample adjacent to footwall contact). The parapyroxenite sample contains elevated amounts of Zn (2731 ppm), this is an indication that Zn increases with increasing depth towards the footwall rocks. Y also shows a negative correlation with MgO in feldspathic pyroxenite (Fig 7-7K) with concentrations of up to 10 ppm. Zr concentrations display a strong negative correlation with MgO (11 – 44 ppm) in feldspathic pyroxenite (Fig 7-7L).


A
Rb (ppm)
MgO (wt.%)
B
Sr (ppm)
MgO (wt.%)
C
Ba (ppm)
MgO (wt.%)
D
Sc (ppm)
MgO (wt.%)
E
V (ppm)
MgO (wt.%)
F
Cr (ppm)
MgO (wt.%)
G
Co (ppm)
MgO (wt.%)
H
Ni (ppm)
MgO (wt.%)

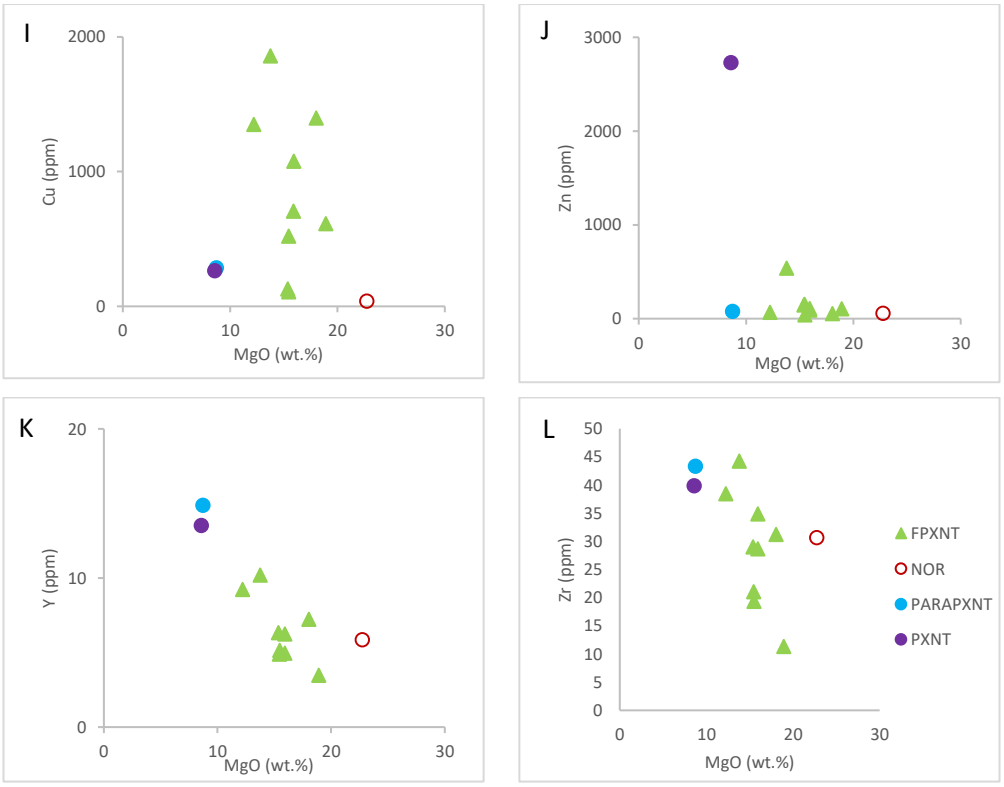
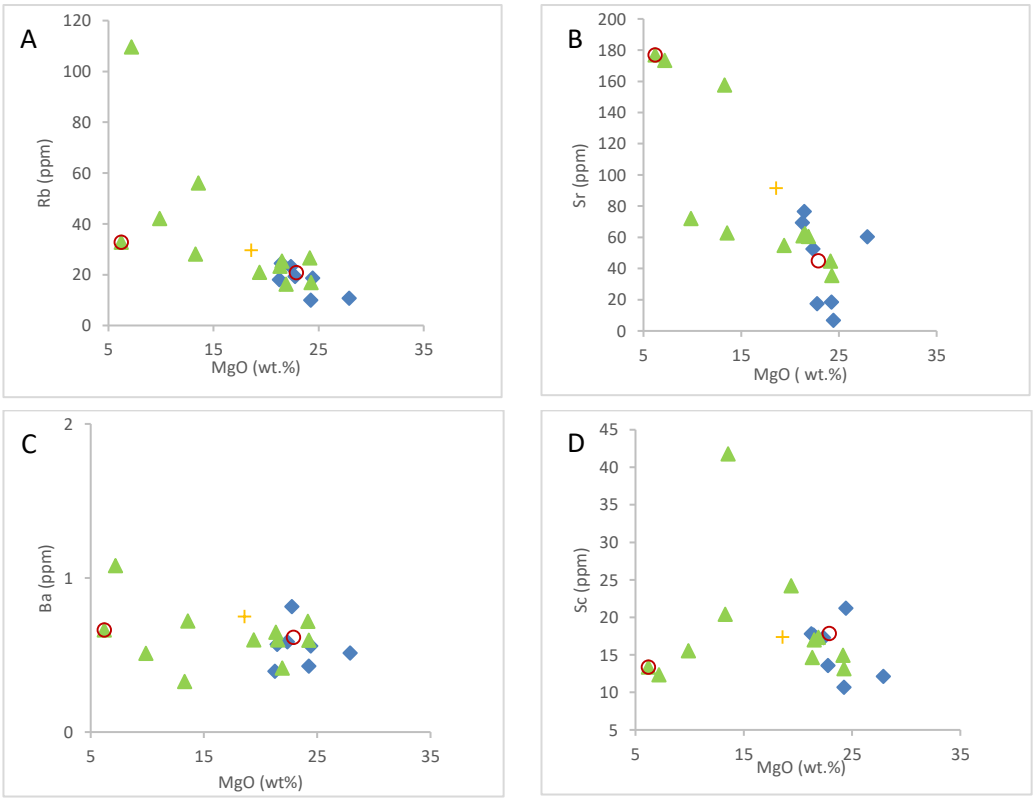


Figure 7-7: Binary variation diagrams showing selected trace elements (Rb, Sr, Ba, Sc, V, Cr, Co, Ni, Cu, Zn, Y, Zr & Ga) concentrations (ppm) versus MgO content (wt.%) in borehole Z19 lithologies.

Most of the trace elements in borehole Z20 samples display negative correlations with MgO content (Fig 7-8). The Rb displays a moderately strong negative correlation with MgO in both feldspathic pyroxenite and feldspathic harzburgite samples (Fig 7-8A), with their Rb values ranging between 17 – 110 ppm and 10 – 24 ppm respectively. Sr concentrations also decrease with increasing MgO contents within the feldspathic pyroxenite and feldspathic harzburgite samples (Fig 7-8B), the Sr values vary from 36 – 178 ppm and 19 – 77 ppm. The concentration of Ba is generally <1 ppm in both feldspathic pyroxenite and feldspathic harzburgite samples, both displaying negative correlations with MgO (Fig 7-8C). Vanadium content shows a negative trend with MgO, with values varying from 58 – 304 ppm in feldspathic pyroxenite and 68 – 268 ppm in feldspathic harzburgite samples (Fig 7-8E). The Cr concentration shows a moderately strong positive correlation with MgO in both feldspathic pyroxenite and feldspathic harzburgite samples, Cr contents range between 590.33 – 10375 ppm and 3032 – 26007 ppm respectively (Fig 7-8F). In feldspathic harzburgites, Co (81 – 194 ppm) shows a positive correlation, however a negative correlation between Co and MgO is observed in feldspathic pyroxenites (61 – 597 ppm) (Fig 7-8G). A negative correlation between Ni (318 – 4301.2 ppm) and MgO is observed in feldspathic pyroxenite samples while a positive Ni (610 – 3566 ppm) correlation is observed in feldspathic harzburgite samples (Fig 7-8H). Positive Cu correlations with MgO are observed in both feldspathic pyroxenite and feldspathic harzburgite samples, with Cu values ranging

between 74 – 1685 ppm and 266 – 6612 ppm respectively (Fig 7-8I). Other trace elements such as Sc, Y, Zr, Zn, and Ga also display weak to strong negative correlations with the MgO content within feldspathic pyroxenite and feldspathic harzburgite lithologies in borehole Z20.

In both boreholes, higher Cr concentrations are associated with feldspathic harzburgite units. The Cr/MgO ratios have been used to distinguish between the Critical Zone and the Main Zone in the eastern and western limbs, the Critical Zone has Cr/MgO values ranging between 80 – 120 while the Main Zone has lower Cr/MgO values ranging between 40 – 60 (Seabrook, 2005). Cr/MgO ratios for the studied rocks are presented in Appendix C, Tables 13 and 14. Samples from borehole Z19 have Cr/MgO >100, except for the pyroxenite (Cr/MgO = 41) sampled adjacent to the footwall contact (Fig 7-9A). In borehole Z20 (Fig 7-9B), the feldspathic harzburgites, gabbro as well as majority of the feldspathic pyroxenites have Cr/MgO >80, only one out of three norite samples also recorded Cr/MgO >80. Although some of the samples have Cr/MgO <80, the majority of the mafic and ultramafic lithologies at the southwestern portion of the Uitloop farm appear to be of the Critical Zone affinity (Fig 7-9).



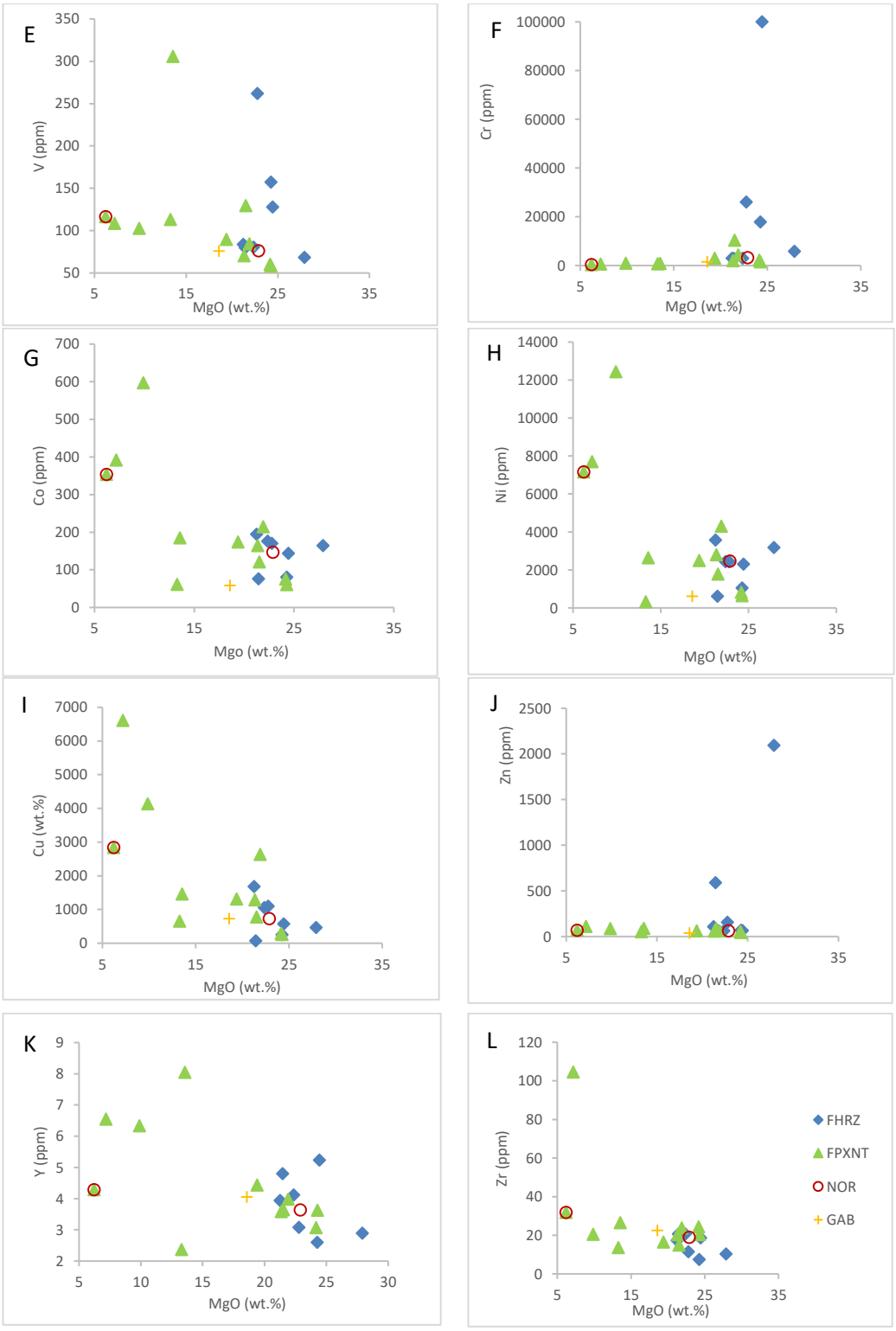


Figure 7-8: Binary variation diagrams showing selected trace elements (Rb, Sr, Ba, Sc, V, Cr, Co, Ni, Cu, Zn, Y & Zr) concentrations (ppm) versus MgO content (wt.%) in borehole Z20 lithologies.

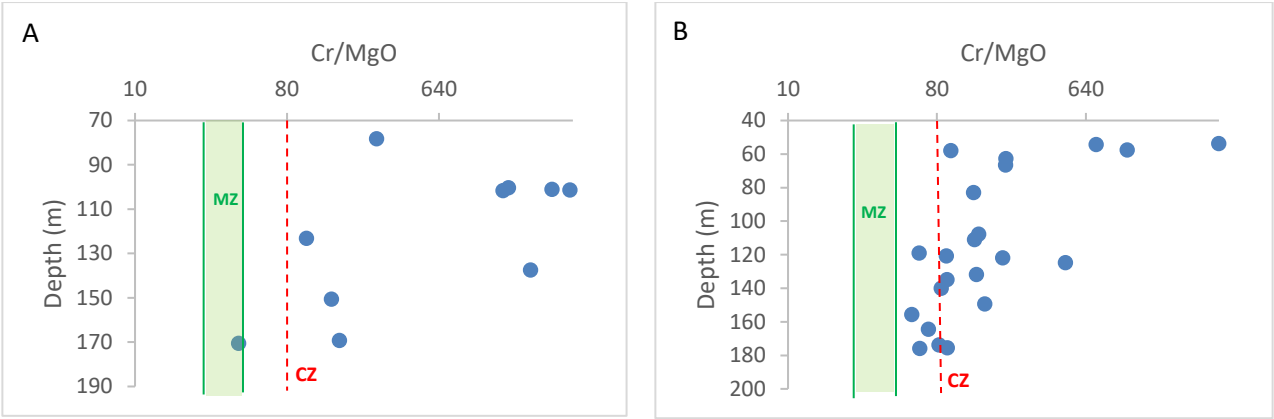


Figure 7-9: Cr/MgO vs depth for boreholes Z19 (A) and Z20 (B) showing that majority of the mafic/ultramafic rocks from the southwestern part of the Uitloop farm have Cr/MgO >80 and thus are of Critical Zone affinity. (MZ = Main Zone, CZ = Critical Zone).

7.4 DISTRIBUTION OF RARE EARTH ELEMENTS

According to Hofmann (1988), rare Earth Elements (REE) are commonly displayed as normalised data. Here REE data are expressed as the analysed concentrations in the rock divided by its average concentration in so-called primitive mantle, a hypothetic geochemical reservoir that is suggested to be a source of high-Mg melts. It is known that REE with odd atomic numbers are less abundant than their even numbered neighbours, so normalization helps to avoid the saw-tooth distribution of the REE and to demonstrate their similarity or dissimilarity to the model reservoir.

The REE in boreholes Z19 and Z20 display flatter patterns of the heavy REE and steeper slope of light REE (Fig 7-10 & 7-11). In Z19 (Fig 7-10), the majority of the feldspathic pyroxenites do not show an Eu anomaly while some display a negative Eu anomaly, the same morphology of the REE patterns of feldspathic pyroxenites indicates their common source. A pronounced negative Eu anomaly is observed in the pyroxenite and parapyroxenite samples. In Z20 (Fig 7-11), there are variable distributions with some feldspathic harzburgite samples displaying negative Eu anomalies while some of the feldspathic pyroxenite samples have positive Eu anomalies. It is known that plagioclase accommodates preferably divalent Eu compared to the remaining REE. So melts that experienced plagioclase crystallisation and removal will show negative Eu and Sr anomalies whereas high Sr and positive Eu anomaly in feldspathic harzburgite reflect a presence of intercumulus plagioclase.

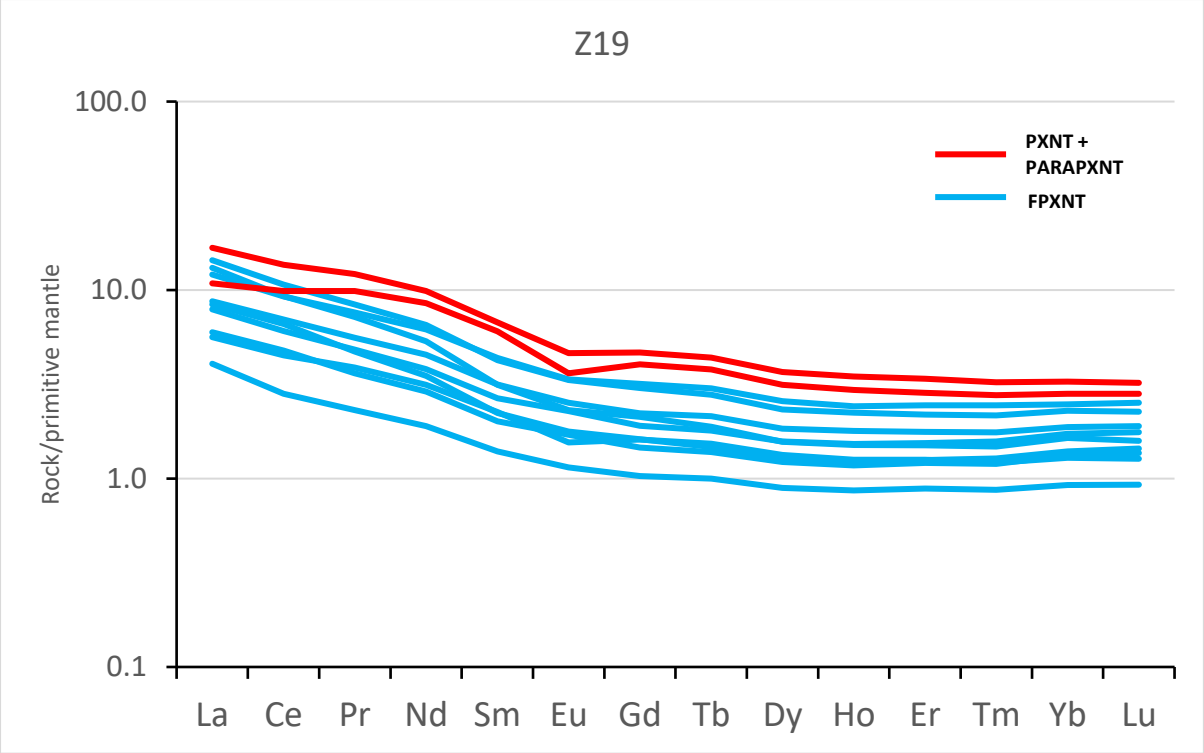


Figure 7-10: Primitive mantle normalized REE graphs (normalised to data by Hoffman (1988)) of the feldspathic pyroxenite (FPXNT) and pyroxenite (PXNT) + parapyroxenites (PARAPXNT) from borehole Z19 of the southwestern portion of Uitloop farm.

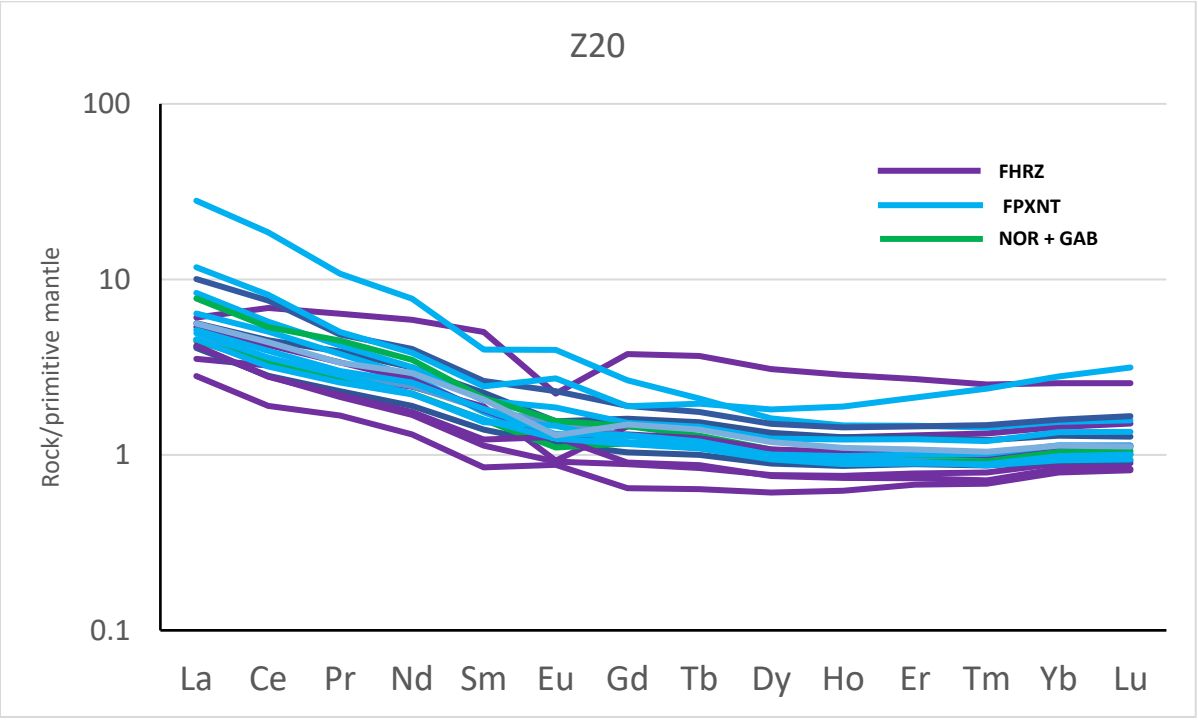


Figure 7-11: Primitive mantle normalized REE graphs (normalised to data by Hoffman (1988)) of the feldspathic pyroxenite (FPXNT) and feldspathic harzburgite (FHRZ) and Norite (NOR) + gabbro (GAB) from borehole Z20 of the southwestern portion of Uitloop farm.

7.5 DISCUSSION

It can be deduced that the whole-rock geochemistry of lithologies within boreholes Z19 and Z20 from the southwestern portion of the Uitloop farm is highly variable; however similar trends can be observed within the two boreholes. The major element concentrations within feldspathic harzburgite, feldspathic pyroxenite, pyroxenite, gabbro, norite and parapyroxenite samples also vary. The major element oxides, MgO, Fe_2O_3, TiO_2 and MnO are components of Mg-bearing silicates (pyroxenes, olivine and chromite), while Al_2O_3, CaO, Na_2O and K_2O are feldspathic components. The chalcophile element distribution is largely controlled by sulphides, although significant Ni can be accommodated by high-Mg olivine and chromite.

7.5.1 MAJOR ELEMENT CHEMISTRY

7.5.1.1 COMPARISON OF GEOLOGICAL LOGS WITH ROCK CHEMISTRY

All the major element oxides, except MgO, decrease with increasing depth in both in boreholes Z19 and Z20 (Figures 7.5 & 7.6). The highest MgO concentrations coincide with the ultramafic lithologies, particularly the feldspathic harzburgite and feldspathic pyroxenite units higher up in the stratigraphy. The major peaks in Na_2O and K_2O concentrations in borehole Z19 coincide with feldspathic pyroxenite units at 101.6 m and 169.2 m while in Z20 major peaks are observed within gabbro and feldspathic pyroxenite units at 140.1 m and 173 m, these peaks are an indication of an increase in feldspar within the mafic and ultramafic rocks. The highest CaO concentrations in boreholes Z19 are observed in parapyroxenite at 174.9 m as well as in borehole Z20 in a noritic unit at 153.5 m. These CaO peaks are associated with increases in metamorphic clinopyroxene in parapyroxenite and plagioclase in norite. Elevated Al_2O_3 contents are observed in chromite-bearing feldspathic pyroxenite and parapyroxenite units in borehole Z19 at 101.4 m and 174.9 m respectively. The high Al_2O_3 in the feldspathic pyroxenite could be attributed to either the chromite crystals or an increase in feldspar minerals, while Al_2O_3 concentrations in parapyroxenite could be a result of the high proportion of Al-bearing clinopyroxene, plagioclase and phyllosilicates (biotite and phlogopite). Silica increases with increasing magma differentiation and, as expected, higher concentrations are associated with the more mafic (noritic or gabbronoritic) units.

Therefore, the position of the high-Mg rocks at the top of both magmatic sequences in Z19 and Z20 is not consistent with the formation of the Uitloop complex intrusion from a single differentiating batch of melt. The lower parts of the sequences are composed of heterogenous packages dominated by feldspathic pyroxenite with a significant proportion of noritic lithologies. The irregular distribution of

major oxides reflects the irregular intercalation of rock types that is better explained by a model of multiple emplacement of magma influxes or sills with slightly different compositions that were fed from a differentiating source at depth.

The position of the high-Mg and high-Cr feldspathic harzburgite and pyroxenite at the top of the sequence resembles the Platreef stratigraphy on Turfspruit as it is described by Yudovskaya et al. (2017) and Grobler et al. (2018). Harzburgitic and pyroxenitic layers with chromite seams and disturbed lenses are located at the top of the Platreef on Turfspruit and they rest upon an essentially noritic Footwall Unit (Grobler et al., 2018) that is similar to the noritic-gabbronoritic package underlying the ultramafic package. The occurrence of ultramafic rocks at the top of the sequence is interpreted as a result of a later influx of ultramafic magmas that was introduced above the semi-consolidated pyroxene-plagioclase cumulates in a resident chamber.

7.5.1.2 MAGMA DIFFERENTIATION

The binary diagrams show that the major element variations in the ultramafic rocks of the Uitloop farm are consistent with the major mineral constituents and the order in which they crystallise. The MgO concentration is used to monitor differentiation in mafic/ultramafic rocks in layered intrusions such as the Bushveld Complex. According to the Bowen's reaction series the first high temperature minerals to crystallise from the Bushveld-type high-Mg parental magma are Mg-rich olivine and orthopyroxene with additional chromite (Eales and Cawthorn, 1996). Therefore, the MgO content will decrease with increasing SiO_2 with higher degrees of magma fractionation as rocks such as peridotites and pyroxenes form. Conversely, concentrations of Na_2O and K_2O increase with increasing SiO_2 that results in crystallisation of progressively Na-richer plagioclase and micas from evolved residual melts.

In the southwestern portion of the Uitloop farm, the lower MgO content and associated elevated Na_2O content correspond to more plagioclase-rich lithologies that crystallised from differentiated melts. However, the position of these lithologies in the lower parts of the sequence and irregular character of their intercalation testifies that the differentiation is likely to have happened in a staging chamber. The graphite-bearing pyroxenite at the basal part of the sequences shows an increase in Al_2O_3, CaO and Fe_2O_3 contents that indicates magma contamination. However, the hybrid rocks were not among the subjects of this study because their stratigraphic correlation is hampered by the great variability of footwall contaminants in the northern limb (Kinnaird et al., 2005).

7.5.2 TRACE ELEMENT CHEMISTRY

Trace elements give important information about the composition of the magma differentiation as well as contamination. Trace elements partition into the major minerals as isomorphous substitutions and admixtures. Trace elements can be either compatible (Sc, V, Cr, Co & Ni) or incompatible (Rb, Sr, Zr, Cs, Ba & REE) with their melts. Incompatible trace elements preferably partition into residual melt during fractional crystallization and the last crystallise. Concentrations of the compatible trace elements in melts decrease with the increasing fractionation while concentrations of the incompatible trace elements increase with increasing fractionation. Therefore, cumulate rocks are relatively enriched in compatible elements with respect to incompatible trace elements that enrich residual melts.

This general increase in trace element concentration towards the footwall contact is a result of more evolved rock composition at the base but this can be partly also attributed to the assimilation of country rocks by Bushveld magmas, in the case of Uitloop - assimilation of the Duitschland dolomite, magnetite-bearing, carbonaceous and argillaceous shales.

The lithologies in borehole Z20 show a negative correlation between Ni and Cu with MgO as well as a positive correlation between Cr and MgO. However, in borehole Z19; trace elements Ni, Cu and Cr behave differently in different rock types. In feldspathic pyroxenite units, Cu and Ni show negative correlations with MgO as well as a positive correlation between Cr and MgO. The opposite is observed in feldspathic harzburgite units, where Cu and Ni display positive correlations with MgO while Cr displays a negative correlation with MgO. The latter trend is related to a high concentration of Cr in feldspathic harzburgite so Cr_2O_3 will reduce the amounts of all other major oxides, including MgO, within their 100% total. In both boreholes, higher Cr concentrations are associated with feldspathic harzburgite units at the top. The Cr/MgO ratios are used to distinguish between the Critical Zone (Cr/MgO >100) and the Main Zone (Cr/MgO <60), resulting in the majority of the mafic/ultramafic samples from the southwestern part of the Uitloop farm recording Cr/MgO >100 suggesting Critical Zone affinity.

In both boreholes, Ni and Cu concentrations have similar ranges in feldspathic harzburgite and feldspathic pyroxenite lithologies, this suggests a similar amount of sulphide interstitial to olivine and orthopyroxene cumulates. A positive correlation exists between Ni and MgO in Z19 feldspathic harzburgite as Ni was probably scavenged by olivine during the early stages of ultramafic magma differentiation. Where SiO_2 is sufficiently elevated to cause orthopyroxene crystallization rather than olivine crystallization, more Ni should enrich residual melts including immiscible sulphide. Cu is highly incompatible and did not partition notably into silicates, as a result Cu concentration is a more useful

indicator of sulphide mineralisation than Ni as ultramafic rocks contain silica-hosted Ni. The degree of fractionation is however not related to sulphide mineralisation.

The highest concentrations of chalcophile metals (Ni, Cu and Co) occur at the base of the magmatic sequence and in the contact-metamorphosed footwall lithologies. These intervals represent so-called contact-style mineralisation that is typical for the Platreef base along its strike and is related to sulphur assimilation from the footwall (Maier at al., 2008). However, the sulphur data from Sharman et al. (2013) show that the contribution of sulphur from the footwall was relatively minor, The minor peaks of elevated Cu and Ni in ultramafic rocks at the top of the intrusive succession, are associated with some elevated PGE according to the company data (Fig 4-19 & 4-20) forming low-sulphide mineralisation, provisionally of reef-style.

Figure 7-12 displays a comparison of the REE averages for the LZ and Platreef (data supplied by Dr M. Yudovskaya) with those from the southwestern part of the Uitloop farm. Like the Platreef and Lower Zone lithologies, the studied feldspathic pyroxenites and feldspathic harzburgites display a steeper slope for light REE and a flatter slope for the heavy REE (Fig 7-12). The Z19 feldspathic pyroxenites have a similar REE pattern as the LZ orthopyroxenites from Turfspruit with a slight negative Eu anomaly, while the Z20 feldspathic pyroxenites display a similar pattern as the LZ at Sandsloot. Also, the Z20 feldspathic harzburgite show a similar REE pattern, with a negative Eu anomaly, as the LZ harzburgite at Turfspruit. However, the REE abundances are notably higher than those typical for the LZ rocks and 1-order higher than that of the Platreef. The morphology of the REE patterns is the same for both rock types at Uitloop, which indicate absence of notable contamination and derivation from the same melts that have undergone fractionation resulting in modest enrichment in incompatible elements such as REE.

The REE distribution testifies to the similar melt composition and negligible local contamination for the harzburgitic and pyroxenitic rocks. The level of REE content and patterns of their fractionation are more consistent with the Platreef/Critical Zone melt composition than with that of the LZ primitive magmas.

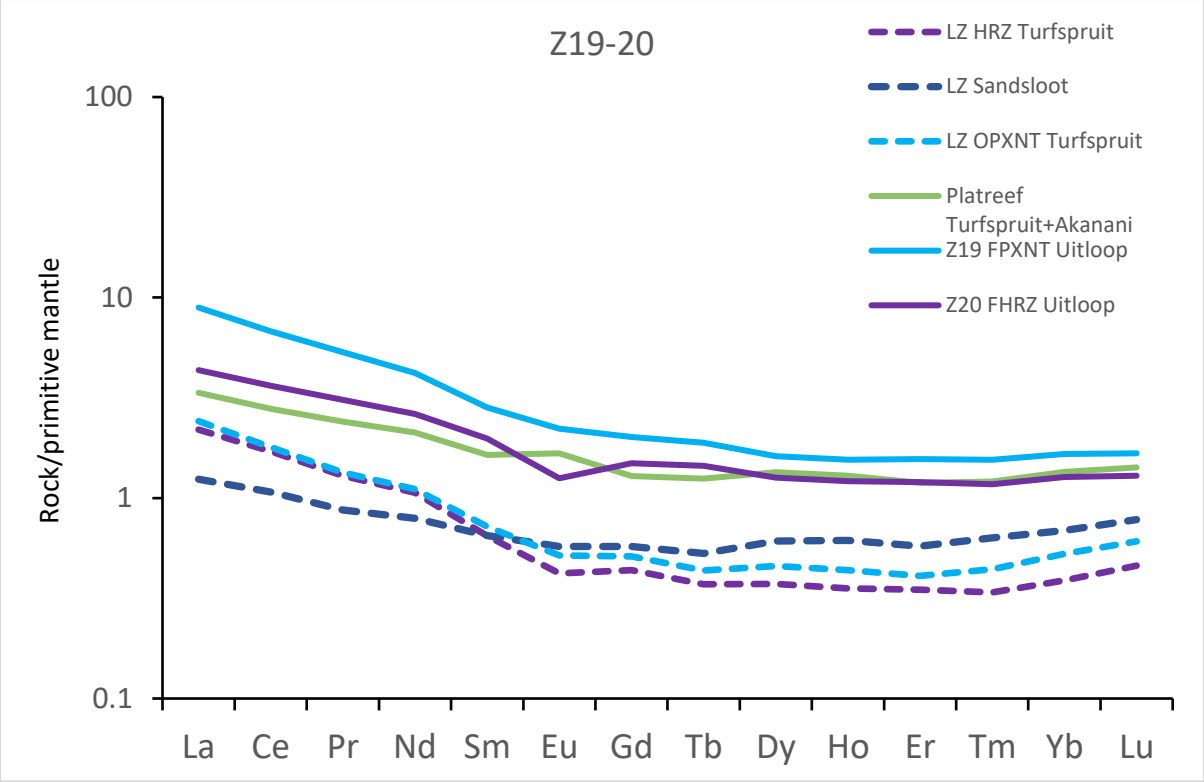


Figure 7-12: Primitive mantle normalized REE graphs (normalised to data by Hoffman (1988)) of the ultramafic rocks from the southwestern part of the Uitloop farm compared to the Lower Zone data from Turfspruit and Sandsloot and Platreef data from Turfspruit and Akanani (data supplied by Dr M. Yudovskaya).

CHAPTER 8

MINERAL CHEMISTRY OF CHROMITE AND OLIVINE IN MAGMATIC LITHOLOGIES ON THE SOUTHWESTERN PART OF THE UITLOOP FARM

8.1 INTRODUCTION

The magmatic chromite in the Bushveld Complex is associated with mafic/ultramafic igneous rocks, particularly peridotites and pyroxenites. Chromite crystals are widely used in exploration geology as an indicator mineral for Ni-Cu-PGE-Cr deposits because it is one of the earliest phases to crystallize from primitive magma and also chromites are refractory and resistant to alteration in comparison to other high temperature phases (Barnes & Roeder, 2001). The composition of chromites reflects magmatic conditions such as the temperature, pressure and composition of the initial partial melt. The cores of the chromite crystals may retain their original magmatic chemistry at metamorphic temperatures of up to 500 °C (or higher), the chemistry of the chromites can be used to deduce magma types, magmatic processes and tectonic settings in metamorphosed mafic/ultramafic intrusions such as the Bushveld Complex.

Chromite belongs to the spinel group of minerals which have a general formula; $\mathbf{AB_2O_4}$, where **A** represents the divalent cation space filled by $Fe^{2+}$and Mg^{2+} (occasionally; Ni, Mn, Co, Zn) while **B** represents trivalent cation space filled by Cr^{3+}, Fe^{3+} and Al^{3+}. This group of minerals can be subdivided into three series based on the most abundant trivalent cations; spinel (Al^{3+}), chromite (Cr^{3+}) and magnetite (Fe^{3+}) (Table 1) (Deer et al., 1992).

Table 8-1: Spinel group minerals (Deer et al., 1992).

	Spinel series (Al^{3+})	Chromite series (Cr^{3+})	Magnetite series (Fe^{3+})
Mg^{2+}	Spinel	Magnesiochromite	Magnesioferrite
Fe^{2+}	Hercynite	Chromite	Magnetite
Zn	Gahnite		Franklinite
Mn	Galaxite		Jacobsite
Ni			Trevorite

The spinel group minerals, particularly chromite, are also good petrogenetic indicators because of their extensive solid solution series spanning a wide range of conditions (Roeder and Campbell, 1985). For example, in the chromite crystal lattice; magnesium (Mg^{2+}) frequently substitutes for iron (Fe^{2+}) in the divalent cation site. Thus, a solid solution exists between chromite ($Fe^{2+}(Cr^{3+})_2O_3$) and magnesiochromite ($Mg^{2+}(Cr^{3+})_2O_3$), resulting in intermediate varieties with either iron-rich ((Fe, Mg) Cr_2O_4) or magnesium-rich ((Mg, Fe) Cr_2O_4) compositions. There are also other solid solution paths between chromite and minerals of the spinel series (e.g. hercynite ($FeAl_2O_4$), spinel ($MgAl_2O_4$)) and the magnetite series (e.g. magnesioferrite ($MgFe_2O_4$), magnetite (Fe_3O_4)). Numerous mineral compositions exist in these solid solution paths, as a result any end member with high Cr_2O_3 content is referred to as chromite. Chromite has a chemical formula of **$((Fe, Mg)(Cr, Fe, Al)_2O_4)$**.

The major constituent in chromite; chromium (Cr^{3+}), is derived from the mantle by partial melting of a source rock. In the magma chamber, Cr^{3+} together with other principal elements; Mg^{2+}, Fe^{2+} and Al^{3+}, then combine and crystallize to form chromite. During partial melting and crystallization, the trivalent cations (Cr^{3+}, Al^{3+}) diffuse at a slower rate than the divalent cations (Mg^{2+}, Fe^{2+}), therefore; the amount of chromite that can crystallize from the partial melt is small.

The chromium number (Cr# = (Cr/(Cr + Al)) is an atomic ratio representative of the Cr-Al substitution in the trivalent site, this variable increases during partial melting and therefore is used as an indicator for partial melting (Barnes and Roeder, 2001). The magnesium number (Mg# = (Mg/(Mg + Fe^{2+})) is an atomic ratio representative of Mg – Fe^{2+} substitutions in the divalent site. Fluctuations in Cr# and Mg# values may indicate changes in magma composition that result from e.g. repeated magma injections and/or processes during fractional crystallization. The Mg# and Cr# generally decrease upwards stratigraphically in most chromitite layers due to a decrease in Mg^{2+} and Cr^{3+} in the residual melt, as a result Mg# is usually an indicator for the degree of crystal fractionation (Irvine, 1977; Hulbert & von Gruenewaldt, 1985).

According to Naldrett et al. (2009) and Yudovskaya and Kinnaird (2010), the compositional variations of chromite crystals can also be attributed to post-magmatic processes such as; a) re-equilibration due to interaction of chromite crystals with intercumulus silicate melt and the surrounding silicate minerals, resulting in ion exchange (e.g. Fe^{2+} and Mg^{2+}), b) Fe-exchange between chromite crystals and sulphides, c) alteration by hydrothermal fluids and contact metamorphism. These processes collectively lead to decreasing magnesium (Mg^{2+}) and aluminium (Al^{3+}) as well as elevated ferrous (Fe^{2+}) and ferric (Fe^{3+}) iron contents in the chromite crystals .

8.2 CHROMITE DISTRIBUTION

In the southwestern part of the Uitloop farm, chromite occurs in feldspathic pyroxenite and feldspathic harzburgite as dense disseminations at different stratigraphic levels in borehole Z19; at 100.3 m to 101.8 m and at 137.7 m to 137.85 m below surface (Fig 4-19, Fig 8-1). In borehole Z20, there is a 10 mm thick chromite stringer and sparse chromite disseminations in feldspathic harzburgite at 54.25 m and 57.5 m below surface respectively (Fig 4-20, Fig 8-2).



Figure 8-1: A photograph of borehole core sample showing chromite disseminations in feldspathic pyroxenite, sample Z19-137.7.

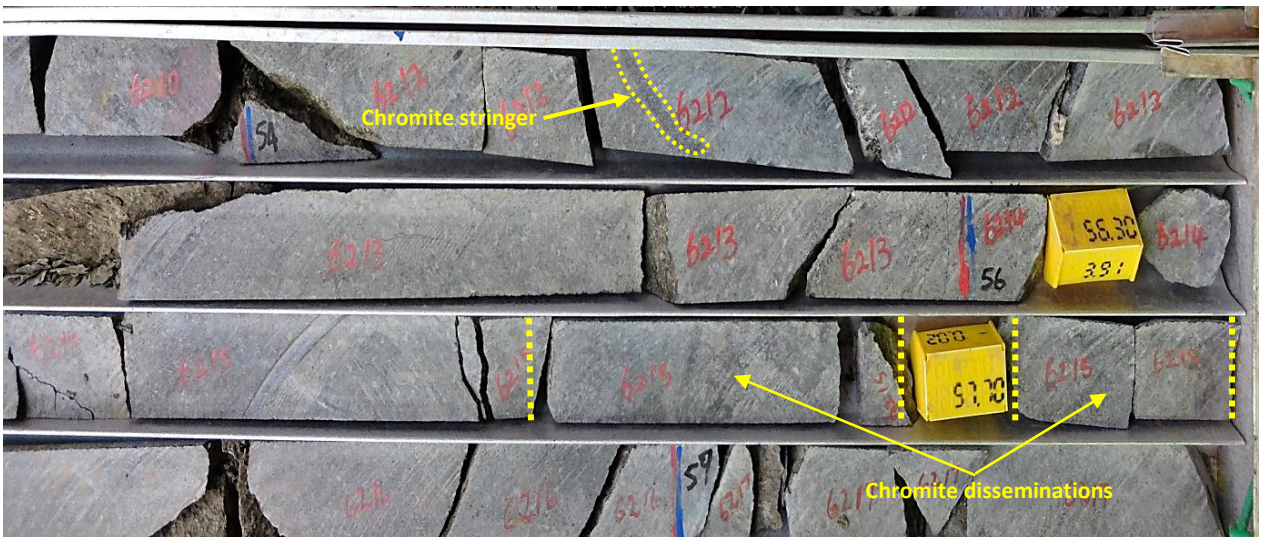
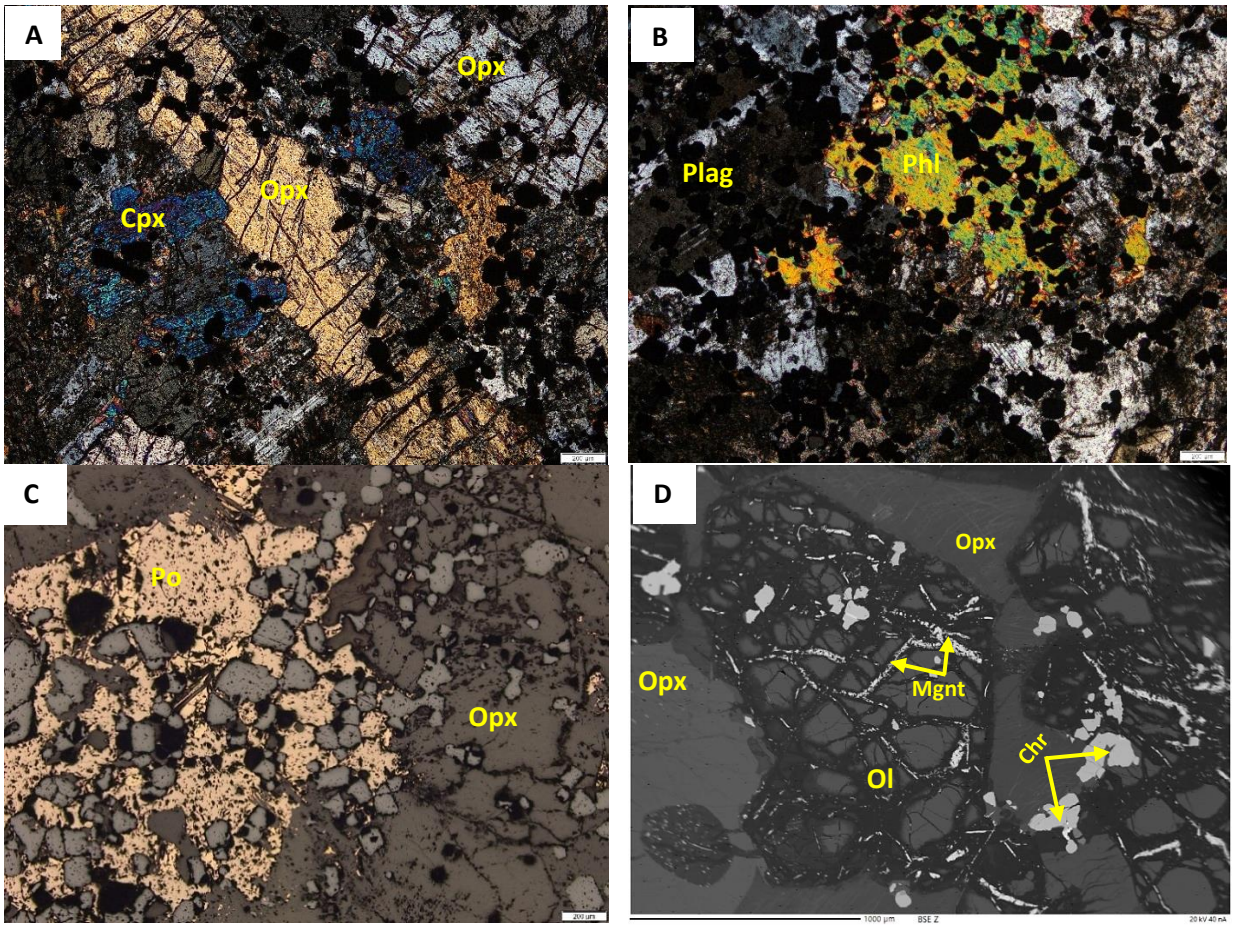


Figure 8-2: A photograph of borehole core sample showing a chromite stringer and chromite disseminations in feldspathic harzburgite at depths of 54.25 m and 57.5 m respectively in borehole Z20.

Six chromite-bearing samples were investigated in polished thin sections; four FROM feldspathic pyroxenite (Z19-100.35, Z19-101.4, Z19-101.6 & Z19-135.7) and two FROM feldspathic harzburgite (Z20-66.5 & Z20-111) samples. The feldspathic pyroxenites consist of predominantly cumulus orthopyroxene, intercumulus plagioclase and occasionally clinopyroxene crystals as well as minor accessory phases such as phlogopite, quartz and base metal sulphides. The feldspathic harzburgite samples consist of cumulus olivine and orthopyroxene with intercumulus plagioclase and accessory minerals.

The chromite content in these samples ranges from 5 to 20 vol. %. In thin section, chromite is observed as a cumulus phase enclosed by silicate constituents and base metal sulphides (Fig 8-3) but it also shows textural features of prolonged postcumulus growth (Figs 8-3A-D). In sample Z19-100.35, a rare occurrence of chromite in close association with zircon and a uranium-rich mineral is observed (Fig 8-3F). The compositions of chromite crystals hosted by the different lithologies were determined using electron microprobe analysis (EPMA)at the University of Johannesburg as described under the methodology section in Appendix A.



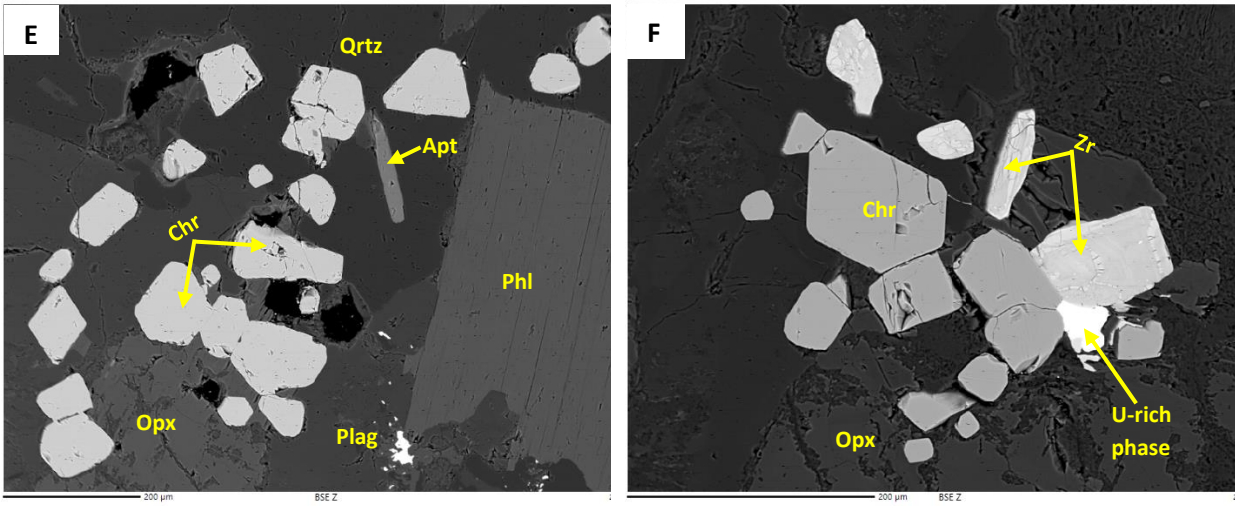


Figure 8-3: Photomicrographs of cumulus chromite in feldspathic pyroxenite (A-C & E) and feldspathic harzburgite (D). (A) Z20-101, under XPL; chromite in orthopyroxene and clinopyroxene, (B) Z20-101, under XPL in transmitted light; chromite in phlogopite and altered plagioclase, (C) Z20-137.5, in reflected light; chromite in Base Metal Sulphides (pyrrhotite), (D) Z20-66.5-4_39, BSE; chromite in olivine with characteristic fractures filled by magnetite and serpentine. (E) Z19-100.35-1_17, BSE; euhedral and rounded chromite and apatite crystals hosted by a quartz-phlogopite-plagioclase interstitial assemblage, (F) Z19-100.35-2, BSE; euhedral chromite hosted by orthopyroxene and plagioclase in close association with zircon and a uranium-rich mineral phase. (Chr= chromite, Opx= orthopyroxene, Ol = olivine, Cpx = clinopyroxene, Plag = plagioclase, Apt = apatite, Qrtz = quartz, Ph = phlogopite, Po = pyrrhotite, Mgnt = magnetite, U-rich = uranium-rich).

8.3 CHROMITE MORPHOLOGY

The chromite crystals vary in size from coarse- to fine-grained and commonly occur as either inclusions or interstitial to the silicates in the ultramafic rocks. The morphology of the cumulus chromite crystals is mainly euhedral, subhedral and rounded. Fishhook morphologies are observed in some of the anhedral interstitial chromite crystals (Fig 8-5A). Most of the interstitial chromites appear to have been replaced (corroded) by phlogopite, resulting in relics with irregular crystal boundaries (Figs 8-5B-F).

The euhedral and rounded chromite crystals are the most abundant and tend to have annealled when they are in contact with one another to form larger crystals during cooling processes (Fig 8-4E), this leads to changes in size and shape of the chromite crystals. Euhedral and rounded chromite crystals generally lack inclusions (Figs 8-4F), however euhedral chromite in feldspathic pyroxenite sometimes hosts rutile inclusions that are likely the products of solid state exsolution (Fig 8-4B). The anhedral, interstitial and corroded chromite crystals usually contain sulphide (Fig 8-5A) and silicate inclusions (Fig 8-5), the majority of these chromite crystals have altered to magnetite and a fine-grained Fe-rich phase along their boundaries, especially where chromite is in contact with phlogopite (Figs 8-5C & D). Besides chromite,

there is also the presence of Cr-bearing spinel (Cr-bearing magnetite) observed in feldspathic harzburgite (Fig 8-4C).

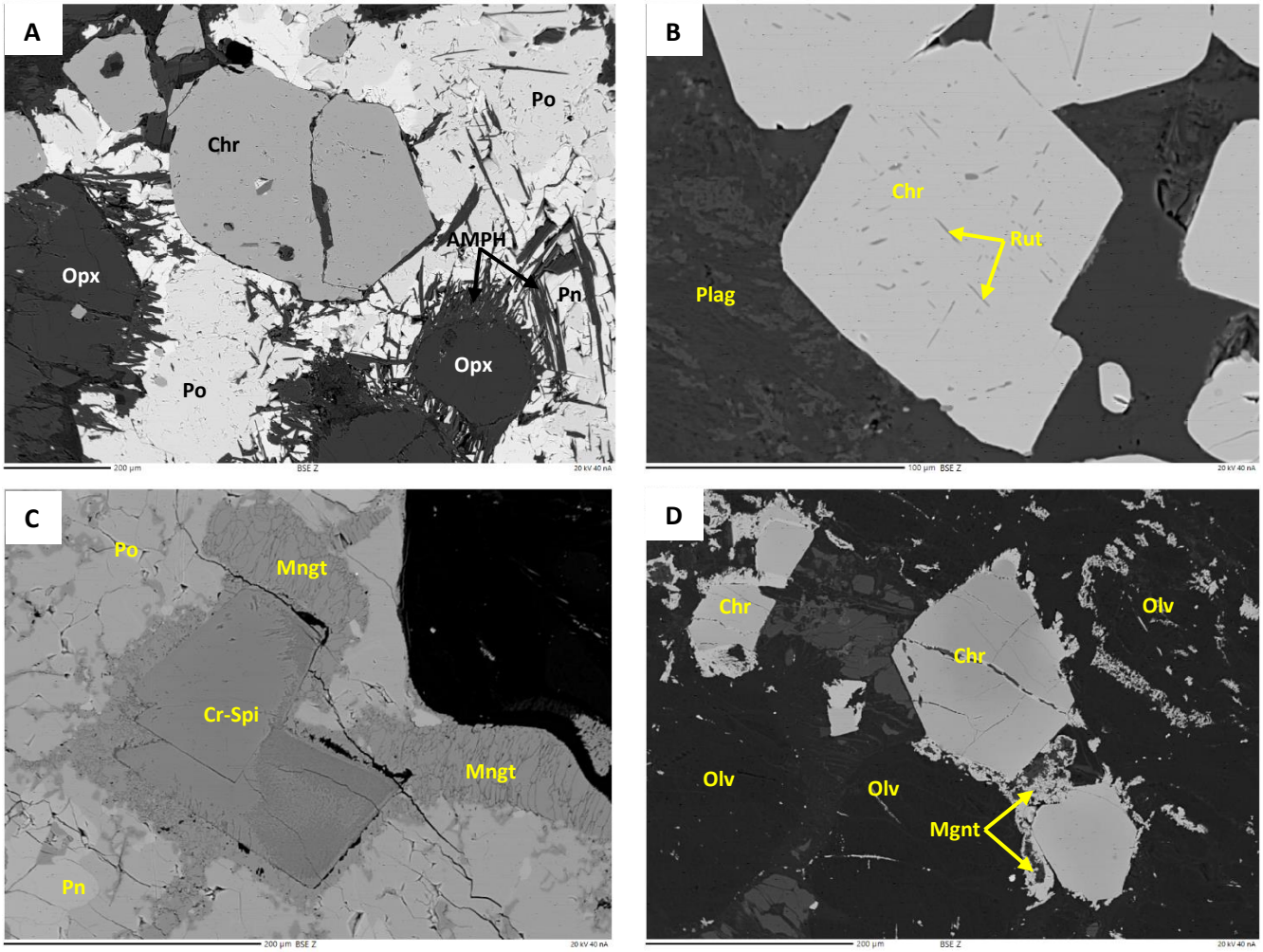


Figure 8-4: The morphology of chromite crystals from the southwestern part of the Uitloop farm. (A) Z20-100.35-3_9, subrounded chromite crystals enclosed by sulphides with needle-like amphibole intergrowths. (B) Z19-101.4_29, cumulus euhedral chromite with rutile exsolutions in plagioclase. (C) Z20-66.5_23, BSE; Cr-Spinel with secondary magnetite along crystals boundaries enclosed by sulphide minerals. (D) Z20-66.5_26, BSE; chromite crystals rimmed by magnetite hosted by olivine. (Chr= chromite, Opx= orthopyroxene, Amph = Amphibole, Plag = plagioclase, Phl = phlogopite, Po = pyrrhotite, Pn = pentlandite, Mgnt = magnetite, Cr-Spi = Chromium-spinel, Rut = rutile).

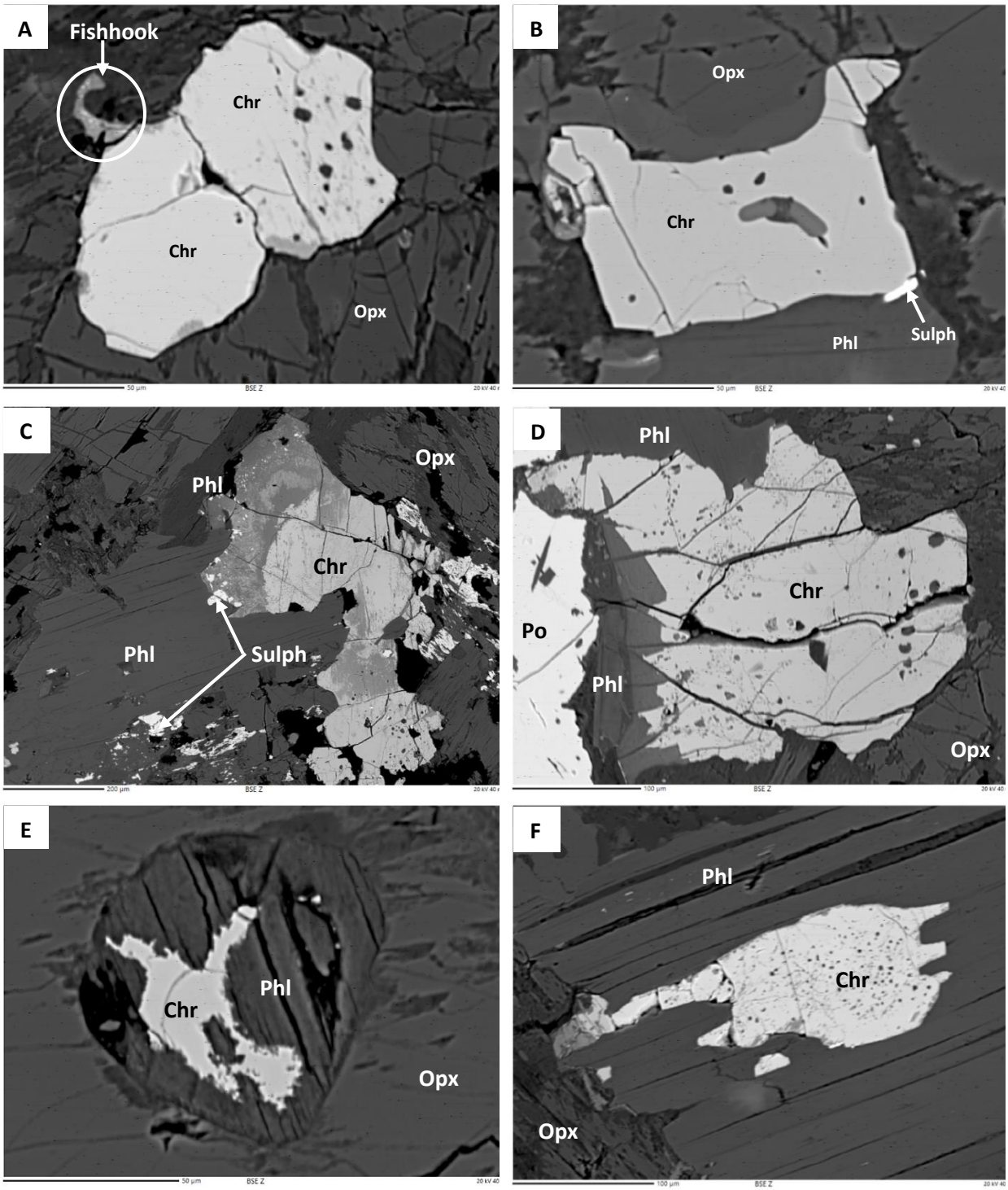


Figure 8-5: The morphology of the chromite crystals from the southwestern part of the Uitloop farm. (A) Z20-111-1_46, BSE; coarse interstitial anhedral chromite crystals with fish-hook, magnetite along crystals boundaries and silicate inclusions. B) Z20-111-1_47, BSE; fish-hook chromite set between orthopyroxene and corroded by phlogopite, this chromite crystal also has silica inclusions. (C) Z20-111-2_48, BSE; amoeboidal chromite corroded by phlogopite, with sulphides and secondary magnetite (a fine-grained spinel phase) along crystals boundaries. (D) Z20-111-2_49, BSE; corroded sieve-textured chromite replaced by phlogopite and magnetite, (E) Z20-111-2_50, BSE; chromite relic within secondary phlogopite. (F) Z20-111-1_45, BSE; sieve textured chromite relic within secondary phlogopite. (Chr= chromite, Opx= orthopyroxene, Plag = plagioclase, Sulph = sulphide, Phl = phlogopite).

8.4 CHROMITE CHEMISTRY

8.4.1 CHROMITE COMPOSITIONS IN DIFFERENT LITHOLOGIES

The mineral chemistry of analyzed chromite is presented in Appendix D. Binary variation diagrams of selected major element concentrations are presented in this segment to illustrate the composition of chromites from the studied lithologies.

Table 8-2: Summary of selected major element concentrations in chromite crystals from the southwestern part of the Uitloop farm lithologies.

Sample#	Rock type	Major element concentrations (wt.%) in chromite crystals.			
		Cr_2O_3	TiO_2	MgO	Al_2O_3
Z19-100.35	FPYXT	39.75 – 45.46	0.57 – 1.28	1.77 – 2.38	6.13 – 6.78
Z19-101.4	FPYXT	46.28 – 47.58	0.57 – 0.78	3.97 – 4.57	7.70 – 9.49
Z19-101.6	FPYXT	41.05 – 46.07	0.68 – 1.05	1.10 – 3.67	5.89 – 8.94
Z19-137.5	FPYXT	42.77 – 46.32	0.62 – 1.47	5.35 – 6.81	11.09 – 14.50
Z20-66.5	FHBZ	15.89 – 36.06	0.10 – 1.93	2.44 – 13.70	4.40 – 15.75
Z20-111	FHBZ	17.12 – 35.22	0.33 – 1.57	0.51 – 1.94	2.94 – 5.75

8.4.1.1 FELDSPATHIC PYROXENITE

The concentration of Cr_2O_3 ranges between (40 – 48 wt.%) and displays a negative correlation with MgO in all chromite crystals except in chromites in samples Z19-101.6 where the data displays two separate groups, chromites with the lower MgO content show a negative correlation with Cr_2O_3 while chromites with higher MgO content show a positive correlation with Cr2O3 (Fig 8-6A). This further validates the observation that chromite crystals within the same seam can differ considerably. A positive correlation is observed between Al_2O_3 and MgO within the feldspathic pyroxenite samples (Fig 8-6B), with the disseminated chromites in sample Z19-137.5 having higher Al_2O_3 and MgO than chromites from the chromite seam samples (Z19-101.4 & Z19-101.6) (Fig 8-6C). The FeO and quantities of chromite crystals in the feldspathic pyroxenite samples increase with decreasing MgO (Fig 8-6C). Fe_2O_3 displays a negative correlation with MgO in Z19-101.6 chromites, however; a positive correlation is observed in samples Z19-100.35 and Z19-137.5 chromites while Fe_2O_3 is relatively constant in Z19-101.4 chromite crystals (Fig 8-6D).

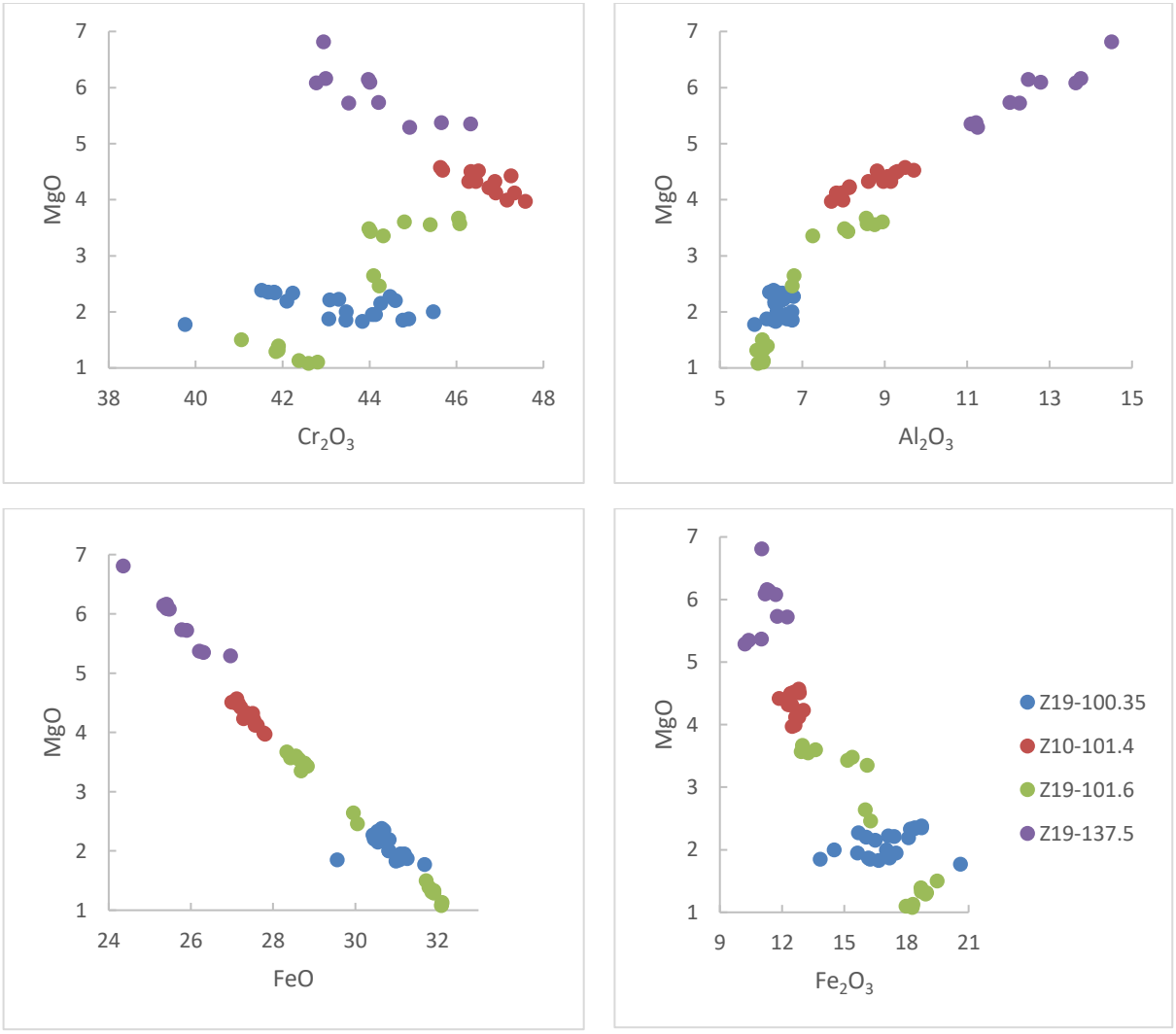


Figure 8-6: Geochemical graphs of chromite composition from feldspathic pyroxenite lithologies from the southwestern portion of the Uitloop farm; (A) Cr_2O_3 vs MgO (B) Al_2O_3vs MgO (C) FeO vs MgO (D) Fe_2O_3 vs MgO.

The Cr_2O_3 content of chromite crystals in samples Z19-101.4 and Z19-137.5 increases with decreasing Al_2O_3, conversely, Cr_2O_3 displays strong positive correlations with Al_2O_3 in chromites in samples Z19-100.35 and Z19-101.6 (Fig 8-7A). The Cr_2O_3 content in these chromites also increases with decreasing TiO_2 . The chromites from Z19-137.5 are however an exception as their Cr_2O_3 content increases with increasing TiO_2 (Fig 8-7B). As previously established, although chromite crystals in samples Z19-101.4 and Z19-101.6 are from the same seam, they do not have the same chemistry. The Z19-101.4 chromites have a lower TiO_2 and higher Cr_2O_3 concentrations than chromites in Z19-101.6 (Fig 8-7B). Al_2O_3 in the feldspathic pyroxenite-hosted chromites displays very strong negative trends with TiO_2 content (Fig 8-7C).

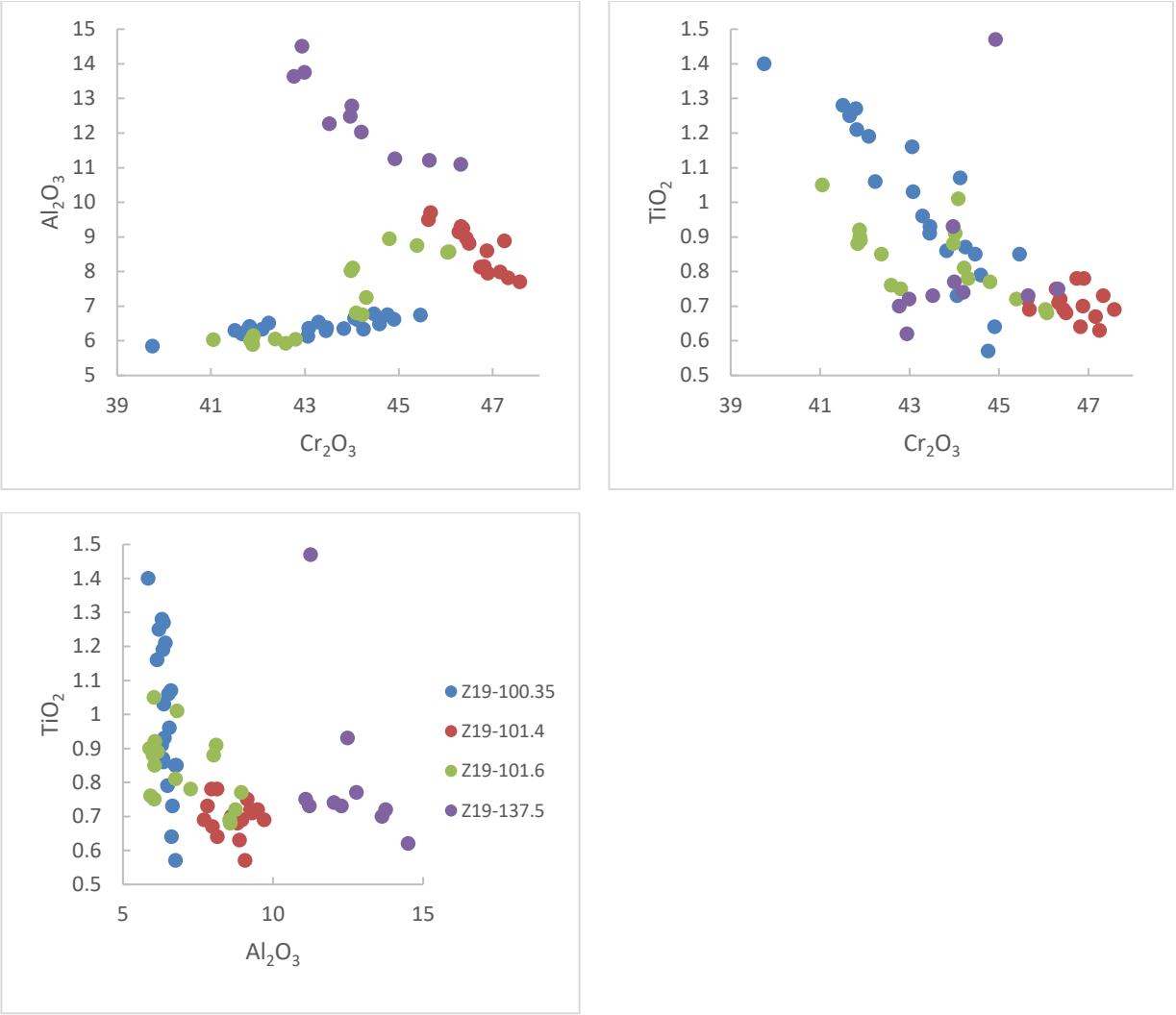


Figure 8-7: Geochemical graphs of chromite composition from feldspathic pyroxenite lithologies from the southwestern portion of the Uitloop farm; (A) Cr_2O_3 vs Al_2O_3 (B) Cr_2O_3 vs TiO_2 (C) Cr_2O_3 vs TiO_2.

8.4.1.2 FELDSPATHIC HARZBURGITE

The composition of chromite crystals hosted by feldspathic harzburgite vary considerably with stratigraphic height, with chromite crystals in sample Z20-66.5 having higher Cr_2O_3 and MgO proportions in comparison to the chromite crystals in sample Z20-111. In Z20-66.5, the majority of the chromite crystals display a weak negative correlation of Cr_2O_3 with MgO (Fig 8-8A). Chromite crystals in sample Z20-111 show a strong positive correlation between Cr_2O_3 and MgO (Fig 8-8A). In both samples, the chromites show very strong negative correlations of Al_2O_3 and FeO with MgO (Fig 8-8B & C). The chromite crystals hosted by the two feldspathic harzburgite samples display dissimilar Fe_2O_3 – MgO trends; Z20-66.5

chromites show a positive correlation between Fe_2O_3 and MgO while Z20-111 chromites display a negative trend (Fig 8-8).

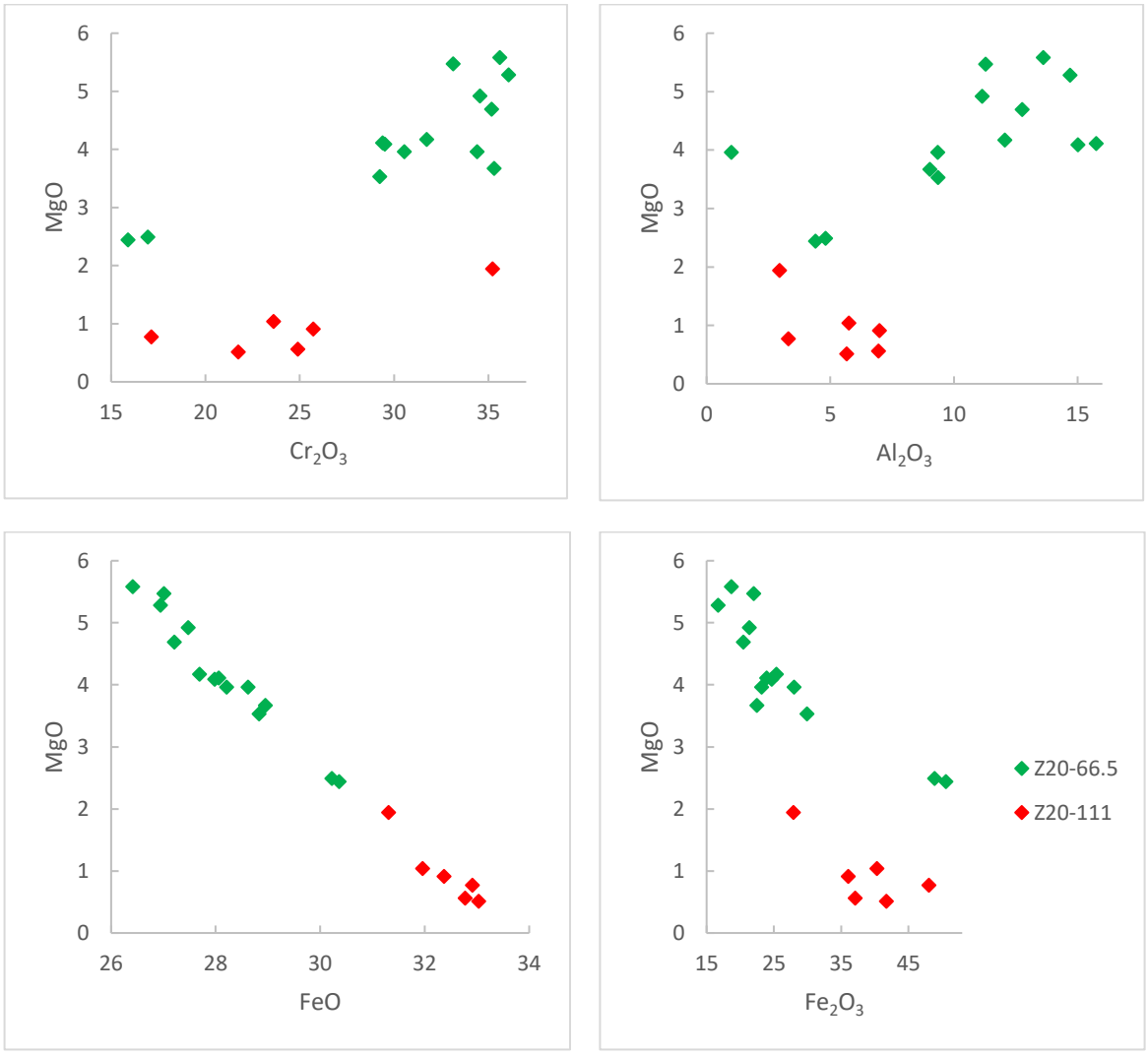


Figure 8-8: Geochemical graphs of chromite composition from feldspathic harzburgite lithologies from the southwestern portion of the Uitloop farm; (A) Cr_2O_3vs MgO (B) Al_2O_3 vs MgO (C) FeO vs MgO (D) Fe_2O_3 vs MgO

The chromite crystals hosted by the two feldspathic harzburgite samples have different Cr_2O_3 – Al_2O_3 trends; a negative correlation is observed between Cr_2O_3 and Al_2O_3 in Z20-66 chromites while sample Z20-111 chromites show a strong positive correlation (Fig 8-9A). The TiO_2 content in the chromites in both Z20-66.5 and Z20-111 also increases with increasing Cr_2O_3 (Fig 8-9B). However, chromites in Z20-66.5 generally have higher Cr_2O_3 and TiO_2 proportions than those in sample Z20-111 (Fig 8-9B).

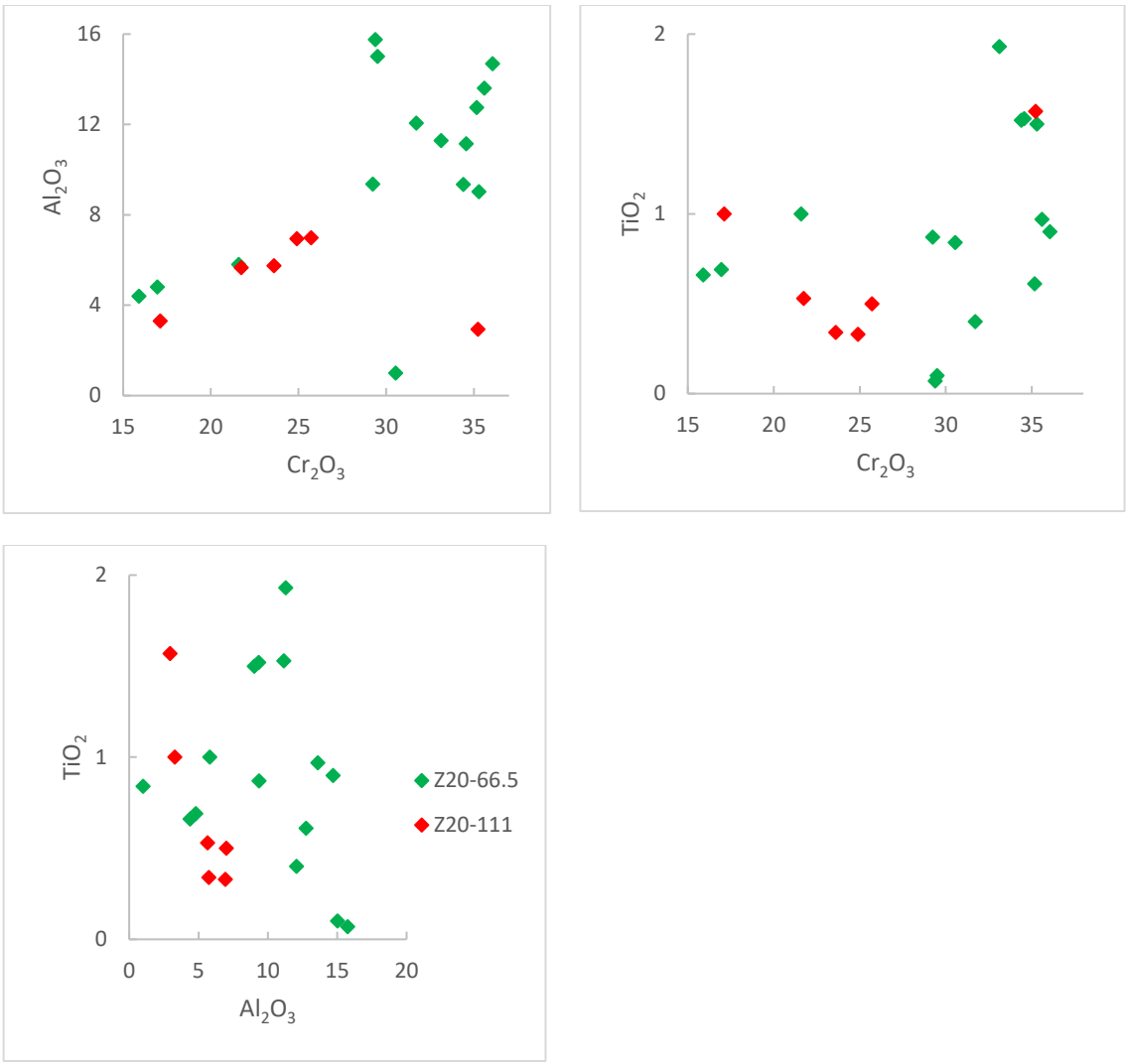


Figure 8-9: Geochemical graphs of chromite composition from feldspathic harzburgite lithologies from the southwestern portion of the Uitloop farm; (A) Cr_2O_3 vs Al_2O_3 (B) Cr_2O_3 vs Ti02 (C) Al_2O_3 vs TiO_2.

8.4.1.3 Cr# vs Mg#

The Uitloop chromite data ranges between chromites with high Cr# with moderate Mg# as well as those with higher Cr# with lower Mg# (Fig 8-10). Chromites in all the feldspathic pyroxenite samples show a negative trend between Cr# and Mg# (Fig 8-10), the chromites in sample Z19-137.5 have the lowest Cr# (avg. 70.01) and the highest Mg# (avg. 25.89) in comparison to chromites in other feldspathic pyroxenite samples. Although the chromites in samples Z19-101.4 and Z19-101.6 are from the same chromite stringer, they have different compositions; the chromites in Z19-101.4 have lower Cr# (avg. 78.25) and higher Mg# (avg. 21.69) in comparison to chromites in Z19-101.6 with an average of 79.95) Cr# and 12.20 Mg#. The compositions of chromites in Z19-100.35 have the highest Cr# (avg. 81.90) and the lowest Mg# (avg. 10.61) in comparison to chromites in the other feldspathic pyroxenite samples.

The composition of chromites is the feldspathic harzburgite samples display two compositional trends; chromites within sample Z20-66.5 show a negative trend of increasing Cr# with decreasing Mg#, while chromites in Z20-111 show increasing Cr# with increasing Mg# (Fig 8-10). The chromites in sample Z20-66.5 have average of 63.99 Cr# and 19.93 Mg# while sample Z20-111 chromites have elevated Cr# (avg. 79.79) with very low Mg# (avg. 6.31).

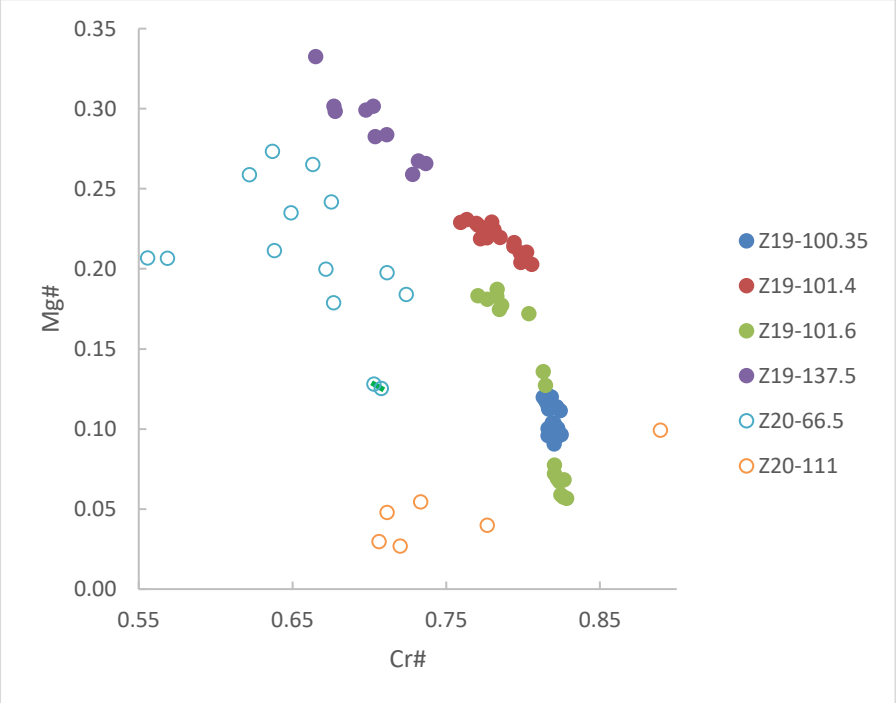


Figure 8-10: Cr# vs Mg# graphs for chromites hosted by magmatic lithologies from the southwestern portion of the Uitloop farm. Feldspathic pyroxenite (blue, marron, green and purple s) and feldspathic harzburgites (blue and orange), showing the proximity of chromite crystals to their original cumulus compositions.

8.4.2 CHROMITE COMPOSITION IN RELATION TO DIFFERENT MINERAL HOSTS

8.4.2.1 FELDSPATHIC PYROXENITE

The euhedral cumulus chromite crystals within the ultramafic rocks occur as inclusions within the silicate constituents of the rocks. In feldspathic pyroxenite samples, chromite crystals occur as inclusions within orthopyroxene, clinopyroxene, interstitial plagioclase, phlogopite and seldom within quartz and sulphides. The chromite crystals also show features of postcumulus growth occurring as an anhedral amoeboidal phase associated with plagioclase and orthopyroxene or corroded by phlogopite or altered to magnetite along crystal boundaries.

Looking at Figure 8-11, it appears that orthopyroxene-hosted chromite crystals in the feldspathic pyroxenite samples have a lower Cr_2O_3 content in comparison to plagioclase-hosted chromite. In both samples Z19-137.5 and Z19-101.4, chromites hosted within interstitial plagioclase have a higher Cr_2O_3 and lower MgO contents in comparison to chromites in cumulus orthopyroxene oikocrysts which have lower Cr_2O_3 with higher MgO proportions. On the contrary, the plagioclase-hosted chromites in Z19-101.6 have higher MgO and Cr_2O_3 concentrations than orthopyroxene-hosted chromite crystals. In sample Z19-101.4, there are also clinopyroxene-hosted chromite crystals which have the highest Cr_2O_3 and lowest MgO contents than the plagioclase-hosted and orthopyroxene-hosted chromites in the sample.

Orthopyroxene-hosted chromite crystals were not analysed in sample Z19-100.35; however, the plagioclase-hosted chromites in the sample have higher Cr_2O_3 contents in comparison to chromites associated by most other minerals such as phlogopite and base metal sulphides. Anhedral chromite crystals corroded by phlogopite appear to have higher Cr_2O_3 and lower MgO contents than some of the chromites in plagioclase in Z19-100.35 and orthopyroxene-hosted chromites in Z19-101.6. The chromites hosted by quartz in sample Z19-100.35 have higher MgO and somewhat similar Cr_2O_3 to the plagioclase-hosted chromites (Fig 8-11). In samples Z19-101.4 and Z19-137.5, the Al_2O_3 content is higher in orthopyroxene-hosted chromites than in plagioclase-hosted chromites; however, the opposite occurs in sample Z19-101.6. The Cr_2O_3 concentration of chromite crystals in orthopyroxene, plagioclase and clinopyroxene increases with decreasing Al_2O_3 in Z19-101.4 and Z19-137.5 (Fig 8-12). Chromite crystals in Z19-100.35 and orthopyroxene-hosted chromites in Z19- 101.6 are however exceptions as their Cr_2O_3 concentrations increase with increasing Al_2O_3 (Fig 8-12).

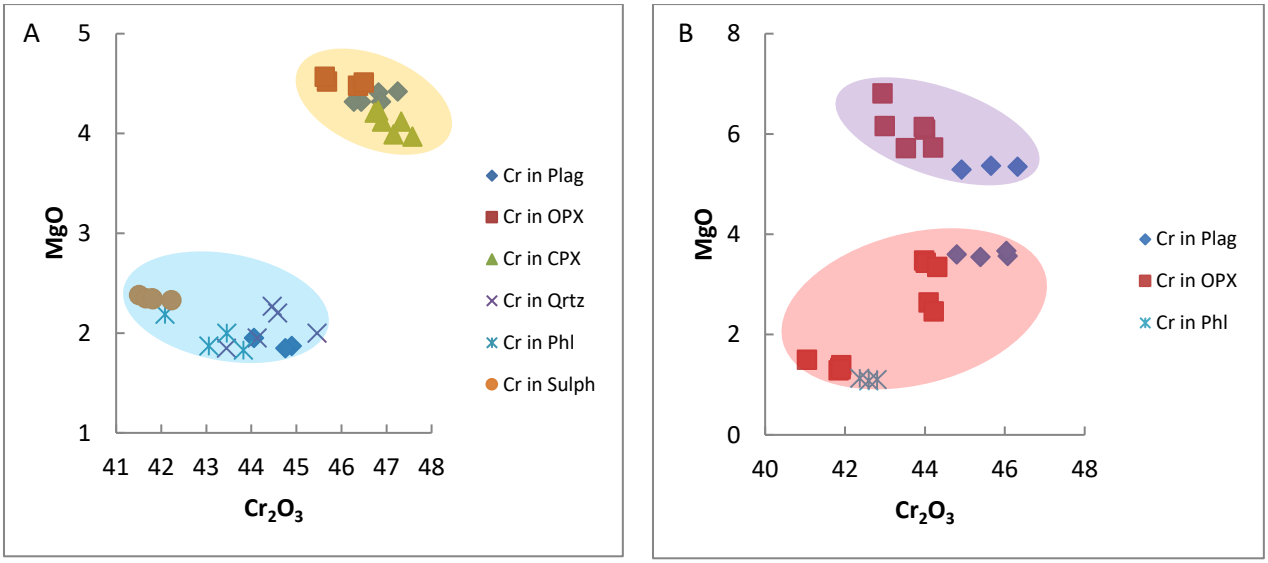


Figure 8-11: Geochemical graphs of chromite composition from feldspathic pyroxenite lithologies from the southwestern portion of the Uitloop farm; (A) Cr_2O_3 vs MgO (Blue: Z19-100.35, Orange: Z19-101.4) (B) Cr_2O_3 vs MgO (Red: Z19-101.6, Purple: Z19-137.5).

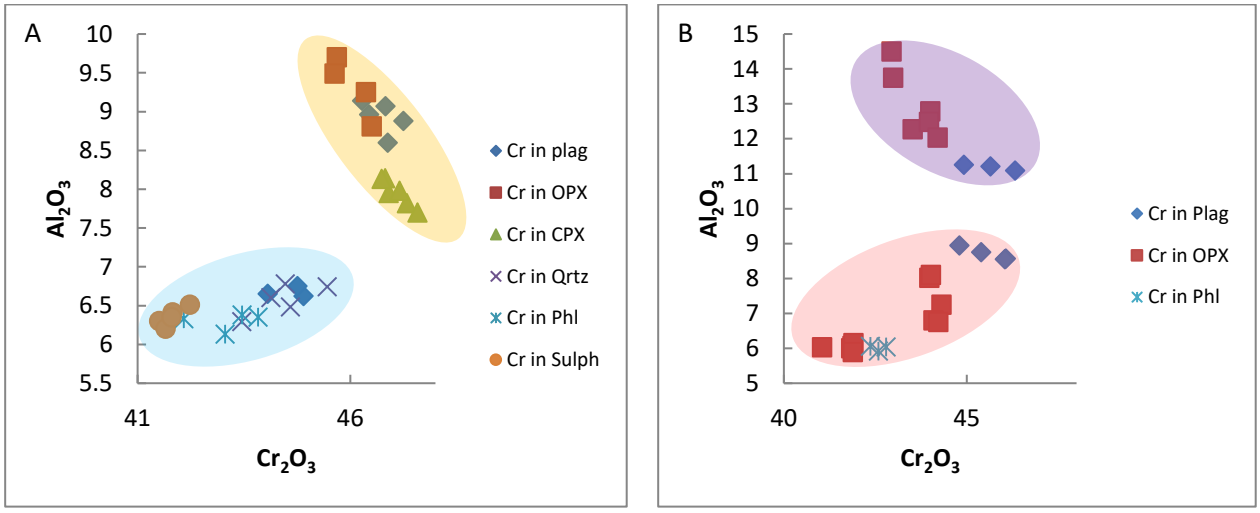


Figure 8-12: Geochemical plots of chromite composition from feldspathic pyroxenite lithologies from the southwestern portion of the Uitloop farm; (A) Cr_2O_3 vs Al_2O_3 (Blue: Z19-100.35, Orange; Z19-101.4) (B) Cr_2O_3 vs Al_2O_3. (Red: Z19-101.6, Purple: Z19-137.5).

A uniform trend of increasing Al_2O_3 with increasing MgO in chromite hosted by orthopyroxene, clinopyroxene, plagioclase, phlogopite and quartz is observed in all the chromite crystals analyzed Fig 8-13). In samples Z19-137.5 and Z19-101.4 the Al_2O_3 and MgO proportions are higher in orthopyroxene-hosted chromites than in plagioclase-hosted chromite crystals. In contrast, plagioclase-hosted chromites in Z19-101.4 have higher Al_2O_3 and MgO contents than in orthopyroxene-hosted chromites (Fig 8-13B). In both samples Z19-100.35 and Z19-101.6 chromite crystals corroded by phlogopite have the lowest Al_2O_3 content in comparison to chromites hosted by

other silicate constituents. Also, quartz-hosted chromite crystals in sample Z19-100.35 have the highest Al_2O_3 compared to plagioclase, base metal sulphides and phlogopite (Fig 8-13A).

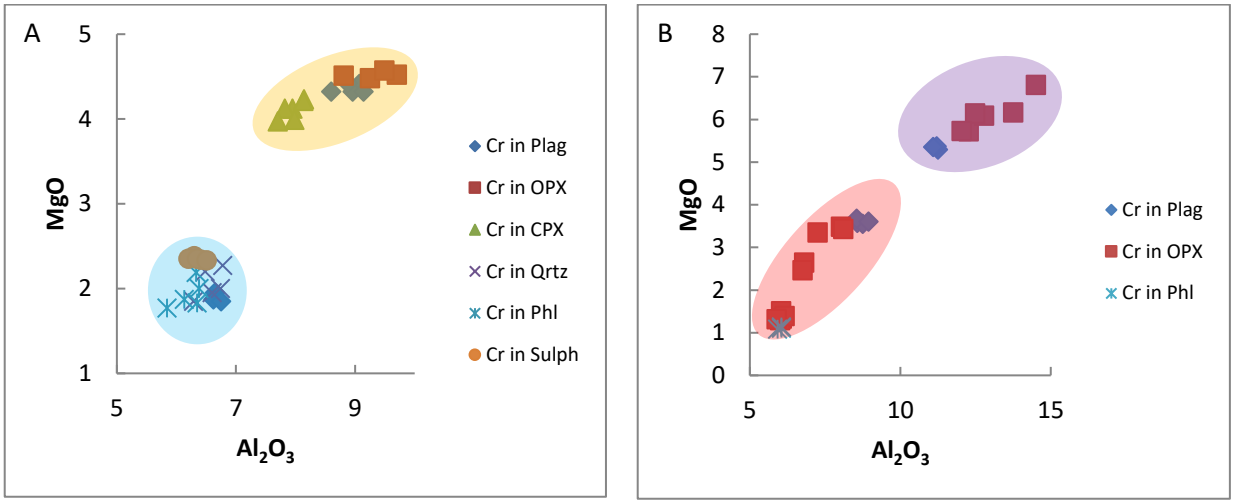


Figure 8-13: Geochemical graphs of chromite composition from feldspathic pyroxenite lithologies from the southwestern portion of the Uitloop farm; (A) Al_2O_3 vs MgO (Blue: Z19-100.35, Orange: Z19-101.4) (B) Al_2O_3 vs MgO Red: Z19-101.6, Purple: Z19-137.5).

The Cr_2O_3 in majority of the chromites increases with decreasing TiO_2 regardless of the different host minerals (Fig 8-14), with the silicate-hosted chromites in samples Z19-100.35 and Z19-101.4 having the least amount of TiO_2 and therefore the highest Cr_2O_3 concentration (Fig 8-14A). The compositions of orthopyroxene-hosted chromites in Z19-137.5 range from high TiO_2 with high Cr_2O_3 and low TiO_2 with low Cr_2O_3 (Fig 8-14B). Chromite crystals from the same seam may also have variable compositions as seen in samples Z19-101.4 and Z19-101.6, where the former generally has higher Cr_2O_3 and low TiO_2 proportions while the latter contains lower Cr_2O_3 with high TiO_2 contents. The composition of chromite disseminations within the same thin sections may also differ as is the case in sample Z19-100.35 where chromite crystals vary in composition from those with high Cr_2O_3 and low TiO_2 to those with low Cr_2O_3 and high TiO_2 (Fig 8-14). In the feldspathic pyroxenite samples, the plagioclase hosted chromites have somewhat similar TiO_2 contents ranging from 0.57 wt. % to 0.77 wt. %. The orthopyroxene-hosted chromites in Z19-101.6 have higher TiO_2 and the lowest Al_2O_3 contents in comparison to chromites in the other samples (Fig 8-15). The phlogopite-, sulphide- and quartz-hosted chromites have elevated TiO_2 and slightly lower Al_2O_3 and Cr_2O_3 contents in comparison to most plagioclase-hosted chromites from the same seam. Clinopyroxene-hosted chromite is characterized by relatively elevated Cr_2O_3 and reduced Al_2O_3 content Fig 8-15).

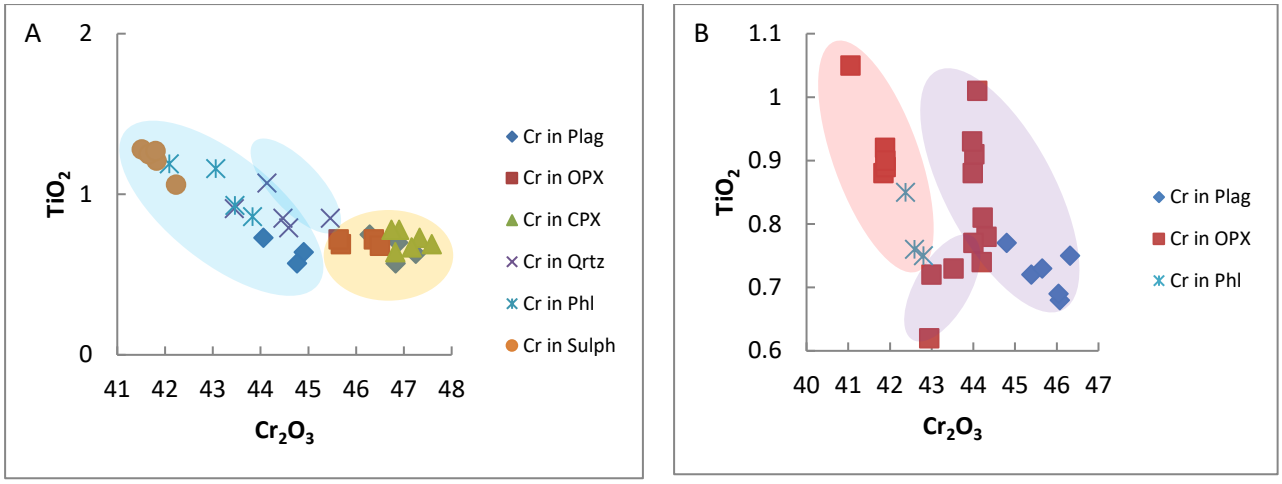


Figure 8-14: Geochemical graphs of chromite composition from feldspathic pyroxenite lithologies from the southwestern portion of the Uitloop farm; (A) Cr_2O_3 vs MgO (Blue: Z19-100.35, Orange: Z19-101.4) (B) Cr_2O_3 vs MgO (Red: Z19-101.6, Purple: Z19-137.5).

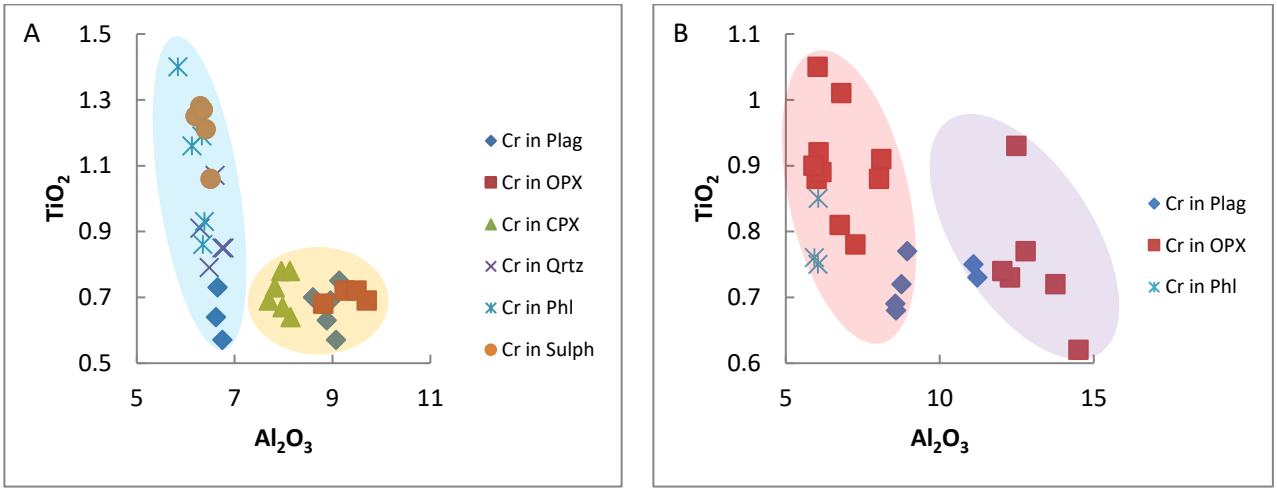


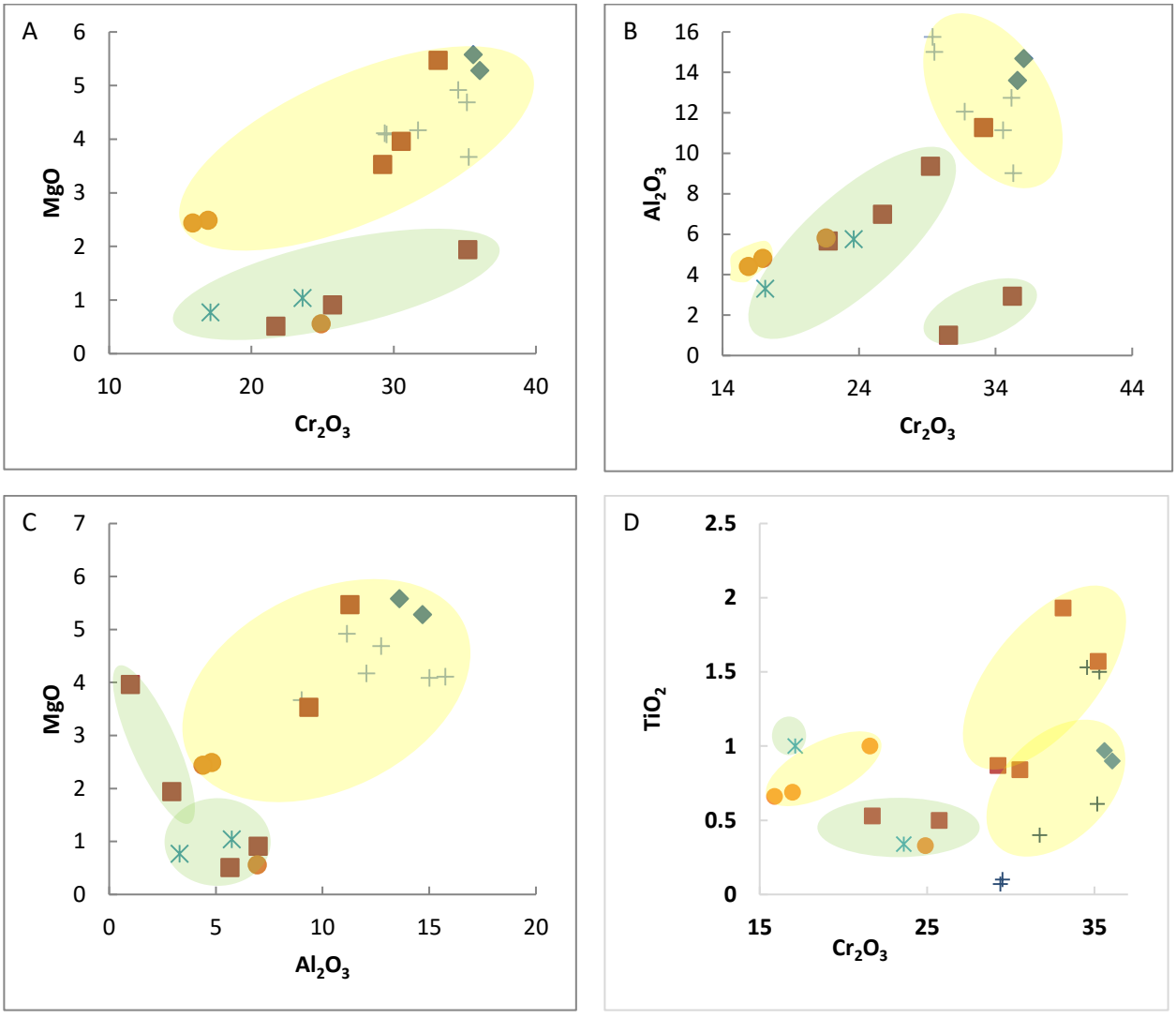
Figure 8-15: Geochemical plots of chromite composition from feldspathic pyroxenite lithologies from the southwestern portion of the Uitloop farm; (A) Al_2O_3 vs TiO_2 (Blue: Z19-100.35, Orange: Z19-101.4) (B) Al_2O_3 vs TiO_2 (Red: Z19-101.6, Purple: Z19-137.5).

8.4.2.2 FELDSPATHIC HARZBURGITE

The chromites hosted by silicate minerals (plagioclase, olivine and orthopyroxene) in sample Z20-66.5 not only have higher amounts of Cr_2O_3 but also high MgO and Al_2O_3 than chromites hosted by sulphide minerals (Fig 8-16A & B). The Cr_2O_3 content in Z20-66.5 chromites also display a general a positive trend with TiO_2 regardless of the host mineral (Fig 8-16D). In chromite crystals hosted by olivine and plagioclase, the lower the TiO_2 the higher Al_2O_3 while the sulphide- and orthopyroxene-hosted chromites show increasing Al_2O_3 with increasing TiO_2 (Fig 8-16E).

In sample Z20-111, only chromites hosted by orthopyroxene and sulphides as well as chromites corroded by phlogopite were analyzed. As expected, orthopyroxene-hosted chromite crystals

generally have higher concentrations of Cr_2O_3, MgO, Al_2O_3 and TiO_2. Although there are very few data points for chromites corroded by phlogopite, it appears that their Cr_2O_3 increases with increasing MgO (Fig 8-16A) and Al_2O_3 (Fig 8-16B) and decreasing TiO_2 (Fig 8-16D). The higher the MgO proportion in orthopyroxene-hosted chromites the lower the Al_2O_3 (Fig 8-16C), on the other hand, Al_2O_3 increases with increasing MgO in corroded chromites. Also, the Al_2O_3 concentration in the corroded and plagioclase-hosted chromites increases with decreasing TiO_2 (Fig 8-16E).



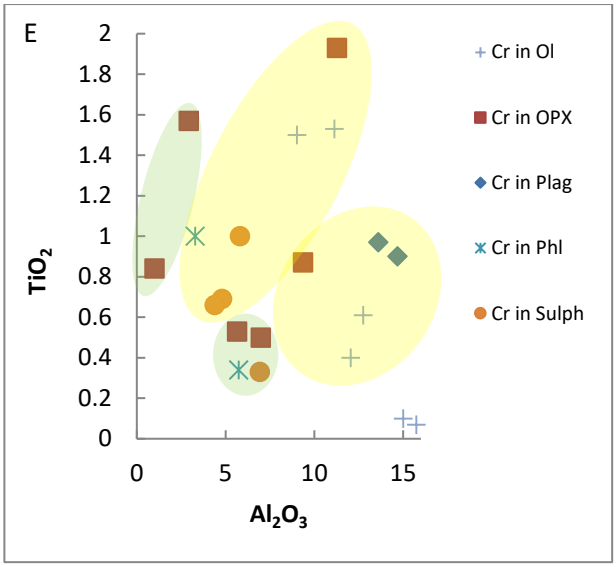


Figure 8-16: Geochemical graphs of chromite composition from feldspathic harzburgite (Yellow: Z20-66.5 & Green: Z20-111) lithologies from the southwestern portion of the Uitloop farm; (a) Cr_2O_3 vs MgO (b) Cr_2O_3vs Al_2O_3 c) Al_2O_3 vs MgO D) Cr_2O_3 vs $Ti0_2$ E) Al_2O_3 vs TiO_2.

The chromite crystals that have been corroded by phlogopite in samples Z19-100.35 and Z19-101.6 have higher Cr# and lower Mg# than chromites hosted/associated with other minerals (Fig 8-17). The compositions of plagioclase-hosted chromites in Z19-100.35 have the highest Mg# and the lowest Cr# in comparison to plagioclase-hosted chromites in samples Z19-101.4, Z19-101.6 and Z19-137.5. Orthopyroxene-hosted chromites in samples Z19-100.35 and Z19-101.6 also have a higher Cr# and much lower Mg# than those in samples Z19-101.4 and Z19-137.5. Chromite crystals associated with sulphide minerals in sample Z19-100.35 have much higher Cr# and lower Mg# in comparison to sulphide-hosted chromites in sample Z19-137.5 (Fig 8-17). However, chromites hosted by orthopyroxene oikocrysts in both samples Z19-101.4 and Z19-137.5 are closer to the original cumulus compositions than chromites associated with other silicate minerals and sulphides. The compositions of plagioclase-hosted chromites in sample Z20-66.5 generally have lower Cr# with higher Mg# than chromites associated with olivine, orthopyroxene and sulphide minerals. Figure 8-17 shows that chromite crystals associated with similar mineral constituents in feldspathic pyroxenite and feldspathic harzburgite lithologies at different stratigraphic levels do not have similar compositions.

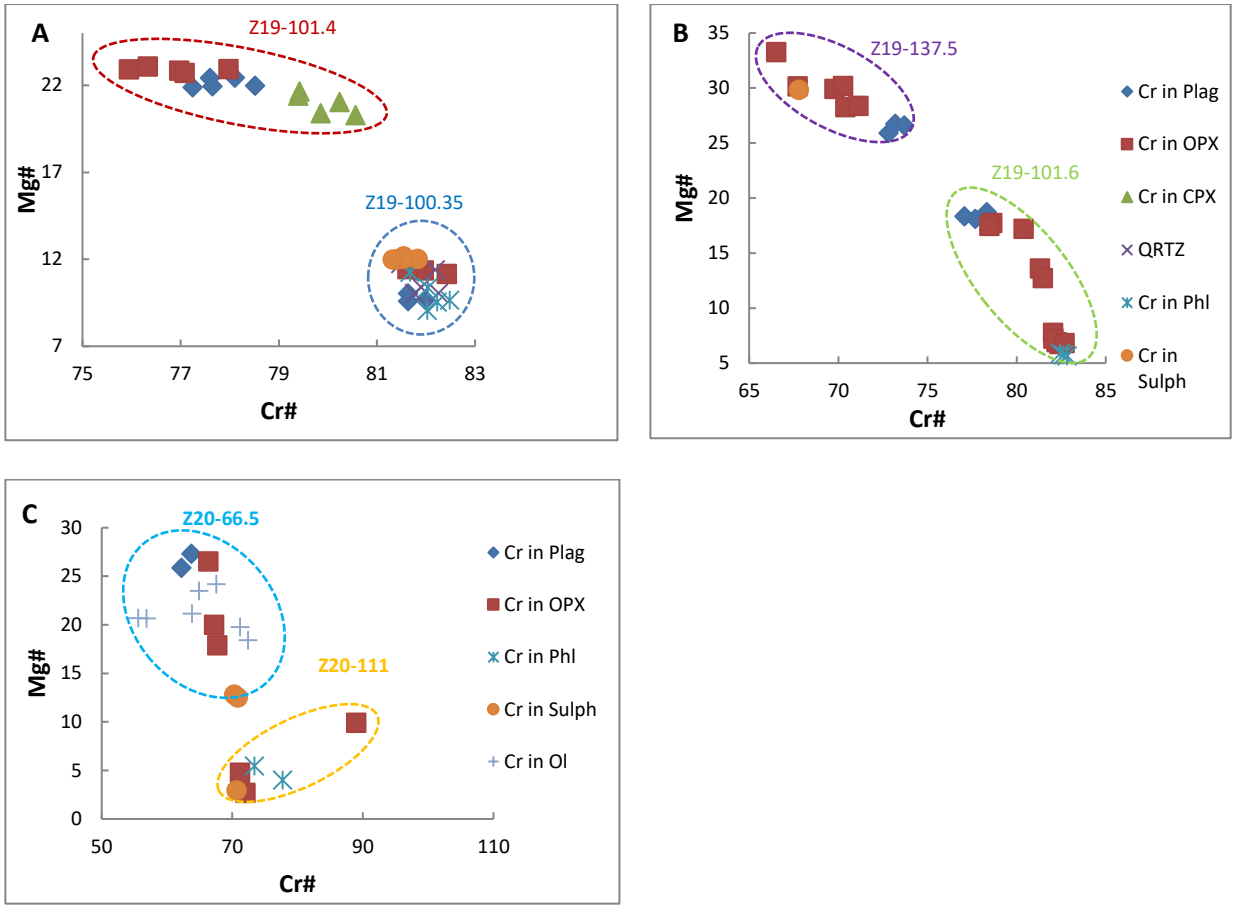


Figure 8-17: Cr# vs Mg# variation diagrams for chromites from the southwestern portion of the Uitloop farm magmatic lithologies.

8.5 COMPARISON TO OTHER BUSHVELD COMPLEX CHROMITE COMPOSITIONS

The chromite compositions in this study have been compared to the composition of chromites from the Platreef and Lower Zone (Turfspruit, Sandsloot) (Yudovskaya & Kinnaird, 2010) and the Lower Zone (Grasvally) (Hulbert, 1983) in the northern limb as well as the Merensky Reef (Li et al., 2005) and the UG-2 chromitite layer (Mondal & Mathez, 2007).

8.5.1 COMPARISON TO PLATREEF CHROMITE COMPOSITIONS

The composition of chromite in this study were compared to Platreef chromite data, specifically from the farms Macalacaskop, Turfspruit, Sandsloot, Vaalkop, Zwartfontein and Overysel (Fig 8-18). According to Yudovskaya and Kinnaird (2010), the Platreef chromites can be subdivided into two groups; the Upper Chromite Zone (UCR) and Lower Chromite (LCR), based on their location relative to the top and bottom contacts of the Platreef. The UCR chromitites are hosted by mainly feldspathic pyroxenite or restricted to boundaries between feldspathic pyroxenite and olivine-bearing lithologies

whereas the LCR chromitites are observed at the contact between pyroxenite and harzburgite lithologies as well as within feldspathic pyroxenites and norites 20 – 50 m above the basal contact.

According to Yudovskaya and Kinnaird (2010), the composition of the Platreef chromitites is dependent on the host rock type; norite- and pyroxenite-hosted chromites have the highest Cr_2O_3 content while harzburgite-hosted chromites are generally Cr- and Mg-poor. The pyroxenite-hosted chromites in the UCR have Cr_2O_3 content ranging between 40.7 – 46.6 wt.%, while chromites from a seam at the contact between harzburgites and pyroxenites have Cr_2O_3 content of about 27.5 – 39.6 wt.%. The norite- and feldspathic pyroxenite-hosted chromites have the highest Cr_2O_3 (49.6 wt.%) content recorded in the upper portion of the LCR.

Figure 8-18 shows that the data for feldspathic pyroxenite-hosted chromites from borehole Z19 is generally well clustered in comparison to that of feldspathic harzburgite-hosted chromites in Z20. Overall, the chromites in this study have lower Ti as well as generally lower Mg and Al contents in comparison to the Platreef data. The chromites in Z19 have a higher Cr_2O_3 (avg. 44.32 wt.%) with lower TiO_2 (avg. 0.99 wt.%), while Z20 chromites contain considerably lower Cr_2O_3 (avg. 26.51 wt.%) and TiO_2 (avg. 0.67 wt.%) contents in comparison to majority of the Platreef data, however, some of the Z19 chromite data overlaps with that of the chemistry of chromites from Zwartfontein, Sandsloot, Vaalkop, Turfspruit and Overysel farms. The high TiO_2 content in the Platreef chromites was interpreted as a result of local melt contamination during emplacement (Yudovskaya and Kinnaird 2010).

The chromites from Uitloop, especially Z19 chromites, display a wider Mg# range over a narrower Cr# range which results in a steeper primary trend line. In the Cr# vs Mg# binary diagram (Fig 8-18D); the Z19 chromites generally plot within the same range as data from Macalacaskop and Sandsloot, although some of the Z19 data plots at higher Mg# with similar Cr#. In contrast, the majority of the Z20 chromites plot within the same range as Overysel as well as some of the chromites from Zwartfontein and Turfspruit.

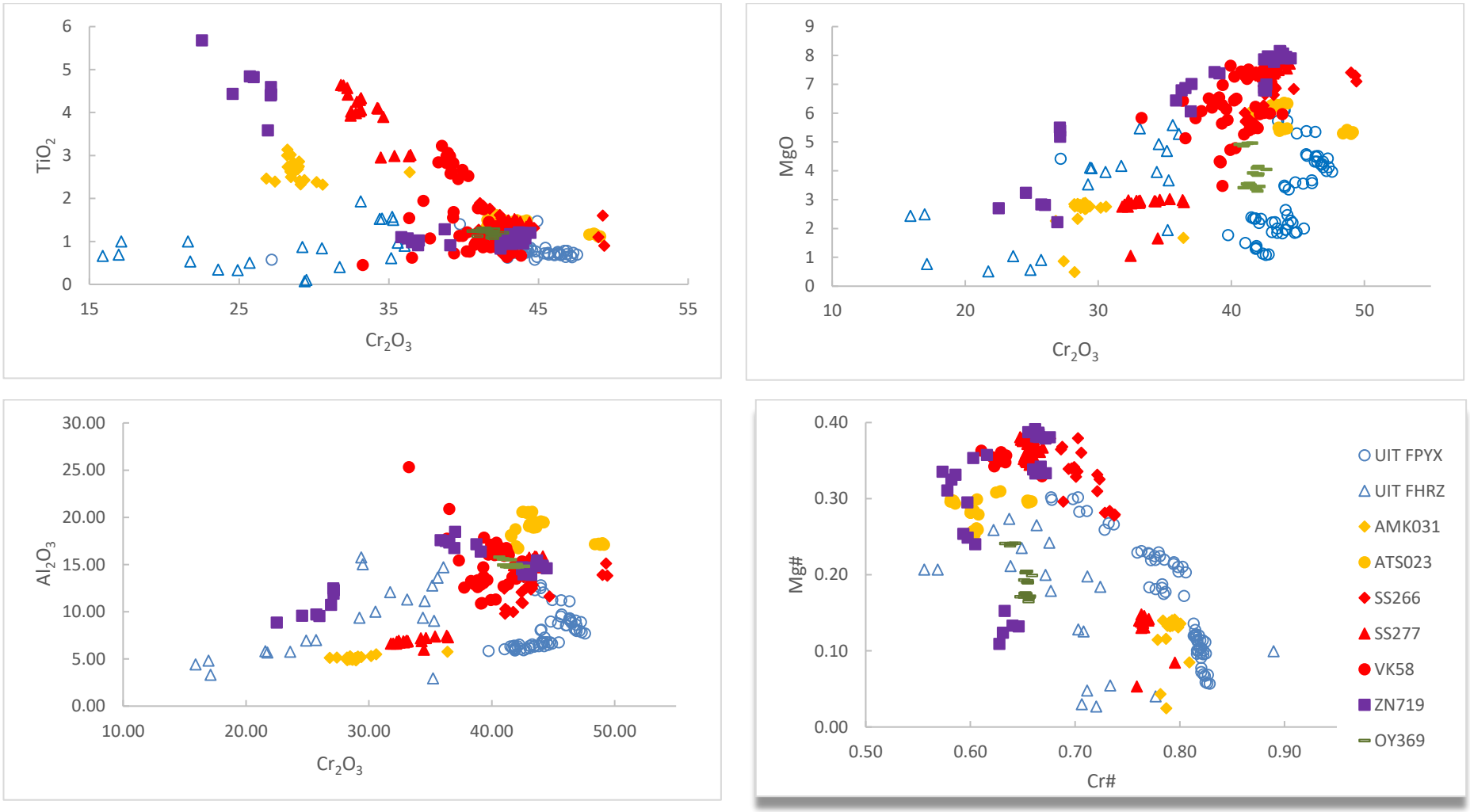


Figure 8-18: Compositional variation diagrams comparing the compositions of chromites from the southwestern portion of the Uitloop farm magmatic lithologies to those from different parts of the Platreef (Yudovskaya & Kinnaird, 2010) in the northern limb. (UIT = Uitloop, AMK = Macalacaskop, ATS = Turfspruit, SS = Sandsloot, VK = Vaalkop, ZN = Zwartfontein and OY = Overysel).

8.5.2 COMPARISON TO LOWER ZONE (GRASVALLY) CHROMITE COMPOSITIONS

The LZ chromitites in the northern limb have considerably higher chromium content in comparison to the CZ chromitites. The Cr_2O_3 content in the LZ is controlled by the modal chromite content within the host rocks (Hulbert, 1983). Van der Merwe (1978) indicated that the chromitites in the LZ offshoot intrusions contain 52.43 % Cr_2O_3 with the Cr/Fe ratio of 2.22, while the Lower and Upper chromitites in the Grasvally body have Cr_2O_3 contents of 57.88 % and 57.11 % with Cr/Fe ratios of 2.99 and 2.69 respectively, these values are the highest reported for chromitites in the Bushveld Complex (Van der Merwe, 1978).

The LZ and chromites in this study contain more or less similar amounts of TiO_2 (Fig 8-19A). Figure 8-19 also illustrates that the LZ chromite crystals contain higher amounts of Cr_2O_3, MgO and Al_2O_3 in comparison to the chromites in this study. The Mg# in the LZ chromites is also much higher than that of the Uitloop chromites, however the feldspathic pyroxenite hosted chromite in this study generally has higher Cr# than the LZ chromites. The latter is explained by Al content of the Uitloop chromites where significant trivalent Fe has substituted for Al.

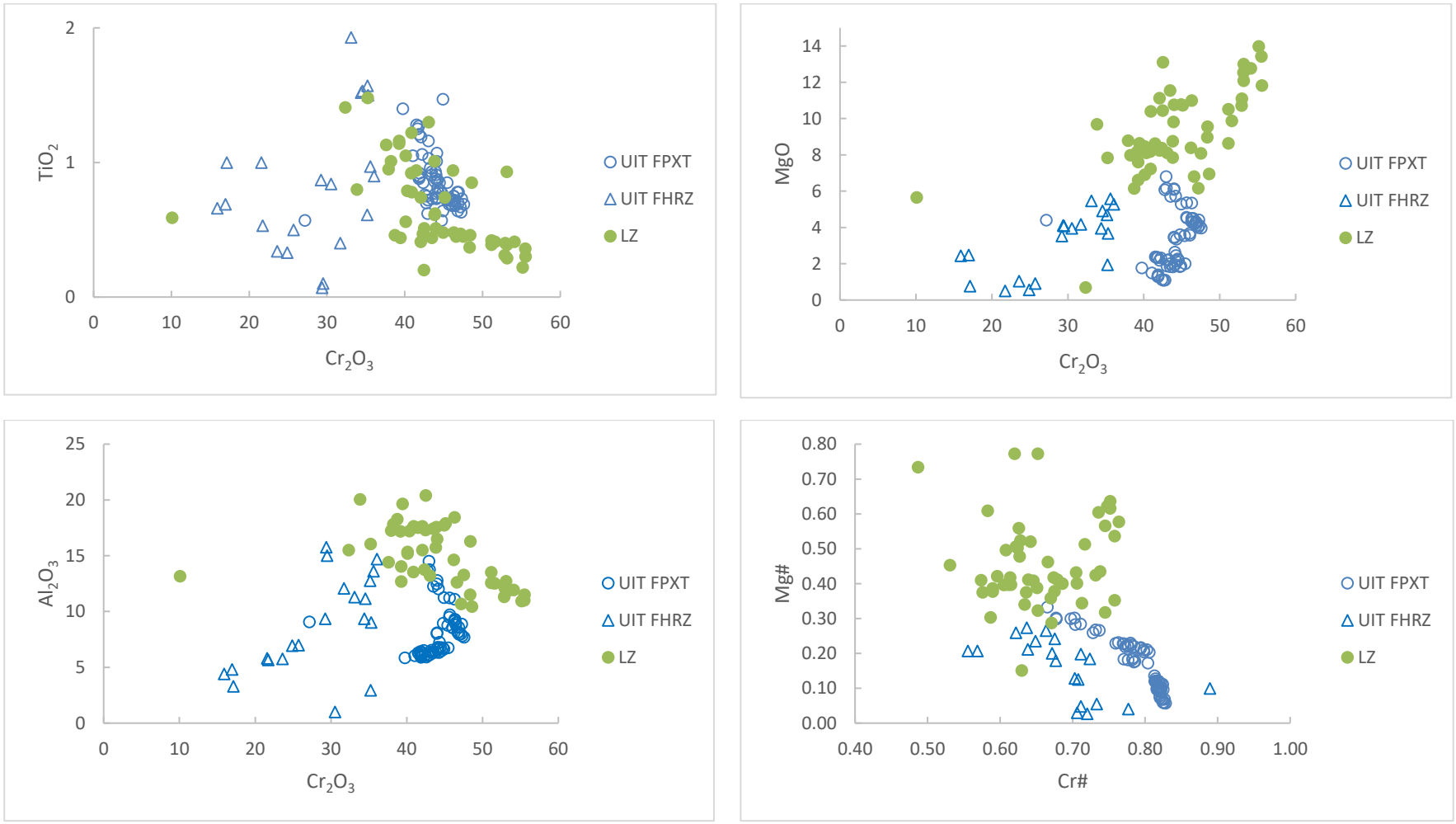


Figure 8-19: Compositional variation diagrams comparing the compositions of chromites from the southwestern portion of the Uitloop farm magmatic lithologies to those from the Lower Zone lithologies south of Mokopane (Hulbert, 1983) in the northern limb. (UIT FPXT = Uitloop feldspathic pyroxenite, UIT FHRZ = Uitloop feldspathic harzburgite, LZ =Lower Zone).

8.5.3 COMPARISON TO CRITICAL ZONE CHROMITE COMPOSITIONS

The chromitite occurrences in the eastern and western limbs are restricted to the Critical Zone. The chromium content (Cr_2O_3) of chromite in the CZ stratigraphy decreases upwards from 46 – 47 % Cr_2O_3 in the LG-6 chromitites to 44 – 46 % Cr_2O_3 in the MG chromitites and eventually 43 % Cr_2O_3 in the UG-2 chromitites (Schurmann et al., 1998). This is reflected in the upward decrease in the Cr/Fe ratio; which ranges between 1.56 – 1.60 in the LG-6 chromitites, 1.35 – 1.50 in the MG chromitites and 1.26 – 1.40 in the UG-2 chromitites (Kinnaird et al., 2002). The Merensky Reef in the Upper Critical Zone commonly comprises two very thin chromitites, the lower and upper chromitite layers, which both attain maximum thicknesses of a few centimetres (Li et al., 2005). The chromite crystals from the lower chromitite layer of the Merensky Reef have higher Mg# values with lower Cr# as well as $Ti0_2$ and Fe_2O_3 contents in comparison to the chromites in the upper chromitite layer (Vukmanovic et al., 2013). The composition of chromites in this study will only be compared to those of the UG-2 and Merensky Reef.

Figure 8-20A shows that the chemistry of the feldspathic pyroxenite-hosted chromites in this study cluster together with the UG-2 and Merensky Reef chromites, however these Uitloop chromites generally contain considerably higher Cr_2O_3 and lower MgO contents in comparison to the Merensky Reef and UG-2 chromites. In contrast, the feldspathic harzburgite-hosted chromites have much lower Cr_2O_3 contents with highly variable TiO_2 content in comparison to the UG-2 and Merensky Reef chromites. The UG-2 and Merensky Reef chromites have much higher MgO and Al_2O_3 contents than the Uitloop chromites (Fig 8-20B). Lastly, just like the Merensky Reef and UG-2 chromites, the Uitloop farm chromites show an increase in Cr# with decreasing Mg#. However, the Uitloop chromites generally have much higher Cr# with lesser Mg# in comparison to the Merensky Reef and UG-2 chromites (Fig 8-20D).

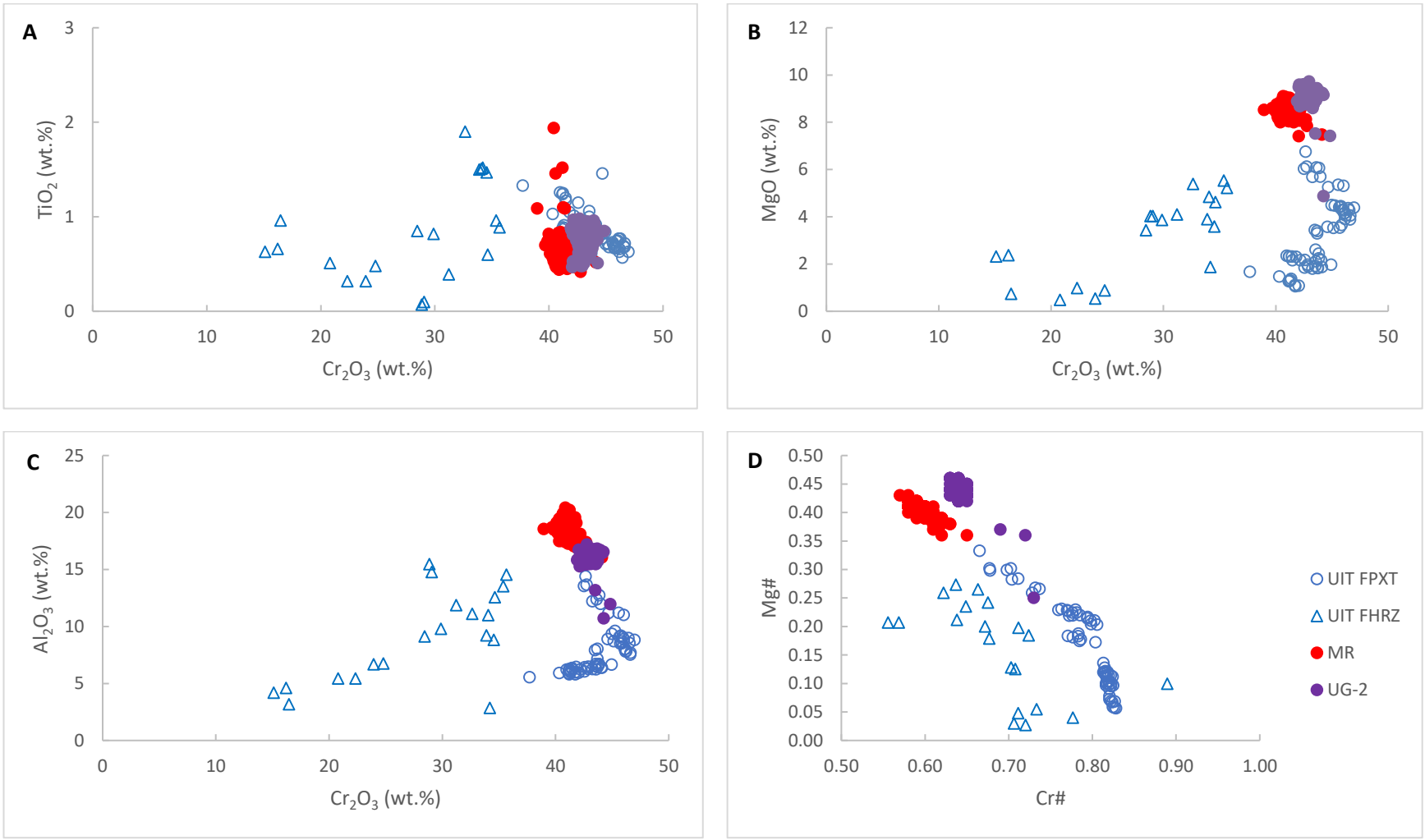


Figure 8-20: Compositional variation diagrams comparing the compositions of chromites from the southwestern portion of the Uitloop farm to those of the Merensky Reef (Li et al., 2005) and the UG-2 chromitite layer (Mondal & Mathez, 2007). (UIT FPXT = Uitloop feldspathic pyroxenite, UIT FHRZ = Uitloop feldspathic harzburgite, MR = Merensky Reef, UG-2 = UG-2 = Chromitite layer).

8.6 OLIVINE CHEMISTRY

Majority of the olivine-bearing rocks from the southwestern portion of the Uitloop farm are highly serpentinised, however one feldspathic pyroxenite sample (Z20-66.5) contains relatively fresh olivine crystals that were analysed. As a result, there is a limited data set for olivine composition. The chemistry of olivines in this study will be compared to that of the Platreef and Lower Zone olivine (Turfspruit and Sandsloot) (Yudovskaya et al, 2013) as well as olivine from the Lower Zone (Grasvally) (Hulbert, 1983) and the Merensky Reef (Naldrett et al., 2009).

Thin exsolution lamellae of chromite and clinopyroxene are distributed throughout the olivine crystals in sample Z20-66.5 (Fig 8-22). Yudovskaya et al (2013) also observed a similar feature within Lower Zone olivines from Turfspruit and Sandsloot, these exsolution lamellae are commonly described to be a stable product of the breakdown of Cr-bearing olivine in meteorites and rocks of mantle affinity.

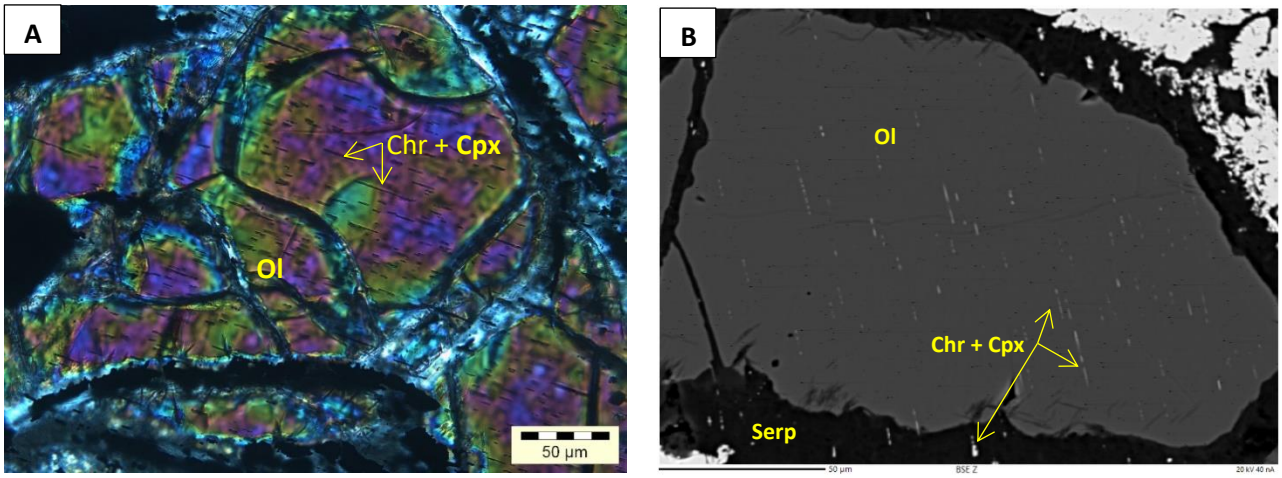


Figure 8-21: Photomicrographs of olivine crystals under XPL (A) and BSE (B). (A) Z20-66.5, transmitted cross polarized light; chromite and clinopyroxene lamellae in olivine. (B) Z20-66.5-3_44, BSE; chromite and clinopyroxene lamellae in olivine. (Ol = Olivine, Serp = Serpentine, Chr = Chromite, Cpx =Clinopyroxene).

The Lower zone on Grasvally consists of more chemically primitive minerals than those from the Lower Zone of the Eastern and Western limbs. Grasvally olivine is not depleted in Ni with respect to LZ olivine from the Western and Eastern limbs, however, Grasvally Lower Zone olivine is depleted in Ni compared to LZ olivine from Sandsloot to the north, that contains almost 0.5 wt.% NiO. Lower Zone olivine is also relatively depleted in Ni compared to olivine from the PGE reefs (including Merensky Reef and reefs of the Platreef). The olivine from the sulphide-bearing intervals may contain more than 0.4 wt.% NiO at relatively lower Mg# not exceeding 84 that is likely explained by subsolidus exchange between olivine and sulphides.

The olivines in the Lower Zone lithologies at Turfspruit farm are also relatively depleted in Ni compared to olivine from LZ in the adjacent Sandsloot area, this has been thought to be a result of melt contamination with carbon-rich Duitschland shales on Turfspruit (Yudovskaya et al., 2013). Like the olivine crystals from Turfspruit, Sandsloot and Merensky Reef, the Uitloop farm olivine crystals show a good correlation between SiO_2 and MgO (Fig 8-23A) and FeO and MgO (Fig 8-23D) in accordance with the crystalochemical formula. The olivines in this study have MnO and TiO_2 contents ranging from 0.17 to 0.22 wt.% and up to 0.07 wt.% respectively. The TiO_2 content in these olivine crystals is higher than in olivines from Turfspruit, Sandsloot and the Merensky Reef but much lower in comparison to the Grasvally olivines (Fig 8-23B). The olivine crystals in this study have somewhat similar MnO content as the Lower Zone olivines from Turfspruit, Sandsloot and Grasvally farms, while the Merensky Reef and Platreef olivines have elevated MnO concentrations (Fig 8-23C) that are consistent with their lower Mg#.

The olivines from the southwestern portion of the Uitloop farm have slightly higher NiO (0.29 – 0.34 wt.%) in comparison to the Lower Zone olivines from the Turfspruit and Grasvally farms as well as the Platreef olivines from Turfspruit and Sandsloot farms (Fig 8-24B). However, the olivine crystals from the Merensky Reef and the Lower Zone at Sandsloot have higher NiO concentrations. The Mg# of the olivine crystals in this study ranges between 73.76 – 84.54, these values fall within the same range as the Platreef olivines from Turfspruit and Sandsloot farms as well as the Merensky Reef. The olivine crystals from the Lower Zone in the northern limb have much higher Mg# values up to 92 (Fig 8-24) (Yudovskaya et al., 2013).

The MnO concentrations in olivine is a measure of the degree of magma fractionation, while the NiO content in olivine crystals is controlled by the composition of the fractionated melt as well as partitioning into any coexisting sulphide melt (Hulbert, 1983; Yudovskaya et al, 2013). The most primitive Mg# corresponds to the lowest MnO content, as is the case with the Lower Zone Grasvally olivines (Fig (Fig 8-24D). Thus, the olivine crystals from the Merensky Reef as well as Turfspruit and Uitloop farms are formed from more differentiated melts in comparison to the Lower Zone olivines from Sandsloot and Grasvally farms. The olivine crystals in this study are associated with chromite and contain tiny needle-like exsolutions of chromite and clinopyroxene. Therefore, the elevated Cr_2O_3 content ranging up to 0.54 wt.% and associated elevated Ti and Al in olivine composition are likely to reflect the presence of these exsolutions within the Zone of electron excitation during the WDS analysis. Similar exsolutions were observed in the LZ olivine in the northern limb (Yudovskaya et al., 2013). Their occurrence indicates that liquidus olivine had elevated Ti and Cr admixtures in its composition, however, their concentrations when measured now do not correspond to their initial values as these components were re-distributed during solid solution breakdown.

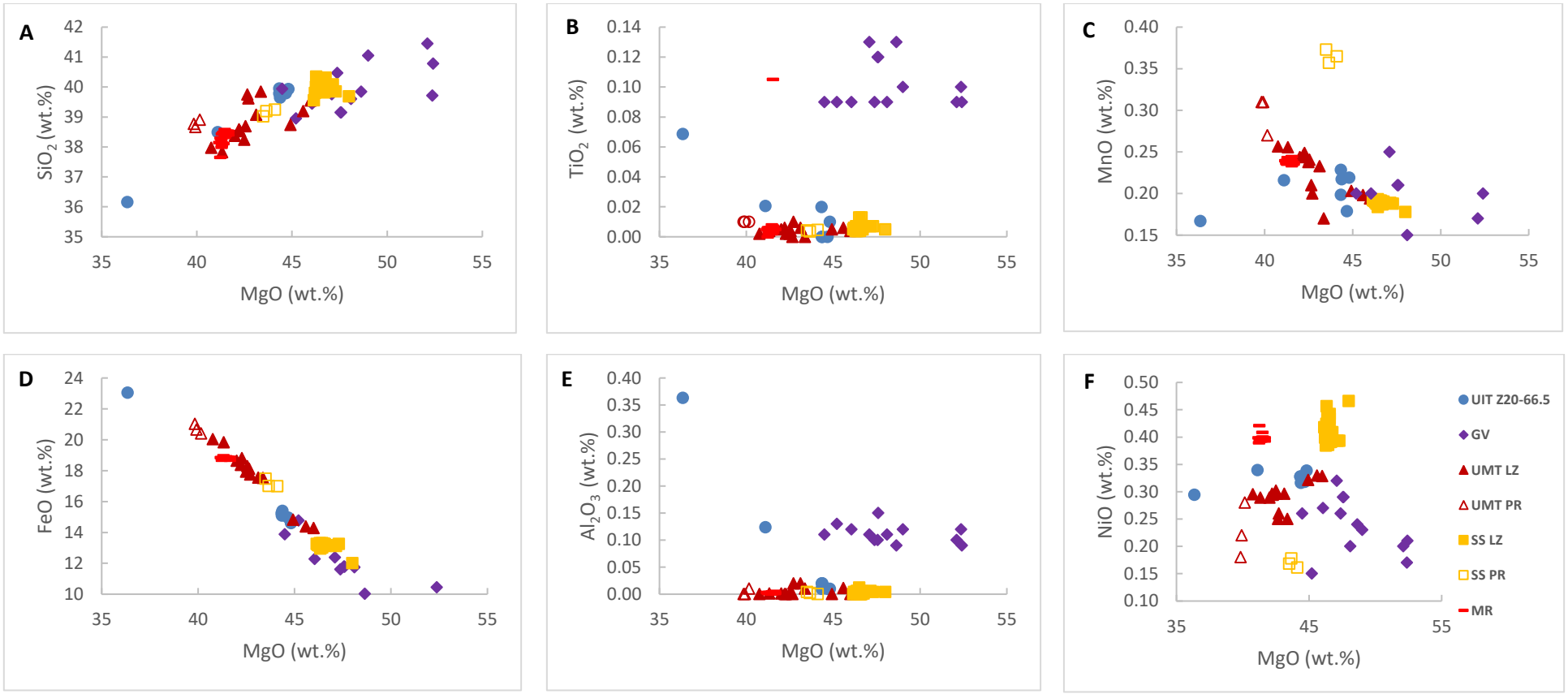


Figure 8-22: Compositional variation diagrams comparing the compositions of olivine crystals from the southwestern portion of the Uitloop farm magmatic lithologies to the Lower Zone olivine crystals from Turfspruit, Sandsloot (Yudovskaya & Kinnaird, 2010), Grasvally farms (Hulbert, 1983) and the Merensky Reef (Naldrett et al., 2009). (UIT = Uitloop, LZ = Lower Zone, PR = Platreef, GV = Grasvally, UMT = Turfspruit, SS = Sandsloot, MR = Merensky Reef).

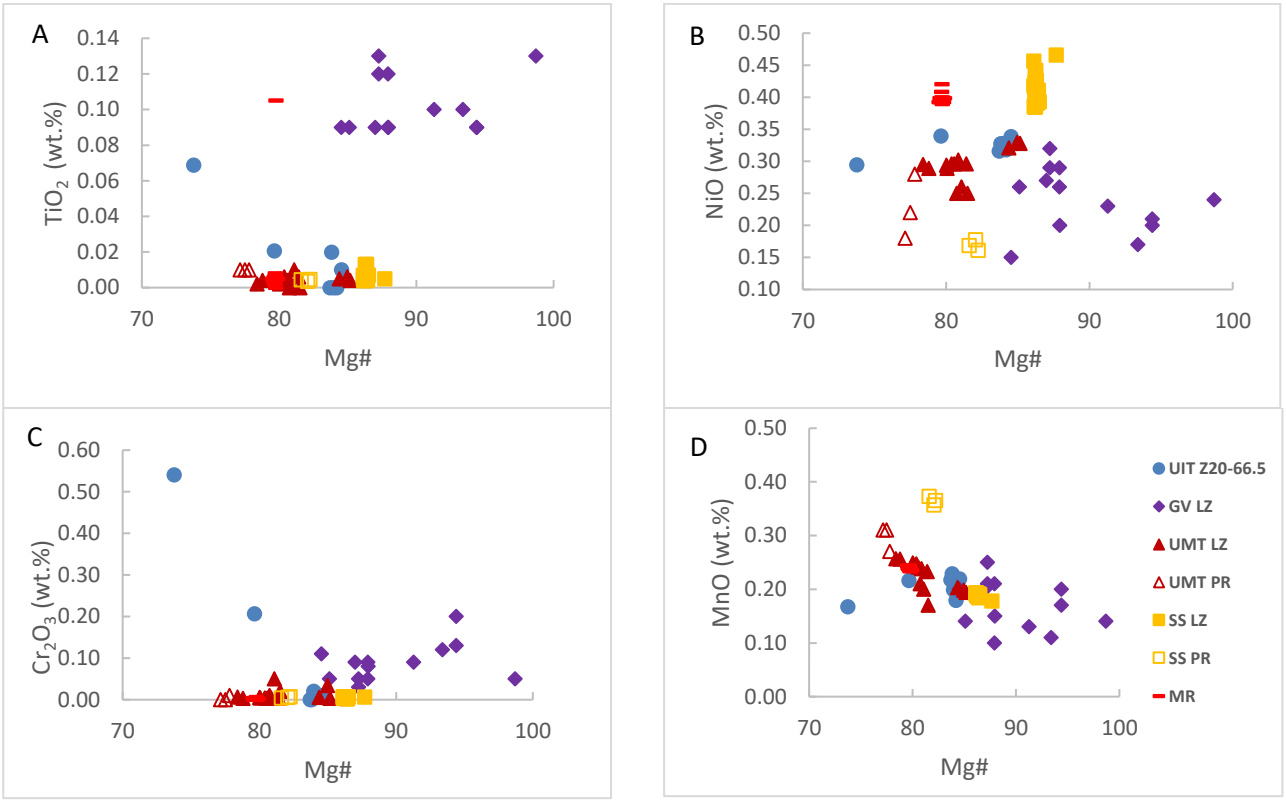


Figure 8-23: Compositional variation diagrams comparing the compositions of olivine crystals from the southwestern portion of the Uitloop farm (UIT) magmatic lithologies to those of the Lower Zone (LZ) and Platreef (PR) olivine crystals from Turfspruit (UMT), Sandsloot (SS) (Yudovskaya & Kinnaird, 2013), Grasvally farms (GV) (Hulbert, 1983) and Merensky Reef (MR) (Naldrett et al., 2009).

8.7 MINERAL CHEMISTRY SUMMARY

8.7.1 CHROMITE

The chromite from the southwestern portion of the Uitloop farm is associated with feldspathic pyroxenite and feldspathic harzburgite lithologies, mainly as seams and patches of densely disseminated grains and accessory disseminations. A thin chromitite stringer is also observed adjacent to the hanging wall contact in borehole Z20. The chromite in borehole Z19 is intersected at two depth intervals at 78.3 – 101.6 m and 137.7 – 137.8 m, within feldspathic harzburgite and feldspathic pyroxenite respectively. The same is observed in borehole Z20 with chromite occurring at 54.25 and 57.5 m within feldspathic harzburgite units. However, these horizons in boreholes Z19 and Z20 cannot be correlated as a result of differing host rocks as well as their occurrence at different stratigraphic levels.

Petrographic investigations indicate that the chromite content within host lithologies ranges between 0.5 to 20 %. The chromite crystals vary in size from coarse- to fine-grained and commonly occur as either inclusions or interstitial to silicate constituents (pyroxenes, olivine, plagioclase and phlogopite) while some are enclosed by BMS (pyrrhotite). Chromite crystals within boreholes Z19 and Z20 display varying textures throughout the stratigraphic intervals, the cumulus chromite crystals are mainly euhedral, subhedral and rounded while anhedral chromites show evidence of prolonged postcumulus growth to result in the formation of amoeboidal and sieve-textured crystals with common fishhooks. Most of the anhedral chromites have been replaced (corroded) by phlogopite, resulting in relics with irregular crystal boundaries. The euhedral and rounded chromite crystals are the most abundant and tend to anneal to form larger crystals. These chromite crystals generally lack inclusions; however, needle-like rutile inclusions (exsolution lamellae) were observed in some of the euhedral chromites in the feldspathic pyroxenite samples. The anhedral interstitial and corroded chromite crystals usually contain sulphide and silicate inclusions, these chromites are also altered to magnetite and a fine-grained Fe-rich phase along their crystal boundaries, especially where chromite is in contact with phlogopite.

The chemistry of the chromite differs depending on the type of host rock and associated minerals as well as stratigraphic position. The chromites in feldspathic pyroxenites show a general trend of increasing Cr_2O_3 with decreasing MgO and TiO_2, however the composition of chromite in sample Z19-101.6 deviate as a positive correlation exists between Cr_2O_3 and MgO. The MgO content in all the feldspathic pyroxenite-hosted chromites also increases with increasing Al_2O_3 and decreases with increasing FeO and Fe_2O_3. In contrast, the Cr_2O_3 content in crystals hosted by feldspathic harzburgite

displays a positive trend with MgO and Al_2O_3 while their TiO_2 content decreases. The MgO content in these crystals also decreases with increasing FeO and Fe_2O_3, but increases with increasing Al_2O_3 in some chromites and decreases with increasing Al_2O_3 in samples adjacent to the footwall contact. The concentration of MgO and Al_2O_3 in silicate-hosted chromites is higher because of cation exchange (Mg^{2+} and Al^{3+}) that may have occurred between the silicate melt and previously crystallised chromites.

The chemistry of chromites is also influenced by the associated silicate minerals of the host rocks, chromites occur as cumulus inclusions within olivine (in feldspathic harzburgite samples), orthopyroxene, clinopyroxene, plagioclase and seldom within phlogopite, quartz and BMS. The chromite crystals with high Cr# and Mg# are closest to the primary composition as it was suggested for the similar Platreef chromite by Yudovskaya and Kinnaird (2010). An increase in the Cr# in samples is a result of the decrease in Al content during alteration processes, whereas, low Mg# in chromite resulted from ion exchange reactions between chromites and associated silicate constituents of the host rock (Holwell & McDonald, 2006).

The chromites with high Cr# but low Mg# contents may have been altered by either subsolidus re-equilibration that took place between the chromites and the adjacent silicate minerals such as pyroxenes and olivine or due to phlogopite replacement. The re-equilibration processes result in an increase in Cr, Fe and Ti and a decrease in Mg and Al. The Mg and Al contents in chromite decrease due to their remobilization from the chromites into the surrounding silicates, this in turn resulted in the increase of the Cr# and decrease of the Mg#. Interaction of the chromites with sulphide-rich melt (Fig 8-4A & C) initiated iron exchange between the two phases, resulting in chromites with high Fe and low Ti contents as well as a decrease in the Mg#. Where chromites have been corroded by phlogopite (Fig 8-4B-F), there is an increase in Cr and Ti due to transfer of Mg and Al from chromite into phlogopite, resulting in a high Cr# and lower Mg#.

Chromite crystals with elevated Cr# and very low Mg# have undergone alteration and phlogopite replacement. This feature is observed in Uitloop farm lithologies as chromite crystals that have been corroded by phlogopite, have increased in Cr_2O_3 and TiO_2 due to the removal of Al and Mg, resulting in a higher Cr# with lower Mg#.

This study has shown that majority of chromite crystals in the feldspathic pyroxenite samples are closer to the original cumulus compositions (e.g. Z19-137.5) with moderate Mg# and Cr#, whereas some chromites with elevated Cr# and very low Mg# (e.g. sample Z19-100.35) changed their primary composition as a result of reactions with the intercumulus silicates through post-crystallisation re-

equilibration (Fig 8-10). In general, the Uitloop Feldspathic harzburgite-hosted accessory chromite is notably Cr and Mg-poorer with respect to chromite from feldspathic pyroxenite-hosted disseminated seams (Fig 8-20) that is consistent with the similar tendency in the Platreef chromite chemistry (Yudovskaya & Kinnaird, 2010). The relatively modest Ti in the Uitloop chromite seems to reflect a relatively Ti-depleted composition of Uitloop melts whereas the remarkably low Mg content in feldspathic harzburgite-hosted chromite is resulted from superimposed fluid induced alteration that affected both chromite chemistry and textures. The modal proportion of chromite is higher in feldspathic harzburgite compared to their abundance in feldspathic pyroxenite which is consistent with up to more than 10 wt.% Cr in the sample Z20-53.7 according to the analytical data (Appendix D: table 12). The chromite crystals hosted by feldspathic pyroxenites in borehole Z19 generally get increasingly closer to primary composition with increasing depth. The opposite is observed in the feldspathic harzburgite lithologies in borehole Z20 where the chromites high up in the stratigraphy are closer to the original cumulus compositions (Fig 8-10).

The composition of the studied chromites is generally similar to the majority of the Platreef chromite data and is distinctly different to the composition of the LZ chromite as documented for Grasvally (Hulbert and von Gruenewaldt, 1986). The LZ chromites have the highest Cr content in the Bushveld Complex and they are chemically different to the Uitloop chromite in terms of Cr and Mg content that suggest different compositions of their parental melts. The Uitloop chromites are generally more altered in comparison to the uCZ chromites and their textural and chemical transformations match those described for the Platreef disseminated chromites. The chemistry of the feldspathic pyroxenite-hosted Uitloop chromites correlate better with data from the pyroxenite-hosted UG-2 and the Merensky Reef whereas feldspathic harzburgite-hosted chromite compositions do not seem to have analogues in the eastern and western limbs.

8.7.2 OLIVINE

The olivines from ultramafic rocks both from the LZ and Platreef are commonly Ca-poor with very low Cr, Al, and Ti contents, these olivine crystals are also enriched in Ni, Zn, Co, and Li (Yudovskaya et al., 2013). Olivine crystals from the southwestern portion of the Uitloop farm have an Mg# range overlapping with that of Lower Zone and the Platreef olivines at neighbouring Turfspruit and Sandsloot farms.

The olivine crystals have a higher NiO content (0.29 – 0.34 wt.%) in comparison with the Lower Zone olivine crystals from Grasvally and Turfspruit farms as well as Platreef olivines from Sandsloot and Turfspruit unmineralized rocks (Fig 8-23). However, the olivine crystals from the Merensky Reef, high-

grade PGE reefs of the Platreef as well as the Lower Zone at Sandsloot have comparable and even higher NiO concentrations (up to 0.6 wt.% NiO) than those of the Uitloop farm (Fig 8-23). Therefore, the high Mg# (83 – 84) and high Ni content of analysed olivine suggest that the feldspathic harzburgite sample Z20-66.5 may represent a component of a mineralised chromitiferous reef at Uitloop. This part can be provisionally correlated with harzburgitic reef lithologies at the top of the Platreef at Turfspruit that contains olivine Mg# 84 with 0.34 – 0.6 wt.% Ni (Yudovskaya et al., 2017). The Turfspruit high grade PGE reef is believed to be a stratigraphic analogue of the Merensky Reef in the northern limb (Grobler et al., 2018). This preliminary conclusion is supported by the elevated PGE abundances of the chromitiferous interval according to the company data (Fig 4-19 & 4-20). A high degree of superimposed alteration that affected silicates, sulphides and chromite possibly diluted the initial base metal and PGE grades.

The MnO concentrations within olivine crystals are a measure of the degree of magma fractionation (Hulbert, 1983; Yudovskaya et al., 2013). The most primitive Mg# corresponds to the lowest MnO content, as is the case with the Lower Zone olivines at Grasvally. The elevated Ti and Cr in the analyses of the Uitloop olivine are derived from exsolution spinel lamellae, the occurrence of which, however, reflects a primary Cr-Ti-enriched nature of the olivine matching that of the Lower Zone olivine.

CHAPTER 9

DISCUSSION AND CONCLUSION

9.1 DISCUSSION

This study has investigated the mineralogical and geochemical characteristics of the unexposed magmatic sequence intersected by two boreholes (Z19 and Z20) in the southwestern part of the Uitloop farm, with the intention of determining whether the intrusion here is of Platreef or Lower Zone affinity. The footwall and hanging wall to the RLS lithologies consists of shales and dolomites that have been metamorphosed to hornfels and calcsilicates. Previous studies have noted the significant influence that the footwall variation has on the lithologies and mineralisation of the Platreef along strike (Harris & Chaumba, 2001; Armitage et al., 2002; Hutchinson & Kinnaird, 2005). Therefore, the geology of the Uitloop farm has been compared to portions of the Platreef which are underlain by similar footwall rocks, such as at Macalacaskop and Turfspruit in the southern sector (Kinnaird et al., 2005; Yudovskaya et al., 2013; Kekana, 2014; Grobler et al., 2018) as well as at Tweefontein Hill and Tweefontein north in the central sector (Nex, 2005; McCutcheon, 2005).

9.1.1 STRATIGRAPHY

The RLS lithologies in the southwestern portion of the Uitloop farm are bound by the Duitschland Formation lithologies that have undergone contact metamorphism. The footwall consists of calcsilicate with thick magnetite bands as well as varieties of hornfels units (cordierite-quartz hornfels, phlogopite-biotite hornfels and pyroxene-plagioclase hornfels). The hanging wall to the RLS lithologies in the study area also consist of metamorphosed dolomite of the Duitschland Formation. Minor finger-like intrusions of orthopyroxenite, consisting entirely of granular orthopyroxenite, are observed within hornfels layers in borehole Z20 and are provisionally assigned to the Marginal Zone sills. The RLS lithologies at southwestern part of the Uitloop farm consist of predominantly feldspathic harzburgite and feldspathic pyroxenite with minor pyroxenite, melanorite, leuconorite, gabbro, gabbronorite and parapyroxenite with grain sizes ranging from medium- to very coarse-grained.

Whole-rock trace element data indicates a positive correlation between Cr and MgO, with the highest Cr concentration over 10 % Cr_2O_3 recorded in feldspathic harzburgite, the Cr/MgO ratios in Z19 range between 147 – 3854 for feldspathic pyroxenite. The Cr/MgO ratios in Z20 lithologies range from 136 – 4093 in feldspathic harzburgites and 62 – 482 for feldspathic pyroxenite rocks. In both boreholes; the Cr/MgO ratio decreases with increasing depth, this is mostly related to the major lithological

changes as ultramafic rock are predominantly located at the top of the sequences whereas the basal parts are composed of norite. Within the set of pyroxenite rocks, some degree of Cr depletion downwards can be related to the contamination of magma during country rock assimilation.

The noritic rocks in the study area, except the thin norite unit at 67 – 81 m intervals in Z19, generally contain low concentrations of mafic components (Mg, Ti, Cr, Mn and Fe) with elevated feldspathic components (Na, K, Ca and Al). A parapyroxenite sample analysed from Z19 has elevated mafic components, except MgO and Cr_2O_3 and very low feldspathic components except Al that reflect a predominance of clinopyroxene in the composition. The parapyroxenite also recorded very high values for incompatible trace elements (e.g. Sr, Ba, etc) and very low compatible trace element concentrations, particularly Ni and Cr.

Lithologies at Macalacaskop and Turfspruit farms consist of mainly feldspathic pyroxenites with intercalated norites, melanorites, peridotites, serpentinites and gabbronorites, there are also micronorite units ascribed to the Marginal Zone. Xenoliths in the lithologies of Macalacaskop consist of quartzite and hornfels, whereas calcsilicate xenoliths and large rafts of hornfels are common at Turfspruit (Kinnaird, 2005; Kinnaird et al., 2005; Hutchinson & Kinnaird, 2005). The Platreef on Tweefontein is composed mainly of pyroxenites with minor norites and basal micronorites (Viljoen & Schurmann, 1998; Nex, 2005; McCutcheon, 2012). The highest Ni and Cu concentrations at Turfspruit, Macalacaskop, Tweefontein Hill and Tweefontein north farms are recorded within contaminated rocks adjacent to the footwall contact, as is the case at the southwestern part of the Uitloop farm, these elements are indicative of concentration of sulphides. However, the thick PGE low-sulphide reef-style mineralisation occurs in feldspathic harzburgite and feldspathic pyroxenite at the top of the Platreef sequence at Turfspruit at depth. The thickness of these mineralised reefs reaches 90 m with around 20 m on average that is more comparable with the 15 m thick feldspathic harzburgite in Z19, however it is much higher than the thickness of the feldspathic harzburgite layers in Z20, which does not exceed 5 m. The multiple narrow intervals of ultramafic rocks in Z20 may testify to a cross-cutting finger-like morphology of the harzburgitic body.

The thick noritic intervals with minor pyroxenite in Z20 could correspond to the so-called Footwall Unit or Noritic Cycles on Turfspruit (Grobler et al., 2018). However, the borehole logs do not conform to a cyclic nature of the intercalation and this provisional correlation should be taken with care as the position of the Uitloop sequence is rather indefinite. In the other Platreef areas the stratigraphy is defined by the obvious upper Platreef in contact with of the Main Zone, however, in the southwestern portion of the Uitloop farm, no Main Zone lithologies are encountered. It is concluded in this report that the studied body represents an offshoot of Platreef-affinity magma between metasedimentary

units in a similar manner to that of the Lower Zone offshoots nearby that are described by van der Merwe (1978) and McDonald and Holwell (2007). By definition, the Platreef is overlain by the Main Zone, therefore, the studied body does not match that definition and should be considered as a separate offshoot intrusion of Platreef magma.

9.1.2 BASE METAL SULPHIDE OCCURRENCE

Base metal sulphides occur throughout the stratigraphic sequence on the southwestern portion of the Uitloop farm and consists mainly of pyrrhotite and pentlandite with minor chalcopyrite and pyrite. The sulphide textures vary from finely disseminated to blebby and net-textured towards the footwall contact, the amount of sulphide increases from top to bottom. Sulphide occurrence in the Platreef also increase significantly with increasing depth, with massive and submassive sulphides observed towards the base and within the footwall rocks. The occurrence of contact-style sulphide mineralisation at the base of the Platreef is attributed to addition of external sulphur caused by country rock assimilation (Sharman-Harris et al., 2005; Holwell & McDonald, 2006; Maier et al., 2008).

The primary sulphides display a fractionated texture where the sulphide droplets consist of a pyrrhotite core with pentlandite and chalcopyrite generally confined to the margins, with flame exsolution of pentlandite in pyrrhotite is common. Platinum-group minerals occur at the margins of the sulphide blebs that is consistent with later PGM crystallization from Cu-rich residual melts. In some cases, pyrrhotite and chalcopyrite droplets are replaced by needle-like amphibole (tremolite) intergrowths or later magnetite rims. The pyrrhotite is a predominant sulphide of contact (marginal) style mineralisation within rocks adjacent to the footwall contact occurring as pyrrhotite bands, veins and rims around plagioclase and orthopyroxene crystals likely as a result of late stage hydrothermal fluid activity. Pyrite in these lithologies is an alteration product of pyrrhotite.

Although Cu and Ni are highly compatible with sulphides, Cu is a more useful indicator of sulphide mineralisation than Ni as Ni also enters silicate and spinels. Whole-rock trace element data shows an increase in Ni (up to 3852 ppm in Z19 and 12437 ppm Z20) and Cu (up to 1860 ppm in Z19 and 6612 ppm in Z20) with increasing depth. The increase in Ni and Cu with depth is most likely a result of their extraction into immiscible sulphides from the mafic/ultramafic melts that reach sulphide saturation due to the assimilation of external sulphur.

9.1.3 CHROMITE MINERALISATION

Chromite from the southwestern portion of the Uitloop farm is associated with feldspathic pyroxenite and feldspathic harzburgite lithologies, mainly as accessory disseminations although also forming zones of dense disseminations and disturbed seams of disseminated chromite. A thin chromitite stringer is also observed at the top of the sequence in borehole Z20. The chromites occur as euhedral, subhedral and rounded cumulus crystals within olivine, pyroxene, plagioclase and occasionally phlogopite and quartz. The euhedral chromite crystals generally lack inclusions; however, needle-like rutile exsolution lamellae are observed in some crystals, particularly within the feldspathic pyroxenite samples. Anhedral chromite crystals have amoeboidal, irregular and sieve-textured morphologies with typical fish-hooks intergrowths into adjacent silicates indicating postcumulus growth. The anhedral chromite is commonly corroded by secondary phlogopite and replaced by magnetite, resulting in relics with irregular boundaries.

Electron microprobe analysis was used to investigate the chemistry of individual chromite crystals, the results revealed that the composition of chromites from the southwestern portion of the Uitloop farm lithologies are variably influenced by host rocks and associated minerals. Chromite crystals hosted by feldspathic pyroxenites have a higher Cr_2O_3 content (up to 46.96 wt.% Cr_2O_3) than those hosted by feldspathic harzburgites (up to 35.66 wt.% Cr_2O_3). In both boreholes Z19 and Z20, the plagioclase-hosted chromite crystals (and clinopyroxene-hosted chromites in Z19 feldspathic pyroxenites) have higher Cr_2O_3 content (up to 46.96 wt.% Cr_2O_3) than olivine- and orthopyroxene hosted chromites. This variability reflects re-equilibration due to interaction of the chromite crystals with intercumulus silicate melt and the surrounding mafic minerals (olivine and pyroxene), resulting in ion exchange. Chemical re-equilibration of chromite composition is widely recognised since the earlier studies (Cameron,1975; Roeder & Campbell, 1985) and its degree is commonly much higher in disseminated chromite compared to the massive ones (Naldrett et al., 2009). However, chromite with coupled highest Mg and Cr content should have a composition most close to the primary magmatic one. Using this approach, it can be concluded that Uitloop primary chromite contains roughly up to 46.96 wt.% Cr_2O_3, 6.76 wt.% MgO and 1.9 wt.% TiO_2. These range of composition fall into the compositional field of the Critical Zone chromite as the Lower Zone chromites are distinguished by much higher Cr (up to 55.55 wt.% Cr_2O_3) and Mg (up to 13.98 wt.% MgO) contents (Hulbert & Gruenewaldt, 1985).

The Cr_2O_3 content of chromite crystals within feldspathic harzburgite lithologies of the southwestern portion of the Uitloop farm is comparable to chromite from the Platreef on Macalacaskop, Zwartfontein and Sandsloot (SS277) but significantly lower than chromites from the Merensky Reef and UG-2 chromitite layer (Fig 8-20). In contrast, chromite crystals within feldspathic pyroxenite

samples have similar Cr_2O_3 concentrations to chromites from the Merensky Reef and UG-2 chromitite layer as well as the Platreef chromites (Fig 8-20), particularly from Turfspruit, Vaalkop, Zwartfontein, Sandsloot (SS266) and Overysel (Fig 8-18). The chromites from the studied area on the Uitloop farm also have MgO and TiO_2 concentrations that are more or less similar to those of the Platreef (Fig 8-18). Essentially, the studied chromite crystals from the Uitloop farm, like the Platreef chromites in general, have elevated Ti and lower Mg compared to Merensky Reef and UG-2 chromites.

9.2 CONCLUSION

The studied magmatic sequence intersected by Z19 and Z20 boreholes in the southwestern part of the Uitloop farm is more similar to the Platreef than to the LZ. The Uitloop sequence is composed of feldspathic pyroxenite, feldspathic harzburgite, pyroxenite, norite, gabbro, gabbronorite and leuconorite. The observed lithological heterogeneity with the major presence of the cumulus plagioclase have much in common with the characteristics of the Critical Zone. These lithologies are bound by metasedimentary sequences of the Duitschland Formation including calcsilicate with thick magnetite bands as well as varieties of hornfels (cordierite-quartz hornfels, phlogopite-biotite hornfels and pyroxene-plagioclase hornfels). The presence of parapyroxenite common within the magmatic sequence and in the footwall units and the style of contamination resembles that of the Platreef. The high degree of alteration is consistent with a high fluid flux derived from contact-metamorphosed sediments above and below the relatively thin intrusion.

The primary magmatic sulphides form two styles of PGE-Cu-Ni mineralisation: 1) the reef-style horizon that is associated with irregular or disturbed chromitites at the top of the intersection in borehole Z20 (Fig 4-20) and 2) contact-style mineralisation rich in sulphides (with high Ni and Cu contents and modest PGE) that is confined to the lower part of the magmatic sequence and to the footwall (Fig 4-19).

Like the Platreef, the high sulphide content observed within lithologies at the southwestern part of the Uitloop farm can be attributed to magma-country rock interaction. This sulphide mineralisation is characterised by a high crustal component which is expressed by an increase in incompatible trace elements which decrease upwards, thus indicating that contamination decreases upwards. The Cr/MgO ratios (>100) as well as the REE concentrations and patterns of their fractionation suggest that the mafic/ultramafic rocks from the southwestern part of the Uitloop farm formed from magmas of Platreef/Critical Zone affinity rather than Lower Zone primitive magmas.

Chromite occurs as accessory disseminations, disturbed seams of disseminated chromite and a thin stringer that are hosted by the layers of feldspathic pyroxenite and feldspathic harzburgite. The similar ultramafic rocks with intercumulus plagioclase host irregular chromitite seams and stringers in the Platreef on Turfspruit and Zwartfontein north of the studied area. The composition of chromite on the southwestern part of the Uitloop farm is distinguished by lower Mg# and higher Cr# compared to the Merensky Reef chromites, however, the composition of Uitloop chromites closely matches that of Platreef chromites. The chromite phenocrysts underwent significant re-equilibration and ion exchange with the intercumulus liquid and host silicates that resulted in wide variations of their chemical composition and the occurrence of the specific textures of postcumulus growth.

It can be envisaged that the studied magmatic sequence represents a Platreef offshoot that was formed by multiple injections or via coalescence of several sills emplaced into the metasedimentary succession. The mechanism and direction of the emplacement were likely similar to that of the Uitloop II Lower Zone offshoot nearby.

REFERENCES

Armitage, P. E. B., McDonald, I., Edwards, S. J. and Manby, G. M. 2002. Platinum-group element mineralisation in the Platreef and calc-silicate footwall at Sandsloot, Potgietersrus District, South Africa. Applied Earth Science: Transactions of the Institute of Mining and Metallurgy, 111, 36 – 45.

Barnes, S. J. and Roeder, P. L. 2001. The range of spinel compositions in terrestrial mafic and ultramafic rocks. Journal of Petrology, 42:12, 2279 – 2302.

Barnes, S. J., Holwell, D. A., and Le Vaillant, M. 2017. Magmatic sulphide ore deposits. Elements, 13, 89 – 95

Barnes, S-J. and Ripley, E. M. 2016. Highly siderophile and strongly chalcophile elements in magmatic ore deposits. Reviews in Mineralogy and Geochemistry, 81, 725-774.

Buchanan, D. L., Nolan, J., Suddaby, P., Rouse, J. E., Viljoen, M. J. and Davenport, J. W. J. 1981. The genesis of sulphide mineralisation in a portion of the Potgietersrus limb of the Bushveld complex. Economic Geology, 76, 3, 568 – 579.

Cameron, E.N. 1975. Postcumulus and subsolidus equilibration of chromite and coexisting silicates in the eastern Bushveld Complex. Geochim Cosmochim Acta, 39, 1021–1033

Cameron, E. N. 1977. Chromite in the central sector of the eastern Bushveld Complex, South Africa. American Mineralogist, 62, 1082 – 1096.

Cameron, E. N. 1978. The Lower Zone of the eastern Bushveld Complex in the Olifants River trough. Journal of Petrology, 19, 437 – 462.

Cameron, E. N. 1982. The upper Critical Zone of the eastern Bushveld Complex – precursor of the Merensky Reef. Economic Geology, 77, 1307 – 1327.

Cawthorn, R. G., Barton, J.R. and Viljoen, M.J. 1985. Interaction of floor rocks with the Platreef on Overysel, Potgietersrus, Northern Transvaal. Economic Geology, 80, 988 – 1006.

Cawthorn, R. G. and Walraven, F. 1998. Emplacement and crystallization time for the Bushveld Complex. Journal of Petrology, 39, 9, 1669 – 1687.

Cawthorn, R. G. 1996. Re-evaluation of magma compositions and processes in the Upper critical zone of the Bushveld complex. Mineralogical magazine, 60, 131 – 148.

Cawthorn, R. G. 1999. Platinum-group element mineralisation in the Bushveld Complex – a critical reassessment of geochemical models. South African Journal of Geology, 102, 268 – 281.

Cawthorn, R. G., Merkle, R. and Viljoen, M. J. 2002. Platinum-group Element Deposits in the Bushveld Complex, South Africa. In: Cabri, L.J. ed. The geology, geochemistry, mineralogy and mineral beneficiation of platinum-group elements. Vol. 54 (Special). Canadian Institute of Mining, Metallurgy and Petroleum, p. 582.

Clarke, B. M., Uken, R. and Reinhardt, J. 2009a. Structural and compositional constraints on the emplacement of the Bushveld Complex, South Africa. Lithos, 111, 21 – 36.

Clarke, B.M., Uken, R. and Reinhardt, J. 2009b. The geometry and emplacement mechanisms of a Bushveld Complex peridotite body. South African Journal of Geology, 112, 141 – 162.

Cousins, C. A. and Feringa, G. 1964. The chromite deposits of the western belt of the Bushveld Complex. In: The geology of some ore deposits in southern Africa. Ed: S.H. Haughton. Spec. Pub. Geol. Soc. S. Afr, 2, 183 – 202.

Croll, R., Clarke, B., Hall, M., and Sexton. J. 2012. Preliminary Economic Assessment for the Zebediela Nickel Project. Prepared by MSA Geoservices (Pty) Ltd., on behalf of: Umnex Minerals Limpopo (Pty) Ltd.

Deer, W. A., Howie, R.A. and Zussman, J. 1992. An introduction to the Rock-Forming Minerals. Pearson Education Limited, England.

Du Toit, A. L. 1926. The Bushveld Igneous Complex and the associated rocks. London: Oliver & Boyd, 136 – 150.

Eales, H. V., Botha, W.J., Hatting, P.J., Klerk, W.J. de, Maier, W.D., and Odgers, A.T.R. 1993. "The mafic rocks of the Bushveld Complex: a review of emplacement and crystallisation history, and mineralisation, in the light of recent data." Journal of African Earth Sciences, 16, 1/2, 121 – 142.

Eales, H. V. and Cawthorn, R. G. 1996. The Bushveld Complex. In: Cawthorn, R.G. ed. Layered Intrusions. Elsevier Science, 181 – 230.

Eales, H. V. 2000. Implications of the chromium budget of the western limb of the Bushveld Complex. S.A.J.G. 103, 141 – 150.

Eales, H. V., and Costin, G. 2012. Crustally contaminated komatiite: primary source of the chromitites and Marginal, Lower, and Critical zone magmas in a staging chamber beneath the Bushveld Complex: Economic Geology, 107, 645 – 665.

Finn, C. A., Bedrosian, P. A., Cole, J. C., Khoza, T. D., Webb, S. J., Jul. 2015. Mapping the 3D extent of the Northern Lobe of the Bushveld layered mafic intrusion from geophysical data. Precambrian Research, 268, 279–294.

Friese, A. and Chunnet, G. 2004. Tectono-magmatic igneous development of the northern limb of the Bushveld Igneous Complex with special reference to the mining area of Potgietersrus Platinum Limited. Geoscience Africa, University of the Witwatersrand, Johannesburg, South Africa, 209 – 210.

Gain, S. B. and Mostert, A. B. 1982. The geological setting of the platinoid and base metal sulphide mineralisation in the Platreef of the Bushveld complex in Drenthe, north of Potgietersrus. Economic Geology, 77:6, 1395 – 1404.

Grobler, D. F., Brits, J. A. N., Maier, W. D., and Crossingham, A. 2018. Litho- and Chemostratigraphy of the Flatreef PGE deposit, northern limb Bushveld Complex. Mineralium Deposita, 54:1, 3 – 28.

Harney, D. M. W. and von Gruenewaldt, G. 1995. Ore-forming processes in the upper part of the Bushveld Complex, South Africa. Journal of African Earth Sciences, 20, 77 – 89.

Harris, C. and Chaumba, J. B. 2001. Crustal contamination and fluid-rock interaction during the formation of the Platreef, northern limb of the Bushveld Complex, South Africa. Journal of Petrology 42:7, 1321 – 1347.

Hatton, C.J. and Von Gruenewaldt, G. 1987. The geological setting and petrogenesis of the Bushveld chromitite layers. In Stowe, C.W. (Ed), Evolution of chromium ore fields. Van Nostrand Reinhold, New York. 109 – 143.

Hofmann, A.W. 1988. Chemical differentiation of the Earth: the relationship between mantle, continental crust and oceanic crust: Earth and Planetary Science Letters, 90, 297 – 314.

Holwell, D. A., Armitage, P. E. B. McDonald, I. 2005. Observations on the relationship between the Platreef and its hanging wall. Transaction, Institute of mining and metallurgy B, 114, 199 – 207.

Holwell, D. A., McDonald, I. and Armitage, P. E. B. 2006. Platinum-group mineral assemblages in the Platreef at the Sandsloot Mine, northern Bushveld Complex, South Africa. Mineralogical Magazine 70, 1, 83 – 101.

Holwell, D. A. and McDonald, I. 2006. Petrology, geochemistry and mechanisms determining the distribution of platinum-group element and base metal sulphide mineralization in the Platreef at Overysel, northern Bushveld Complex, South Africa. Mineralium deposita, 41, 575 – 598.

Holwell. D. A. and Jordaan, A. 2006. Three-dimensional mapping of the Platreef at the Zwartfontein South mine: implications for timing of magmatic events in the northern Limb of the Bushveld Complex, South Africa. Appl.Earth Sci. (Trans.Inst. Min. Metall.B.), 115, 41 – 48.

Holwell, D. and McDonald, I. 2007. Distribution of platinum-group elements in the Platreef at Overysel, northern Bushveld Complex: a combined PGM and LA-ICP-MS study. Contributions to Mineralogy and Petrology, 154, 2, 171 – 190.

Holwell, D. A. and McDonald, I. 2010. A review of the behaviour of platinum group elements within natural magmatic sulphide ore systems. Platinum Metals Review, 54, 1, 26 – 36.

Hulbert, L. J. and von Gruenewaldt, G. 1982. Nickel, copper, and platinum mineralisation in the lower zone of the Bushveld Complex, south of Potgietersrus. Economic Geology, 77, 6, 1296 – 1306.

Hulbert, L. J. 1983. A petrological investigation of the Rustenburg layered suite and associated mineralisation south of Potgietersrus. Ph.D. thesis, University of Pretoria, 511p.

Hulbert, L. J. and von Gruenewaldt, G. 1985. Textural and compositional features of chromite in the lower and critical zones of the Bushveld complex south of Potgietersrus. Economic Geology 80, 4, 872 – 895.

Hulbert, L. J. and von Gruenewaldt, G. 1986. The structure of the upper and lower chromitite layers on the farms Grasvally and Zoetveld, south of Potgietersrus. In: Anhaeusser, C.R. and Maske, S. eds. Mineral Deposits of Southern Africa. Vol. 2. Johannesburg: Geological Society of Southern Africa, 1237 – 1249.

Hutchinson, D., Kinnaird, J. A. and Schurmann, L. W. 2004. Complex, multistage mineralization history in the southern sector of the Platreef, Bushveld Complex, RSA. In: Geoscience Africa 2004. University of Witwatersrand, Johannesburg. 293 – 294.

Hutchinson, D. and Kinnaird, J. A. 2005. Complex multistage genesis for the Ni-Cu-PGE mineralisation in the southern region of the Platreef, Bushveld Complex, South Africa. Applied Earth Science: Transactions of the Institute of Mining and Metallurgy, 114, 208 – 224.

Huthmann. F. M., Yudovskaya. M. A., Frei. D, Kinnaird. J. A. 2016. Geochronological evidence for an extension of the northern lobe of the Bushveld Complex, Limpopo Province, South Africa. Precambrian research, 280, 61 – 75.

Irvine, T. N. 1975. Crystallization sequences in the Muskox intrusion and other layered intrusions--II. Origin of chromitite layers and similar deposits of other magmatic ores. Geochimica et Cosmochimica Acta, 39, 6-7, 991 – 1020.

Irvine, T. N. 1977. Origin of chromitite layers in the Muskox intrusion and other stratiform intrusions: A new interpretation. Geology, 5, 5, 273 – 277.

Kekana, S. M. 2014. An investigation of mineralisation controls in the upper section of the Platreef in the southern sector, on Turfspruit, northern Limb, Bushveld Complex, South Africa. MSc thesis, University of the Witwatersrand, 128p.

Kinloch, E. D. 1982. Regional trends in the platinum-group mineralogy of the critical zone of the Bushveld Complex, South Africa. Economic Geology, 77, 6, 1328 – 1347.

Kinnaird, J. A., Kruger, F. J., Nex, P. A. M. and Cawthorn, R. G. 2002. Chromitite formation - a key to understanding processes of platinum enrichment. Applied Earth Science: Transactions of the Institute of Mining and Metallurgy, Section B 111, 23 – 35.

Kinnaird, J. A. 2005. Geochemical evidence for multiphase emplacement in the southern Platreef. Applied Earth Science: Transactions of the Institute of Mining and Metallurgy, Section B 114, 225 – 242.

Kinnaird, J. A., Hutchinson, D., Schurmann, L., Nex, P. A. M. and de Lange, R. 2005. Petrology and mineralisation of the southern Platreef: northern limb of the Bushveld Complex, South Africa. Mineralium Deposita 40, 5, 576 – 597.

Kinnaird, J.A. 2005. The Bushveld Large Igneous Province. School of Geosciences, University of the Witwatersrand.

Kinnaird, J.A. & McDonald, I. 2005. An introduction to mineralisation in the northern limb of the Bushveld Complex. Applied Earth Science, (Transactions of the Institute of Mining and Metallurgy B) 114, 194 – 198.

Kinnaird, J. A., Yudovskaya, M., McCreesh, M., Huthmann, F. and Botha, T. J. 2017. The Waterberg Platinum Group Element deposit: Atypical mineralization in mafic-ultramafic rocks of the Bushveld Complex, South Africa. Economic geology, 112, 1376 – 1394.

Kinnaird, J.A. and Iain McDonald. I. 2018. The northern limb of the Bushveld Complex: A New Economic Frontier. Society of Economic Geologists Special Publications, 21, 157 – 176

Kruger, F.J. 1990. The stratigraphy of the Bushveld Complex: a reappraisal and the relocation of the Main Zone boundaries. South African Journal of Geology, v. 93, 376-381.

Kruger, F. 2005. Filling the Bushveld Complex magma chamber: lateral expansion, roof and floor interaction, magmatic unconformities, and the formation of giant chromitite, PGE and Ti–V-magnetitite deposits. Mineralium Deposita, 40, 451 – 472.

Latypov, R., Chistyakova, S., Page, A., and Hornsey, R. 2015. Field evidence for the in-situ crystallization of the Merensky reef: Journal of Petrology, 56, 2341 – 2372.

Lee, C. A. 1996. A review of mineralisation in the Bushveld Complex and some other layered mafic intrusions. In: Cawthorn, R.G. ed. Layered Intrusions. Amsterdam: Elsevier Science, 103 – 146.

Li C, Barnes S-J, Makovicky E, Rose-Hansen J, Makovicky M. 1996. Partitioning of nickel, copper, iridium, rhenium, platinum, and palladium between monosulfide solid solution and sulfide liquid: effects of composition and temperature. Geochimica et Cosmochimica Acta, 60, 1231-1238

Li, C., Ripley, E., Sarkar, A., Shin, D. and Maier, W. 2005. Origin of phlogopite-orthopyroxene inclusions in chromites from the Merensky Reef of the Bushveld Complex, South Africa. Contributions to Mineralogy and Petrology, 150, 1, 119 – 130.

Lowman, G. 2007. Progress Report 1: Uitloop Platinum, Base Metal Project. Prepared by MSA Geoservices (Pty) Ltd. on behalf of: Lesego Platinum Mining (Pty) Ltd.

Maier, W.D., de Klerk, L., Blaine, J., Manyeruke, T., Barnes, S.J., Stevens, M. V. A., and Mavrogenes, J. A. 2008a. Petrogenesis of contact-style PGE mineralisation in the northern lobe of the Bushveld Complex: comparison of data from the farms Rooipoort, Townlands, Drenthe and Nonnenwerth. Miner Deposita, 43, 255 – 280.

Maier, W. and Barnes, S.-J. 2008b. Platinum-group elements in the UG1 and UG2 chromitites, and the Bastard reef, at Impala platinum mine, western Bushveld Complex, South Africa: Evidence for late magmatic cumulate instability and reef constitution. South African Journal of Geology, 111, 2-3, 159 – 176.

Maier, W.D. and Groves, D.I. 2011. Temporal and spatial controls on the formation of magmatic PGE and Ni-Cu deposits. Min Deposita, 46, 841 – 857.

Maier, W.D., & Barnes, S.J., and Grooves, D.I. 2013. The Bushveld Complex, South Africa: formation of platinum, palladium, chrome- and vanadium-rich layers via hydrodynamic sorting of a mobilized cumulate slurry in a large, relatively slowly cooling, subsiding magma chamber. Miner deposita, 48, 1 – 56.

Maier. W. D., Prevec, S. A., Scoates, J. S., Wall, C. J., Barnes, S.-J. & Gomwe. T. 2017. The Uitkomst intrusion and Nkomati Ni-Cu-Cr-PGE deposit, South Africa: trace element geochemistry, Nd isotopes and high-precision geochronology. Miner Deposita

Manyeruke, T. D., Maier, W. D. and Barnes, S.-J. 2005. Major and trace element geochemistry of the Platreef on the farm Townlands, northern Bushveld Complex. South African Journal of Geology, 108, 3, 381 – 396.

MCcreesh, M. J. G. 2013. A study of the Main Zone-Upper Zone boundary beneath a thick succession of Waterberg sediments in the far north of the northern limb of the Bushveld Complex. Honours degree thesis. University if the Witwatersrand. 150p.

McCreesh, M. J. G., Yudovskaya, M. A., Kinnaird, J. A. and Reinke. C. 2018. Platinum-group minerals of the F and T zones, Waterberg Project, far Northern Bushveld Complex: implication for the formation of the PGE mineralization. Mineralogical magazine, 82, 3, 539 – 575.

McCutcheon, S. 2012. Platinum-group mineral assemblages in the Platreef on Tweefontein, northern Bushveld Complex, South Africa. MSc, University of the Witwatersrand, 192p.

McDonald, I., Holwell, D.A., Armitage, P.E.B. 2005. Geochemistry and mineralogy of the Platreef and 'Critical Zone' of the northern lobe of the Bushveld Complex, South Africa: implications for Bushveld stratigraphy and the development of PGE mineralisation. Mineralium Deposita, 40, 5, 526 – 549.

McDonald, I. and Holwell, D. A. 2011. Geology of the northern Bushveld Complex and the setting and genesis of the Platreef Ni-Cu-PGE deposit. In: Li, C. and Ripley, E.M. eds. Reviews in Economic Geology. Economic Geology, 17, 297 – 328.

McLahen, C.H. & De Villiers, J.P.R. 1982. The platinum-group chemistry and mineralogy of the UG-2 chromitite layer of the Bushveld Complex. Economic geology, 77, 1348 – 1366.

Mondal, S. K. and Mathez, E. A. 2007. Origin of the UG2 chromitite layer, Bushveld Complex. Journal of Petrology, 48, 3, 495 – 510.

Naldrett A.J. 2004. Magmatic Sulphide Deposits: Geology, Geochemistry and Exploration, Springer Verlaag, 728p.

Naldrett, A. J., Kinnaird, J. A., Wilson, A., Yudovskaya, M., McQuade, S., Chunnett, G. and Stanley, C. 2009a. Chromite composition and PGE content of Bushveld chromitites: Part 1 the Lower and Middle Groups. Applied Earth Science: Transactions of the Institute of Mining and Metallurgy, Section B 118, 131 – 161.

Naldrett, A. J., Wilson, A., Kinnaird, J. A. and Chunnett, G. 2009b. PGE Tenor and Metal Ratios within and below the Merensky Reef, Bushveld Complex: Implications for its Genesis. Journal of Petrology 50, 4, 625 – 659.

Naldrett, A. J., Wilson, A., Kinnaird, J. A., Yudovskaya, M. and Chunnett, G. 2012. The origin of chromitites and related PGE mineralisation in the Bushveld Complex: new mineralogical and petrological constraints. Mineralium Deposita, 47, 3, 209 – 232.

Nex, P. A. M. 2005. The structural setting of mineralisation on Tweefontein Hill, northern limb of the Bushveld Complex, South Africa. Applied Earth Science: Transactions of the Institute of Mining and Metallurgy, Section B 114, 4, 243 – 251.

Nyama. N., Nex. P. A. M. & Yao. Y. 2005. Preliminary petrological studies of the Platreef on Tweefontein Hill, Bushveld Igneous Complex, South Africa. In: Tormanen T.O & Alapieti, T.T. (eds), 10th International Platinum Symposium, University of Oulu, Ext. Abstracts, 505 – 508.

Penniston-Dorland, S. C., Wing, B. A., Nex, P. A. M., Kinnaird, J. A., Farquhar, J., Brown, M. and Sharman, E. R. 2008. Multiple sulphur isotopes reveal a magmatic origin for the Platreef platinum group element deposit, Bushveld Complex, South Africa. Geology 36, 12, 979 – 982.

Ripley, E. M. and Li, C. 2013. Sulphide Saturation in Mafic Magmas: Is External Sulphur Required for Magmatic Ni-Cu-(PGE) Ore Genesis? Economic Geology, 108, 45 – 58.

Roeder, P. L. and Campbell, I. H. 1985. The effect of postcumulus reactions on composition of chrome-spinels from the Jimberlana intrusion. Journal of Petrology, 26, 763 – 786

Roelofse, F. 2010. Constraints on the magmatic evolution of the Lower Main Zone and Platreef on the northern limb of the Bushveld Complex as inferred from the Moordkopje drill core. PhD, University of the Witwatersrand. 163p.

Sharman, E. R., Penniston-Dorland, S. C., Kinnaird, J. A., Nex, P. A. M., Brown, M. and Wing, B. A. 2013. Primary origin of marginal Ni-Cu-(PGE) mineralisation in layered intrusions: 33S evidence from the Platreef, Bushveld, South Africa. Economic Geology, 108, 2, 365 – 377.

Sharman-Harris, E. R., Kinnaird, J. A., Harris, C. and Horstmann, U. E. 2005. A new look at sulphide mineralisation of the northern limb, Bushveld Complex: A stable isotope study. Applied Earth Science: Transactions of the Institute of Mining and Metallurgy, 114, 4, 252 – 263.

Seabrook, C. L. 2005. The Upper Critical Zone and Lower Main Zone of the eastern Bushveld Complex. Ph.D. thesis, University of the Witwatersrand. 284p.

Schouwstra, R. P., Kinloch, E. D. & Lee, C. A. 2000. A Short Geological Review of the Bushveld Complex. Platinum Metals Rev, 44, 1, 33 – 39.

Schűrmann, L. W., Grabe, P-J. and Steenkamp, C. J. 1998. Chromium. In Wilson, M.G.C. and Anhaeusser, C.R. (eds.), The mineral resources of South Africa: Handbook, Council for Geoscience, 16, 740p.

Spies, L. 2005. The Akanani Platinum Project. In: 2nd Platreef Workshop. Mokopane. Geological Society of South Africa.

Smith, J. W. 2014. The nature and origin of PGE mineralisation in the Rooipoort area, northern Bushveld Complex, South Africa. Ph.D., University of Leicester. 215p.

Van der Merwe, M. J. 1976. The layered sequence of the Potgietersrus limb of the Bushveld Complex. Economic Geology, 71, 7, 1337 – 1351.

Van der Merwe, M. J. 1978. The geology of the basic and ultramafic rocks of the Potgietersrus Limb of the Bushveld Complex. Ph.D., University of the Witwatersrand. 176p.

Van der Merwe, M.J. 2008. The geology and structure of the Rustenburg Layered Suite in the Potgietersrus/Mokopane area of the Bushveld Complex, South Africa. Miner Deposita, 43, 3, 405 – 419.

Vermaak, C.F. 1985. The UG-2layer South Africa's slumbering chromitite giant. Chromium Rev, 5, 9 – 22.

Viljoen, M. J. and Schurmann, L. W. 1998. Platinum group metals. In: Wilson, M.G.C. and Anhaeusser, C.R. eds. The mineral resources of Southern Africa. Council for Geoscience, 532 – 568.

Viljoen, M. 2016. The Bushveld Complex: Host to the world's largest Platinum, Chromium and Vanadium resources. IUGS Episodes, 39, 2, 241 – 268.

von Gruenewaldt, G. 1973. The Main and Upper Zones of the Bushveld Complex in the Roossenekal area, eastern Transvaal. Transactions, Geological Society of South Africa, 76, 207 – 227.

von Gruenewaldt, G., Sharpe, M. R. and Hatton, C. J., 1985. The Bushveld Complex; introduction and review. Economic Geology 80, 4, 803 – 812.

von Gruenewaldt, G., Hulbert, L. J., & Naldrett, A.J. 1989. Contrasting platinum-group element concentration patterns in cumulates of the Bushveld Complex. Mineralium Deposita, 24, 219 – 229.

Vukmanovic. Z., Barnes. S., Reddy, S. M. 2013. Reddy Morphology and microstructure of chromite crystals in chromitites from the Merensky Reef (Bushveld Complex, South Africa). Contrib Mineral Petrol, 165, 1031 – 1050.

White, J. A. 1994. The Potgietersrus Prospect - Geology and Exploration History. In: Anhaeusser, C.R. ed. Proceedings of the XVth CMMI Congress. Vol. 3. Johannesburg: South African Institute of Mining and Metallurgy, 173 – 181.

Yudovskaya, M. A. and Kinnaird, J. A. 2010. Chromite in the Platreef (Bushveld Complex, South Africa): occurrence and evolution of its chemical composition. Mineralium Deposita, 43, 4, 1 – 23.

Yudovskaya, M.A., Kinnaird, J.A., Sobolev, A.V., Kuzmin, D.V., McDonald, I., & Wilson, A.H. 2013. Petrogenesis of the Lower Zone Olivine-Rich Cumulates Beneath the Platreef and their correlation with recognized occurrences in the Bushveld Complex. Economic Geology, 108, 1923 – 1952.

Yudovskaya, M.A., Kinnaird, J.A., Grobler, D.F., Costin. G., Abramova, V.D., Dunnett, T., and Barnes. S.-J. 2017. Zonation of Merensky style platinum mineralisation in Turfspruit thick reef facies (northern limb of the Bushveld Complex). Economic Geology, 112, 6, 1333 – 1365

Zeh, A., Ovtcharova, M., Wilson, A.H., & Schaltegger, U. 2015. The Bushveld Complex was emplaced and cooled in less than one million years – results of zirconology, and geotectonic implications. Earth and Planetary Science Letters, 418, 103 – 114.

http://www.cameca.com/products/epma/technique

http://serc.carleton.edu/research_education/geochemsheets/techniques/EPMA.html

APPENDICES

APPENDIX A

METHODOLOGY

1. SAMPLE COLLECTION

The study utilizes diamond drill cores (Z19 & Z20) belonging to Umbono Capital's Zebediela project, which is based on the Uitloop farm in the Limpopo province. Detailed logging of the two boreholes was conducted in April 2018 at the company's core storage facility in Mokopane (Fig 10-1). A hand lens was used to identify different mineral constituents, their crystal sizes and textures as well as to approximate the modal mineralogy of the rocks. These properties were then used to describe and classify the different rock types.



Figure 11-1: Drill core laid out at Umbono storage facility in Mokopane. Limpopo province.

Sampling was done from the top of the cores to the bottom in accordance with the aims of this study. Interesting parts of the core at different depths were sampled, such as; where there was an appearance of chromite and sulphides. Quarter ore samples that were about 10 – 20 cm long, were collected; 17 samples from borehole Z19 and 31 samples from Z20. The rock types encountered at the Uitloop farm are described in detail in Chapter 4 of this report, while the core log sheets, and photographs of these samples are provided in Appendix B.

2. PETROGRAPHIC ANALYSIS

A total of 41 petrographic thin sections were prepared from sampled rocks. These thin sections were analyzed under transmitted light using a petrographic Olympus BX-51 microscope for more accurate identification of the minerals present, mineral textures and modal abundances to ensure proper rock classification. Reflected light microscopy was also used to assess the characteristics of chromite and to identify different sulphide minerals present within the samples. The petrological study of the Uitloop farm lithologies is discussed in Chapter 5. The characteristics such as; mineral textures, modal abundances and alteration intensities are tabulated in Appendix B. Additional microphotographs of the samples under reflected light are also provided in Appendix B.

3. GEOCHEMISTRY

The X-ray fluorescence (XRF) and the Inductively Coupled Plasma-Mass Spectrometry (ICP-MS) techniques were used to for the geochemical investigation of the Uitloop farm samples. Only 32 of the 48 samples were selected for the study, these samples were then crushed and milled to very fine powders from which fusion discs and press pellets were prepared. The samples were sent to the University of the Witwatersrand, Johannesburg, Earth Lab; where they were analyzed for major, minor and trace elements. Data collected is provided in Appendix C.

3.1 SAMPLE PREPARATION FOR XRF AND ICP-MS

Fresh samples were crushed and milled to a very fine powder, approximately -300mesh, this powder was then dried at 110 °C for about 12 hours. The dry powders were then weighed again to calculate the loss on ignition (LOI). Fusion discs were prepared by mixing 0.28g of the sample powder with 0.5g Li-tetraborate flux to maintain an infinite thickness. Then 0.02g of $NaNO_3$ was added to maintain an oxidizing environment such that all iron is detected as an oxide (Fe_2O_3). This mixture was then melted under very high temperatures; the molten material was then poured onto a cold surface where it cools to form a glass disc. The fusion discs were used to analyze for major elements (SiO_2, MgO, CaO, Al_2O_3, Cr_2O_3, P_2O_5, K_2O, Na_2O and TiO_2 as well as Cr_2O_3 and NiO) using the XRF technique.

Each pressed pellet was prepared by thoroughly mixing 8g of the sample powder with 3g of wax to accomplish a homogenous powder, which was then compressed into an extremely compact disc. These pressed pellets were analysed for trace elements (Sc, V, Cr, Ni, Cu, Zn, As, Br, Rb, Sr, Y, Zr, Nb, Mo, Ag, Cd, Sn, Sb, Ba, TI, Pb, Th and U) and Rare Earth Elements (REE) using the ICP-MS technique.

3.2 X-RAY FLUORESCENCE (XRF) ANALYSIS

XRF analysis (model: PANalytical WD-XRF Axios) is a technique used to acquire whole rock geochemical data. XRF is defined as a bulk analysis technique with a depth of the sample analysed varying from less than 1mm-1cm depending on the energy of the emitted X-ray and sample composition. XRF has detection limits ranging from sodium (Na) to uranium (U); this technique also can detect lighter elements such as fluorine and boron. Whole rock chemistry acquired from this analysis XRF technique can be used to calculate ore grade of a sample.

3.2.1 FUNCTION OF THE WD-XRF MACHINE

- The settings on the PANalytical Axios XFR spectrometer;
    - Maximum current: 66 mA (for trace elements) and 125 Ma
    - Maximum speed level: 4 kW
    - Maximum accelerator voltage: 60kV for trace elements and 32kV for major oxides.
- The samples are first bombarded by a primary X-ray beam, some of the energy is scattered while some is absorbed by the sample depending on the chemistry of that sample. The absorbed energy excites the atoms; electrons transition from higher (M-shell) to lower energy levels (K & L-shell) there by producing secondary fluorescent X-rays. The characteristic secondary X-rays produced fall onto a crystal which diffracts the X-rays with different wavelengths and directions. Each element in the sample produces its own characteristic secondary X-rays. Their intensities can be measured by using various detectors such as the flow counter and scintillation detector.
- The intensities are then recovered as concentrations. Major element results are measured as weight % while the trace elements are expressed as ppm values. The data is then recorded using the PW2450-SuperQ software.

3.3 ICP-MS ANALYSIS

Inductively Coupled Plasma-Mass Spectrometry (ICP-MS) is one of eight types of Mass Spectrometry analytical techniques. This technique is a destructive analytical method that uses a solid or liquid sample, however in this study solid samples were dissolved in acids according to the laboratory protocol. The ICP-MS technique has very low detection limits; it can measure for all elements except for noble gasses. This technique can also be used to analyse for ultra-trace elements such as Ru, Rh, Re, Os, Ir, Pd, Pt and Au.

3.3.1 SAMPLE ANALYSIS

- Solutions are introduced into the plasma (8000 °C) where they are decomposed into constituent atoms (vaporization) and ionized.
- There are two oppositely charged plates in the ionization room. Charged atoms are then accelerated towards a pole with the opposite charge, the positive plates will accelerate the positively charged ions to the analyser tube.
- In the analyser tube, which is surrounded by curved magnets, ions will be deflected according to their mass to charge ratio. Ions with different masses will be deflected to a different extend in a curved path.
- Mass Spectrometry uses atomic mass to obtain chemical information from samples. This technique utilizes the amount of deflection of a charged particle through a magnetic field to determine the relative mass of a molecular ion.

4. ELECTRON PROBE MICROANALYSIS (EPMA)

This analytical technique is like SEM EDX/WDS in that they are both high powered machines that use electrons, however, EPMA technique provides more reliable quantitative results. The EMPA utilized in this study is wavelength dispersive spectroscopy (WDS), which operate based on Bragg's law. EPMA is a quantitative and qualitative non-destructive method which analyses micron-sized volumes at the surface of materials. All elements from B to U can be detected at ppm levels (http://www.cameca.com/products/epma/technique). The qualitative use of an electron microprobe is to identify, characterize phases (shape, size, thickness, surface relief etc.) as well as to identify elements in each phase.

4.1 SAMPLE ANALYSIS

A beam of electrons is accelerated in an evacuated electron column of an EPMA to the sample with sufficient energy to generate characteristic x-rays for the elements analyzed. The characteristic x-rays produced in the sample are then selected using an analytical crystal with specific lattice spacing, only x-rays that satisfy Braggs' law are reflected and a single wavelength is passed onto the detector. Backscattered electrons (BSE) are high energy electrons that are reflected from the surface of the sample because of elastic scattering. The amount of back scattered electrons produced is proportional to the mean atomic number of the sample. These electrons are used to find elements with high atomic numbers within a matrix of elements with low atomic numbers e.g. finding sulphide minerals within silicate-rich rocks. Backscattered electrons are also used to show topography, crystal orientation, grain

boundaries, phase boundaries as well as other crystal features which can be displayed in the form of Backscattered electron images (http://serc.carleton.edu/research_education/geochemsheets/techniques/EPMA.html).

In this study, the back-scattered electron regime was used to capture photos of chromite and platinum-group minerals whereas WDS analysis was used to assess the chemistry of chromite and olivine crystals within the studied lithologies from the southwestern part of the Uitloop farm. Six feldspathic pyroxenite (5) and feldspathic harzburgite (1) polished thin sections were selected for the investigation of the chromite chemistry. Unfortunately, the data collection for the chemistry of olivine crystals was limited to the feldspathic harzburgite thin section (sample Z20-66.5) that contained fresh olivine crystals.

Chromite was analysed on polished thin sections for major and minor elements with wavelength dispersive microprobe Cameca SX-100 at the SPECTRAU labs at the University of Johannesburg. Natural and synthetic oxides and metals were used as standards. A 20 kV accelerating voltage and 40 nA beam current were used for 20 s counting time on the peak of the characteristic X-RAY for each element. The accuracy of the analyses was monitored using a standard reference chromite sample. Sample reproducibility varied by less than 2%.

The results were processed according to the procedure based on spinel stoichiometry and outlined by Barnes and Roeder (2004 version of their template with corrections according to C.J. de Hoog) and are presented as wt. % oxides and cations percentages.

APPENDIX B

PETROLOGICAL ANALYSIS

1. GEOLOGY LOG SHEETS

Table 11-1: Borehole Z19 geological core log sheet.

BHID	From	To	Lithology	Stratigraphy	Grain size	Top Contact	Bottom Contact	Min type	Min Style	Comments
Z19	0	65.6	Dolomite	DLFM (D)	F		S			
Z19	65.6	80.87	Norite	PR	M	S	DIFF			altered and brecciated
Z19	80.87	95.1	Feldspathic harzburgite	PR	M-C	DIFF	DIFF	Po, Pn	DISS	high sulphides (more pyrrhotite than pentlandite), altered olivine,
Z19	95.1	100.3	Feldspathic pyroxenite	PR	M	DIFF	S	SULPH	DISS	high sulphides, with feldspathic veins and patches, randomly oriented OPX laths,
Z19	100.3	101.8	Feldspathic pyroxenite	PR	M-C	S	S	SULPH	DISS	Chromite BLEBS hosted
Z19	101.8	121.1	Norite	PR	M	S	DIFF	SULPH	DISS	Po>>Pn>Ccp
Z19	121.1	124.2	Feldspathic pyroxenite	PR	M	DIFF	GRAD	SULPH	DISS	Sulphide mineralisation (Evenly distributed)
Z19	124.2	127.87	Feldspathic pyroxenite	PR	M	GRAD	S	SULPH	DISS	Sulphide mineralisation (Evenly distributed)
Z19	127.87	129.9	Feldspathic harzburgite	PR	M	S	DIFF	SULPH	DISS	high sulphide disseminations
Z19	129.9	135	Feldspathic harzburgite	PR	M	DIFF	DIFF	SULPH	DISS	high sulphide disseminations
Z19	135	136.4	Feldspathic pyroxenite	PR	M	DIFF	S	SULPH		
Z19	136.4	137.7	Feldspathic pyroxenite	PR	M	S	S	Po, Pn	DISS	Chromite stringer, Po>>Pn
Z19	137.7	139	Feldspathic pyroxenite	PR	M	S	DIFF	SULPH	DISS	
Z19	139	148.1	Pyroxenite	PR	M-C	DIFF	GRAD	SULPH	DISS+BLEB	altered and brecciated
Z19	148.1	156.15	Feldspathic pyroxenite	PR	M	GRAD	GRAD	SULPH	BLEB+NET	high PLAG content
Z19	156.15	170.8	Feldspathic pyroxenite	PR	M	GRAD	S	SULPH	NET	high PLAG content and sulphide mineralisation increases towards the bottom of the unit
Z19	170.8	174.5	Dolomite	DLFM (D)	F	S	S	Po	DISS	with sulphides and calcite veins
Z19	174.5	175.5	Parapyroxenite	A/FW/PR	F	S	S	Po	NET	
Z19	175.5	177.45	Parapyroxenite	A/FW/PR	F-M	S	S	Po, Ccp	NET	with sulphides (Po & Ccp) as well as carbonate veins
Z19	177.45	179.1	Hornfels	DLFM (S/H)	F	S	S			pyroxene hornfels with garnet, bedding visible (banded hornfels)
Z19	179.1	192.2	Parapyroxenite	A/FW/PR	F-M	S	DIFF			Silica rich hornfels with sulphide disseminations along bedding structures where it is associated with magnetite, silica veins and blebs
Z19	192.2	202	Parapyroxenite	A/FW/PR	F-M	DIFF	S	Po	DISS	black hornfels with whitish-grey xenoliths
Z19	202	213	Hornfels	DLFM (S/H)	F	S	E.O.H			with xenoliths increasing towards the bottom, granitic veins (1-3cm)

Table 11-2: Borehole Z20 geological log sheet.

BHID	From	To	Lithology	Stratigraphy	Grain size	Top Contact	Bottom Contact	Min type	Min Style	Comments
Z20	0	50.02	Dolomite	DLFM (D)	M		S	SULPH	BLEB	Ccp> Py> Pn
Z20	50.02	52.09	Parapyroxenite	A/HW/PR	F-M	S				Interaction between dolomite hanging wall with the Platreef
Z20	52.09	52.48	Parapyroxenite	A/HW/PR	F-M		S			Interaction between dolomite hanging wall with the Platreef
Z20	52.48	54.11	Feldspathic harzburgite	PR	M	S	DIFF	Pn, Ccp	DISS	CPX + OPX laths| Pn>Ccp
Z20	54.11	55.49	Feldspathic harzburgite	PR	M	DIFF	DIFF	SULPH, CHR	DISS	Chromite stringer at 54.24 m | OPX>>CPX
Z20	55.49	56.11	Feldspathic harzburgite	PR	M	DIFF	DIFF	SULPH	DISS	(OPX laths>>CPX) + PLAG + OL
Z20	56.11	56.64	Feldspathic harzburgite	PR	M		DIFF	SULPH	DISS	(OPX laths>>CPX) + PLAG + OL
Z20	56.64	57.69	Feldspathic harzburgite	PR	M	DIFF		SULPH, CHR	DISS	Chromite disseminations
Z20	57.69	60.63	Feldspathic pyroxenite	PR	M		S	SULPH	DISS	
Z20	60.63	61.04	Norite	PR	M-C	S	S	SULPH	DISS	(OPX laths>>CPX) + PLAG + OL
Z20	61.04	62.18	Feldspathic pyroxenite	PR	M-C	S		SULPH	NET	Py>Pn>Ccp
Z20	62.18	63.84	Feldspathic pyroxenite	PR	M		DIFF	SULPH	NET	(OPX laths>CPX) + PLAG
Z20	63.84	65.03	Gabbro	PR	M	DIFF	DIFF	SULPH	DISS	(CPX>OPX) + PLAG
Z20	65.03	65.85	Gabbro	PR	M-C	DIFF	GRAD	SULPH	NET + DISS	(CPX ≈ OPX) + PLAG
Z20	65.85	69.4	Feldspathic harzburgite	PR	M-C	GRAD	GRAD	SULPH	NET	(CPX ≈ OPX) + PLAG
Z20	69.4	69.94	Gabbronorite	PR	M-C	GRAD		Ccp	DISS	(CPX ≈ OPX) PLAG | CPY < 1%
Z20	69.94	70.48	Gabbro	PR	M		S	SULPH	DISS	(CPX>>OPX) + PLAG | Po>Pn>Ccp
Z20	70.48	70.72	Leuconorite	PR	M	S				No mineralisation | high PLAG content
Z20	70.72	71.87	Leuconorite	PR	M-C		S			No mineralisation | high PLAG content
Z20	71.87	71.98	Gabbro	PR	M	S	S			No mineralisation | (CPX>>OPX) + PLAG
Z20	71.98	72.2	Leuconorite	PR	M-C	S	S			No mineralisation | high PLAG content
Z20	72.2	72.88	Gabbro	PR	M	S	DIFF	Ccp	DISS	(CPX>>OPX) + PLAG
Z20	72.88	73	Leuconorite	PR	M-C	DIFF	DIFF			No mineralisation | high PLAG content
Z20	73	76.31	Feldspathic pyroxenite	PR	M	DIFF	GRAD	Ccp, Py		(OPX laths > CPX) PLAG | Sulphides < 1%
Z20	76.31	78.76	Gabbro	PR	M	GRAD	GRAD	Ccp	JINF	(CPX>>OPX) + PLAG |Ccp in joints
Z20	78.76	79.41	Norite	PR	M	GRAD		Ccp	DISS	(OPX>>CPX) + PLAG | Ccp <1 %
Z20	79.41	81.93	Norite	PR	M			Ccp	DISS	(OPX laths>>CPX) + PLAG
Z20	81.93	84.94	Feldspathic pyroxenite	PR	M		GRAD	Ccp	DISS	(OPX>>CPX) + PLAG
Z20	84.94	87.01	Norite	PR	M	GRAD		Ccp, Py	DISS	(OPX laths>>CPX) + PLAG + OL
Z20	87.01	89.56	Norite	PR	M		S	Ccp	DISS	(OPX laths>>CPX) + PLAG + OL
Z20	89.56	92.42	Norite	PR	M		S	SULPH	DISS	(OPX laths >> CPX) + PLAG + OL |High sulphide content towards the contact
Z20	92.42	92.46	Leuconorite	PR	M	S	S	Ccp, Po	DISS	High PLAG content
Z20	92.46	92.89	Norite	PR	M	S	DIFF	Ccp, Po	DISS	(OPX laths>CPX) + PLAG + OL
Z20	92.89	94.54	Feldspathic pyroxenite	PR	M	DIFF		Ccp	DISS	Ccp < 1-2%
Z20	94.54	95.03	Feldspathic pyroxenite	PR	M		GRAD	Ccp, Po	DISS	Ccp < 1-2%
Z20	95.03	97.89	Feldspathic pyroxenite	PR	M	GRAD		SULPH	NET	Po>Ccp >> PY
Z20	79.41	81.93	Norite	PR	M			Ccp	DISS	(OPX laths>>CPX) + PLAG
Z20	81.93	84.94	Feldspathic pyroxenite	PR	M		GRAD	Ccp	DISS	(OPX>>CPX) + PLAG
Z20	84.94	87.01	Norite	PR	M	GRAD		Ccp, Py	DISS	(OPX laths>>CPX) + PLAG + OL

Table 11-2 cont.

Z20	87.01	89.56	Norite	PR	M		S	Ccp	DISS	(OPX laths>>CPX) + PLAG + OL
Z20	89.56	92.42	Norite	PR	M		S	Ccp, Py	DISS	(OPX laths >> CPX) + PLAG + OL | High sulphide content towards the contact
Z20	92.42	92.46	Leuconorite	PR	M	S	S	Ccp, Py	DISS	High PLAG content
Z20	92.46	92.89	Norite	PR	M	S	DIFF	Ccp, Py	DISS	(OPX laths>CPX) + PLAG + OL
Z20	92.89	94.54	Feldspathic pyroxenite	PR	M	DIFF		Ccp	DISS	Ccp < 1-2%
Z20	94.54	95.03	FPYRX	PR	M		GRAD	Ccp	DISS	Ccp < 1-2%
Z20	95.03	97.89	FPYRX	PR	M	GRAD		Ccp, Py	NET	Ccp >> Py
Z20	97.89	101.25	Feldspathic pyroxenite	PR			BRK	SULPH	NET	
Z20	101.25	103	Feldspathic pyroxenite	PR	M-C	BRK	GRAD	SULPH	DISS	Po >>Ccp> Py
Z20	103	103.78	Gabbro	PR	M	GRAD	GRAD	Ccp	DISS	
Z20	103.78	110.14	Feldspathic pyroxenite	PR	M	GRAD	DIFF	SULPH	DISS	Pn > Ccp > Py
Z20	110.14	110.54	Norite	PR	M-C	DIFF	DIFF	SULPH	DISS	(OPX laths>> CPY) + PLAG + OL
Z20	110.54	114	Feldspathic harzburgite	PR	M	DIFF	DIFF	Pn	DISS	
Z20	114	114.81	Norite	PR	M	DIFF	S	Pn	DISS	(OPX laths>> CPX) + PLAG
Z20	114.81	114.89	Leuconorite	PR	C	S	S			No mineralisation | high PLAG content
Z20	114.89	119	Feldspathic pyroxenite	PR	M	S	GRAD	Pn, Ccp	DISS	Pn > Ccp towards the contact
Z20	119	121	Feldspathic pyroxenite	PR	M	GRAD	DIFF	SULPH	DISS	High sulphide mineralisation
Z20	121	123	Feldspathic pyroxenite	PR	M	DIFF	DIFF	SULPH	BLEB, DISS	Lesser sulphide mineralisation | (OPX laths > CPX) + PLAG
Z20	123	123.25	Norite	PR	M	DIFF	DIFF	Po	DISS	(OPX laths>CPX) + PLAG + OL (serpentinised)
Z20	123.25	125.95	Feldspathic pyroxenite	PR	M	DIFF	GRAD	SULPH	DISS	
Z20	125.95	127.95	Gabbronorite	PR	M	GRAD	DIFF	Po	DISS	
Z20	127.95	128.65	Leuconorite	PR	M-C	DIFF	S	SULPH	NET	High PLAG content
Z20	128.65	128.87	Gabbronorite	PR	M	S	S	SULPH	DISS	CPX ≈ OPX + PLAG
Z20	128.87	128.97	Leuconorite	PR	M-C	S	DIFF	SULPH	NET	High PLAG content | Pn> Ccp> Py
Z20	128.97	130.1	Gabbronorite	PR	M	DIFF	GRAD	SULPH	NET	(CPX ≈ OPX) + PLAG
Z20	130.1	133.23	Norite	PR	M	GRAD	GRAD	SULPH	DISS	
Z20	133.23	137.58	Feldspathic pyroxenite	PR	M	GRAD	DIFF	SULPH	DISS	
Z20	137.58	140.66	Gabbro	PR	M	DIFF	DIFF	SULPH	BLEB, NET	Sulphides blebby and net textured in parts
Z20	140.66	143.74	Norite	PR	M	DIFF	GRAD	SULPH	BLEB, DISS	Pn > Py > Ccp
Z20	143.74	149	Norite	PR	M	GRAD	S	SULPH	NET	
Z20	149	152.44	Feldspathic pyroxenite	PR		S	S	SULPH	DISS	Po<Pn > Ccp > Py
Z20	152.44	153.81	Leuconorite	PR	M-C	S	S	SULPH	BLEB, DISS	Po > Py > Ccp
Z20	153.81	154.2	Gabbronorite	PR	M	S	S	Pn	DISS	Pn < 1%
Z20	154.2	154.27	Leuconorite	PR	M - C	S	S	Po, Ccp	BLEB	Po >Ccp | High PLAG content
Z20	154.27	156.54	Feldspathic pyroxenite	PR	M	S	S	Pn	DISS	Pn < 1%
Z20	156.54	159.33	Gabbronorite	PR	M		S	Pn	DISS	
Z20	159.33	159.91	Leuconorite	PR	M-C	S	S	SULPH	BLEB	High PLAG content | Pn> Ccp > Py

Table 11-2 cont.

Z20	159.91	160.24	Gabbronorite	PR	M	S	S	Po, Pn	DISS	
Z20	160.24	160.5	Leuconorite	PR	M-C	S	DIFF	Po	BLEB	High PLAG content
Z20	160.5	160.88	Gabbronorite	PR	M	DIFF	S	SULPH	DISS	
Z20	160.88	161	Leuconorite	PR	C	S	S			No sulphide mineralisation
Z20	161	162.74	Gabbronorite	PR	M	S	S	SULPH	DISS	Po> Pn >Ccp
Z20	162.74	162.88	Leuconorite	PR	M-C	S	S	Ccp	VNF	High PLAG content |phlogopite in parts
Z20	162.88	163.58	Gabbronorite	PR	M	S	DIFF	SULPH	DISS, BLEB	Blebby sulphides towards the contact | Po>Pn > Ccp >> Py
Z20	163.58	164.08	Leuconorite	PR	M-C	DIFF	DIFF	Pn, Ccp	BLEB	Sulphide mineralisation mostly Pn in close association with Ccp
Z20	164.08	164.61	Norite	PR	M	DIFF	DIFF	SULPH	DISS	Sulphides < 1%
Z20	164.61	165.28	Norite	PR	M-C	DIFF	DIFF	SULPH	BLEB	Po >> Ccp >Pn
Z20	165.28	166.28	Gabbronorite	PR	M-C	DIFF		SULPH	DISS	Po > Ccp> Pn
Z20	166.28	167.57	Gabbronorite	PR	M		S	SULPH	DISS	Po >> Ccp > Pn
Z20	167.57	167.91	Gabbronorite	PR	C	S	S	Ccp	DISS	(CPX ≈ OPX) + PLAG (coarse)
Z20	167.91	168.31	Gabbronorite	PR	C	S	DIFF	Pn, Ccp	DISS	(CPX ≈ OPX) + PLAG | high PLAG content
Z20	168.31	168.45	Leuconorite	PR	C	DIFF	S	Pn	DISS	High PLAG content
Z20	168.45	172.85	Gabbronorite	PR	M	S	GRAD	SULPH	NET, BLEB	Po >> Ccp > Pn > Py
Z20	172.85	173.85	Feldspathic pyroxenite	PR	M	GRAD	GRAD	SULPH	NET	Sulphide mineralisation increases towards the contact | (OPX laths > CPX) + PLAG
Z20	173.85	174.1	Feldspathic pyroxenite	PR	M	GRAD	DIFF	SULPH	NET, BLEB	Po >> Pn > Ccp ≥ Py
Z20	174.1	174.78	Feldspathic pyroxenite	PR	M	DIFF	DIFF	SULPH	NET, BLEB	Po >> Pn > Ccp ≥ Py
Z20	174.78	175.15	Feldspathic pyroxenite	PR	M-C	DIFF	DIFF	Pn, Ccp	NET	High PLAG content | PN >> CPYY
Z20	175.15	175.23	Feldspathic pyroxenite	PR	F-M	DIFF	DIFF	SULPH	NET	Assimilation zone with footwall hornfels
Z20	175.23	176.65	Feldspathic pyroxenite	PR	F	DIFF	S	SULPH	NET	Hornfels (protolith: shale) | visible bedding planes
Z20	176.65	177.6	Hornfels	DLFM (S/H)	F	S	BRK	SULPH	NET	With quartz veins | visible bedding planes
Z20	177.6	178.28	Hornfels	DLFM (S/H)	F	BRK	BRK			With quartz veins | visible bedding planes
Z20	178.28	178.86	Hornfels	DLFM (S/H)	F	BRK		Po	BND	Sulphide mineralisation oriented along bedding planes
Z20	178.86	180.04	Hornfels	DLFM (S/H)	F		DIFF	Po, Pn	BND	Sulphide mineralisation oriented along bedding planes
Z20	180.04	181.58	Hornfels	DLFM (S/H)	F	DIFF	DIFF	Po, Pn	BND	Sulphide mineralisation oriented along bedding planes
Z20	181.58	182.17	Dolomite	DLFM (D)	F	DIFF	DIFF	SULPH	DISS	(Banded) dolomite interlayered with hornfels
Z20	182.17	182.53	Hornfels	DLFM (S/H)	F	DIFF	S	SULPH	BND	Sulphide oriented along bedding planes
Z20	182.53	183.35	Dolomite	DLFM (D)	F	S	S	SULPH	DISS	
Z20	183.35	184.9	Hornfels	DLFM (S/H)	F	S	S	SULPH	NET, BND	Silica xenoliths (size: 2mm-2 cm)
Z20	184.9	188.27	Hornfels	DLFM (S/H)	F	S	S	SULPH	DISS	Brown mica-rich hornfels (protolith: shale) | quartz veins
Z20	188.27	188.63	Pyroxenite	PR	M	S	S	SULPH	DISS	(OPX laths >> CPX) + PLAG
Z20	188.63	196	Hornfels	DLFM (S/H)	F	S	S	SULPH	DISS	Banded | Brown mica-rich hornfels (protolith: shale) | quartz veins
Z20	196	201.77	Dolomite	DLFM (D)	F	S	S	SULPH	BND	Banded | Dolomite interlayered with shale (hornfels) and magnetite bands
Z20	201.77	201.87	Hornfels	DLFM (S/H)	F	S	S	SULPH	BND	Brown mica-rich hornfels (protolith: shale)
Z20	201.87	204.04	Dolomite	DLFM (S/H)	F	S	S	SULPH	BND, V	Banded | Dolomite interlayered with shale (hornfels) and magnetite bands

Table 11-2 cont.

Z20	204.04	204.1	Hornfels	DLFM (S/H)	F	S	S	SULPH	V	Brown mica-rich hornfels (protolith: shale)
Z20	204.1	204.97	Dolomite	DLFM (D)	F	S	BRK	SULPH	BND	Banded | Dolomite interlayered with shale (hornfels) and magnetite bands
Z20	204.97	205.09	Hornfels	DLFM (S/H)	F	BRK	BRK			Metamorphosed amphibole-rich hornfels (black shinny & slippery cleavage sides)
Z20	205.09	205.88	Dolomite	DLFM (D)	F	BRK	BRK	SULPH	BND	Banded | Dolomite interlayered with shale (hornfels) | Calcite & magnetite veins
Z20	205.88	206.03	Hornfels	DLFM (S/H)	F	BRK	BRK			Metamorphosed amphibole-rich hornfels (black shinny & slippery cleavage sides)
Z20	206.03	206.77	Dolomite	DLFM (D)	F	BRK	BRK	SULPH	BND	Banded | Dolomite interlayered with shale (hornfels)| calcite & magnetite veins
Z20	206.77	207.07	Hornfels	DLFM (S/H)	F	BRK	BRK			Metamorphosed amphibole-rich hornfels (black shinny & slippery cleavage sides)
Z20	207.07	208.29	Dolomite	DLFM (D)	F	BRK	BRK	SULPH	BND, V	Banded | Dolomite interlayered with shale (hornfels)
Z20	208.29	208.61	Hornfels	DLFM (S/H)	F	BRK	BRK			Metamorphosed amphibole-rich hornfels (black shinny & slippery cleavage sides)
Z20	208.61	209.09	Hornfels	DLFM (S/H)	F	BRK	BRK	SULPH	V	Banded hornfels
Z20	209.09	209.13	Hornfels	DLFM (S/H)	F	BRK	BRK			Metamorphosed amphibole-rich hornfels (black shinny & slippery cleavage sides)
Z20	209.13	209.75	Dolomite	DLFM (D)	F	BRK		SULPH	BND	Banded | Dolomite interlayered with shale (hornfels)
Z20	209.75	212.61	Dolomite	DLFM (D)	F		BRK	SULPH	BND	Banded| Dolomite interlayered with shale (hornfels)
Z20	212.61	212.83	Hornfels	DLFM (S/H)	F	BRK	BRK			Metamorphosed amphibole-rich hornfels (black shinny & slippery cleavage sides)
Z20	212.83	213.12	Hornfels	DLFM (SH)	F	BRK	S			Brown mica-rich hornfels (protolith: shale) separate
Z20	213.12	213.29	Dolomite	DLFM (D)	F	S	S			
Z20	213.29	213.82	Dolomite	DLFM (D)	F	S		SULPH	BND	Banded | Dolomite interlayered with shale (hornfels) & magnetite bands
Z20	213.82	216.4	Pyroxenite	PR	F		BRK			No mineralisation | intrusion into shale (hornfels)
Z20	216.4	216.49	Hornfels	DLFM (S/H)	F	BRK	BRK			Brown mica-rich hornfels (protolith: shale)
Z20	216.49	220.84	Dolomite	DLFM (D)	F	BRK	E.O.H	SULPH	BND	Banded | Dolomite interlayered with shale (hornfels) & magnetite bands

2. SAMPLE PHOTOGRAPHS



Figure 11-2: A Photograph of sample Z19-78.3 (norite).



Figure 11-3: A photograph of sample Z19-100.35 (feldspathic pyroxenite).



Figure 11-4: A photograph of sample Z19-101. 4 (feldspathic pyroxenite).



Figure 11-5: A photograph of sample Z19-101.6 (feldspathic pyroxenite).



Figure 11-6: A photograph of sample Z19-123.2 (feldspathic pyroxenite).

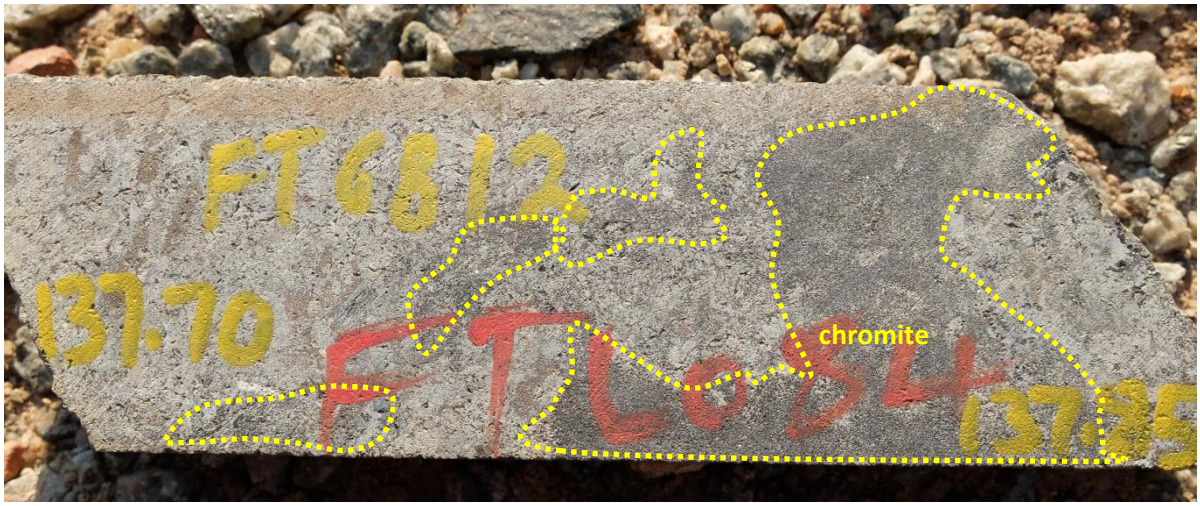


Figure 11-7: A photograph of sample Z19-137.7 (feldspathic pyroxenite).



Figure 11-8: A photograph of sample Z19-150.6 (feldspathic pyroxenite).



Figure 11-9: A photograph of sample Z19-167.1 (feldspathic pyroxenite).



Figure 11-10: A photograph of sample Z19-169.2 (feldspathic pyroxenite).



Figure 11-11: A photograph of sample Z19-170.5 (pyroxenite).



Figure 11-12: A photograph of sample Z19-174.9 (parapyroxenite).



Figure 11-13: A photograph of sample Z19-177.9 (hornfels).

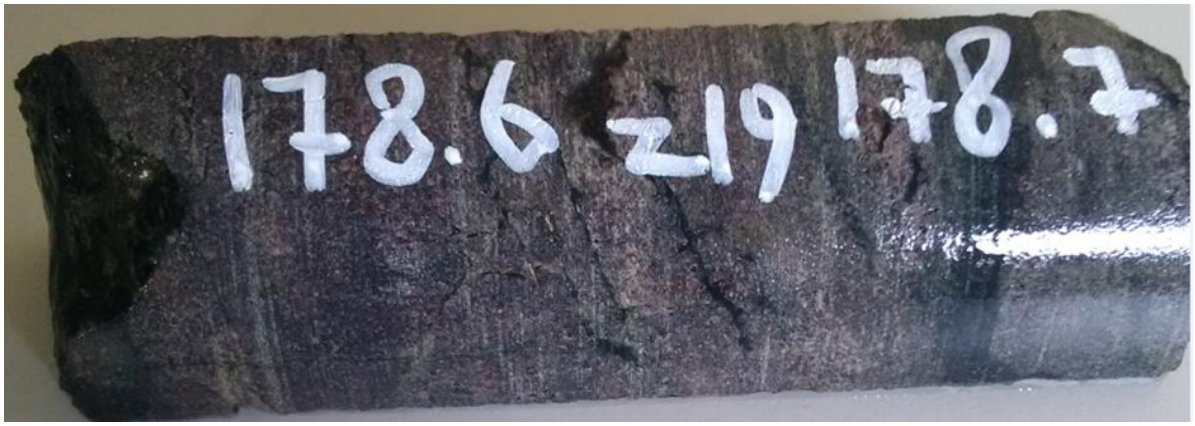


Figure 11-14: A photograph of sample Z19-178.6 (hornfels).



Figure 11-15: A photograph of sample Z19-195.7 (pyroxenite).



Figure 11-16: A photograph of sample Z19-199 (parapyroxenite).



Figure 11-17: A photograph of sample Z19-203.2 (hornfels with calcsilicate inclusions (metasedimentary breccia)).



Figure 11-18: A photograph of sample Z20-53.7 (harzburgite).



Figure 11-19: A photograph of sample Z20-54.25 (harzburgite with a thin chromite stringer).



Figure 11-20: A photograph of sample Z20-57.5 (feldspathic harzburgite with chromite disseminations).



Figure 11-21: A photograph of sample Z20-59.5 (feldspathic pyroxenite).



Figure 11-22: A photograph of sample Z20-62.7 (feldspathic pyroxenite).



Figure 11-23: A photograph of sample Z20-66.5 (feldspathic harzburgite).



Figure 11-24: A photograph of sample Z20-83 (feldspathic pyroxenite).



Figure 11-25: A photograph of sample Z20-107.7 (feldspathic pyroxenite).



Figure 11-26: A photograph of sample Z20-111 (feldspathic harzburgite).



Figure 11-27: A photograph of sample Z20-119 (feldspathic pyroxenite).



Figure 11-28: A photograph of sample Z20-120.1 (feldspathic pyroxenite).



Figure 11-29: A photograph of sample Z20-120.75 (feldspathic pyroxenite).



Figure 11-30: A photograph of sample Z20-121.9 (feldspathic pyroxenite).



Figure 11-31: A photograph of sample Z20-124.8 (feldspathic pyroxenite).



Figure 11-32: A photograph of sample Z20-131.8 (feldspathic pyroxenite).



Figure 11-33: A photograph of sample Z20-134.8 (feldspathic pyroxenite).



Figure 11-34: A photograph of sample Z20-140.1 (gabbro).



Figure 11-35: A photograph of sample Z20-149.3 (feldspathic pyroxenite).



Figure 11-36: A photograph of sample Z20-153.5 (leuconorite).



Figure 11-37: A photograph of sample Z20-164.5 (norite with a silica vein).



Figure 11-38: A photograph of sample Z20-173. 7 (feldspathic pyroxenite).



Figure 11-39: A photograph of sample Z20-175.5 (feldspathic pyroxenite).

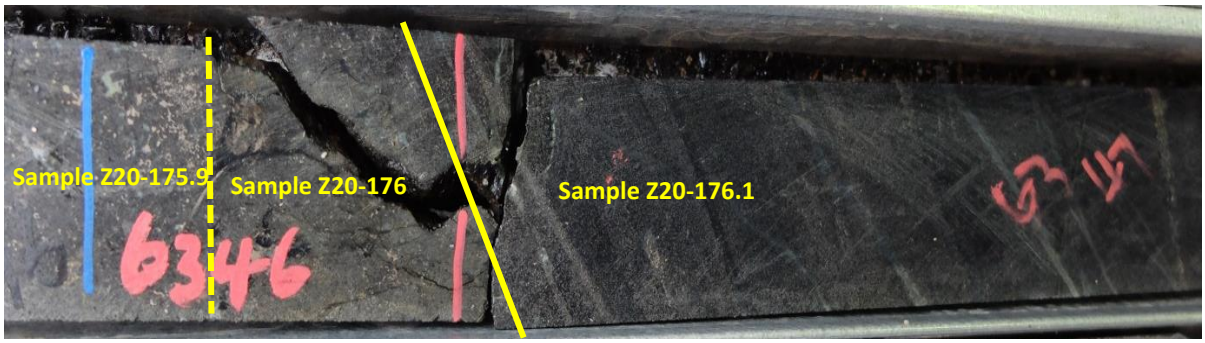


Figure 11-40: A photograph showing a sharp contact between the Rustenburg Layered Suite (RLS) (feldspathic pyroxenite) and the metasedimentary footwall lithologies (hornfels) at a depth of ~176.1m in borehole Z20. A transitional contact is observed between sample Z20-175.9 (feldspathic pyroxenite) and sample Z20- 176 (feldspathic pyroxenite).



Figure 11-41: A photograph of sample Z20-183.5, hornfels with inclusions of quartz-cordierite hornfels rimmed by base metal sulphides.



Figure 11-42: A photograph of sample Z20-184.4, hornfels with inclusions of quartz-cordierite hornfels associated with base metal sulphides.



Figure 11-43: A photograph of sample Z20-186, hornfels with inclusions of quartz-cordierite hornfels.



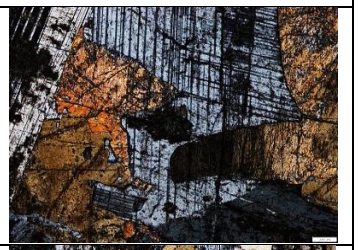
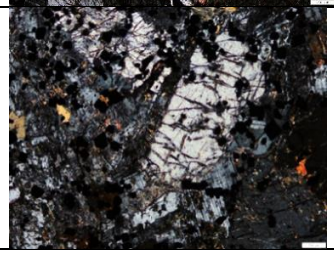
Figure 11-44: A photograph of sample Z20-194.4, hornfels with silica veins.

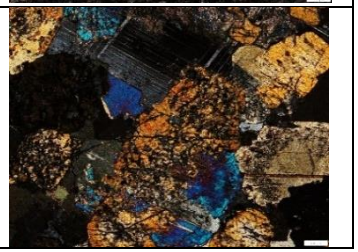


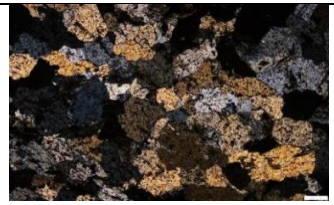
Figure 11-45: A photograph of sample Z20-212.5, dolomite with magnetite bands.

3. PETROGRAPHIC DESCRIPTIONS OF POLISHED THIN SECTIONS

Table 11-3: Petrographic analysis of borehole Z19 samples.

Sample Number	Major Minerals	Minor Minerals	Textures	Alteration	% of Alteration	Reflected light observations	Other Features	Modal Abundance (%) & Rock Name.	Photomicrographs under XPL
Z19-78.3	Orthopyroxene, clinopyroxene & plagioclase	K-feldspar, sulphides, phlogopite, Biotite & sericite	Lamellar twinning in plagioclase, Cumulus plagioclase laths, Carlsbad twinning in K-feldspar,	Saussiritization, Amphibole	5%	Pyrrhotite Pentlandite Chalcopyrite chromite	OPX and CPX exsolution, sulphide replaced by tremolite	Orthopyroxene: 30% Plagioclase: 30% Clinopyroxene: 20% K-feldspar: 5% Opaques: 5% Mica: 3% Clay minerals: 1% Quartz: 1% **Norite**	
Z19-100.35	Orthopyroxene, & plagioclase	Sulphides, chromite, phlogopite, biotite & sericite	Hypidiomorphic granular (euhedral & anhedral OPX), Lamellar twinning in plagioclase	Saussiritization, amphibole	5%	Chromite: 45% Pyrrhotite: 35% Pentlandite: 10% Chalcopyrite:10%	Sulphides replaced by tremolite	Orthopyroxene: 75% Opaques: 12% Plagioclase: 10% Mica: 2% Clay minerals: 1% Amphibole: <1% **Feldspathic pyroxenite**	
Z19-101	Orthopyroxene, plagioclase & clinopyroxene	Chromite, sulphides, sericite, phlogopite & quartz	Hypidiomorphic granular, Crosshatch and lamellar twinning in plagioclase, granophyric quartz	Saussiritization, amphibole	10%	Chromite: 60% Pyrrhotite: 30% Chalcopyrite:10%	CPX and OPX exsolution	Orthopyroxene: 55% Plagioclase: 15% Opaques: 10% Clinopyroxene: 5% Amphibole: 5% Mica: 5% Clay minerals: 4% Quartz: 1% **Feldspathic pyroxenite**	
Z19-101.4	Orthopyroxene, plagioclase & clinopyroxene	Chromite, sulphides, phlogopite & sericite	Intergranular, Lamellar twinning in plagioclase, perthite,	Saussiritization	10%	Pyrrhotite: 80% Chromite: 20%	OPX exsolution	Orthopyroxene: 70% Plagioclase: 15% Opaques: 11% Clinopyroxene:2% Mica: 1% Clay minerals: 1% **Feldspathic pyroxenite**	

Z19-101.6	Orthopyroxene, olivine, clinopyroxene & plagioclase	Sulphides, chromite, serpentine, sericite & phlogopite	Hypidiomorphic granular, twinned CPX, lamellar twinning in plagioclase, granophyric quartz	Saussiritization Serpentinization	10%	Chromite: 50% Pyrrhotite: 40% Pentlandite: 5% Chalcopyrite: 5%	OPX exsolution	Orthopyroxene: 65% Plagioclase: 15% Opaques: 11% Clinopyroxene: 3% Mica: 2% Clay minerals: 1% **Feldspathic pyroxenite**	
Z19-123.2	Orthopyroxene, clinopyroxene & plagioclase	Sulphides, phlogopite & sericite	Twinned CPX, lamellar twinning in plagioclase, largely equigranular (euhedral OPX)	Saussiritization	5%	Pyrrhotite: 90% Pentlandite: 3% Chalcopyrite:2%	CPX and OPX exsolution	Orthopyroxene: 75% Plagioclase: 10% Opaques: 6% Clinopyroxene: 5% Mica:2% Clay minerals: 2% **Feldspathic pyroxenite**	
Z19-137.5	Orthopyroxene, plagioclase, clinopyroxene	Chromite, sulphides & sericite	Cross hatch and lamellar twinning in plagioclase, perthite, CPX twinning	Saussiritization	5%	Chromite: 65% Pyrrhotite: 20% Chalcopyrite:15%	CPX and OPX exsolution,	Orthopyroxene: 60% Opaques: 20% Plagioclase: 15% Clinopyroxene: 3% Clay minerals 2% **Feldspathic pyroxenite**	
Z19-150.6	Orthopyroxene, plagioclase & clinopyroxene	Quartz, phlogopite, biotite, sulphides & sericite	Lamellar twinning in plagioclase, carlsbad twinning in K-feldspar	Saussiritization	15%	Pyrrhotite: 65% Chalcopyrite:35%		Orthopyroxene: 70% Plagioclase: 15% Opaques: 3% K-feldspar: 2% Clinopyroxene: 2% Clay minerals: 2% Mica: 1% **Feldspathic pyroxenite**	
Z19-169.2	Orthopyroxene, plagioclase & clinopyroxene	Quartz, biotite, sericite & sulphides	Granophyric quartz, lamellar twinning in plagioclase	Saussiritization	5%	Pyrrhotite: 50% Chalcopyrite:35% Pentlandite: 15%	OPX and CPX exsolution, secondary sulphides replacing pyroxene minerals	Orthopyroxene: 80% Plagioclase: 10% Opaques: 3% Clinopyroxene: 2% Quartz: 2% Clay minerals: 2% Mica: <1% **Feldspathic pyroxenite**	

Z19-170.5	Orthopyroxene & clinopyroxene	Quartz, carbonate, phlogopite, sericite, magnetite & sulphides	Granoblastic pyroxenes (interlocking)	Saussiritization	15%	Pyrrhotite: 90% Chalcopyrite: 5% Magnetite: 5%	Recrystallised CPX,	Clinopyroxene: 90% Plagioclase: 2% Orthopyroxene: 5% Carbonate minerals: 3% Opaques: 3% Clay minerals: 1% Mica: <1% **Parapyroxenite**	
Z19-174.9	Orthopyroxene	Quartz, phlogopite, carbonates & sulphides	Equigranular	Saussiritization	2%	Pyrrhotite: 95% Chalcopyrite:5%		Clinopyroxene: 85% Carbonate minerals: 5% Opaques: 5% Clay minerals: 5% **Parapyroxenite**	
Z19-177.9	Quartz, phlogopite & biotite	Sulphides, chlorite	Equigranular	Chloritization	2%	Pyrrhotite: 98% Chalcopyrite: 2%		Quartz: 45% Phlogopite: 40% Cordierite: 10% Opaques: 4% Clay minerals: 1% **Phlogopite-hornfels**	
Z19-195.7	Orthopyroxene	Quartz, sulphides, biotite & chlorite	Granublastic	Chloritization, Amphibole	<1%	Pyrrhotite: 95% Magnetite: 5%	Tremolite replacing sulphides	Orthopyroxene: 90% Opaques: 5% Quartz: 2% Clay minerals: 2% Amphibole: 1% Mica: 1% **Orthopyroxenite**	
Z19-199	Orthopyroxene	Sulphides & sericite	Granublastic	Chloritization	<1%	Pyrrhotite: 95% Magnetite: 5%		Orthopyroxene: 90% Opaques: 4% Clay minerals: 1% **Orthopyroxenite**	

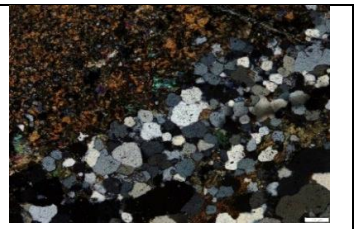
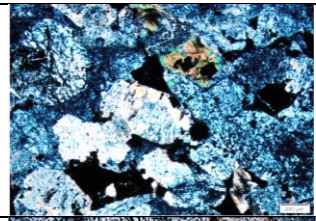
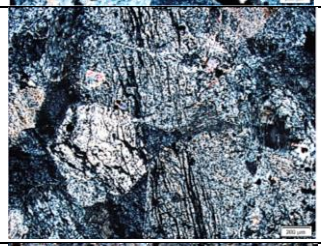
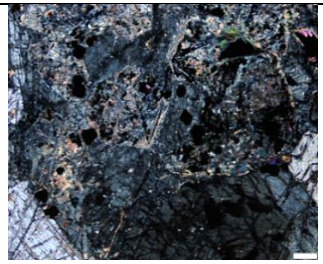
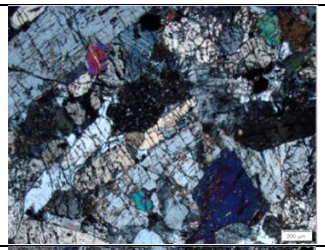
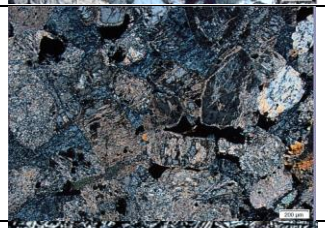
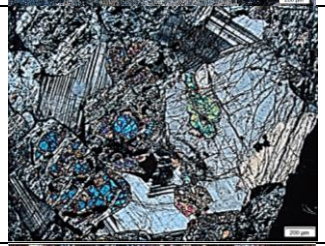
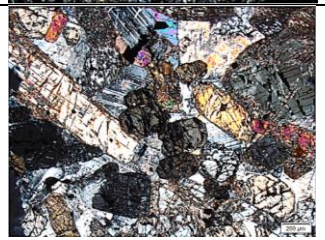
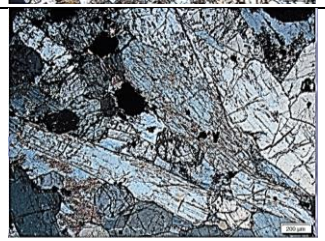
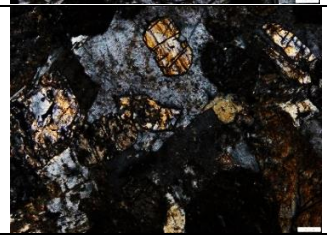
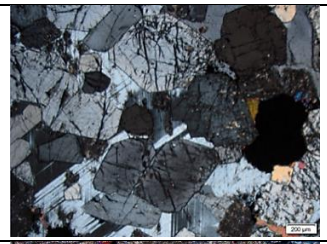
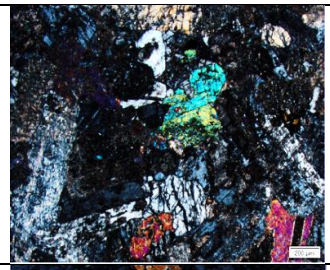
Z19-203.2	Pyroxene	Amphibole, sulphides, magnetite		Tremolite, Chloritization, Saussuritixation	15%	Pyrrhotite: 10% Magnetite: 90%		Pyroxenes: 60% Opaques: 30% Amphibole: 5% Clay minerals: 5% **Pyroxene hormfels**	 **Pyroxene-mica hornfels with quartz-cordierite inclusions**
	Quartz Cordierite		Glomeroporphyritic; quartz clasts in fine grained groundmass					Quartz: 60 % Cordierite: 40% **Quartz-cordierite inclusions**	

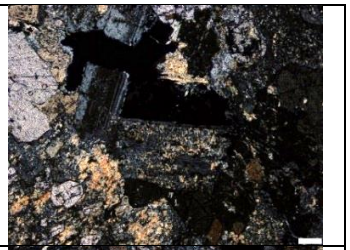
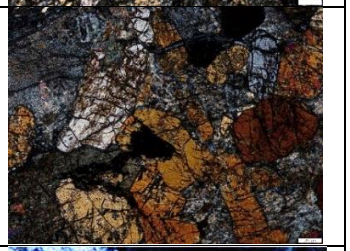
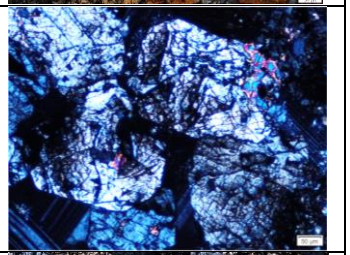
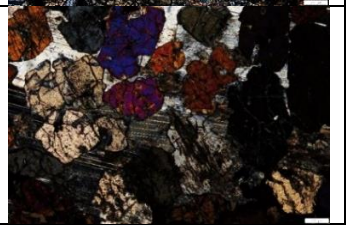
Table 11-4: Petrographic analysis of borehole Z20 samples.

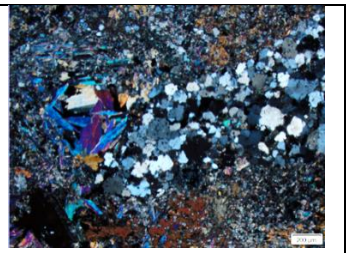
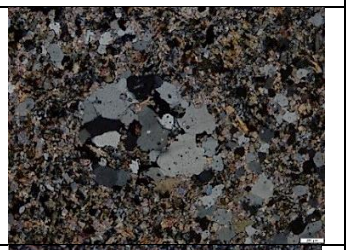
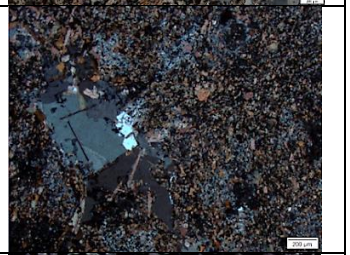
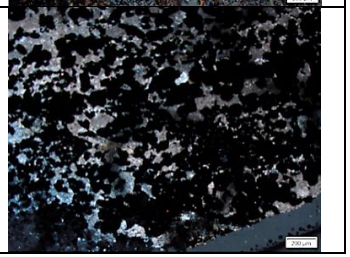
Sample Number (Interval in meters)	Major Minerals	Minor Minerals	Textures	Alteration	% of Alteration	Reflected light observations	Other Features	Modal Abundance (%) & Rock Name.	Photomicrographs under XPL
Z20- 53.7	Olivine, orthopyroxene & clinopyroxene	Phlogopite, magnetite, chromite & sulphides	Euhedral OPX,	Serpentinization	90%	Pyrrhotite: 50% Chromite: 20% Pentlandite: 10% Chalcopyrite:10%	Microfractures in olivine,	Olivine: 45% Orthopyroxene: 25% Serpentine: 15% Opaques:10% Phlogopite: 3% Clinopyroxene: 2% **Feldspathic harzburgite**	
Z20-54.25	Olivine, orthopyroxene, plagioclase & clinopyroxene	Phlogopite, chromite, sulphides & magnetite	Euhedral to subhedral olivine	Serpentinization, Saussuritixation	80%	Pentlandite: 70% Pyrrhotite: 25% Chromite: 5%	Microfractures in olivine	Olivine: 40% Orthopyroxene: 35% Plagioclase: 10% Serpentine: 10% Opaques:9% Clinopyroxene: 5% Phlogopite: 1% **Feldspathic harzburgite**	
Z20-57.5	Orthopyroxene, clinopyroxene, plagioclase & olivine	Phlogopite, sulphides, chromite, magnetite, sericite, amphibole & serpentine	Poikilitic (CPX oikocrysts with OPX chacrysts) Lamellar twinning and crosshatch twinning in plagioclase	Serpentinization Saussuritixation	25%	Pyrrhotite: 60% Chromite: 20% Pentlandite: 10% Chalcopyrite:10%	Microfractures in olivine, tremolite replacing sulphide minerals	Olivine: 40% Orthopyroxene: 30% Plagioclase: 10% Opaques:7% Serpentine: 6% Clay minerals: 3% Clinopyroxene: 3% Amphibole: 1% Phlogopite: 1% **Feldspathic harzburgite**	

Z20-57.9	Orthopyroxene, clinopyroxene & plagioclase	Phlogopite, chromite, sulphides & sericite	Inequigranular, Poiklitic (CPX oikocrysts hosting OPX chadacrysts) lamellar twinning in plagioclase	Saussuritixation	2%	Pyrrhotite: 30% Pentlandite: 40% Chalcopyrite:20% Chromite: 10%	OPX exsolution	Orthopyroxene: 70% Clinopyroxene: 10% Plagioclase: 10% Opaques:5% Clay minerals: 3% Phlogopite: 2% **Feldspathic pyroxenite**	
Z20-62.7	Orthopyroxene, clinopyroxene & plagioclase	Chromite, Sulphides, serpentine, Amphibole, magnetite & phlogopite	OPX oikocrysts hosting OPX inclusions	Serpentinization, Saussuritixation and tremolite	50%	Pyrrhotite: 75% Pentlandite: 10% Chromite: 15% Magnetite: <1%	Tremolite replacing sulphides	Orthopyroxene: 70% Clay minerals: 12% Plagioclase: 10% Opaques:5% Phlogopite: 2% Amphibole: <1% **Feldspathic pyroxenite**	
Z20-66.5	Olivine, orthopyroxene & plagioclase	Chromite, sulphides, serpentine, phlogopite & magnetite	Euhedral olivine, lamellar twinning in plagioclase,	Serpentinization	2%	Pyrrhotite: 35% Pentlandite: 30% Chromite: 25% Magnetite: 10%	Microfractures in olivine	Olivine: 45% Orthopyroxene: 25% Plagioclase: 15% Opaques:10% Serpentine: 4% Phlogopite: 1% Clay minerals: 1% **Feldspathic harzburgite**	
Z20-83	Orthopyroxene, clinopyroxene & plagioclase	Chromite, sulphides, sericite, amphibole & biotite	Lamellar twinning in plagioclase, OPX lathis (ophitic)	Saussuritixation, amphibole	10%	Pentlandite: 80% Chromite: 10%		Orthopyroxene: 65% Clinopyroxene: 10% Plagioclase:15% Opaques: 5% Amphibole: 2% Clay minerals: 2% Biotite:1% **Feldspathic pyroxenite**	
Z20-107.7	Orthopyroxene, Clinopyroxene & plagioclase	Amphibole, sulphides, chromite, sericite, phlogopite	OPX laths (ophitic), lamellar twinning in plagioclase, Poikilitic (CPX oikocrysts with OPX chadacrysts)	Saussuritixation, Amphibole	2%	Pyrrhotite: 85% Pentlandite: 5% Chromite: 8% Chalcopyrite: 2%		Orthopyroxene: 75% Plagioclase: 10% Clinopyroxene: 7% Opaques: 5% Amphibole: 2% Phlogopite: 1% Clay minerals: 1% **Feldspathic pyroxenite**	

Z20-111	Olivine, orthopyroxene, plagioclase & clinopyroxene	Sulphides, chromite, phlogopite, amphibole, serpentine, quartz & biotite	Poikilitic (OPX oikocrysts with OPX and OL chadacrysts) Lamellar twinning in plagioclase,	Serpentinization, Saussuritixation	10%	Pyrrhotite: 95% Pentlandite: 1% Chalcopyrite: 4% Magnetite: <1%	Olivine with characteristic fractures, tremolite replacing sulphides	Orthopyroxene: 45% Olivine: 20% Plagioclase: 10% Clinopyroxene: 5% Opaques: 5% Biotite: 2% Quartz: 1% Amphibole: 1% Clay minerals: 1% **Feldspathic harzburgite**	
Z20-120.75	Orthopyroxene, clinopyroxene & plagioclase	Quartz, biotite, sulphides & Sericite	Lamellar twinning in plagioclase, granophyric quartz,	Saussuritixation	5%	Pyrrhotite: 80% Pentlandite: 20%		Orthopyroxene: 75% Plagioclase: 10% Clinopyroxene: 5% Opaques: 5% Quartz: 2% Clay minerals: 2% Mica: 1% **Feldspathic pyroxenite**	
Z20-121.9	Orthopyroxene, plagioclase & clinopyroxene	Phlogopite, biotite, sulphides. magnetite & sericite	Lamellar twinning in plagioclase, zoned plagioclase, euhedral OPX	Saussuritixation amphibole	10%	Pyrrhotite: 90% Pentlandite: 10% Magnetite: <1%		Orthopyroxene: 65% Plagioclase: 15% Clinopyroxene: 5% Amphibole: 5% Opaques: 5% Mica: 3% Clay minerals: 2% **Feldspathic pyroxenite**	
Z20-124.8	Orthopyroxene & plagioclase	Amphibole, biotite, sulphides & sericite	Poikilitic, Lamellar twinning in plagioclase, ophitic OPX, euhedral OPX	Saussuritixation Amphibole	15%	Pyrrhotite: 70% Chalcopyrite:15% Pentlandite: 10% Chromite: 5%	Secondary sulphides replacing silicate minerals	Orthopyroxene: 80% Plagioclase: 10% Opaques: 5% Amphiboles: 2% Clay minerals: 2% Mica: 1% **Feldspathic pyroxenite**	

Z20-134.8	Orthopyroxene, plagioclase & clinopyroxene	Cordierite, phlogopite, biotite, sulphides & sericite	Euhedral OPX, lamellar twinning in plagioclase, CPX oikocrysts with OPX inclusions, ophitic OPX (LATHS)	Saussuritixation	2%	Pyrrhotite: 75% Pentlandite:15% Chalcopyrite:10%	OPX and CPX exsolution,	Orthopyroxene: 72% Plagioclase: 10% Clinopyroxene: 5% Cordierite: 5% Opaques: 5% Mica: 2% Clay minerals: 1% **Feldspathic pyroxenite**	
Z20-140.1	Clinopyroxene, orthopyroxene & plagioclase	Phlogopite, biotite, sulphides & sericite	Twinned CPX, lamellar twinning in plagioclase, granophyric quartz	Saussuritixation	60%	Pyrrhotite: 45% Chalcopyrite:35% Pentlandite: 15%	Secondary sulphides replacing silicate minerals, needle-like tremolite replacing sulphides	Clinopyroxene: 70% Plagioclase: 15% Orthopyroxene: 5% Opaques: 4% Quartz: 3% Mica: 2% Clay minerals: 1% **Gabbro**	
Z20-149.3	Orthopyroxene, plagioclase & clinopyroxene	Quartz, phlogopite, biotite, sulphides, magnetite & sericite	Twinned CPX, lamellar twinning in PLAG	Saussuritixation	5%	Pyrrhotite: 79% Chalcopyrite:10% Pentlandite: 5% Chromite: 5% Magnetite: 1%	CPX and OPX exsolution	Orthopyroxene: 75% Plagioclase: 10% Clinopyroxene: 5% Opaques: 5% Mica: 2% Clay minerals: 2% Quartz: 1% **Feldspathic pyroxenite**	
Z20-153.5	Orthopyroxene, clinopyroxene, cumulus plagioclase	Olivine, k-feldspar, phlogopite, sulphides, magnetite & sericite	Lamellar twinning in plagioclase, Carlsbad twinning in K-feldspar, twinned CPX	Saussuritixation	30%	Pyrrhotite: 50% Pentlandite: 40% Chalcopyrite:10%		Orthopyroxene: 60% Clinopyroxene: 20% Plagioclase: 10% Clay minerals: 5% Opaques: 3% Mica: 1% K-feldspar: 1% **Norite**	
Z20-164.5	Cumulus Plagioclase, orthopyroxene & clinopyroxene	K-feldspar, phlogopite, sulphides, magnetite & sericite	Ophitic, Inequigranular, Plagioclase laths with lamellar twinning, carlsbad twinning	Saussuritixation	2%	Pyrrhotite: 90% Magnetite: 10%	OPX and CPX exsolution,	Plagioclase: 40% Orthopyroxene: 35% Clinopyroxene: 12% K-feldspar: 5% Opaques: 5% Clay minerals: 2% Mica: 1% **Norite**	

Z20-173.7	Orthopyroxene, plagioclase	Cordierite, sulphides, magnetite, phlogopite, chlorite & sericite	Sieve textured OPX, lamellar twinning in plagioclase	Saussuritixation	20%	Pyrrhotite: 80% Chalcopyrite:10% Magnetite: 5% Pentlandite: 5%	OPX exsolution, secondary sulphides replacing silicate minerals	Orthopyroxene: 75% Plagioclase: 12% Opaques: 7% Mica: 3% Clay minerals: 3% **Feldspathic pyroxenite**	
Z20-175.5	Orthopyroxene, plagioclase	Quartz, phlogopite, sulphides & sericite	Inequigranular, euhedral OPX	Saussuritixation	15%	Pyrrhotite: 75% Chalcopyrite:20% Pentlandite: 5%	OPX exsolution,	Orthopyroxene: 78% Plagioclase: 10% Opaques: 5% Clay minerals: 4% Quartz: 1% **Feldspathic pyroxenite**	
Z20-175.9	Orthopyroxene, plagioclase	Quartz, graphite, phlogopite, biotite, sulphides & magnetite	Euhedral OPX, plagioclase with lamellar twinning, granophyric quartz	Saussuritixation	5%	Pyrrhotite: 90% Pentlandite: 7% Magnetite: 3%	Graphite rims around quartz grains	Orthopyroxenes: 75% Plagioclase: 10% Quartz: 5% Opaques: 5% Mica: 4% Graphite: 1% **Feldspathic pyroxenite**	
Z20-176	Orthopyroxene, plagioclase	Quartz, phlogopite, sulphides & sericite	Euhedral OPX plag with lamellar twinning,	Saussuritixation	10%	Pyrrhotite: 60% Chalcopyrite:40%	Graphite rims around quartz grains	Orthopyroxene: 75% Plagioclase: 15% Opaques: 5% Quartz: 2% Clay minerals: 2% Mica: 1% **Feldspathic pyroxenite**	
Z20-176.1	Orthopyroxene, plagioclase	Quartz, cordierite, phlogopite, biotite, sulphides and sericite	Sub-ophitic, lamellar twinning in plag,	Saussuritixation	2%	Pyrrhotite: 70% Pentlandite: 5% Chalcopyrite: 5% Magnetite: 20%		Orthopyroxene: 70% Plagioclase: 10% Mica: 8% Opaques: 3% Quartz: 3% Cordierite: 2% **Feldspathic pyroxenite**	

Z20-183.5	Pyroxene	Phlogopite, biotite, sulphides, amphibole (tremolite)		Tremolite Talc	10%	Pyrrhotite: 80% Magnetite: 10% Pentlandite: 5% Chalcopyrite: 5%		Pyroxene: 70% Mica: 20% Amphibole: 5% Opaques: 5% **Pyroxene-mica hornfels**	 **Pyroxene-mica hornfels with quartz-cordierite hornfels inclusions**
	Quartz Cordierite		Glomeroporphyritic; quartz clasts in fine grained pyroxene dominated groundmass			Pyrrhotite: 100%		**Quartz:55%** **Cordierite: 40%** **Opaques:5%** **quartz-cordierite hornfels inclusions**	
Z20-184.4	Quartz, phlogopite & biotite	Cordierite, sulphides, magnetite & amphibole	Glomeroporphyritic; quartz clasts in fine grained groundmass	Talc Chloritization	10%	Pyrrhotite: 70% Magnetite: 30% Chalcopyrite: 5%		Quartz: 40% Opaques: 20% Mica: 25% Cordierite: 10% Amphibole: 5% **Phlogopite hornfels**	
Z20-194.4	Quartz, biotite & phlogopite	Sulphides, magnetite, sericite & graphite	Glomeroporphyritic; quartz clasts in fine grained groundmass	Saussuritixation	15%	Pyrrhotite: 90% Pentlandite: 5% Chalcopyrite: 5%		Mica: 45% Quartz: 30% Opaques: 15% Graphite: 5% Clay minerals: 5% **Biotite hornfels**	
Z20-212.5	Clinopyroxene, carbonate minerals	Magnetite, sulphides, chlorite & sericite	Porphyritic	Chloritization Saussuritixation	70%	Pyrrhotite: 10% Magnetite: 90%		Clinopyroxene: 5% Opaques: 40% Carbonate minerals: 20% Clay minerals: 15% Groundmass: 20% **Calcsilicate with magnetite bands**	

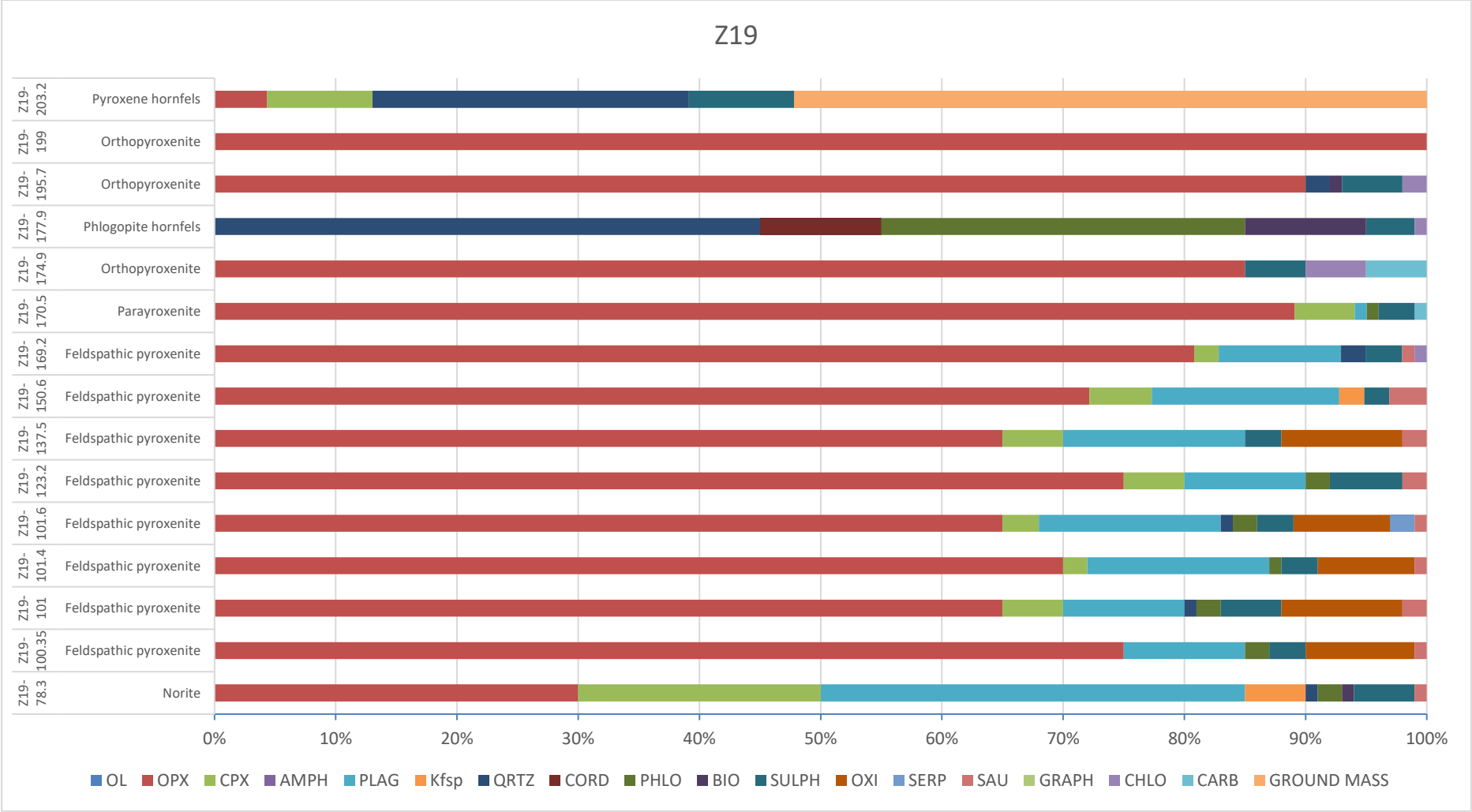


Figure 11-46: Modal mineralogy estimation bar chart for borehole Z19 thin sections.

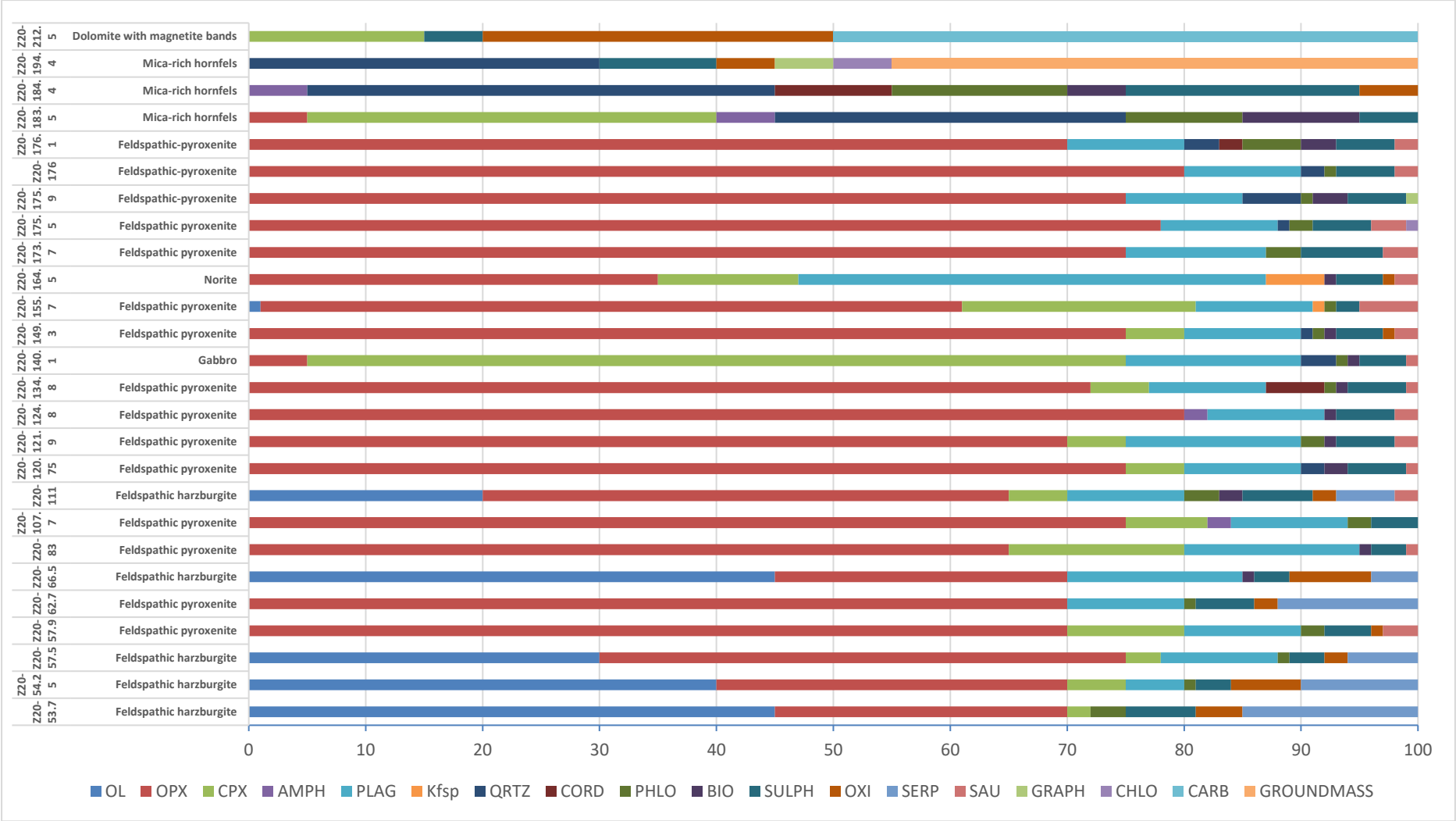


Figure 11-47: Modal mineralogy estimation bar chart for borehole Z20 thin sections.

4. SAMPLE LIST

Table 11-5: Samples list

BHID	From	To	Sample #	Initial rock classification (Macroscopic)	Final rock classification (Microscopic)
Z19	78.3	78.4	Z19-78.3	Norite	Norite
Z19	100.35	100.55	Z19-100.35	Feldspathic harzburgite	Feldspathic pyroxenite
Z19	101	101.1	Z19-101	Feldspathic harzburgite	Feldspathic pyroxenite
Z19	101.4	101.5	Z19-101.4	Feldspathic harzburgite	Feldspathic pyroxenite
Z19	101.6	101.7	Z19-101.6	Feldspathic harzburgite	Feldspathic harzburgite
Z19	123.2	123.37	Z19-123.2	Feldspathic pyroxenite	Feldspathic pyroxenite
Z19	137.5	137.7	Z19-137.5	Feldspathic pyroxenite	Feldspathic pyroxenite
Z19	150.6	150.73	Z19-150.6	Feldspathic pyroxenite	Feldspathic pyroxenite
Z19	169.2	169.3	Z19-169.2	Feldspathic pyroxenite	Feldspathic pyroxenite
Z19	170.5	170.7	Z19-170.5	Pyroxenite	Parapyroxenite
Z19	174.9	175.1	Z19-174.9	Parapyroxenite	Orthopyroxenite
Z19	177.9	178.7	Z19-177.9	Hornfels	Phlogopite Hornfels
Z19	195.7	195.8	Z19-195.7	Parapyroxenite	Orthopyroxenite
Z19	199	199.1	Z19-199	Parapyroxenite	Orthopyroxenite
Z19	203.2	203.4	Z19-203.2	Hornfels	Pyroxene hornfels
Z20	53.7	53.88	Z20- 53.7	Feldspathic harzburgite	Harzburgite
Z20	54.25	54.4	Z20-54.25	Feldspathic harzburgite	Feldspathic harzburgite
Z20	57.5	57.9	Z20-57.5	Feldspathic harzburgite	Feldspathic harzburgite
Z20	57.9	59.6	Z20-57.9	Feldspathic pyroxenite	Feldspathic pyroxenite
Z20	62.7	62.9	Z20-62.7	Feldspathic pyroxenite	Feldspathic pyroxenite
Z20	66.5	66.6	Z20-66.5	Feldspathic harzburgite	Feldspathic harzburgite
Z20	83	83.2	Z20-83	Feldspathic pyroxenite	Feldspathic pyroxenite
Z20	107.7	107.9	Z20-107.7	Feldspathic pyroxenite	Feldspathic pyroxenite
Z20	111	111.2	Z20-111	Feldspathic harzburgite	Feldspathic harzburgite
Z20	120.75	120.9	Z20-120.75	Feldspathic pyroxenite	Feldspathic pyroxenite
Z20	121.9	122	Z20-121.9	Feldspathic pyroxenite	Feldspathic pyroxenite
Z20	124.8	124.9	Z20-124.8	Feldspathic pyroxenite	Feldspathic pyroxenite
Z20	134.8	135.1	Z20-134.8	Feldspathic pyroxenite	Feldspathic pyroxenite
Z20	140.1	140.2	Z20-140.1	Gabbro	Gabbro
Z20	149.3	149.5	Z20-149.3	Feldspathic pyroxenite	Feldspathic pyroxenite
Z20	153.5	153.9	Z20-155.7	Feldspathic pyroxenite	Feldspathic pyroxenite
Z20	164.5	164.7	Z20-164.5	Norite	Norite
Z20	173.7	173.8	Z20-173.7	Feldspathic pyroxenite	Feldspathic pyroxenite
Z20	175.5	175.7	Z20-175.5	Feldspathic pyroxenite	Feldspathic pyroxenite
Z20	175.9	176	Z20-175.9	Feldspathic pyroxenite	Feldspathic pyroxenite
Z20	176	176.1	Z20-176	Feldspathic pyroxenite	Feldspathic pyroxenite
Z20	176.1	176.4	Z20-176.1	Feldspathic pyroxenite	Feldspathic pyroxenite
Z20	183.5	183.7	Z20-183.5	Hornfels	Pyroxene-rich hornfels
Z20	184.4	184.5	Z20-184.4	Hornfels	Phlogopite-rich hornfels
Z20	194.4	194.5	Z20-194.4	Hornfels	Biotite-rich hornfels
Z20	212.5	212.7	Z20-212.5	Dolomite with magnetite bands	Calcsilicate with magnetite bands

5. REFLECTED LIGHT MICROPHOTOGRAPHS

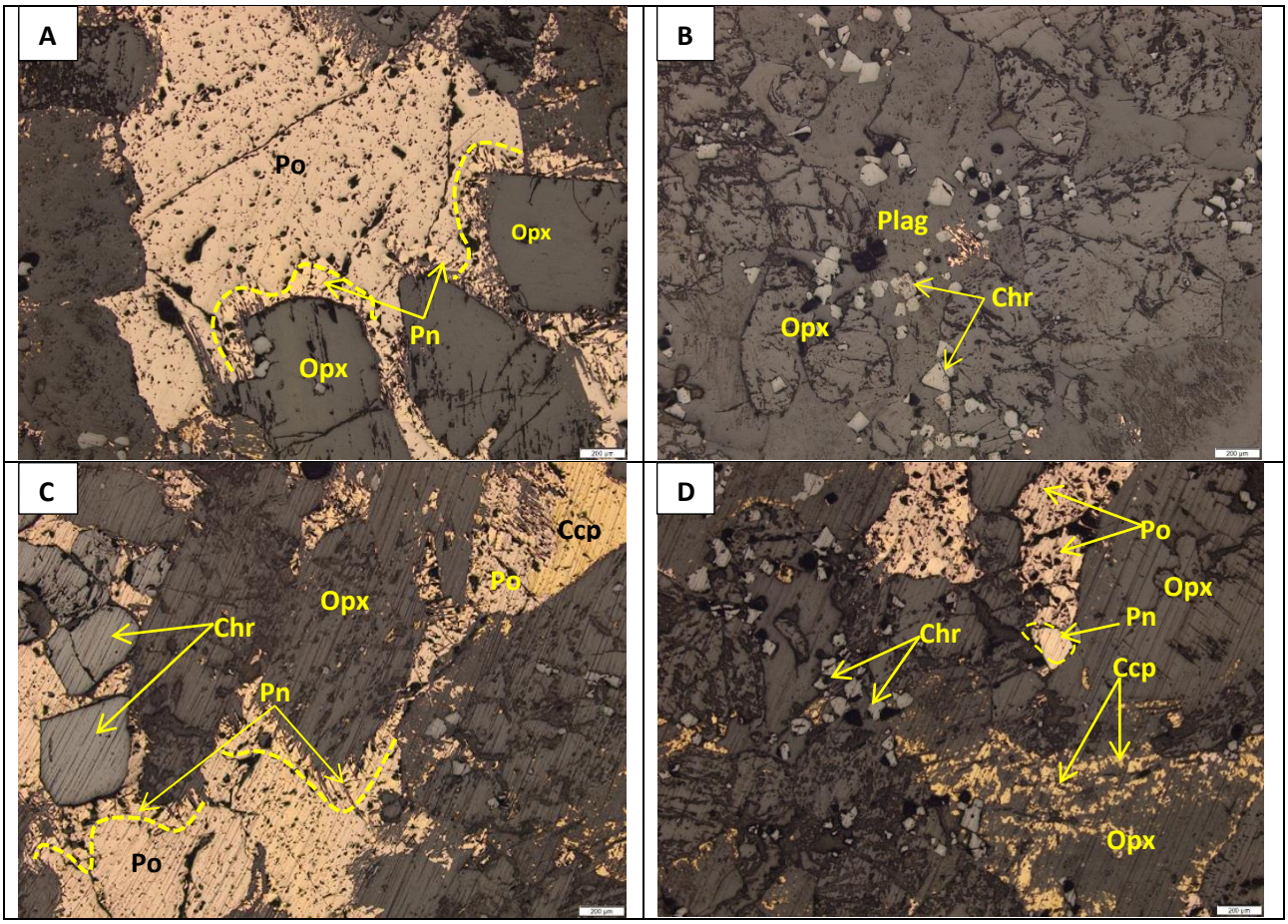


Figure 11-48: Photomicrographs, under reflected light, of sample Z19-78.3 (feldspathic pyroxenite) from the southwestern part of Uitloop farm.

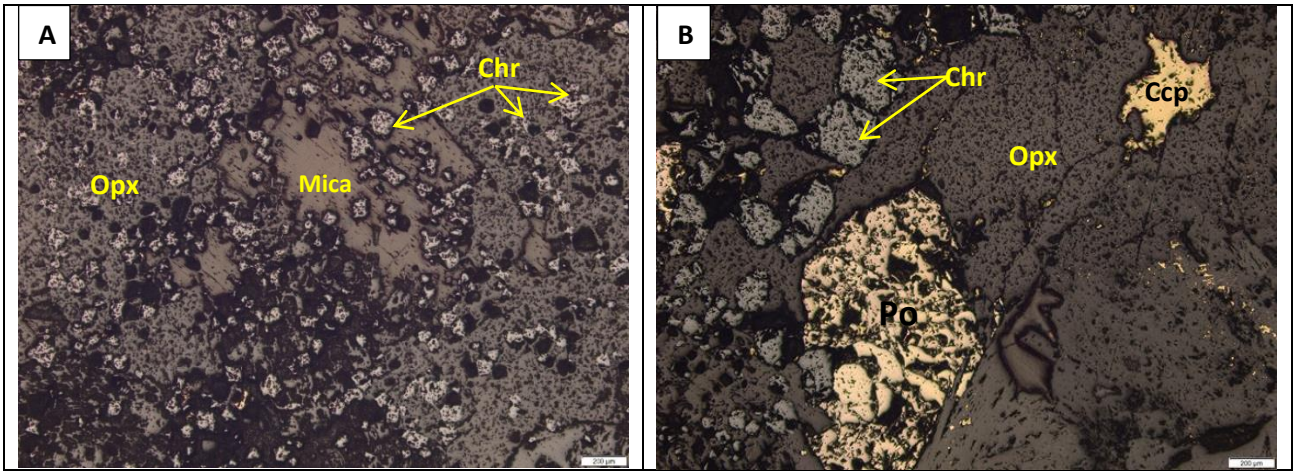


Figure 11-49: Photomicrographs, under reflected light, of sample Z19-100.35 (feldspathic pyroxenite) from the southwestern part of Uitloop farm.

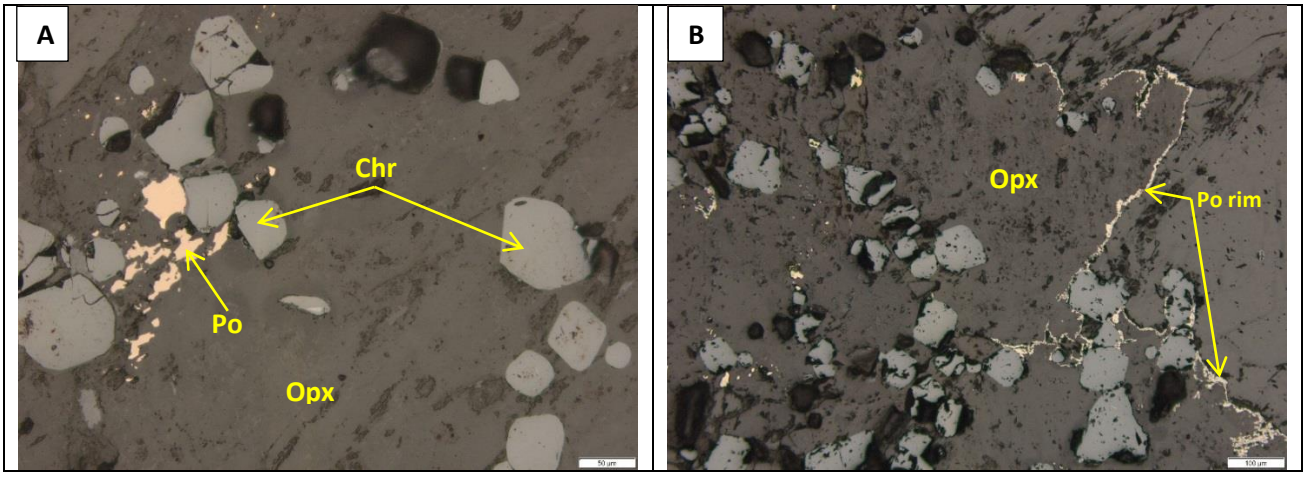


Figure 11-50: Photomicrographs, under reflected light, of sample Z19-101 (feldspathic pyroxenite) from the southwestern part of Uitloop farm.

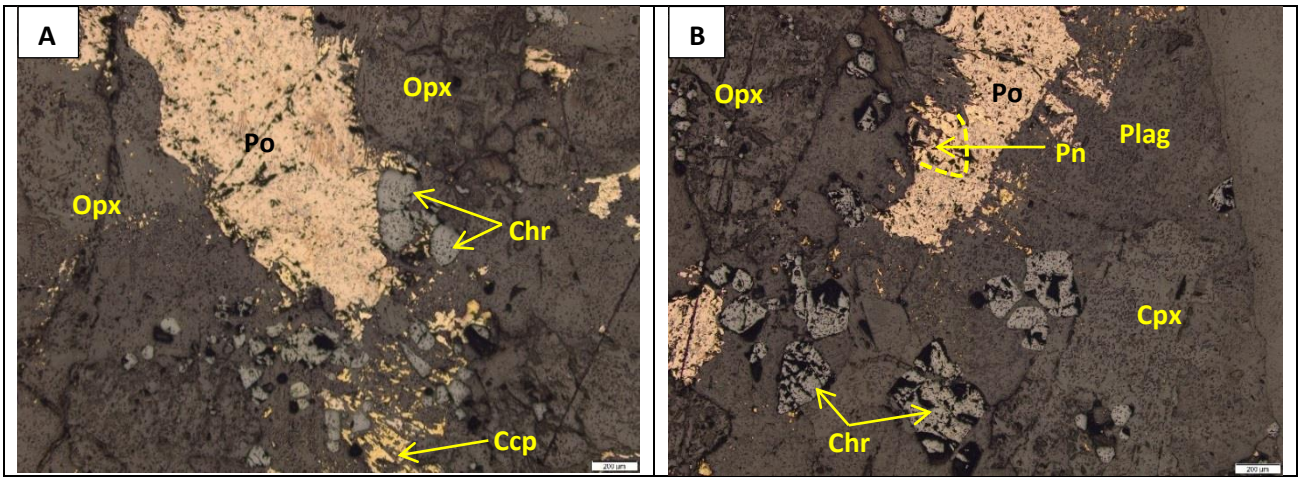


Figure 11-51: Photomicrographs, under reflected light, of sample Z19- 101.4 (feldspathic pyroxenite) from the southwestern part of Uitloop farm.

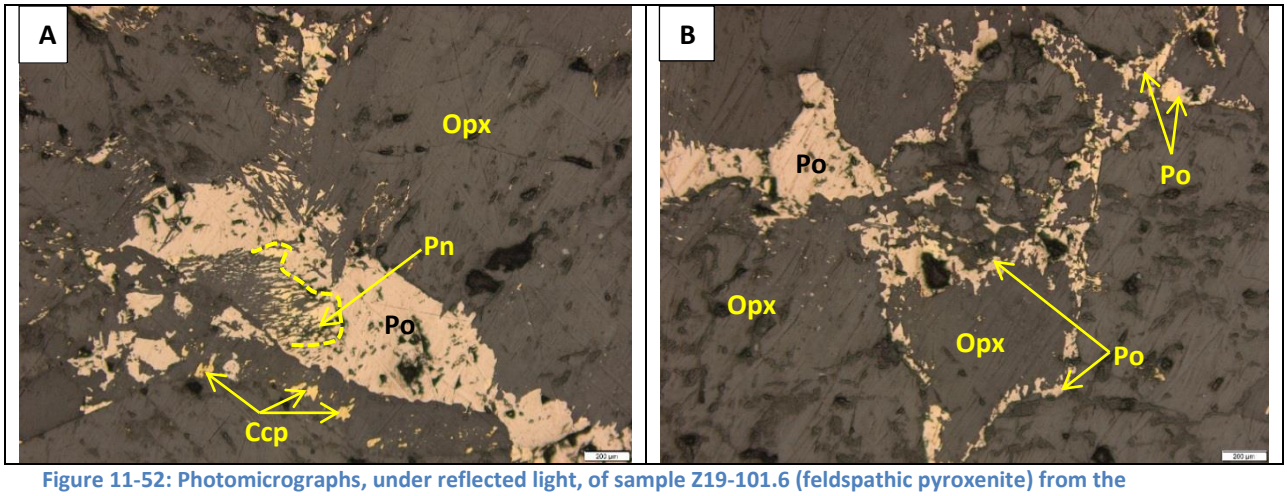


Figure 11-52: Photomicrographs, under reflected light, of sample Z19-101.6 (feldspathic pyroxenite) from the southwestern part of Uitloop farm.

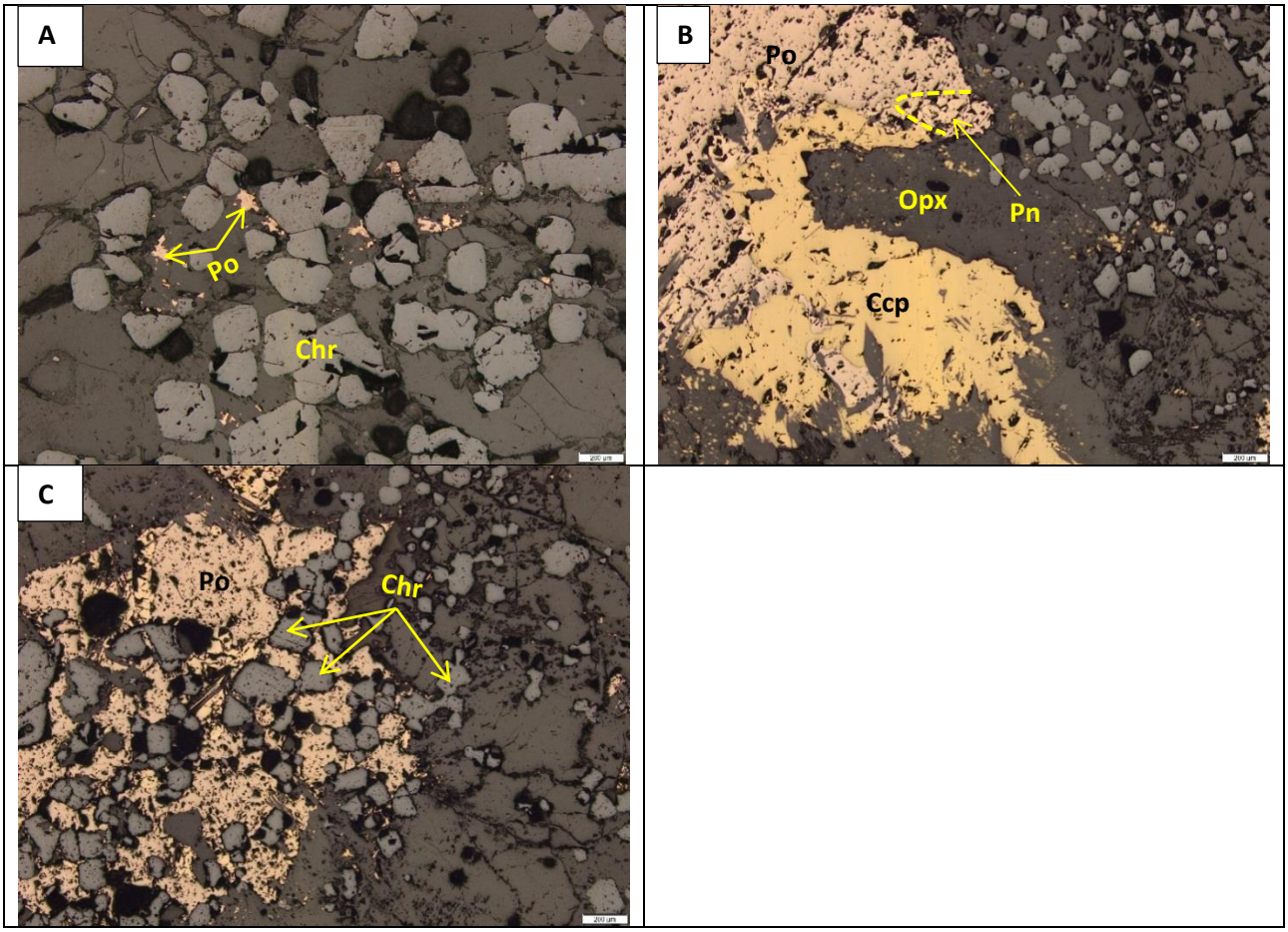


Figure 11-53: Photomicrographs, under reflected light, of sample Z19-123.2 (feldspathic pyroxenite) from the southwestern part of Uitloop farm.

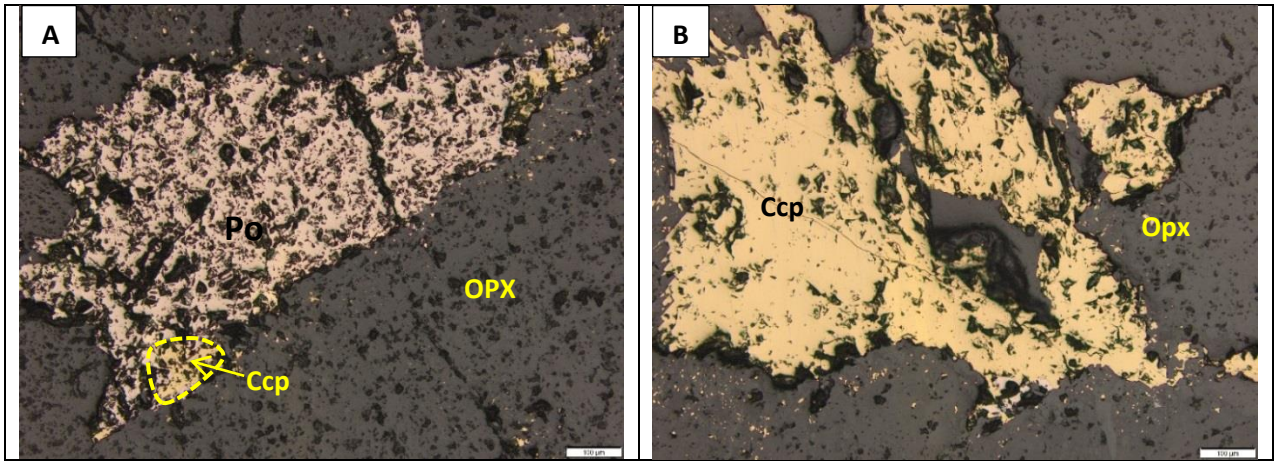


Figure 11-54: Photomicrographs, under reflected light, of sample Z19-150.6 (feldspathic pyroxenite) from the southwestern part of Uitloop farm.

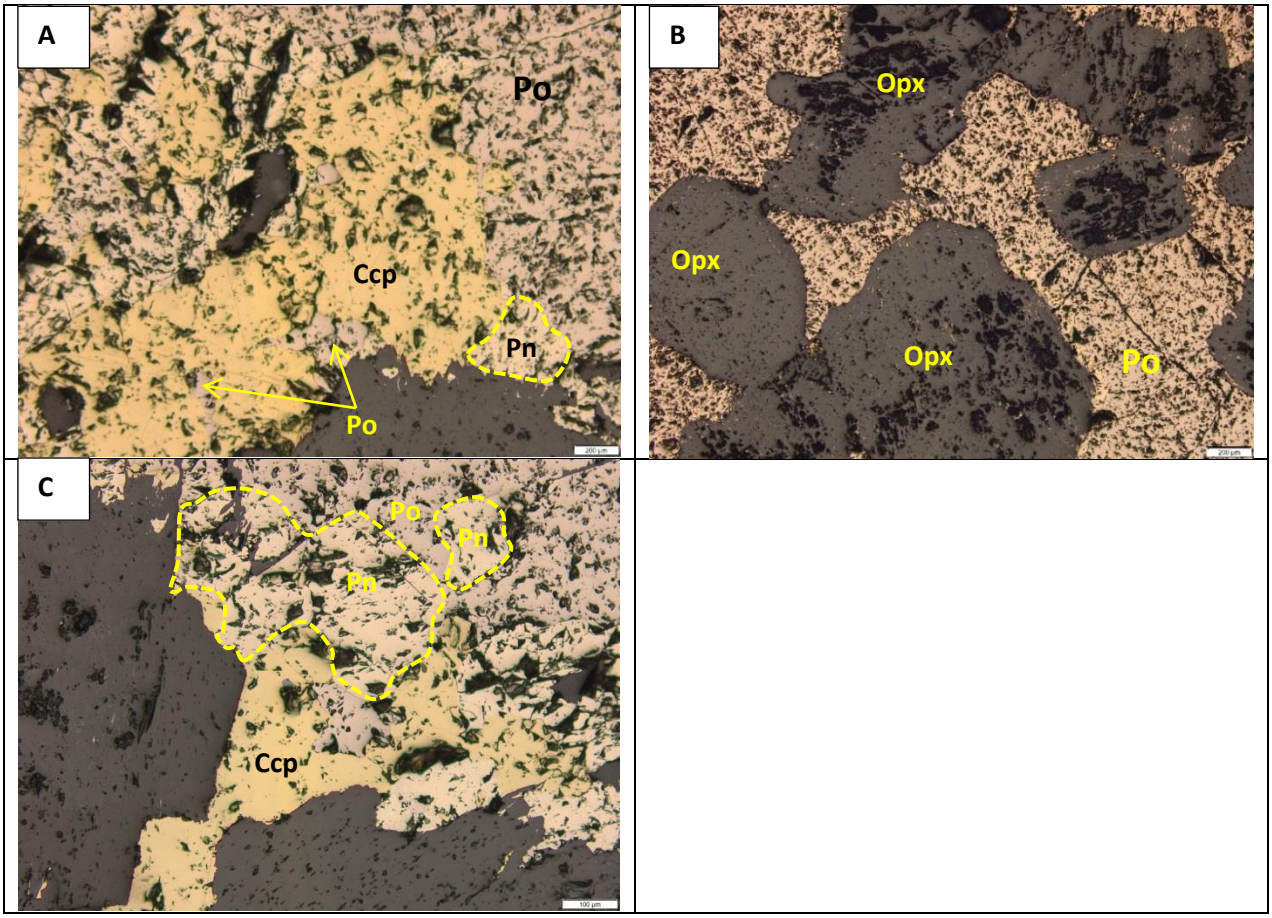


Figure 11-55: Photomicrographs, under reflected light, of sample Z19-169.2 (feldspathic pyroxenite) from the southwestern part of Uitloop farm.

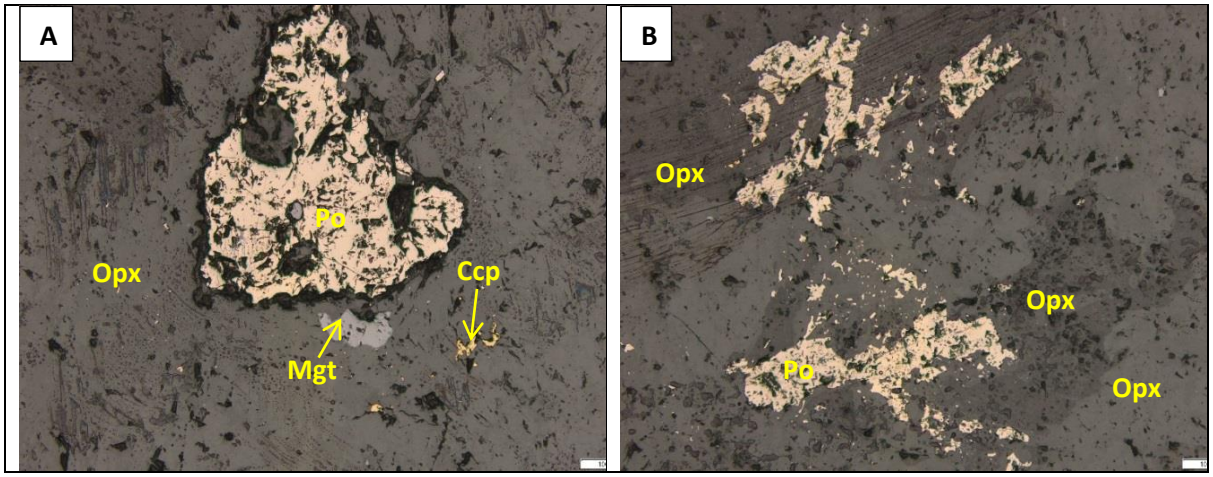


Figure 11-56: Photomicrographs, under reflected light, of sample Z19-170.5 (parapyroxenite) from the southwestern part of Uitloop farm.

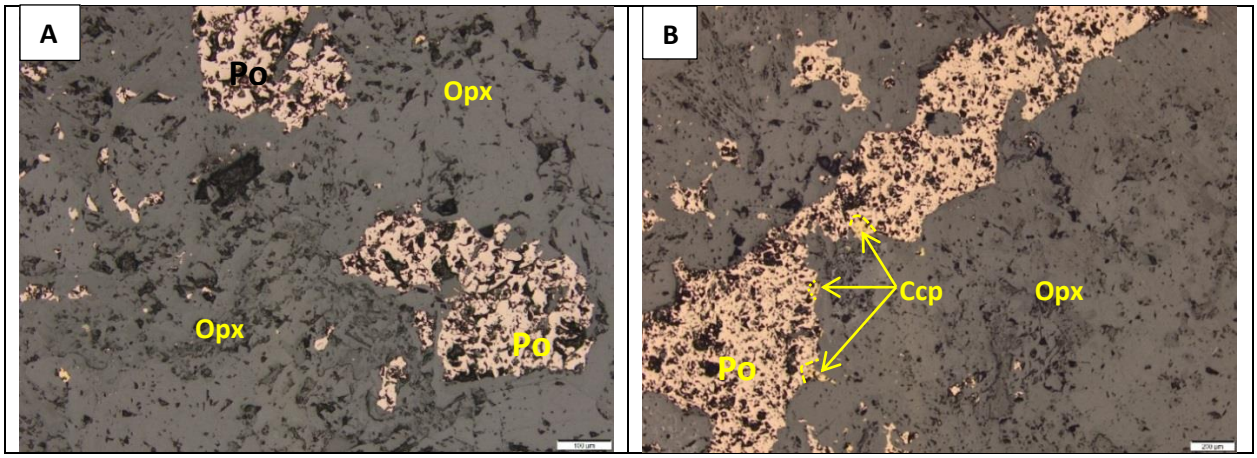


Figure 11-57: Photomicrographs, under reflected light, of sample Z19-174.9 (parapyroxenite) from the southwestern part of Uitloop farm.

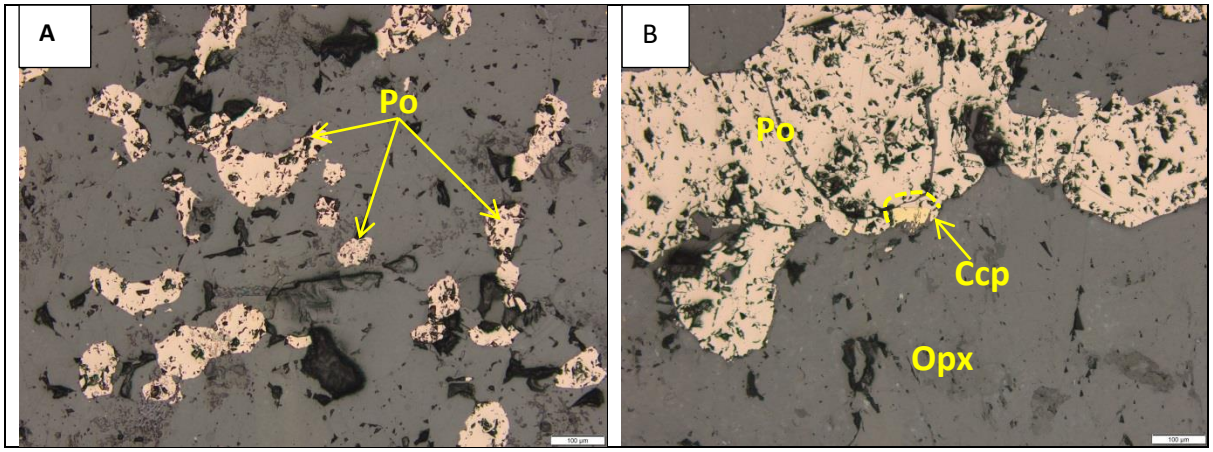


Figure 11-58: Photomicrographs, under reflected light, of sample Z19-195.5 (orthopyroxenite) from the southwestern part of Uitloop farm.

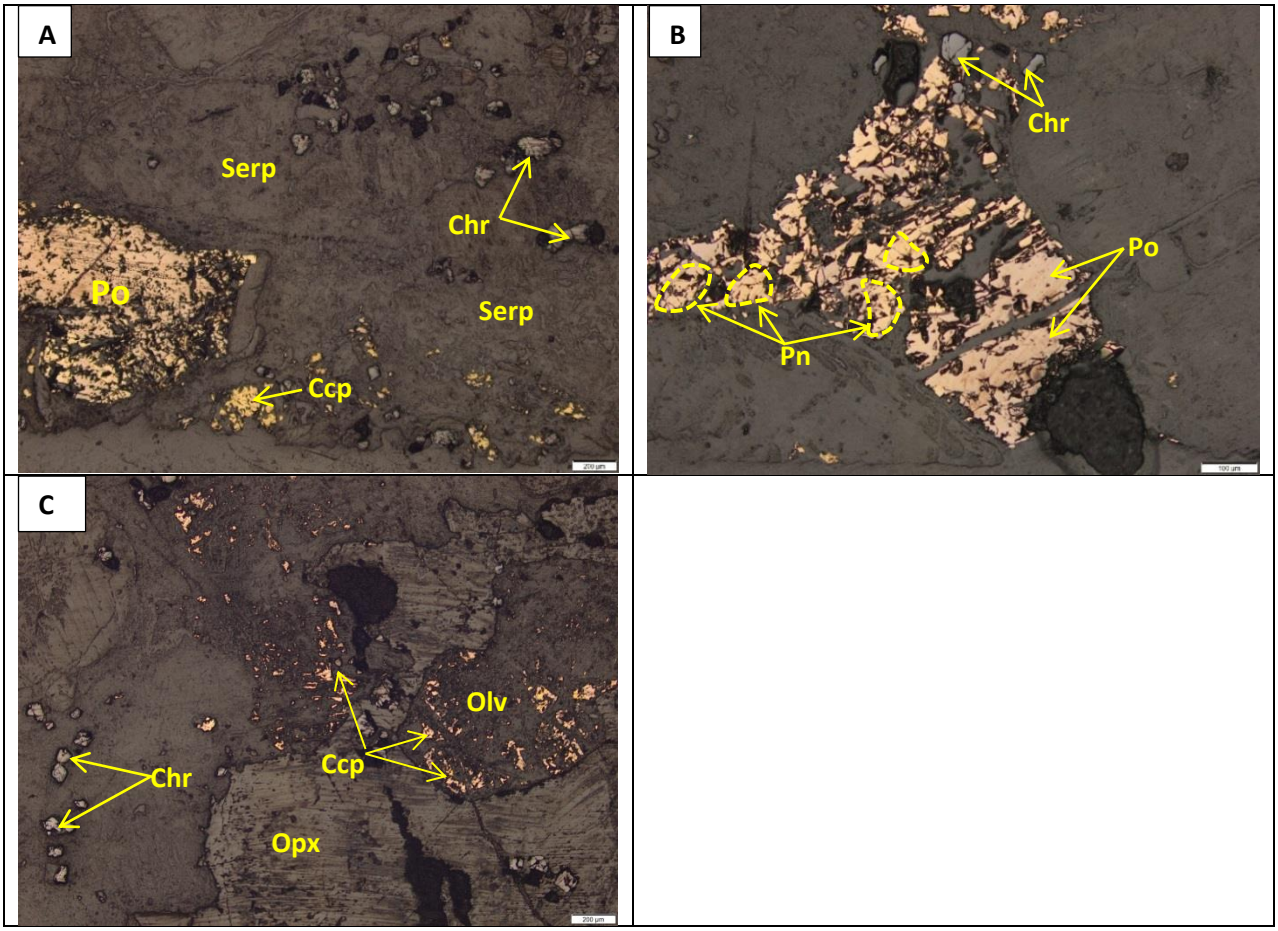


Figure 11-59: Photomicrographs, under reflected light, of sample Z20-53.7 (harzburgite) from the southwestern part of Uitloop farm.

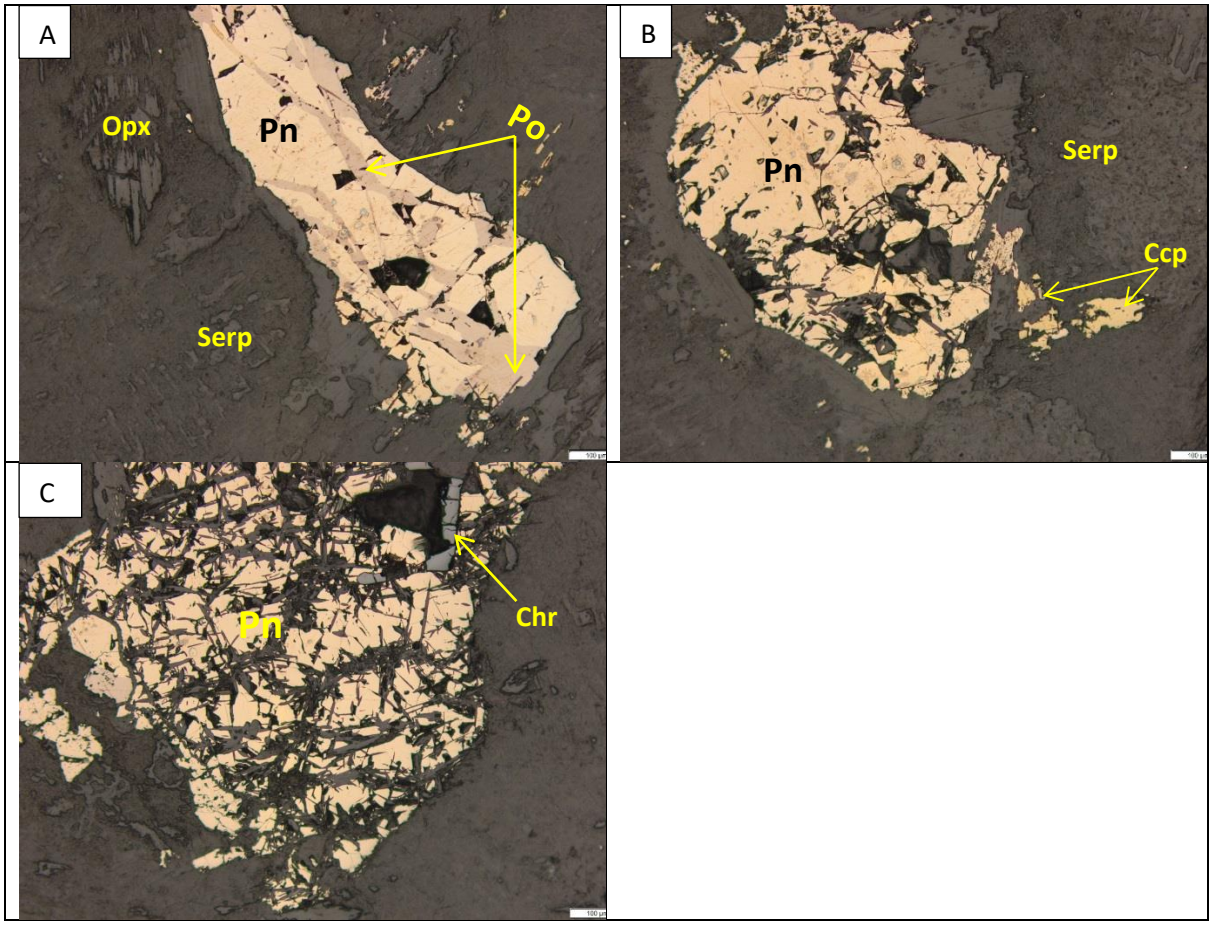


Figure 11-60: Photomicrographs, under reflected light, of sample Z20-54.25 (harzburgite) from the southwestern part of Uitloop farm.

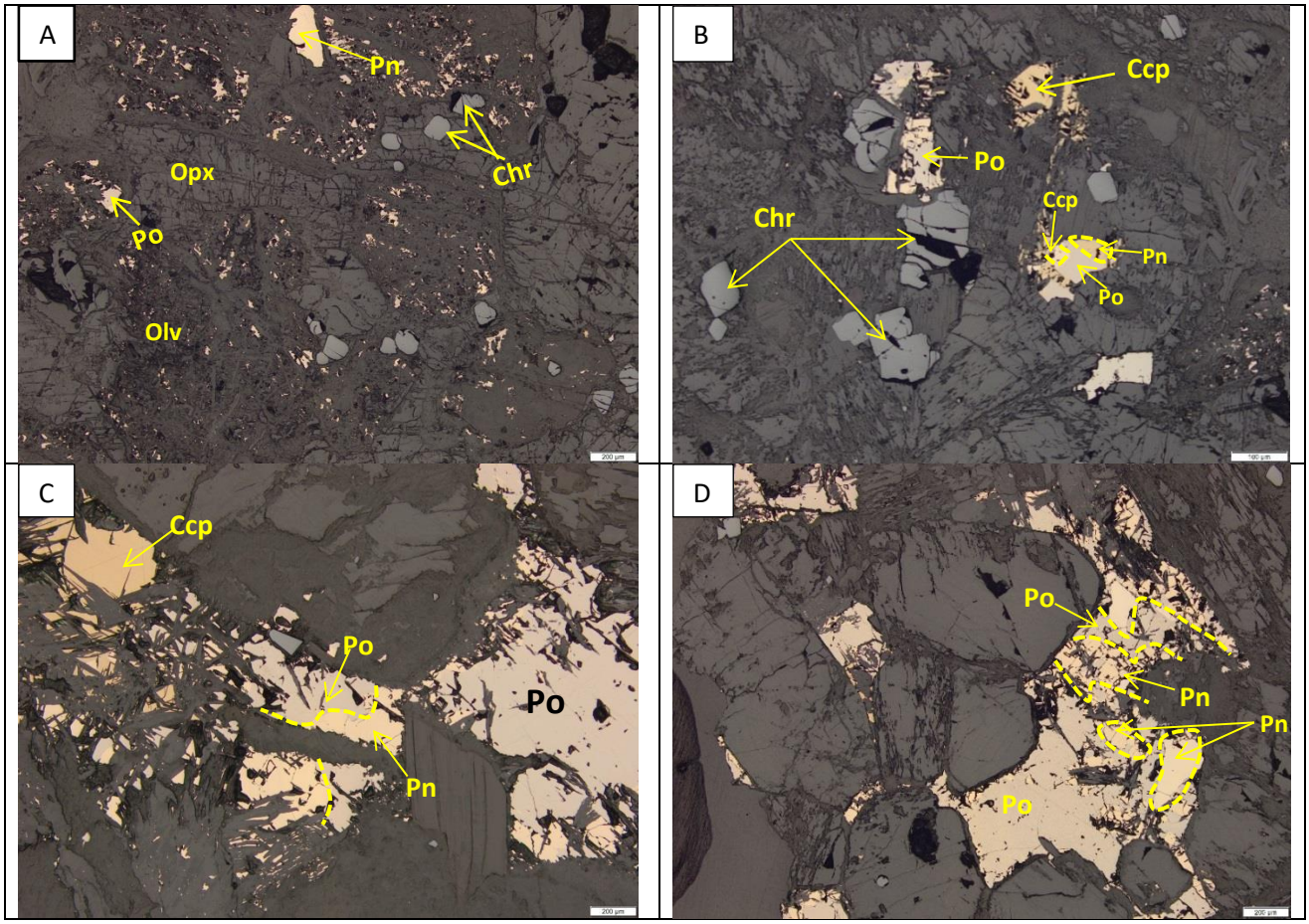


Figure 11-61: Photomicrographs, under reflected light, of sample Z20-57.5 (feldspathic harzburgite) from the southwestern part of the Uitloop farm.

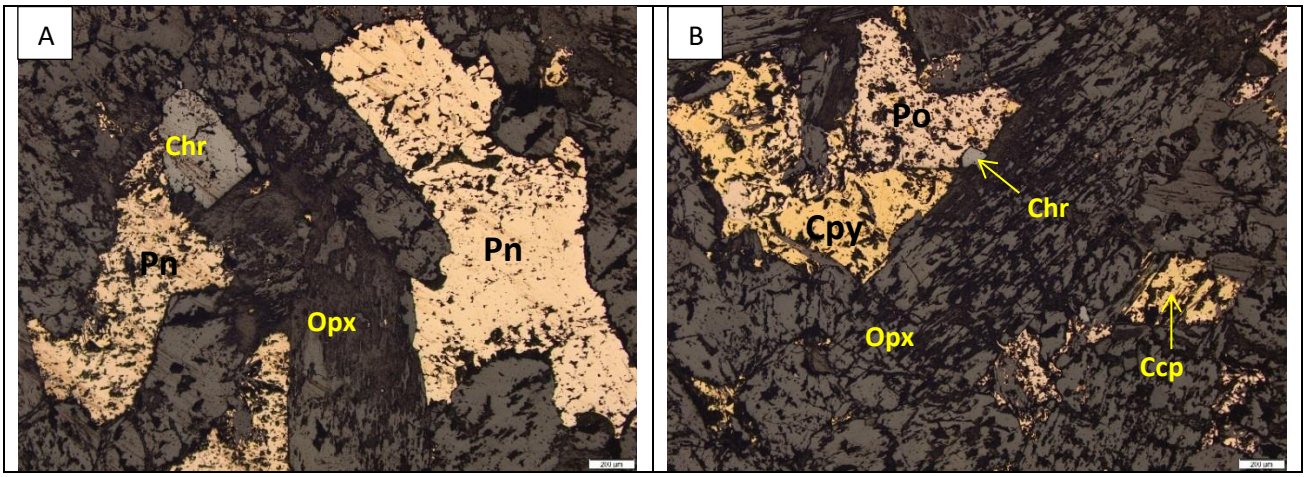


Figure 11-62: Photomicrographs, under reflected light, of sample Z20-57.9 (feldspathic pyroxenite) from the southwestern part of the Uitloop farm.

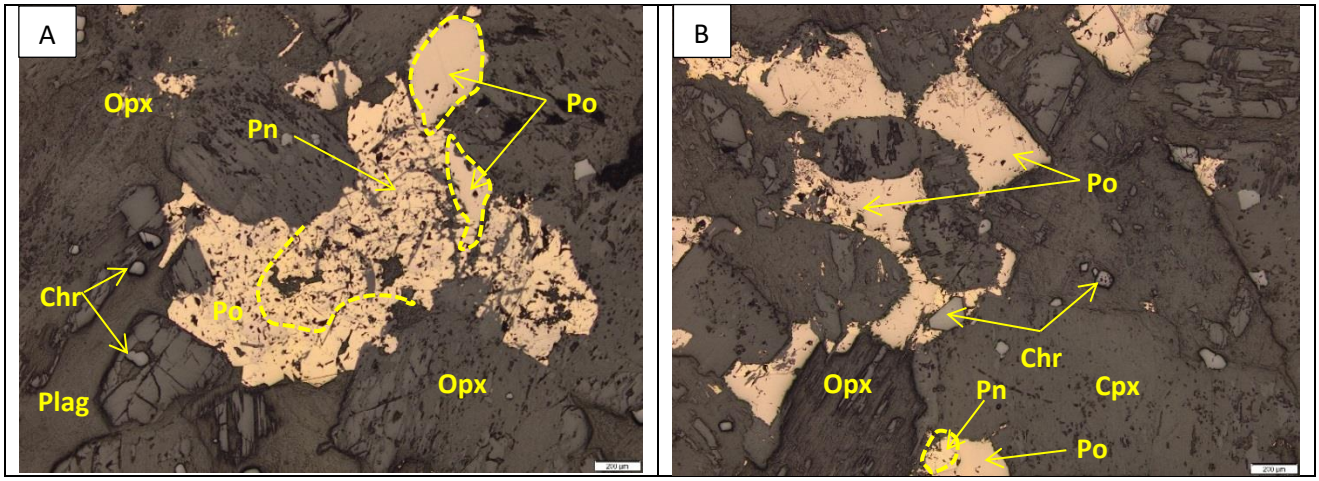


Figure 11-63: Photomicrographs, under reflected light, of sample Z20-62.7 (feldspathic pyroxenite) from the southwestern part of the Uitloop farm.

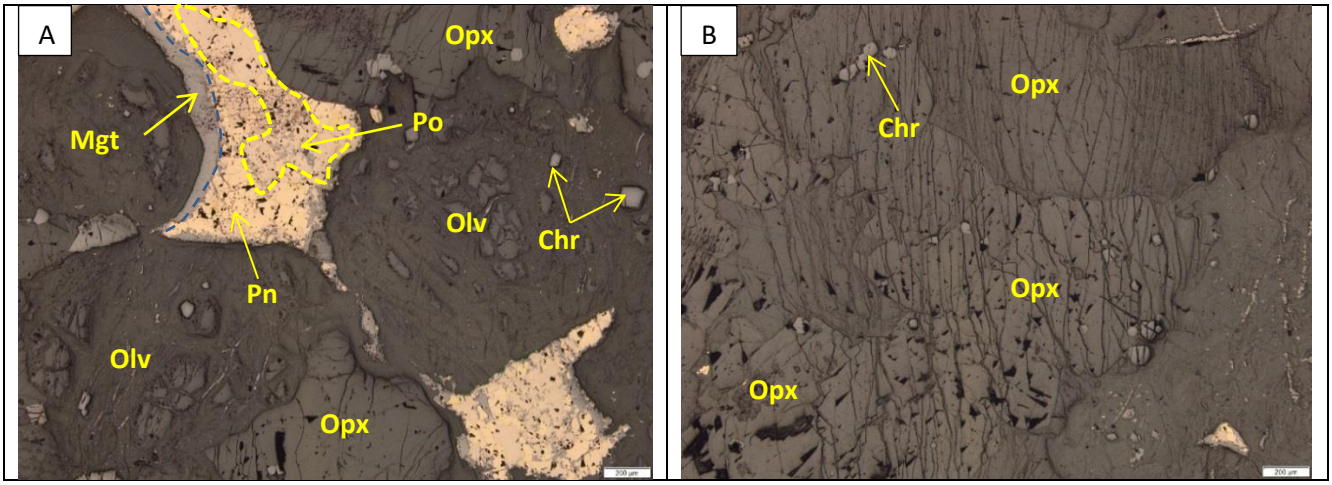


Figure 11-64: Photomicrographs, under reflected light, of sample Z20-66.5 (feldspathic harzburgite) from the southwestern part of the Uitloop farm.

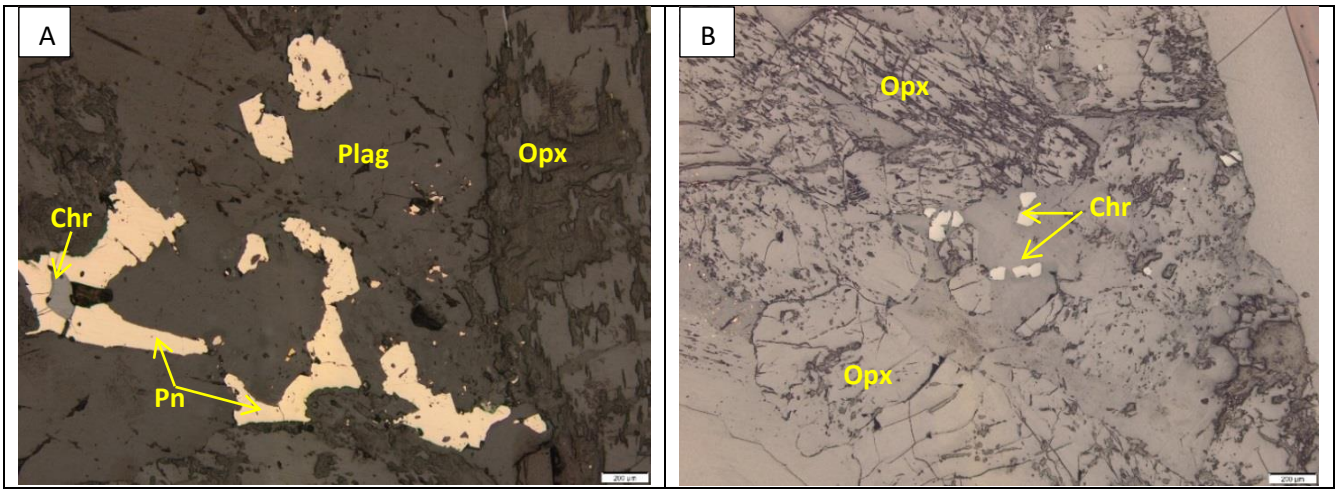


Figure 11-65: Photomicrographs, under reflected light, of sample Z20-83.2 (feldspathic pyroxenite) from the southwestern part of the Uitloop farm.

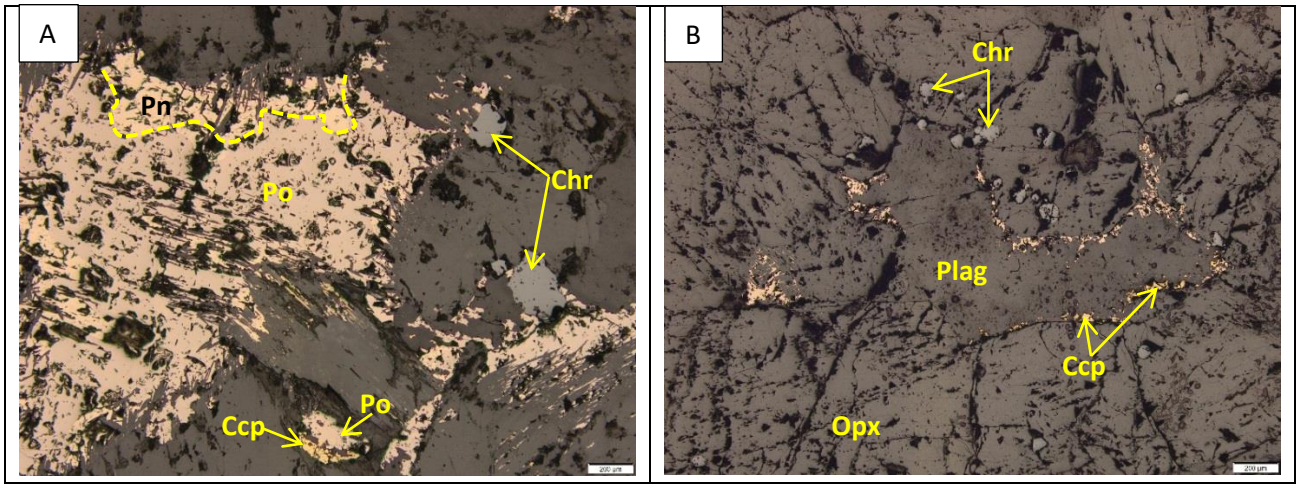


Figure 11-66: Photomicrographs, under reflected light, of sample Z20-107.7 (feldspathic pyroxenite) from the southwestern part of the Uitloop farm.

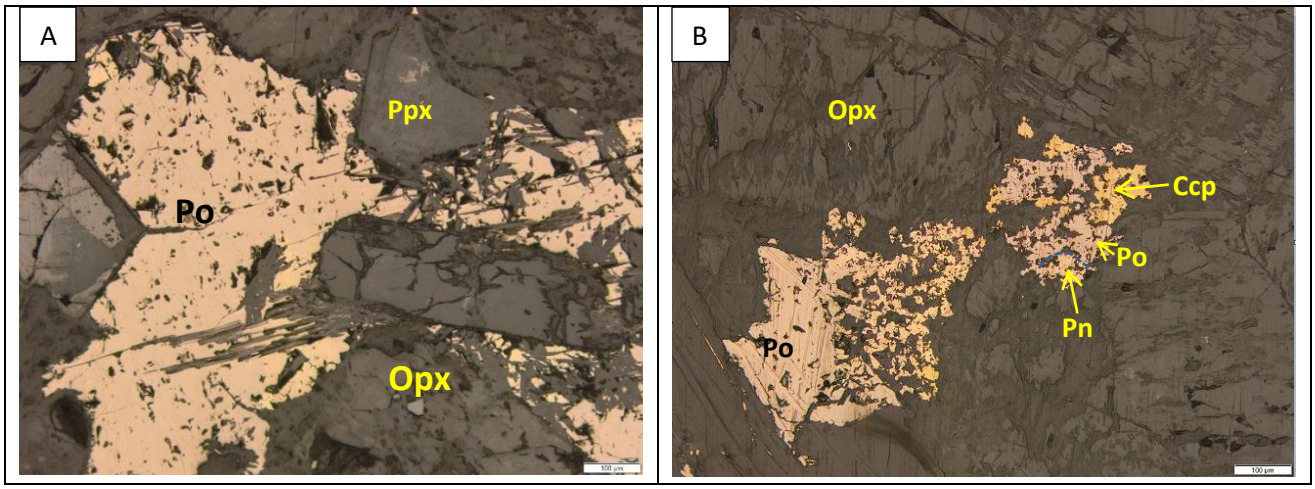


Figure 11-67: Photomicrographs, under reflected light, of sample Z20-111 (feldspathic harzburgite) from the southwestern part of the Uitloop farm.

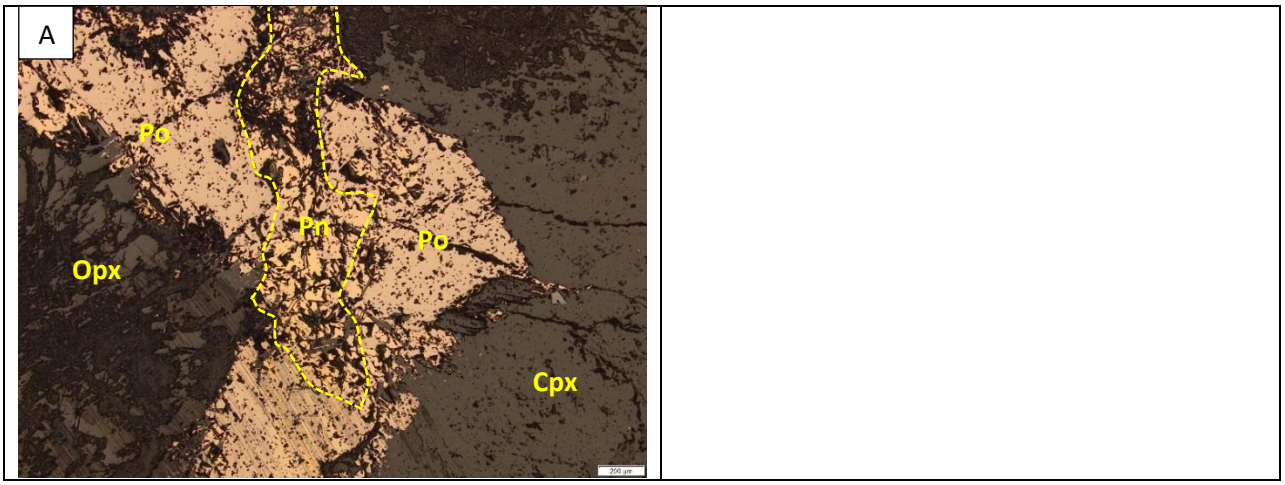


Figure 11-68: Photomicrographs, under reflected light, of sample Z20-120.75 (feldspathic pyroxenite) from the southwestern part of the Uitloop farm.

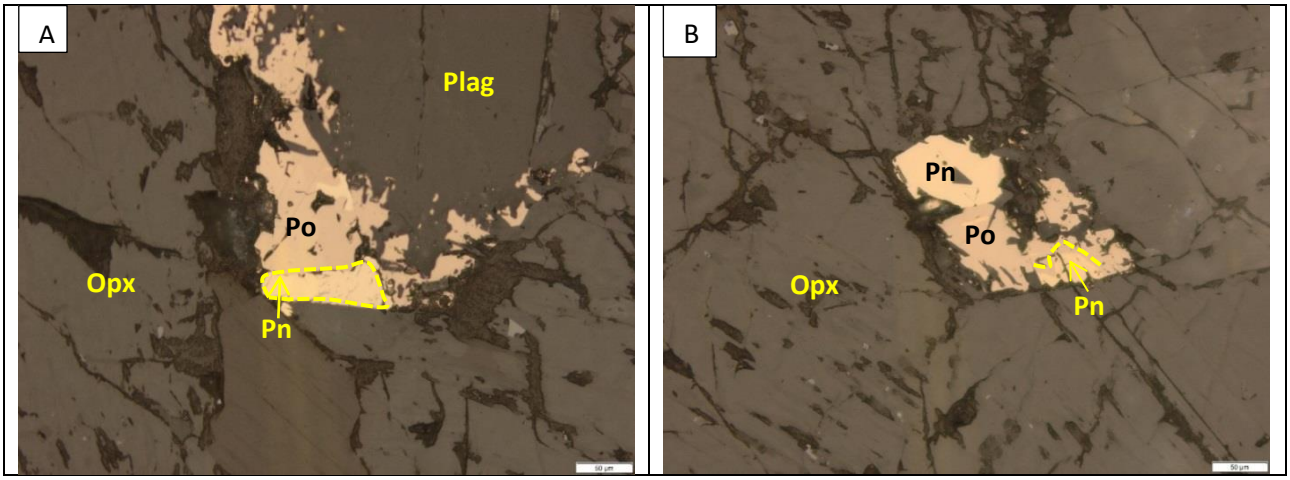


Figure 11-69: Photomicrographs, under reflected light, of Sample Z20-121.9 (feldspathic pyroxenite) from the southwestern part of the Uitloop farm.

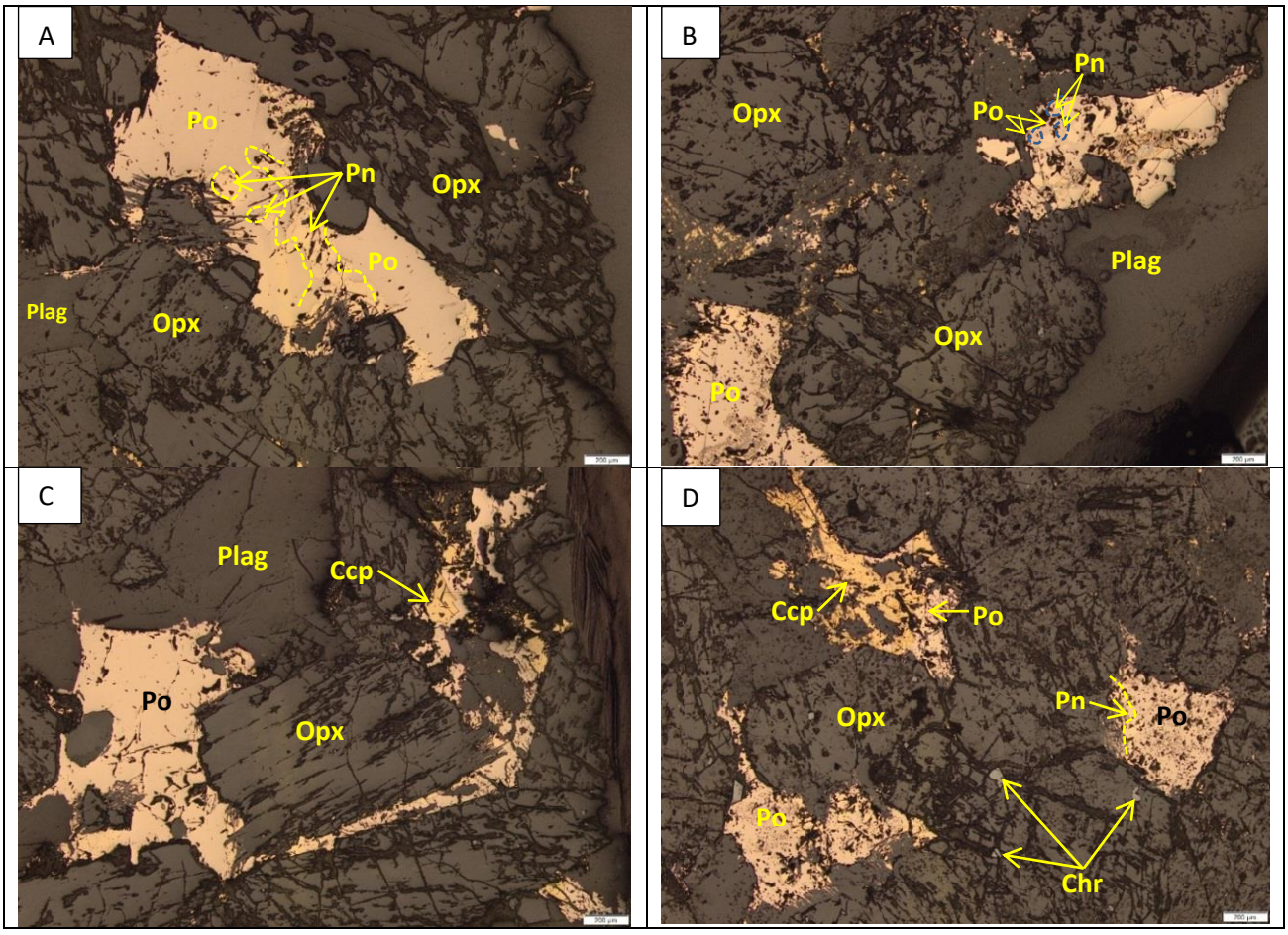


Figure 11-70: Photomicrographs, under reflected light, of feldspathic pyroxenite (Sample Z20-124.8) from the southwestern part of the Uitloop farm.

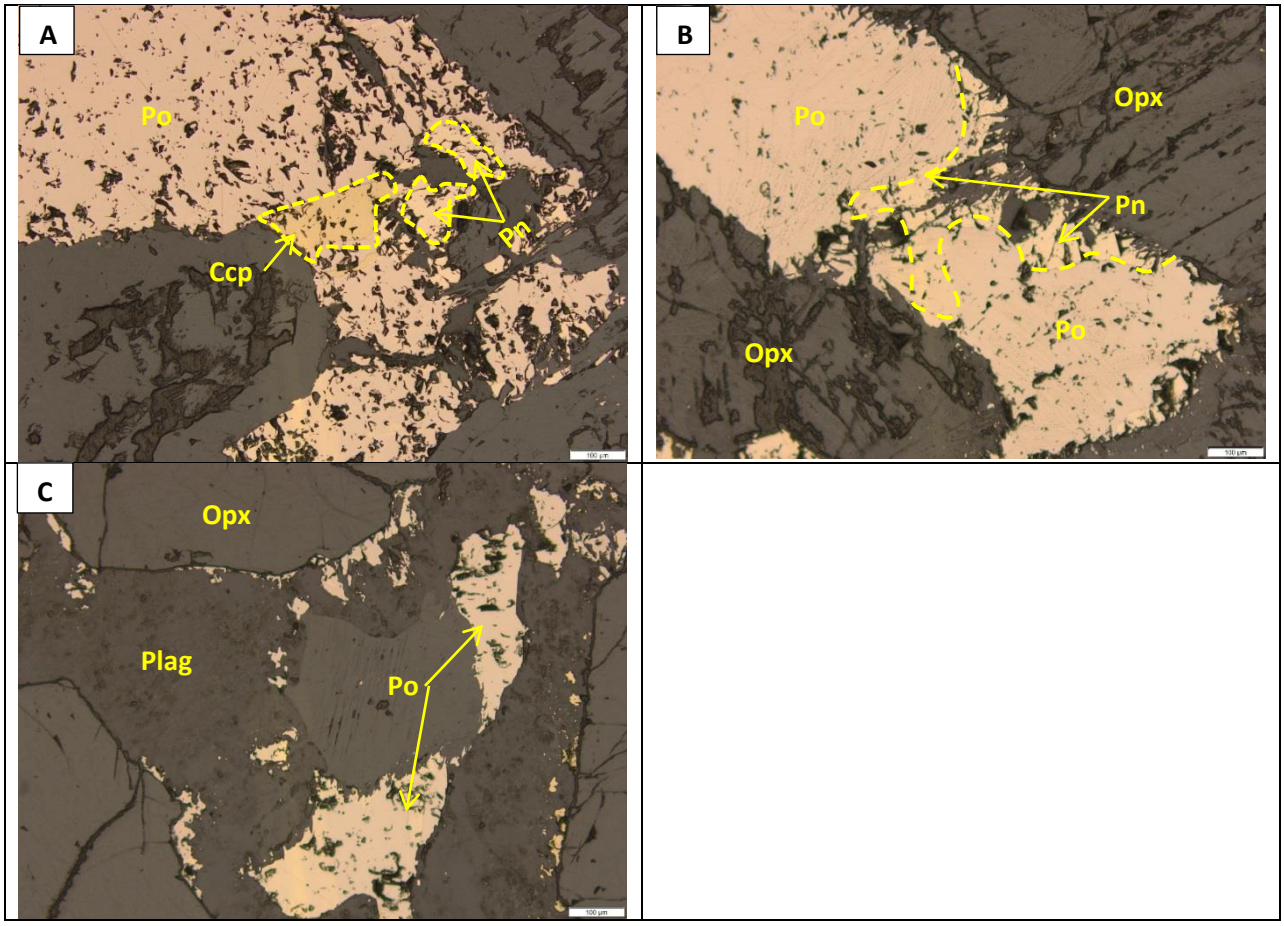


Figure 11-71: Photomicrographs, under reflected light, of feldspathic pyroxenite (Sample Z20-134.8) from the southwestern part of the Uitloop farm.

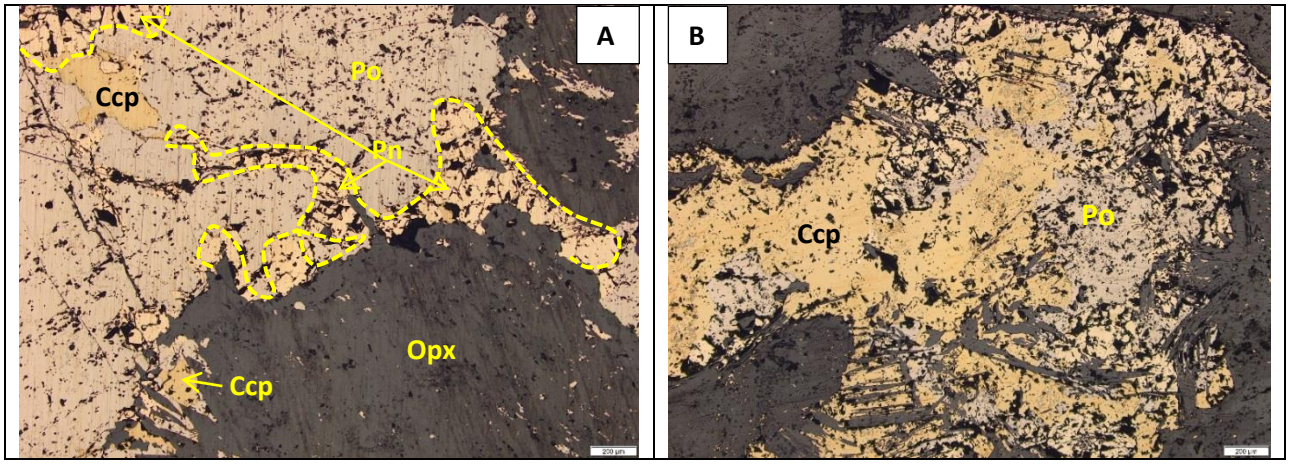


Figure 11-72: Photomicrographs, under reflected light, of gabbro (sample Z20-140.1) from the southwestern part of the Uitloop farm.

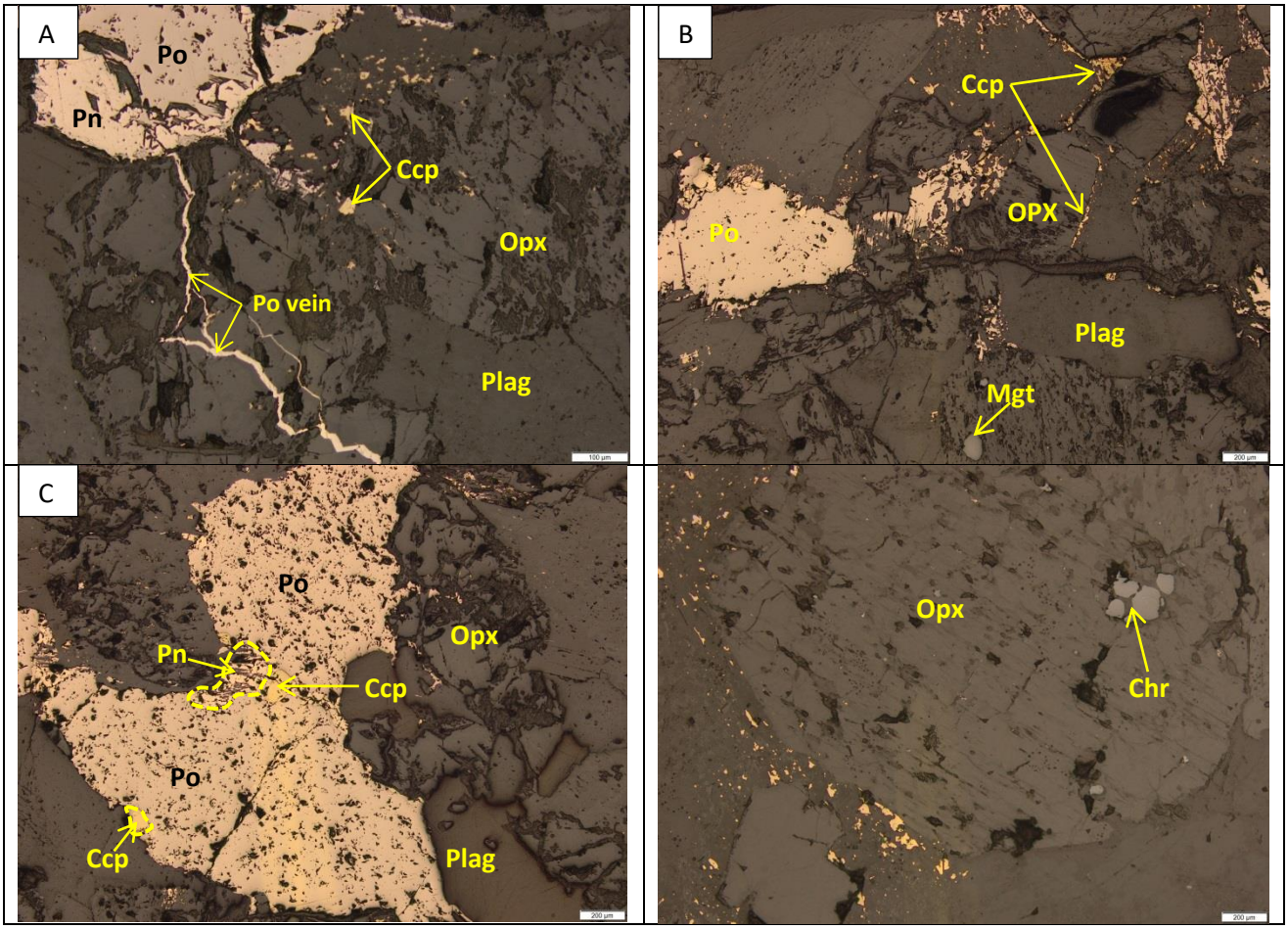


Figure 11-73: Photomicrographs, under reflected light, of feldspathic pyroxenite (sample Z20-149.3) from the southwestern part of the Uitloop farm.

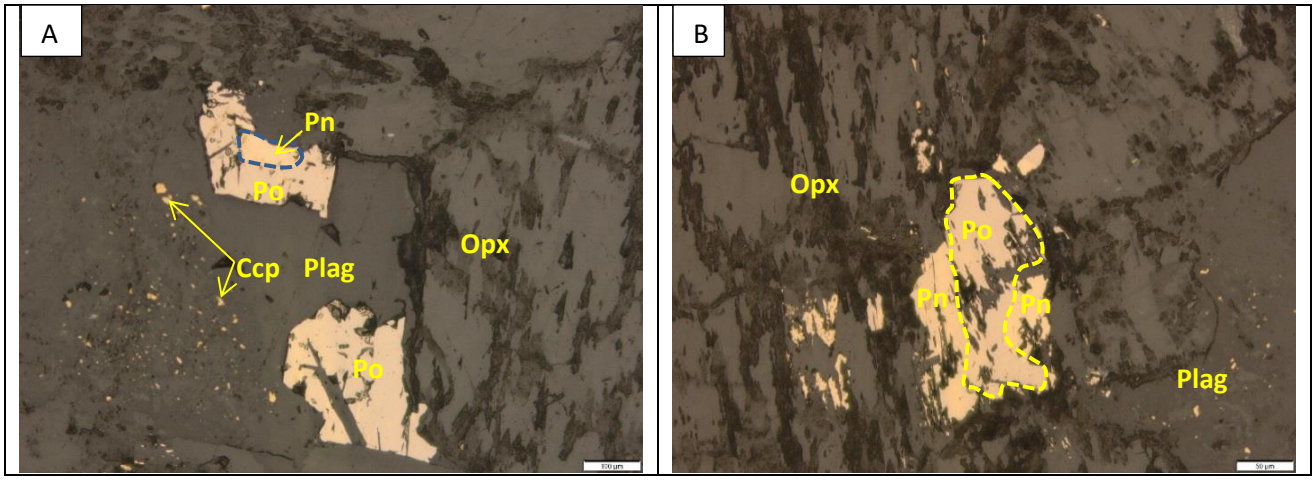


Figure 11-74: Photomicrographs, under reflected light, of feldspathic pyroxenite (sample Z20-155.7) from the southwestern part of the Uitloop farm.

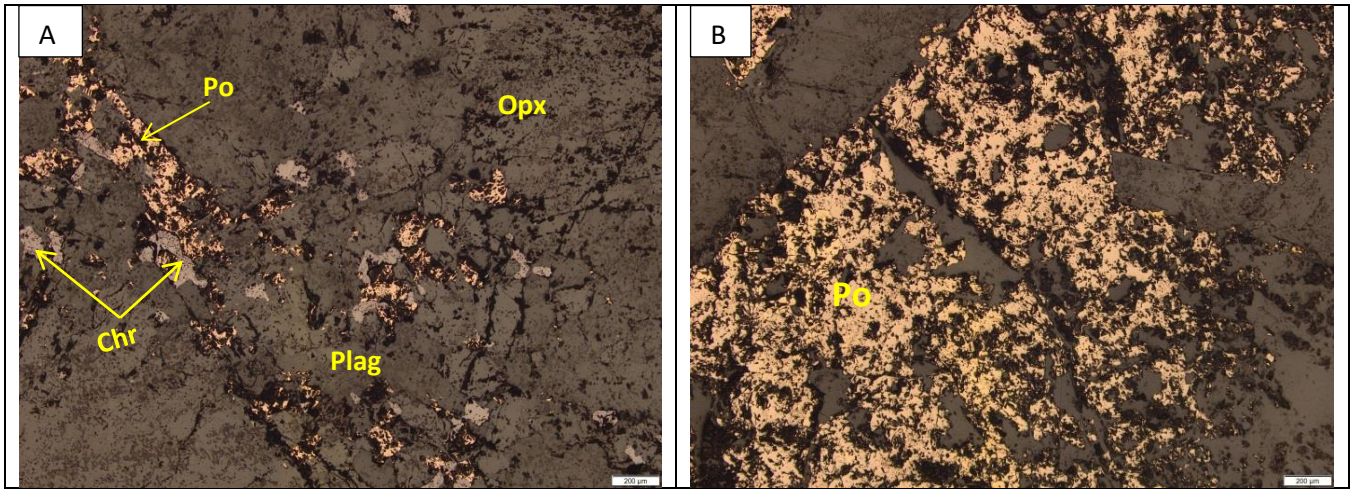


Figure 11-75: Photomicrographs, under reflected light, of norite (sample Z20-153.5) from the southwestern part of the Uitloop farm.

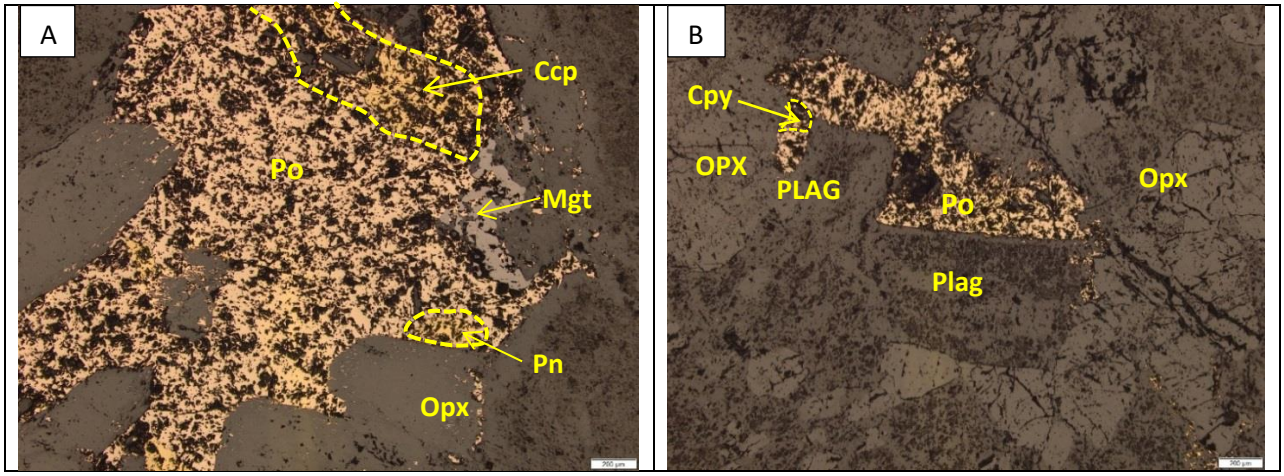


Figure 11-76: Photomicrographs, under reflected light, of feldspathic pyroxenite (sample Z20-173.7) from southwestern part of the Uitloop farm.

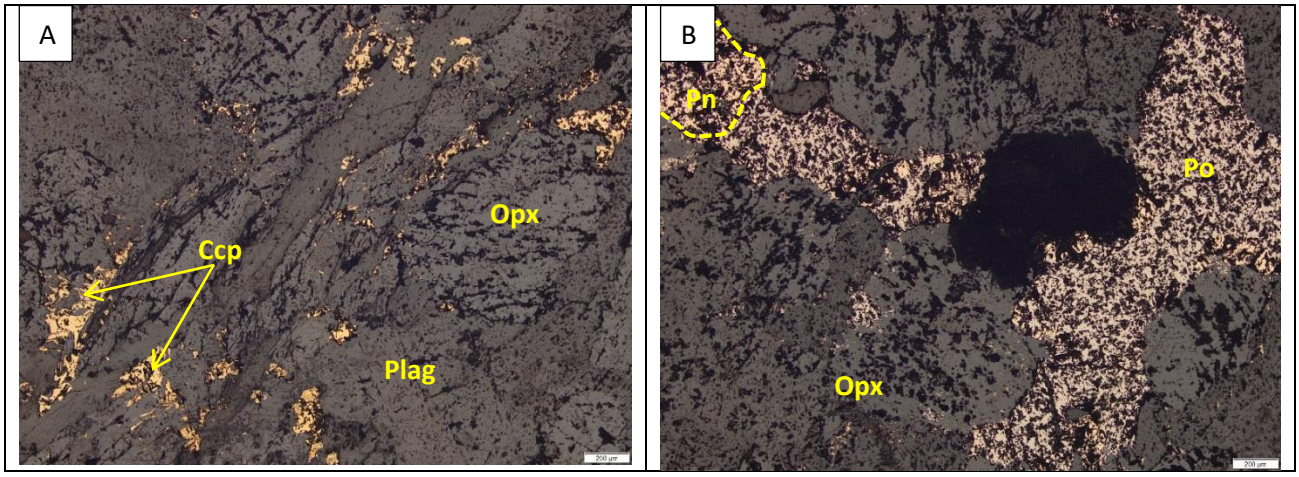


Figure 11-77: Photomicrographs, under reflected light, of feldspathic pyroxenite (sample Z20-175.5) from the southwestern part of the Uitloop farm.

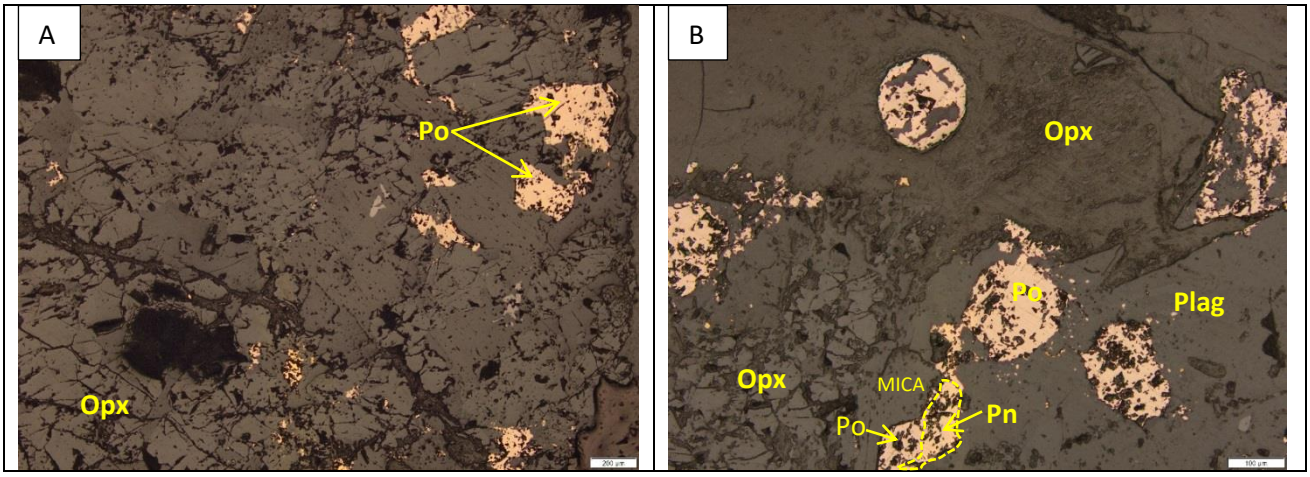


Figure 11-78: Photomicrographs, under reflected light, of feldspathic pyroxenite (sample Z20-175.9) from the southwestern part of the Uitloop farm.

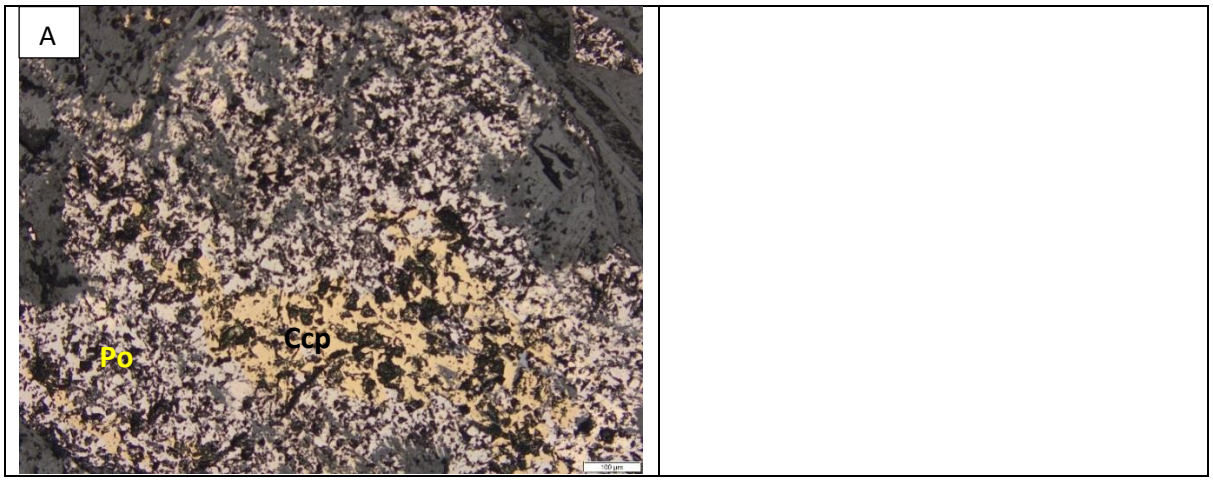


Figure 11-79: Photomicrographs, under reflected light, of feldspathic pyroxenite (sample Z20-176) from the southwestern part of the Uitloop farm.

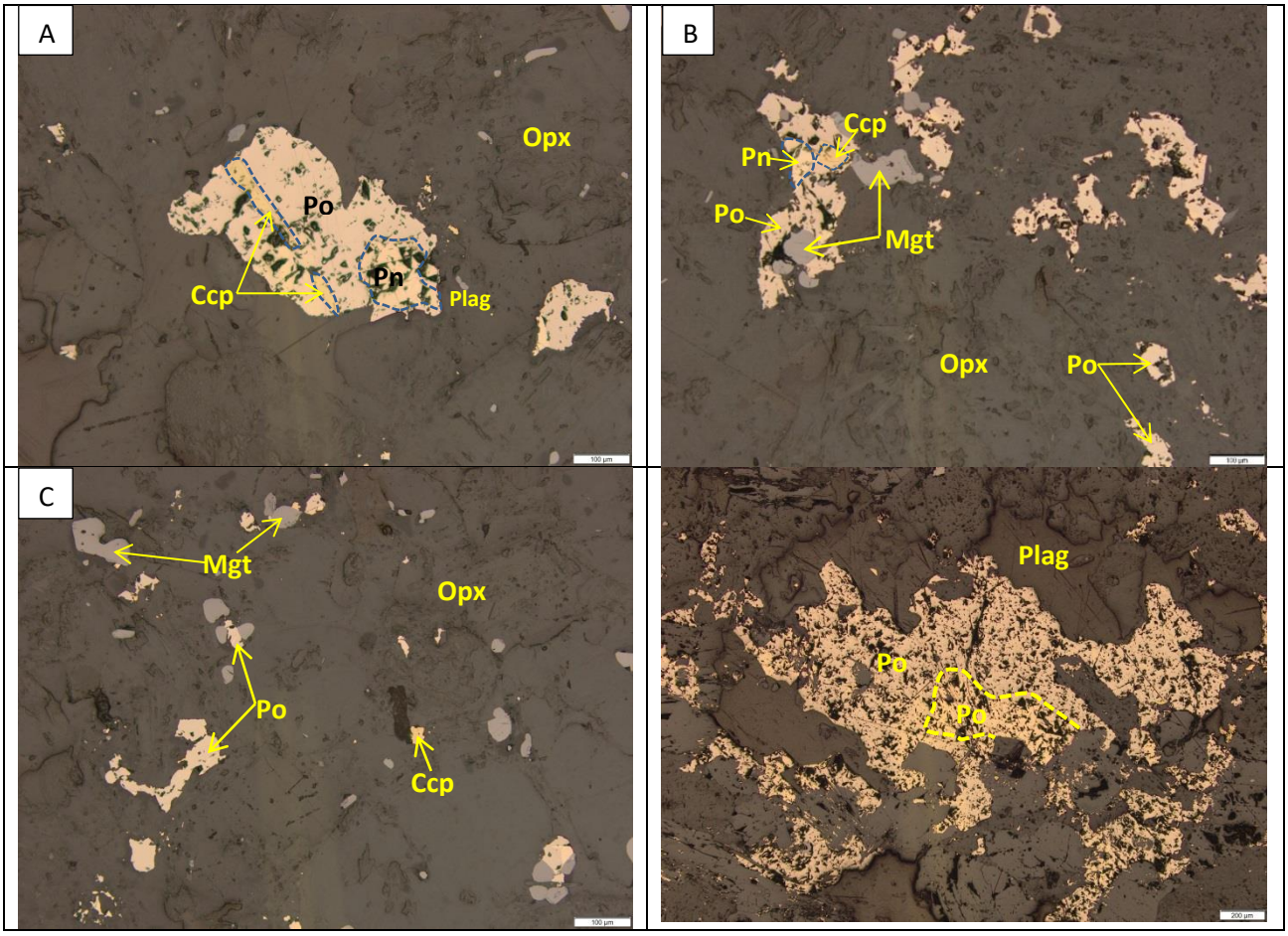


Figure 11-80: Photomicrographs, under reflected light, of feldspathic pyroxenite (sample Z2-176.1) from the southwestern part of the Uitloop farm.

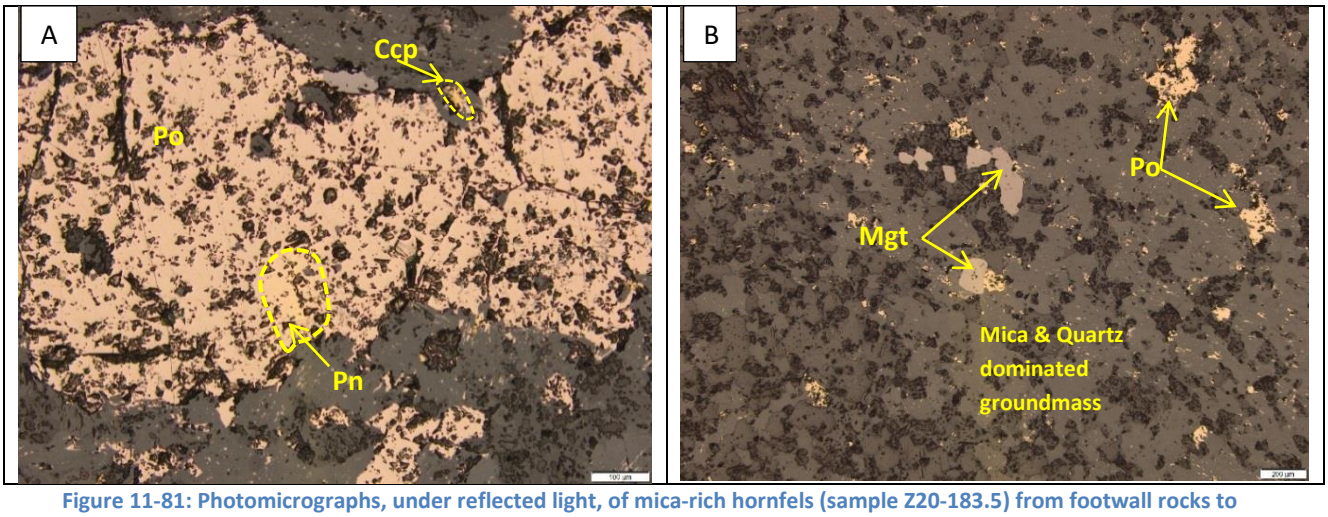


Figure 11-81: Photomicrographs, under reflected light, of mica-rich hornfels (sample Z20-183.5) from footwall rocks to the southwestern part of the Uitloop farm.

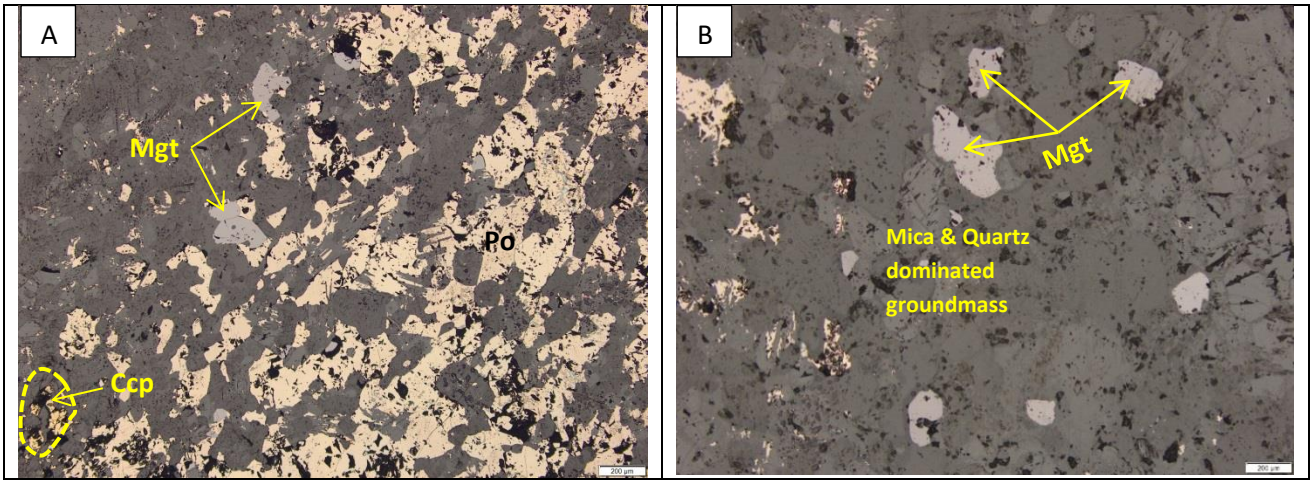


Figure 11-82: Photomicrographs, under reflected light, of mica-rich hornfels (sample Z20-184.4) from footwall rocks to the southwestern part of the Uitloop farm.

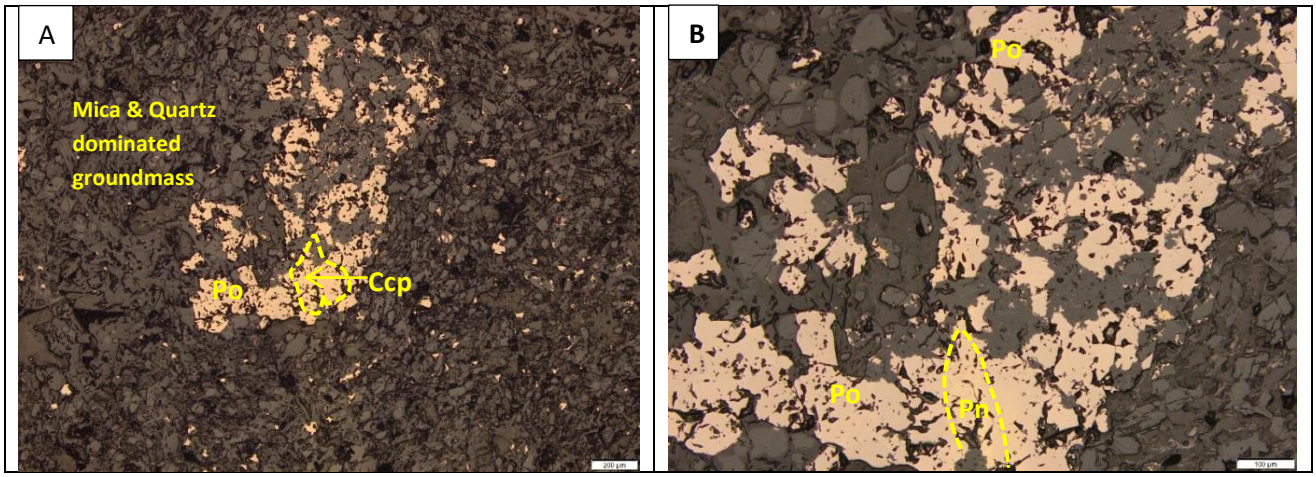


Figure 11-83: Photomicrographs, under reflected light, of mica-rich hornfels (Sample Z20-194.4) from footwall rocks to the southwestern part of the Uitloop farm under reflected light. A & B show a close relationship between pyrrhotite and pyrite.

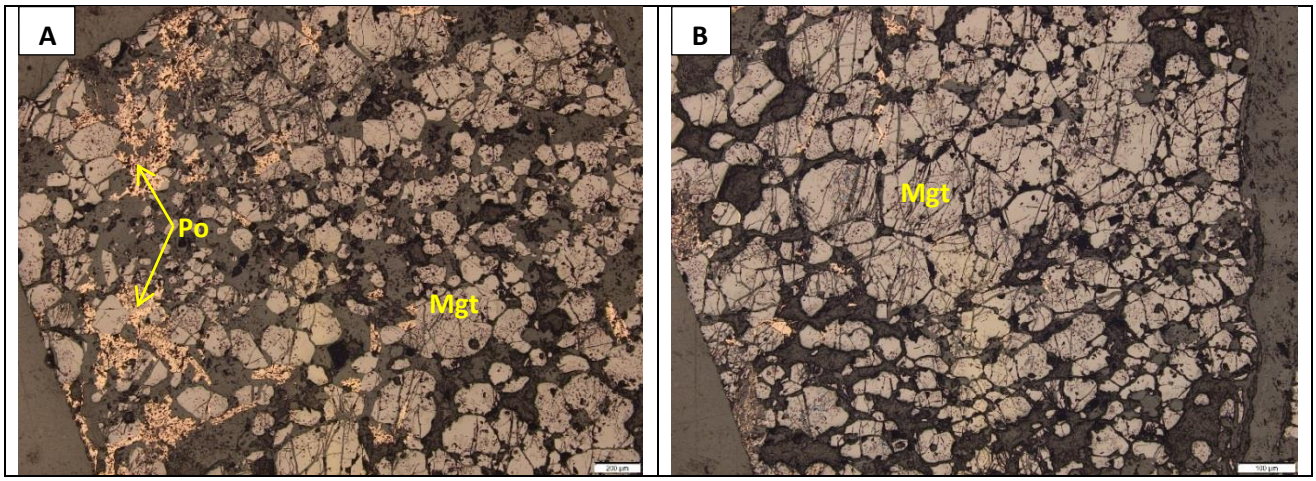


Figure 11-84: Photomicrographs, under reflected light, of dolomite with alternating magnetite bands (sample Z20-212.5) from footwall rocks southwestern part of the Uitloop farm.

APPENDIX C

GEOCHEMICAL DATA

1. REFERENCE MATERIALS

Table 11-6: Reference Materials used for calibration in major element analysis.

RMs	SiO2	Al2O3	Fe2O3	FeO	MnO	MgO	CaO	Na2O	K2O	TiO2	P2O5	Cr2O3	NiO	TOTAL	LOI
W2	53.04	15.54	1.09	8.86	0.17	6.46	11.01	2.23	0.63	1.12	0.13	0.02	0.01	100.29	0.19
NIM-S	64.41	17.51	0.14	1.13	0.01	0.46	0.69	0.36	15.46	0.05	0.12	0	0	100.34	0.42
GSP2	67.2	15.01	0.5	4.04	0.04	0.97	2.14	2.83	5.51	0.69	0.3	0	0	99.25	0.87
BCR2	55.02	13.69	1.39	11.29	0.2	3.63	7.21	3.23	1.82	2.39	0.36	0.01	0	100.25	0.1
NIM-N	53.37	16.71	0.91	7.34	0.19	7.55	11.59	2.47	0.25	0.2	0.02	0	0.02	100.63	0.04
NIM-G	76.28	12.21	0.2	1.61	0.02	0.04	0.79	3.32	5.06	0.1	0.01	0	0	99.63	0.73
PCC1	44.86	0.74	0.87	7.06	0.13	45.86	0.59	0.05	0.01	0.01	0.01	0.45	0.33	100.97	5.09
BHVO2	50.36	13.7	1.24	10.06	0.17	7.3	11.45	2.24	0.52	2.89	0.27	0.05	0.02	100.27	-0.48
AGV2	60.16	17.2	0.68	5.51	0.1	1.81	5.3	4.32	2.94	1.11	0.49	0.01	0	99.61	1.8
G2	69.83	15.5	0.27	2.17	0.03	0.76	1.95	4.08	4.54	0.51	0.14	0	0	99.78	0.64
DTS1	40.59	0.26	0.86	6.99	0.12	49.9	0.16	0.08	0	0.01	0.01	0.61	0.31	99.93	-0.02

Table 11-7: Reference Materials used for calibration in minor and trace element analysis.

	NIM-G	BHVO2	NIMG	BHVO2
Li	12.343	4.865	12	5
P	22.213	1185.432	44	1178
Sc	1.612	30975	1	31
Ti	446.713	162165	539	15621
V	0.29	331.238	2	329
Cr	10.421	284.395	12	285
Co	0.284	45.432	4	47
Ni	1.71	110.385	8	112
Cu	12.658	141.593	12	142
Zn	55.017	98.058	50	107
Ga	30.161	19.008	27	21
Rb	320	8.139	320	10.1
Sr	9.004	379.564	10	382
Y	130.911	25.34	143	23
Zr	301.112	178.559	300	179
Nb	52.731	16.484	53	16.4
Ba	3.845	1.479	4	2.7
Sn	1.225	0.093	1	0.11
Cs	115.599	133.793	120	128.7
La	116.277	14.681	109	15.6
Ce	201.406	35.86	195	37
Pr	22.341	4.873		5
Nd	74.637	23.182	72	24
Sm	15.66	5.853	15.8	5.8
Eu	0.352	1.99	0.35	2
Gd	15.035	5.52	14	5.9
Tb	2.842	0.911	3	0.86
Dy	17.577	4.744	17	4.9
Ho	3.956	0.91		0.91
Er	12.125	2.295		2.3
Tm	1.944	0.309	2	0.3
Yb	13.984	2.052	14.2	2.02
Lu	1.912	0.273	2	0.26
Hf	11.998	3.779	12	4.1
Ta	4.432	1.033	4.5	0.94
W	1.916	0.27		0.27
Pb	42.314	1.617	40	1.4
Th	52.553	1.146	51	1.18
U	14.878	0.356	15	0.44

2. GEOCHEMICAL RESULTS

Table 11-8: Major oxide data from boreholes Z19 and Z20 lithologies at the southwestern part of the Uitloop farm by XRF.

Sample #	Rock name	SiO_2	Al_2O_3	Fe_2O_3	MnO	MgO	CaO	Na_2O	K_2O	TiO_2	P_2O_5	Cr_2O_3	NiO	LOI	TOTAL
Z19-78.3	Norite	51.9	5.59	9.29	0.15	22.74	3.63	0.64	0.32	0.21	0.05	1.2	0.09	4.53	100.34
Z19-100.35	Feldspathic pyroxenite	45.82	8.49	17.01	0.17	15.93	3.81	0.86	0.87	0.31	0.05	5.09	0.6	2.15	101.15
Z19-101	Feldspathic pyroxenite	44.82	9.23	14.33	0.2	15.38	4.73	1.02	0.72	0.33	0.04	7.64	0.1	1.69	100.23
Z19-101.4	Feldspathic pyroxenite	42.36	10.36	15.57	0.21	15.45	4.23	0.99	0.79	0.38	0.03	6.4	0.08	0.85	97.7
Z19-101.6	Feldspathic pyroxenite	45.96	9.2	14.6	0.17	15.92	5.09	1.04	0.66	0.3	0.03	5.36	0.32	2.93	101.59
Z19-123.2	Feldspathic pyroxenite	50.43	6.82	15.78	0.17	18.04	4.88	1.05	0.65	0.2	0.04	0.42	0.62	2.08	101.17
Z19-137.5	Feldspathic pyroxenite	40.04	8.47	16.46	0.21	18.91	3.69	0.69	0.32	0.4	0.02	5.58	0.34	0.53	95.65
Z19-150.6	Feldspathic pyroxenite	51.46	8.83	10.87	0.17	15.47	9.44	1.08	0.69	0.16	0.02	0.5	0.27	1.66	100.64
Z19-169.2	Feldspathic pyroxenite	50.03	7.65	17.8	0.17	13.77	6.02	1.28	0.74	0.37	0.05	0.5	0.67	1.99	101.03
Z19-170.5	Pyroxenite	48.79	9.73	18.52	0.2	12.22	6.09	1.02	1.44	0.35	0.05	0.26	0.6	1.82	101.09
Z19-174.9	Parapyroxenite	44.32	10.36	14.68	0.3	8.57	18.48	0.4	0.51	0.3	0.13	0.01	0.01	2.19	100.27
Z19-178.6	Hornfels	45.53	7.03	20.2	0.29	8.73	12.69	1.39	0.76	0.32	0.03	0.09	0.57	3.1	100.71
Z20- 53.7	Feldspathic harzburgite	47.49	4.78	12.19	0.11	24.43	2.34	0.15	0.29	0.28	0.04	2.12	0.36	6.37	100.94
Z20-54.25	Feldspathic harzburgite	44.15	6.06	13.59	0.18	24.26	1.85	0.32	0.25	0.26	0.02	3.19	0.26	2.55	96.95
Z20-57.5	Feldspathic harzburgite	42.76	6.05	16.58	0.2	22.77	2.11	0.24	0.36	0.36	0.03	3.93	0.38	3.84	99.61
Z20-57.9	Feldspathic pyroxenite	54.08	4.57	10.74	0.18	23.71	3.45	0.64	0.66	0.18	0.03	0.48	0.18	1.31	100.22
Z20-62.7	Feldspathic pyroxenite	46.67	3.47	14.48	0.16	22.69	5.2	0.14	0.2	0.31	0.04	0.86	0.91	4.63	99.77
Z20-66.5	Feldspathic harzburgite	43.9	5.26	12.54	0.16	27.9	2.91	0.43	0.22	0.16	0.03	1.05	0.52	5.3	100.38
Z20-83	Feldspathic pyroxenite	53.73	6.64	9.68	0.16	21.45	4.13	0.98	0.57	0.22	0.03	0.6	0.1	1.42	99.7
Z20-107.7	Feldspathic pyroxenite	50.72	5.19	13.71	0.17	21.25	4.51	0.9	0.39	0.21	0.04	0.6	0.57	2.04	100.31
Z20-111	Feldspathic harzburgite	49.57	5.55	13.39	0.17	22.36	3.8	0.69	0.43	0.2	0.03	0.59	0.39	3.03	100.21
Z20-119	Feldspathic pyroxenite	51.34	3.7	10.35	0.18	24.27	2.98	0.6	0.64	0.18	0.04	0.49	0.13	0.81	95.71
Z20-120.75	Feldspathic pyroxenite	54.91	4.65	10.07	0.18	24.16	2.94	0.64	0.73	0.19	0.03	0.46	0.14	1.39	100.49
Z20-121.9	Feldspathic pyroxenite	49.45	5.72	14.45	0.17	21.9	3.27	0.91	0.33	0.2	0.03	0.85	0.7	2.07	100.05

Z20-124.8	Feldspathic pyroxenite	50.68	5.79	12.77	0.18	21.52	3.85	0.84	0.58	0.24	0.03	1.94	0.29	1.58	100.28
Z20-131.8	Norite	52.48	5.01	12.77	0.19	22.89	3.6	0.68	0.47	0.16	0.03	0.62	0.4	1.28	100.57
Z20-134.8	Feldspathic pyroxenite	51.25	5.45	13.9	0.18	21.34	4.11	0.73	0.58	0.18	0.03	0.5	0.46	1.26	99.98
Z20-140.1	Gabbro	52.71	7.99	8.76	0.13	18.58	4.57	1.38	0.81	0.17	0.03	0.39	0.11	3.88	99.51
Z20-149.3	Feldspathic pyroxenite	50.03	5.03	14.89	0.17	19.39	6.04	0.68	0.49	0.18	0.02	0.6	0.39	2.11	100.03
Z20-164.5	Norite	46.51	13.76	18.67	0.14	6.21	7.34	2	1.21	0.23	0.04	0.08	1.08	3.07	100.34
Z20-173.7	Feldspathic pyroxenite	44.05	11.14	22.66	0.14	7.18	5.28	0.99	1.81	0.55	0.1	0.1	1.16	4.12	99.29
Z20-175.5	Feldspathic pyroxenite	35.71	6.49	36.45	0.17	9.88	3.14	0.49	0.81	0.33	0.06	0.16	1.83	4.78	100.29
Z20-175.9	Feldspathic pyroxenite	48.43	7.22	25.51	0.21	13.56	1.65	0.81	0.98	0.38	0.03	0.16	0.42	0.75	100.12

Table 11-9: Trace element data for borehole Z19 samples by ICP-MS.

ppm	Z19-78.3	Z19-100.35	Z19-101	Z19-101.4	Z19-101.6	Z19-123.2	Z19-137.5	Z19-150.6	Z19-169.2	Z19-170.5	Z19-174.9	Z19-178.6
Li	25.018	2.622	13.614	11.395	9.181	4.077	2.402	5.049	5.428	15.1	16.232	7.697
P	138.484	149.543	107.59	73.521	95.769	120.906	118.355	39.469	150.649	82.798	484.07	160.319
Sc	25.536	17.068	26.109	19.363	23.538	23.664	13.167	34.387	25.269	33.871	10.755	20.333
Ti	1059.6	1514.924	1689.736	1791.14	1445.201	912.758	1922.225	715.198	1711.219	1597.595	1597.104	1675.079
V	89.291	205.257	312.536	387.396	222.341	82.037	304.389	98.115	125.933	184.469	80.27	111.196
Cr	6217.399	26404.96	46257.9	59537.46	24496	1884.047	42339.25	2277.967	2261.967	504.681	139.481	1192.53
Co	75.76	242.032	108.992	129.109	146.799	209.064	112.929	105.877	221.637	200.216	19.226	217.056
Ni	533.553	3794.034	671.025	483.577	1926.409	3653.213	1656.133	1578.492	3852.305	3463.215	100.033	3555.247
Cu	37.597	1076.615	128.605	107.978	705.98	1397.476	612.927	520.594	1859.951	285.732	264.081	1350.056
Zn	57.27	92.442	144.192	151.488	107.678	53.283	106.107	40.72	536.602	77.629	2731.234	66.11
Ga	4.476	9.067	12.169	13.913	10.056	5.451	9.245	5.342	6.826	7.104	10.623	7.966
Rb	19.792	28.957	33.356	30.365	28.608	28.778	8.777	29.396	32.037	30.229	14.354	67.262
Sr	41.777	65.031	103.322	110.651	102.102	100.528	49.823	111.719	112.963	139.523	163.081	155.834
Y	5.862	4.95	6.332	4.895	6.246	7.234	3.471	5.142	10.18	14.87	13.519	9.22
Zr	30.646	34.856	29.021	21.015	28.631	31.217	11.347	19.331	44.259	43.333	39.847	38.443
Nb	1.582	1.745	1.5	0.96	1.775	1.562	0.814	0.842	2.531	2.078	2.314	2.845
Ba	0.497	0.873	0.677	0.638	1.714	0.66	0.76	1.251	0.887	0.876	1.459	1.025
Sn	4.487	1.583	2.509	1.968	2.273	2.414	1.137	1.84	2.309	0.733	0.197	2.801
Cs	54.134	119.324	119.969	113.078	116.616	86.376	48.579	108.207	119.27	129.739	157.719	169.845
La	5.046	5.151	4.848	3.666	8.052	5.351	2.495	3.452	7.418	10.288	6.662	8.837
Ce	9.616	10.565	9.707	7.652	14.868	11.186	4.514	7.207	14.793	21.837	15.844	17.092
Pr	1.103	1.139	1.169	0.876	1.738	1.35	0.558	0.939	1.842	2.935	2.389	2.029
Nd	4.035	4.171	4.527	3.44	6.348	5.402	2.255	3.739	7.345	11.74	10.124	7.774
Sm	0.899	0.862	1.032	0.778	1.213	1.218	0.539	0.872	1.687	2.602	2.329	1.641
Eu	0.245	0.258	0.332	0.248	0.336	0.368	0.167	0.226	0.489	0.673	0.526	0.485
Gd	0.892	0.827	0.976	0.748	1.091	1.139	0.529	0.825	1.628	2.394	2.07	1.547

Tb	0.153	0.138	0.169	0.13	0.177	0.201	0.094	0.144	0.283	0.412	0.356	0.262
Dy	0.923	0.8	1.001	0.78	1	1.172	0.569	0.85	1.638	2.343	2.005	1.482
Ho	0.202	0.172	0.217	0.167	0.214	0.255	0.123	0.179	0.344	0.495	0.42	0.318
Er	0.598	0.523	0.642	0.505	0.626	0.738	0.369	0.525	1.021	1.409	1.186	0.911
Tm	0.094	0.082	0.101	0.077	0.095	0.113	0.056	0.078	0.157	0.208	0.178	0.139
Yb	0.652	0.577	0.715	0.55	0.68	0.778	0.382	0.533	1.025	1.353	1.168	0.95
Lu	0.102	0.092	0.112	0.087	0.101	0.121	0.059	0.081	0.161	0.205	0.179	0.144
Hf	0.71	0.778	0.737	0.531	0.682	0.733	0.329	0.522	1.064	1.064	1.004	0.932
Ta	0.095	0.11	0.083	0.022	0.122	0.092	0.008	0.02	0.177	0.13	0.209	0.203

Table 11-10: Trace element data for borehole Z20 samples by ICP-MS.

Ppm	Z20-53.7	Z20-54.25	Z20-57.5	Z20-57.9	Z20-62.7	Z20-66.5	Z20-83	Z20-107.7	Z20-111	Z20-119	Z20-120.75	Z20-121.9	Z20-124.8	Z20-131.8	Z20-134.8	Z20-140.1	Z20-149.3	Z20-164.5	Z20-173.7	Z20-175.5	Z20-175.9
Li	32.341	7.304	12.001	1.836	12.674	5.747	2.914	2.221	4.119	1.142	2.867	2.293	3.433	5.16	0.769	4.876	2.542	9.54	11.887	10.094	11.345
P	127.057	37.955	60.016	77.056	117.709	69.412	91.052	89.334	81.731	77.229	70.54	86.939	81.483	63.355	76.517	74.288	56.347	118.691	400.721	183.175	66.47
Sc	21.248	10.695	13.594	16.875	28.335	12.138	17.65	17.832	17.318	13.16	14.976	17.346	17.011	17.847	14.649	17.381	24.214	13.392	12.37	15.57	41.801
Ti	1393.755	730.788	1734.433	811.864	1518.635	774.627	1019.339	957.662	959.556	703.503	868.914	942.105	1071.203	725.835	750.783	677.151	803.563	1138.911	2785.705	1588.82	1774.965
V	127.813	157.33	261.955	65.155	123.66	68.27	79.972	83.61	80.63	58.335	60.148	84.383	129.674	76.386	70.361	76.053	89.548	116.6	108.692	102.725	305.872
Cr	>10%	17938.82	26006.73	2305.317	4754.641	5834.694	2863.814	3047.274	3031.641	1513.894	2204.516	4382.143	10374.98	3185.259	1965.124	1577.506	3028.113	441.851	590.33	915.506	854.901
Co	144.027	80.673	170.052	92.121	236.046	164.477	76.157	194.469	176.021	60.991	75.32	214.136	121.084	146.49	164.269	58.272	173.613	353.254	391.584	596.827	184.808
Ni	2297.165	1048.358	2431.616	1106.212	5743.114	3184.489	609.946	3566.138	2429.373	646.495	820.872	4301.247	1783.422	2468.822	2802.797	612.689	2498.04	7152.211	7703.514	12437.42	2638.233
Cu	577.197	259.795	1102.086	396.435	1799.121	466.872	74.021	1684.483	1061.294	265.465	300.842	2638.705	781.806	735.567	1289.795	253.424	1314.068	2846.319	6612.256	4138.376	1464.676
Zn	65.604	69.563	158.174	74.458	62.441	2094.556	591.079	108.126	63.002	44.821	53.884	62.029	86.669	62.563	60.355	38.394	64.51	68.173	111.588	87.136	89.158
Ga	5.776	5.507	9.485	3.214	4.124	4.423	4.978	4.029	4.107	2.132	3.318	4.431	4.969	3.76	3.567	4.275	3.977	9.844	11.029	6.811	8.434
Rb	18.726	10.021	19.266	25.307	15.723	10.758	24.442	18.007	23.156	16.88	26.559	16.234	25.388	20.797	23.392	29.626	20.961	32.784	109.633	42.065	56.123
Sr	6.813	18.59	17.566	49.137	10.231	60.277	76.577	69.364	52.591	35.471	44.808	60.518	62.501	44.889	60.994	91.604	54.807	176.928	173.348	72.092	62.84
Y	5.239	2.604	3.08	4.031	11.41	2.9	4.808	3.943	4.118	3.63	3.072	3.992	3.654	3.645	3.586	4.056	4.442	4.293	6.55	6.34	8.051
Zr	18.78	7.566	11.522	23.983	29.711	10.334	20.731	17.485	20.682	20.432	24.416	23.867	14.989	19.067	20.457	22.655	16.543	31.892	104.602	20.646	26.586
Nb	1.086	0.281	0.529	1.268	1.418	0.594	2.178	0.98	1.056	1.581	2.25	1.279	1.119	0.861	1.03	1.445	0.786	2.002	6.501	2.038	1.912
Ba	0.56	0.428	0.816	0.674	0.817	0.513	0.571	0.395	0.586	0.597	0.72	0.417	0.6	0.616	0.648	0.75	0.6	0.664	1.081	0.511	0.721
Sn	5.76	3.043	4.213	2.958	3.275	2.507	3.605	1.85	3.769	1.65	2.597	2.583	2.639	2.719	1.948	3.648	1.946	1.56	6.009	2.59	6.091
Cs	20.144	27.485	31.555	51.736	13.408	63.509	72.591	41.171	47.946	51.799	70.811	38.829	63.183	47.707	59.603	86.777	40.123	150.832	168.726	62.751	78.839
La	2.163	1.726	2.534	3.922	3.72	2.571	5.137	2.79	3.285	3.942	2.85	3.029	2.796	2.725	3.152	4.777	3.434	6.279	17.223	6.163	7.196
Ce	5.171	3.044	4.501	8.058	11.001	4.456	9.201	5.482	6.744	6.513	6.09	5.734	5.106	5.383	6.272	8.559	7.023	11.635	29.591	12.134	13.081
Pr	0.672	0.405	0.517	0.907	1.54	0.53	1.017	0.701	0.815	0.795	0.73	0.689	0.625	0.64	0.727	1.084	0.811	1.1	2.603	1.174	1.215
Nd	2.905	1.555	2.006	3.329	6.993	2.083	3.749	2.933	3.187	2.891	2.716	2.653	2.631	2.658	3.065	4.142	3.476	4.357	9.216	4.782	4.542
Sm	0.729	0.328	0.437	0.674	1.934	0.472	0.789	0.7	0.696	0.601	0.545	0.593	0.613	0.613	0.704	0.817	0.798	0.904	1.536	1.018	0.948
Eu	0.135	0.128	0.133	0.181	0.325	0.184	0.271	0.222	0.189	0.154	0.16	0.213	0.18	0.16	0.191	0.227	0.188	0.449	0.577	0.335	0.397
Gd	0.745	0.331	0.453	0.66	1.922	0.463	0.78	0.657	0.67	0.579	0.52	0.605	0.592	0.595	0.664	0.748	0.763	0.834	1.365	0.973	0.971
Tb	0.134	0.06	0.079	0.11	0.344	0.082	0.136	0.111	0.117	0.099	0.086	0.105	0.102	0.103	0.112	0.121	0.131	0.136	0.197	0.165	0.184
Dy	0.818	0.389	0.489	0.653	1.967	0.484	0.79	0.661	0.684	0.595	0.512	0.64	0.601	0.61	0.638	0.685	0.755	0.749	1.03	0.957	1.157
Ho	0.179	0.089	0.108	0.144	0.407	0.105	0.174	0.14	0.148	0.129	0.11	0.14	0.126	0.128	0.132	0.142	0.156	0.153	0.209	0.204	0.268

Er	0.537	0.282	0.327	0.42	1.126	0.306	0.512	0.398	0.427	0.384	0.319	0.419	0.372	0.379	0.381	0.415	0.448	0.43	0.611	0.605	0.883
Tm	0.085	0.044	0.051	0.064	0.162	0.046	0.077	0.06	0.064	0.057	0.047	0.065	0.057	0.059	0.056	0.064	0.067	0.063	0.092	0.095	0.153
Yb	0.598	0.329	0.369	0.456	1.06	0.346	0.557	0.424	0.465	0.41	0.347	0.47	0.408	0.42	0.386	0.442	0.467	0.432	0.638	0.658	1.161
Lu	0.096	0.052	0.057	0.07	0.163	0.053	0.086	0.065	0.072	0.064	0.053	0.072	0.064	0.064	0.06	0.067	0.071	0.064	0.1	0.106	0.2
Hf	0.482	0.198	0.345	0.588	0.833	0.281	0.558	0.485	0.546	0.561	0.615	0.579	0.433	0.53	0.567	0.6	0.466	0.822	2.288	0.523	0.823
Ta	0.047	0.000	0.000	0.047	0.071	0.000	0.118	0.029	0.024	0.064	0.126	0.056	0.001	0.003	0.005	0.049	0.004	0.084	0.496	0.071	0.076
W	0.214	0.102	0.215	0.259	0.212	3.233	0.408	0.235	0.243	0.337	0.437	0.13	0.378	0.243	0.251	0.272	0.242	0.369	0.678	0.624	0.472
Pb	2.002	4.572	3.64	6.526	2.498	7.411	6.076	6.375	11.156	9.708	6.072	4.472	13.942	6.642	7.226	7.315	12.211	20.162	21.851	8.707	11.793
Th	0.777	0.491	0.342	1.125	0.969	0.518	1.278	1.071	0.595	1.282	1.58	0.865	0.7	0.832	0.77	1.76	0.947	2.208	5.657	1.041	1.438
U	0.325	0.074	0.17	0.388	0.454	0.23	0.662	0.246	0.169	0.47	0.485	0.382	0.477	0.553	0.352	0.362	0.38	0.782	1.621	0.297	0.76

Table 11-11: Cr/MgO ratios for borehole Z19 lithologies.

Sample#	Rock name	Cr (ppm)	MgO (wt.%)	Cr/MgO
Z19-78.3	Norite	6217	22.74	273
Z19-100.35	Feldspathic pyroxenite	26405	15.93	1658
Z19-101	Feldspathic pyroxenite	46258	15.38	3008
Z19-101.4	Feldspathic pyroxenite	59537	15.45	3854
Z19-101.6	Feldspathic pyroxenite	24496	15.92	1539
Z19-123.2	Feldspathic pyroxenite	1884	18.04	104
Z19-137.5	Feldspathic pyroxenite	42339	18.91	2239
Z19-150.6	Feldspathic pyroxenite	2278	15.47	147
Z19-169.2	Feldspathic pyroxenite	2262	13.77	164
Z19-170.5	Pyroxenite	505	12.22	41

Table 11-12:Cr/MgO ratios for borehole Z20 lithologies.

SAMPLE#	Rock name	Cr (ppm)	MgO (wt.%)	Cr/MgO
Z20- 53.7	Feldspathic harzburgite	100000	24.43	4093
Z20-54.25	Feldspathic harzburgite	17939	24.26	739
Z20-57.5	Feldspathic harzburgite	26007	22.77	1142
Z20-57.9	Feldspathic pyroxenite	2305	23.71	97
Z20-62.7	Feldspathic pyroxenite	4755	22.69	209
Z20-66.5	Feldspathic harzburgite	5835	27.9	209
Z20-83	Feldspathic pyroxenite	2864	21.45	134
Z20-107.7	Feldspathic pyroxenite	3047	21.25	143
Z20-111	Feldspathic harzburgite	3031	22.36	136
Z20-119	Feldspathic pyroxenite	1514	24.27	62
Z20-120.75	Feldspathic pyroxenite	2205	24.16	91
Z20-121.9	Feldspathic pyroxenite	4382	21.9	200
Z20-124.8	Feldspathic pyroxenite	10375	21.52	482
Z20-131.8	Norite	3185	22.89	139
Z20-134.8	Feldspathic pyroxenite	1965	21.34	92
Z20-140.1	Gabbro	1578	18.58	85
Z20-149.3	Feldspathic pyroxenite	3028	19.39	156
Z20-164.5	Norite	442	6.21	71
Z20-173.7	Feldspathic pyroxenite	590	7.18	82
Z20-175.5	Feldspathic pyroxenite	916	9.88	93
Z20-175.9	Feldspathic pyroxenite	855	13.56	63

APPENDIX D

MINERAL CHEMISTRY DATA

1. CHROMITE CHEMISTRY

Table 11-13: Analysis of the chromite Standard Reference Material.

Reference Material (wt%)		Mg	Al	Si	Cr	Fe	V	Ca	Ti	Mn	Co	Ni	Zn	O	Total	MgO	Al_2O_3	SiO_2	Cr_2O_3	FeO	V_2O_5	CaO	TiO_2	MnO	CoO	NiO	ZnO	Total
Alma_PH1	1/1.	1.5	11.15	17.52	0.01	27.89	0	2.69	0.04	0.15	0.01	0	0.01	40.01	100.99	2.48	21.06	37.49	0.01	35.88	0.01	3.77	0.06	0.19	0.01	0	0.02	100.99
Alma_PH1	2/1.	1.44	11.17	17.49	0.01	27.86	0	2.75	0.05	0.14	0	0	0.01	39.98	100.91	2.39	21.11	37.42	0.01	35.85	0	3.85	0.08	0.18	0	0	0.01	100.91
Diop_PH1	3/1.	11.25	0.02	25.82	0.01	0.66	0.02	18.28	0.02	0.08	0.01	0	0.02	44.38	100.55	18.66	0.04	55.24	0.01	0.85	0.03	25.57	0.03	0.1	0.01	0	0.02	100.55
Diop_PH1	4/1.	11.21	0.02	25.78	0.01	0.64	0.01	18.4	0.02	0.07	0.01	0	0.01	44.34	100.5	18.58	0.04	55.15	0.01	0.82	0.02	25.74	0.03	0.08	0.01	0	0.02	100.5
Chro_MA1	5/1.	5.77	8.91	0.03	30.06	21.15	0.23	0	0.53	0.16	0.03	0.15	0.08	32.34	99.43	9.56	16.83	0.06	43.93	27.21	0.4	0.01	0.88	0.21	0.04	0.19	0.1	99.43
Chro_MA1	6/1.	5.72	8.81	0.02	30.45	21.14	0.23	0	0.54	0.15	0.03	0.15	0.08	32.39	99.72	9.49	16.64	0.05	44.51	27.19	0.42	0	0.89	0.19	0.04	0.2	0.09	99.72

Table 11-14: The initial results of major oxide compositions by microprobe analysis.

Analysis (borehole-depth-spot#)	Rock type	Mineral	Host mineral	SiO_2	TiO_2	V_2O_5	Al_2O_3	Cr_2O_3	FeO	MnO	MgO	CoO	NiO	ZnO	Total
Z19-100.35-1	FPYX	Chr	Plag	0.02	0.71	0.4	6.47	42.88	45.67	0.38	1.9	0.05	0.05	0.11	98.65
Z19-100.35-2	FPYX	Chr	Plag	0.03	0.62	0.45	6.44	43.7	44.97	0.37	1.84	0.05	0.03	0.12	98.65
Z19-100.35-3	FPYX	Chr	Plag		0.56	0.43	6.6	43.75	45.17	0.34	1.83		0.04	0.11	98.87
Z19-100.35-4	FPYX	Chr	Phl		1.33	0.45	5.54	37.69	47.61	0.31	1.68	0.04	0.08	0.07	94.82
Z19-100.35-5	FPYX	Chr	Phl		1.17	0.47	6.24	41.47	46.4	0.34	2.16	0.04	0.09	0.1	98.52
Z19-100.35-6	FPYX	Chr	Phl		0.92	0.44	6.29	42.83	45.46	0.37	1.97	0.05	0.08	0.12	98.56
Z19-100.35-7	FPYX	Chr	Phl		1.15	0.46	6.06	42.55	46.17	0.35	1.85	0.02	0.06	0.12	98.82
Z19-100.35-8	FPYX	Chr	Phl	0.03	0.85	0.45	6.27	43.25	45.37	0.38	1.81	0.04	0.06	0.13	98.68
Z19-100.35-9	FPYX	Chr	Sulph	0.02	1.26	0.45	6.22	40.97	46.88	0.31	2.35	0.03	0.08	0.12	98.7
Z19-100.35-10	FPYX	Chr	Sulph		1.2	0.44	6.35	41.44	46.77	0.35	2.32		0.07	0.13	99.08
Z19-100.35-11	FPYX	Chr	Sulph	0.02	1.24	0.45	6.13	41.17	46.92	0.35	2.32	0.03	0.08	0.1	98.82
Z19-100.35-12	FPYX	Chr	Sulph		1.25	0.44	6.26	41.21	46.58	0.35	2.32	0.03	0.06	0.09	98.59
Z19-100.35-13	FPYX	Chr	Sulph	0.02	1.05	0.42	6.44	41.8	46.42	0.34	2.31	0.03	0.06	0.09	98.98
Z19-100.35-14	FPYX	Chr	Opx	0.02	1.01	0.42	6.23	42.18	45.34	0.34	2.16	0.04	0.08	0.08	97.91
Z19-100.35-15	FPYX	Chr	Opx		0.86	0.41	6.23	43.56	44.68	0.35	2.12	0.04	0.04	0.13	98.43
Z19-100.3516	FPYX	Chr	Opx	0.02	0.94	0.42	6.43	42.58	45.24	0.35	2.18	0.04	0.05	0.1	98.36
Z19-100.35-17	FPYX	Chr	Qrtz	0.04	0.84	0.47	6.68	43.83	43.9	0.34	2.24	0.05	0.07	0.11	98.56
Z19-100.35-18	FPYX	Chr	Qrtz		1.06	0.47	6.51	43.52	44.53	0.35	1.92	0.03	0.07	0.13	98.62
Z19-100.35-19	FPYX	Chr	Qrtz	4.53	0.92	0.43	6.38	44.09	42.62	0.35	1.88	0.04	0.08	0.1	101.47
Z19-100.35-20	FPYX	Chr	Qrtz	0.03	0.78	0.44	6.4	44.03	44.34	0.31	2.17	0.03	0.08	0.11	98.75
Z19-100.35-21	FPYX	Chr	Qrtz	0.06	0.84	0.45	6.66	44.93	43.36	0.33	1.98	0.04	0.07	0.11	98.84
Z19-101.4-19	FPYX	Chr	Cpx	0.03	0.77	0.43	7.84	46.23	38.57	0.36	4.06	0.06	0.09	0.08	98.57
Z19-101.4-20	FPYX	Chr	Cpx	0.03	0.63	0.4	8.02	46.15	38.43	0.38	4.17	0.05	0.08	0.11	98.56
Z19-101.4-21	FPYX	Chr	Cpx	0.02	0.72	0.42	7.7	46.62	38.35	0.34	4.06	0.05	0.07	0.11	98.51
Z19-101.4-22	FPYX	Chr	Cpx	0.03	0.66	0.43	7.81	46.16	38.29	0.33	3.91	0.05	0.05	0.09	97.88
Z19-101.4-23	FPYX	Chr	Cpx	0.03	0.68	0.44	7.54	46.6	38.23	0.33	3.89	0.04	0.07	0.08	97.95
Z19-101.4-24	FPYX	Chr	Cpx	0.02	0.77	0.41	8.02	46.09	38.53	0.33	4.15	0.05	0.09	0.07	98.61
Z19-101.4-25	FPYX	Chr	Plag		0.57	0.39	8.99	46.43	37.81	0.33	4.37	0.06	0.07	0.1	99.15
Z19-101.4-26	FPYX	Chr	Plag	0.03	0.68	0.39	8.88	46	38.22	0.3	4.28	0.07	0.09	0.12	99.06

Z19-101.4-27	FPYX	Chr	Plag		0.63	0.39	8.83	46.96	37.64	0.31	4.39	0.06	0.05	0.12	99.39
Z19-101.4-28	FPYX	Chr	Plag		0.69	0.41	8.54	46.53	38.2	0.33	4.29	0.06	0.07	0.1	99.25
Z19-101.4-29	FPYX	Chr	Plag	0.02	0.74	0.38	9.07	45.91	38.25	0.31	4.29	0.04	0.06	0.11	99.21
Z19-101.4-30	FPYX	Chr	Opx		0.7	0.28	9.18	45.75	37.75	0.33	4.44	0.06	0.1	0.13	98.74
Z19-101.4-31	FPYX	Chr	Opx		0.71	0.28	9.1	45.64	37.7	0.32	4.41	0.06	0.09	0.09	98.42
Z19-101.4-32	FPYX	Chr	Opx	0.02	0.68	0.34	9.61	45.24	38.05	0.35	4.48	0.07	0.09	0.1	99.04
Z19-101.4-33	FPYX	Chr	Opx		0.71	0.35	9.35	44.96	38.06	0.33	4.5	0.05	0.08	0.1	98.53
Z19-101.4-34	FPYX	Chr	Opx	0.02	0.67	0.31	8.68	45.82	37.96	0.34	4.44	0.08	0.1	0.08	98.54
Z19-101.6-1	FPYX	Chr	Opx	0.03	1.03	0.48	5.92	40.32	48.37	0.33	1.47	0.04	0.08	0.14	98.22
Z19-101.6-2	FPYX	Chr	Opx		0.91	0.48	5.98	41.3	48.07	0.34	1.31		0.08	0.12	98.62
Z19-101.6-3	FPYX	Chr	Opx		0.87	0.47	5.9	41.16	48.14	0.3	1.27	0.03	0.07	0.16	98.38
Z19-101.6-4	FPYX	Chr	Opx		0.88	0.48	6.07	41.37	47.99	0.33	1.37	0.02	0.07	0.15	98.74
Z19-101.6-5	FPYX	Chr	Opx		0.89	0.47	5.79	41.21	48.13	0.33	1.29	0.03	0.06	0.16	98.37
Z19-101.6-6	FPYX	Chr	Phl	0.02	0.74	0.49	5.8	41.73	47.55	0.34	1.06	0.03	0.04	0.15	97.97
Z19-101.6-7	FPYX	Chr	Phl		0.84	0.44	5.95	41.69	47.8	0.33	1.11	0.03	0.06	0.14	98.4
Z19-101.6-8	FPYX	Chr	Phl	0.03	0.74	0.46	5.93	42.04	47.42	0.32	1.08		0.07	0.13	98.23
Z19-101.6-9	FPYX	Chr	Plag		0.67	0.4	8.5	45.7	39.71	0.34	3.54	0.06	0.09	0.14	99.19
Z19-101.6-10	FPYX	Chr	Plag		0.72	0.45	8.7	45.13	40.32	0.33	3.53	0.05	0.08	0.11	99.43
Z19-101.6-11	FPYX	Chr	Plag		0.69	0.42	8.51	45.85	39.85	0.34	3.65	0.06	0.09	0.11	99.59
Z19-101.6-12	FPYX	Chr	Plag		0.77	0.43	8.9	44.6	40.62	0.36	3.58	0.04	0.1	0.14	99.55
Z19-101.6-14	FPYX	Chr	Opx		0.87	0.42	7.93	43.48	42.11	0.31	3.44	0.04	0.12	0.11	98.86
Z19-101.6-15	FPYX	Chr	Opx	0.02	0.9	0.42	8.04	43.69	42.14	0.33	3.4	0.05	0.13	0.11	99.24
Z19-101.6-16	FPYX	Chr	Opx	0.03	0.77	0.43	7.15	43.69	42.56	0.36	3.3	0.05	0.14	0.11	98.6
Z19-101.6-17	FPYX	Chr	Opx	0.02	1	0.46	6.71	43.53	43.79	0.38	2.61	0.04	0.09	0.12	98.74
Z19-101.6-18	FPYX	Chr	Opx		0.8	0.45	6.69	43.83	44.29	0.39	2.44	0.04	0.08	0.11	99.12
Z19-137.5-51	FPYX	Chr	Plag		1.46	0.38	11.18	44.66	35.93	0.3	5.26	0.05	0.09	0.09	99.42
Z19-137.5-52	FPYX	Chr	Plag		0.73	0.38	11.19	45.56	36.03	0.3	5.36	0.04	0.07	0.1	99.8
Z19-137.5-53	FPYX	Chr	Plag	0.02	0.75	0.38	11.02	46.01	35.4	0.29	5.31	0.02	0.05	0.09	99.34
Z19-137.5-54	FPYX	Chr	Opx & Plag	0.02	0.62	0.3	14.4	42.64	34.02	0.3	6.76	0.03	0.1	0.11	99.3
Z19-137.5-55	FPYX	Chr	Opx & Plag	0.02	0.72	0.33	13.67	42.74	35.33	0.29	6.12	0.03	0.08	0.08	99.43
Z19-137.5-56	FPYX	Chr	Sulph		0.7	0.32	13.55	42.5	35.77	0.32	6.04	0.02	0.06	0.1	99.38
Z19-137.5-57	FPYX	Chr	Opx		0.73	0.37	12.2	43.25	36.68	0.32	5.69	0.02	0.04	0.09	99.39

Z19-137.5-58	FPYX	Chr	Opx		0.77	0.38	12.74	43.85	35.35	0.32	6.07	0.04	0.04	0.09	99.67
Z19-137.5-59	FPYX	Chr	Opx	0.03	0.92	0.33	12.38	43.61	35.26	0.3	6.09	0.06	0.12	0.08	99.17
Z19-137.5-60	FPYX	Chr	Opx	0.02	0.74	0.37	11.97	43.97	36.16	0.33	5.7	0.06	0.07	0.09	99.47
Z20-66.5-23	FHZB	Chr	Sulph	0.02	0.66	0.33	4.59	16.2	70.94	0.17	2.38	0.04	0.15	0.1	95.58
Z20-66.5-24	FHZB	Cr-Spi	Sulph	0.03	0.63	0.34	4.18	15.11	72.12	0.13	2.32		0.11	0.09	95.07
Z20-66.5-26	FHZB	Chr	Ol		0.1	0.21	14.78	29.05	49.41	0.35	4.03	0.06	0.16	0.27	98.48
Z20-66.5-27	FHZB	Chr	Ol		0.07	0.22	15.46	28.84	48.67	0.33	4.03	0.04	0.15	0.32	98.16
Z20-66.5-28	FHZB	Chr	Opx	0.02	0.82	0.37	9.79	29.88	52.23	0.33	3.87	0.04	0.29	0.19	97.85
Z20-66.5-29	FHZB	Chr	Opx	0.02	0.85	0.36	9.11	28.44	54.25	0.33	3.43	0.04	0.29	0.19	97.3
Z20-66.5-30	FHZB	Chr	Opx	0.02	1.9	0.46	11.11	32.63	46.13	0.32	5.39	0.06	0.35	0.14	98.53
Z20-66.5-31	FHZB	Chr	Ol	0.02	1.5	0.39	9.21	33.89	48.77	0.35	3.9	0.09	0.24	0.22	98.56
Z20-66.5-32	FHZB	Chr	Ol	0.03	1.47	0.38	8.83	34.54	48.13	0.38	3.59	0.07	0.25	0.21	97.87
Z20-66.5-33	FHZB	Chr	Ol		0.39	0.25	11.86	31.21	49.7	0.35	4.1	0.08	0.24	0.2	98.38
Z20-66.5-34	FHZB	Chr	Ol		1.51	0.34	10.98	34.06	46.03	0.34	4.85	0.06	0.23	0.17	98.59
Z20-66.5-35	FHZB	Chr	Plag		0.96	0.34	13.52	35.37	42.92	0.29	5.54	0.06	0.2	0.14	99.36
Z20-66.5-36	FHZB	Chr	Plag	0.03	0.89	0.35	14.53	35.66	41.52	0.31	5.22	0.07	0.18	0.13	98.9
Z20-66.5-37	FHZB	Chr	Ol	0.02	0.6	0.33	12.56	34.63	44.9	0.35	4.62	0.06	0.17	0.23	98.48
Z20-111-45	FHZB	Chr	Phl	0.09	0.96	0.8	3.17	16.45	73.18	0.37	0.74	0.02	0.18	0.12	96.09
Z20-111-46	FHZB	Chr	Opx	0.03	0.48	0.33	6.74	24.78	62.46	0.32	0.88	0.02	0.1	0.23	96.39
Z20-111-47	FHZB	Chr	Opx	0.03	1.52	0.98	2.85	34.18	54.77	0.31	1.88	0.06	0.19	0.16	97.06
Z20-111-48	FHZB	Chr	Opx		0.51	0.37	5.42	20.8	67.55	0.28	0.49	0.02	0.1	0.18	95.72
Z20-111-49	FHZB	Chr	Sulph		0.32	0.37	6.67	23.92	63.53	0.36	0.54	0.02	0.08	0.24	96.06
Z20-111-50	FHZB	Chr	Phl	0.02	0.32	0.32	5.44	22.32	64.54	0.29	0.98		0.13	0.17	94.59

Table 11-15: Recalculated EMPA oxide results according to the spinel stoichiometry calculation template - latest version Dec 21 2004 developed by S.J. Barnes with correction from C-J De Hoog.

Analysis #	TiO_2	V_2O_5	Al_2O_3	Cr_2O_3	MnO	MgO	CoO	NiO	ZnO	FeO	Fe_2O_3	Total
Z19-100.35-1	0.71	0.4	6.47	42.88	0.38	1.9	0.05	0.05	0.11	30.35	17.02	100.35
Z19-100.35-2	0.62	0.45	6.44	43.7	0.37	1.84	0.05	0.03	0.12	30.39	16.21	100.24
Z19-100.35-3	0.56	0.43	6.6	43.75	0.34	1.83		0.04	0.11	30.52	16.28	100.46
Z19-100.35-4	1.33	0.45	5.54	37.69	0.31	1.68	0.04	0.08	0.07	30.03	19.53	96.76
Z19-100.35-5	1.17	0.47	6.24	41.47	0.34	2.16	0.04	0.09	0.1	30.36	17.82	100.27
Z19-100.35-6	0.92	0.44	6.29	42.83	0.37	1.97	0.05	0.08	0.12	30.37	16.77	100.21
Z19-100.35-7	1.15	0.46	6.06	42.55	0.35	1.85	0.02	0.06	0.12	30.89	16.98	100.49
Z19-100.35-8	0.85	0.45	6.27	43.25	0.38	1.81	0.04	0.06	0.13	30.58	16.43	100.29
Z19-100.35-9	1.26	0.45	6.22	40.97	0.31	2.35	0.03	0.08	0.12	30.24	18.49	100.54
Z19-100.35-10	1.2	0.44	6.35	41.44	0.35	2.32		0.07	0.13	30.36	18.24	100.90
Z19-100.35-11	1.24	0.45	6.13	41.17	0.35	2.32	0.03	0.08	0.1	30.27	18.50	100.66
Z19-100.35-12	1.25	0.44	6.26	41.21	0.35	2.32	0.03	0.06	0.09	30.25	18.14	100.41
Z19-100.35-13	1.05	0.42	6.44	41.8	0.34	2.31	0.03	0.06	0.09	30.23	17.99	100.78
Z19-100.35-14	1.01	0.42	6.23	42.18	0.34	2.16	0.04	0.08	0.08	30.01	17.04	99.61
Z19-100.35-15	0.86	0.41	6.23	43.56	0.35	2.12	0.04	0.04	0.13	30.07	16.23	100.05
Z19-100.3516	0.94	0.42	6.43	42.58	0.35	2.18	0.04	0.05	0.1	30.09	16.84	100.04
Z19-100.35-17	0.84	0.47	6.68	43.83	0.34	2.24	0.05	0.07	0.11	29.99	15.46	100.12
Z19-100.35-18	1.06	0.47	6.51	43.52	0.35	1.92	0.03	0.07	0.13	30.66	15.41	100.13
Z19-100.35-19	0.92	0.43	6.38	44.09	0.35	1.88	0.04	0.08	0.1	29.99	14.04	102.83
Z19-100.35-20	0.78	0.44	6.4	44.03	0.31	2.17	0.03	0.08	0.11	30.08	15.85	100.31
Z19-100.35-21	0.84	0.45	6.66	44.93	0.33	1.98	0.04	0.07	0.11	30.45	14.35	100.27
Z19-101.4-19	0.77	0.43	7.84	46.23	0.36	4.06	0.06	0.09	0.08	27.22	12.62	99.78
Z19-101.4-20	0.63	0.4	8.02	46.15	0.38	4.17	0.05	0.08	0.11	26.89	12.83	99.74
Z19-101.4-21	0.72	0.42	7.7	46.62	0.34	4.06	0.05	0.07	0.11	27.15	12.45	99.71
Z19-101.4-22	0.66	0.43	7.81	46.16	0.33	3.91	0.05	0.05	0.09	27.18	12.35	99.05
Z19-101.4-23	0.68	0.44	7.54	46.6	0.33	3.89	0.04	0.07	0.08	27.23	12.23	99.15
Z19-101.4-24	0.77	0.41	8.02	46.09	0.33	4.15	0.05	0.09	0.07	27.15	12.65	99.80
Z19-101.4-25	0.57	0.39	8.99	46.43	0.33	4.37	0.06	0.07	0.1	26.94	12.08	100.33
Z19-101.4-26	0.68	0.39	8.88	46	0.3	4.28	0.07	0.09	0.12	27.12	12.33	100.30
Z19-101.4-27	0.63	0.39	8.83	46.96	0.31	4.39	0.06	0.05	0.12	27.04	11.78	100.56
Z19-101.4-28	0.69	0.41	8.54	46.53	0.33	4.29	0.06	0.07	0.1	27.15	12.28	100.45
Z19-101.4-29	0.74	0.38	9.07	45.91	0.31	4.29	0.04	0.06	0.11	27.28	12.19	100.40
Z19-101.4-30	0.7	0.28	9.18	45.75	0.33	4.44	0.06	0.1	0.13	26.73	12.24	99.95
Z19-101.4-31	0.71	0.28	9.1	45.64	0.32	4.41	0.06	0.09	0.09	26.73	12.19	99.62
Z19-101.4-32	0.68	0.34	9.61	45.24	0.35	4.48	0.07	0.09	0.1	26.86	12.43	100.28
Z19-101.4-33	0.71	0.35	9.35	44.96	0.33	4.5	0.05	0.08	0.1	26.71	12.61	99.75
Z19-101.4-34	0.67	0.31	8.68	45.82	0.34	4.44	0.08	0.1	0.08	26.59	12.63	99.77
Z19-101.6-1	1.03	0.48	5.92	40.32	0.33	1.47	0.04	0.08	0.14	31.16	19.13	100.13
Z19-101.6-2	0.91	0.48	5.98	41.3	0.34	1.31		0.08	0.12	31.47	18.45	100.44
Z19-101.6-3	0.87	0.47	5.9	41.16	0.3	1.27	0.03	0.07	0.16	31.39	18.61	100.23

Z19-101.6-4	0.88	0.48	6.07	41.37	0.33	1.37	0.02	0.07	0.15	31.39	18.45	100.58
Z19-101.6-5	0.89	0.47	5.79	41.21	0.33	1.29	0.03	0.06	0.16	31.34	18.66	100.23
Z19-101.6-6	0.74	0.49	5.8	41.73	0.34	1.06	0.03	0.04	0.15	31.44	17.90	99.74
Z19-101.6-7	0.84	0.44	5.95	41.69	0.33	1.11	0.03	0.06	0.14	31.60	18.01	100.19
Z19-101.6-8	0.74	0.46	5.93	42.04	0.32	1.08		0.07	0.13	31.53	17.66	99.99
Z19-101.6-9	0.67	0.4	8.5	45.7	0.34	3.54	0.06	0.09	0.14	28.19	12.80	100.43
Z19-101.6-10	0.72	0.45	8.7	45.13	0.33	3.53	0.05	0.08	0.11	28.46	13.18	100.74
Z19-101.6-11	0.69	0.42	8.51	45.85	0.34	3.65	0.06	0.09	0.11	28.22	12.93	100.87
Z19-101.6-12	0.77	0.43	8.9	44.6	0.36	3.58	0.04	0.1	0.14	28.43	13.55	100.90
Z19-101.6-14	0.87	0.42	7.93	43.48	0.31	3.44	0.04	0.12	0.11	28.43	15.20	100.35
Z19-101.6-15	0.9	0.42	8.04	43.69	0.33	3.4	0.05	0.13	0.11	28.61	15.03	100.74
Z19-101.6-16	0.77	0.43	7.15	43.69	0.36	3.3	0.05	0.14	0.11	28.28	15.87	100.18
Z19-101.6-17	1	0.46	6.71	43.53	0.38	2.61	0.04	0.09	0.12	29.58	15.80	100.33
Z19-101.6-18	0.8	0.45	6.69	43.83	0.39	2.44	0.04	0.08	0.11	29.79	16.12	100.73
Z19-137.5-51	1.46	0.38	11.18	44.66	0.3	5.26	0.05	0.09	0.09	26.81	10.14	100.42
Z19-137.5-52	0.73	0.38	11.19	45.56	0.3	5.36	0.04	0.07	0.1	26.15	10.98	100.86
Z19-137.5-53	0.75	0.38	11.02	46.01	0.29	5.31	0.02	0.05	0.09	26.12	10.31	100.37
Z19-137.5-54	0.62	0.3	14.4	42.64	0.3	6.76	0.03	0.1	0.11	24.18	10.94	100.40
Z19-137.5-55	0.72	0.33	13.67	42.74	0.29	6.12	0.03	0.08	0.08	25.25	11.20	100.53
Z19-137.5-56	0.7	0.32	13.55	42.5	0.32	6.04	0.02	0.06	0.1	25.31	11.62	100.54
Z19-137.5-57	0.73	0.37	12.2	43.25	0.32	5.69	0.02	0.04	0.09	25.74	12.16	100.61
Z19-137.5-58	0.77	0.38	12.74	43.85	0.32	6.07	0.04	0.04	0.09	25.33	11.14	100.77
Z19-137.5-59	0.92	0.33	12.38	43.61	0.3	6.09	0.06	0.12	0.08	25.12	11.27	100.31
Z19-137.5-60	0.74	0.37	11.97	43.97	0.33	5.7	0.06	0.07	0.09	25.63	11.70	100.65
Z20-66.5-23	0.66	0.33	4.59	16.2	0.17	2.38	0.04	0.15	0.1	28.88	46.74	100.26
Z20-66.5-24	0.63	0.34	4.18	15.11	0.13	2.32		0.11	0.09	28.87	48.07	99.88
Z20-66.5-26	0.1	0.21	14.78	29.05	0.35	4.03	0.06	0.16	0.27	27.56	24.29	100.85
Z20-66.5-27	0.07	0.22	15.46	28.84	0.33	4.03	0.04	0.15	0.32	27.54	23.48	100.48
Z20-66.5-28	0.82	0.37	9.79	29.88	0.33	3.87	0.04	0.29	0.19	27.61	27.37	100.57
Z20-66.5-29	0.85	0.36	9.11	28.44	0.33	3.43	0.04	0.29	0.19	28.05	29.11	100.23
Z20-66.5-30	1.9	0.46	11.11	32.63	0.32	5.39	0.06	0.35	0.14	26.62	21.69	100.68
Z20-66.5-31	1.5	0.39	9.21	33.89	0.35	3.9	0.09	0.24	0.22	28.21	22.85	100.87
Z20-66.5-32	1.47	0.38	8.83	34.54	0.38	3.59	0.07	0.25	0.21	28.34	22.00	100.08
Z20-66.5-33	0.39	0.25	11.86	31.21	0.35	4.1	0.08	0.24	0.2	27.24	24.96	100.88
Z20-66.5-34	1.51	0.34	10.98	34.06	0.34	4.85	0.06	0.23	0.17	27.08	21.06	100.68
Z20-66.5-35	0.96	0.34	13.52	35.37	0.29	5.54	0.06	0.2	0.14	26.24	18.53	101.20
Z20-66.5-36	0.89	0.35	14.53	35.66	0.31	5.22	0.07	0.18	0.13	26.65	16.53	100.55
Z20-66.5-37	0.6	0.33	12.56	34.63	0.35	4.62	0.06	0.17	0.23	26.80	20.12	100.49
Z20-111-45	0.96	0.8	3.17	16.45	0.37	0.74	0.02	0.18	0.12	31.63	46.18	100.71
Z20-111-46	0.48	0.33	6.74	24.78	0.32	0.88	0.02	0.1	0.23	31.20	34.74	99.85
Z20-111-47	1.52	0.98	2.85	34.18	0.31	1.88	0.06	0.19	0.16	30.39	27.09	99.64
Z20-111-48	0.51	0.37	5.42	20.8	0.28	0.49	0.02	0.1	0.18	31.62	39.94	99.72
Z20-111-49	0.32	0.37	6.67	23.92	0.36	0.54	0.02	0.08	0.24	31.48	35.62	99.62

Table 11-16: Cation proportions recalculated according to the to the spinel stoichiometry calculation template - latest version Dec 21 2004 developed by S.J. Barnes with correction from C-J De Hoog.

sample	Cr	Ti	V	Al	Fe3+	Fe2+	Mn	Mg	Co	Ni	Zn	Cr/3+	Fe/3+	Al/3+	Fe3/Fe	Mg#	Cr#
Z19-100.35-1	1.21	0.02	0.01	0.27	0.46	0.91	0.01	0.10	0.00	0.00	0.00	0.62	0.24	0.14	0.34	0.10	0.82
Z19-100.35-2	1.24	0.02	0.01	0.27	0.44	0.91	0.01	0.10	0.00	0.00	0.00	0.64	0.22	0.14	0.32	0.10	0.82
Z19-100.35-3	1.23	0.02	0.01	0.28	0.44	0.91	0.01	0.10	0.00	0.00	0.00	0.63	0.22	0.14	0.32	0.10	0.82
Z19-100.35-4	1.11	0.04	0.01	0.24	0.55	0.94	0.01	0.09	0.00	0.00	0.00	0.58	0.29	0.13	0.37	0.09	0.82
Z19-100.35-5	1.17	0.03	0.01	0.26	0.48	0.91	0.01	0.12	0.00	0.00	0.00	0.61	0.25	0.14	0.35	0.11	0.82
Z19-100.35-6	1.21	0.02	0.01	0.27	0.45	0.91	0.01	0.11	0.00	0.00	0.00	0.63	0.23	0.14	0.33	0.10	0.82
Z19-100.35-7	1.20	0.03	0.01	0.26	0.46	0.92	0.01	0.10	0.00	0.00	0.00	0.63	0.24	0.13	0.33	0.10	0.82
Z19-100.35-8	1.22	0.02	0.01	0.26	0.44	0.92	0.01	0.10	0.00	0.00	0.00	0.63	0.23	0.14	0.33	0.10	0.82
Z19-100.35-9	1.15	0.03	0.01	0.26	0.50	0.90	0.01	0.12	0.00	0.00	0.00	0.60	0.26	0.14	0.35	0.12	0.82
Z19-100.35-10	1.16	0.03	0.01	0.27	0.49	0.90	0.01	0.12	0.00	0.00	0.00	0.61	0.25	0.14	0.35	0.12	0.81
Z19-100.35-11	1.16	0.03	0.01	0.26	0.50	0.90	0.01	0.12	0.00	0.00	0.00	0.61	0.26	0.13	0.35	0.12	0.82
Z19-100.35-12	1.16	0.03	0.01	0.26	0.49	0.90	0.01	0.12	0.00	0.00	0.00	0.61	0.25	0.14	0.35	0.12	0.82
Z19-100.35-13	1.17	0.03	0.01	0.27	0.48	0.90	0.01	0.12	0.00	0.00	0.00	0.61	0.25	0.14	0.35	0.12	0.81
Z19-100.35-14	1.20	0.03	0.01	0.26	0.46	0.90	0.01	0.12	0.00	0.00	0.00	0.62	0.24	0.14	0.34	0.11	0.82
Z19-100.35-15	1.23	0.02	0.01	0.26	0.44	0.90	0.01	0.11	0.00	0.00	0.00	0.64	0.23	0.14	0.33	0.11	0.82
Z19-100.3516	1.20	0.03	0.01	0.27	0.45	0.90	0.01	0.12	0.00	0.00	0.00	0.62	0.24	0.14	0.33	0.11	0.82
Z19-100.35-17	1.24	0.02	0.01	0.28	0.41	0.89	0.01	0.12	0.00	0.00	0.00	0.64	0.21	0.15	0.32	0.12	0.81
Z19-100.35-18	1.23	0.03	0.01	0.27	0.41	0.92	0.01	0.10	0.00	0.00	0.00	0.64	0.22	0.14	0.31	0.10	0.82
Z19-100.35-19	1.27	0.03	0.01	0.27	0.38	0.91	0.01	0.10	0.00	0.00	0.00	0.66	0.20	0.14	0.30	0.10	0.82
Z19-100.35-20	1.24	0.02	0.01	0.27	0.43	0.90	0.01	0.12	0.00	0.00	0.00	0.64	0.22	0.14	0.32	0.11	0.82
Z19-100.35-21	1.27	0.02	0.01	0.28	0.39	0.91	0.01	0.11	0.00	0.00	0.00	0.66	0.20	0.14	0.30	0.10	0.82
Z19-101.4-19	1.28	0.02	0.01	0.32	0.33	0.80	0.01	0.21	0.00	0.00	0.00	0.66	0.17	0.17	0.29	0.21	0.80
Z19-101.4-20	1.28	0.02	0.01	0.33	0.34	0.79	0.01	0.22	0.00	0.00	0.00	0.66	0.17	0.17	0.30	0.22	0.79
Z19-101.4-21	1.29	0.02	0.01	0.32	0.33	0.80	0.01	0.21	0.00	0.00	0.00	0.67	0.17	0.16	0.29	0.21	0.80

Z19-101.4-22	1.29	0.02	0.01	0.33	0.33	0.80	0.01	0.21	0.00	0.00	0.00	0.66	0.17	0.17	0.29	0.20	0.80
Z19-101.4-23	1.30	0.02	0.01	0.31	0.33	0.81	0.01	0.20	0.00	0.00	0.00	0.67	0.17	0.16	0.29	0.20	0.81
Z19-101.4-24	1.28	0.02	0.01	0.33	0.33	0.79	0.01	0.22	0.00	0.00	0.00	0.66	0.17	0.17	0.30	0.21	0.79
Z19-101.4-25	1.27	0.01	0.01	0.37	0.31	0.78	0.01	0.23	0.00	0.00	0.00	0.65	0.16	0.19	0.29	0.22	0.78
Z19-101.4-26	1.26	0.02	0.01	0.36	0.32	0.79	0.01	0.22	0.00	0.00	0.00	0.65	0.17	0.19	0.29	0.22	0.78
Z19-101.4-27	1.28	0.02	0.01	0.36	0.31	0.78	0.01	0.23	0.00	0.00	0.00	0.66	0.16	0.18	0.28	0.22	0.78
Z19-101.4-28	1.27	0.02	0.01	0.35	0.32	0.79	0.01	0.22	0.00	0.00	0.00	0.66	0.16	0.18	0.29	0.22	0.79
Z19-101.4-29	1.26	0.02	0.01	0.37	0.32	0.79	0.01	0.22	0.00	0.00	0.00	0.65	0.16	0.19	0.29	0.22	0.77
Z19-101.4-30	1.25	0.02	0.01	0.38	0.32	0.78	0.01	0.23	0.00	0.00	0.00	0.64	0.16	0.19	0.29	0.23	0.77
Z19-101.4-31	1.26	0.02	0.01	0.37	0.32	0.78	0.01	0.23	0.00	0.00	0.00	0.64	0.16	0.19	0.29	0.23	0.77
Z19-101.4-32	1.23	0.02	0.01	0.39	0.32	0.78	0.01	0.23	0.00	0.00	0.00	0.63	0.17	0.20	0.29	0.23	0.76
Z19-101.4-33	1.23	0.02	0.01	0.38	0.33	0.78	0.01	0.23	0.00	0.00	0.00	0.63	0.17	0.20	0.30	0.23	0.76
Z19-101.4-34	1.26	0.02	0.01	0.36	0.33	0.77	0.01	0.23	0.00	0.00	0.00	0.65	0.17	0.18	0.30	0.23	0.78
Z19-101.6-1	1.15	0.03	0.01	0.25	0.52	0.94	0.01	0.08	0.00	0.00	0.00	0.60	0.27	0.13	0.36	0.08	0.82
Z19-101.6-2	1.17	0.02	0.01	0.25	0.50	0.95	0.01	0.07	0.00	0.00	0.00	0.61	0.26	0.13	0.35	0.07	0.82
Z19-101.6-3	1.17	0.02	0.01	0.25	0.50	0.95	0.01	0.07	0.00	0.00	0.00	0.61	0.26	0.13	0.35	0.07	0.82
Z19-101.6-4	1.17	0.02	0.01	0.26	0.50	0.94	0.01	0.07	0.00	0.00	0.00	0.61	0.26	0.13	0.35	0.07	0.82
Z19-101.6-5	1.18	0.02	0.01	0.25	0.51	0.95	0.01	0.07	0.00	0.00	0.00	0.61	0.26	0.13	0.35	0.07	0.83
Z19-101.6-6	1.20	0.02	0.01	0.25	0.49	0.95	0.01	0.06	0.00	0.00	0.00	0.62	0.25	0.13	0.34	0.06	0.83
Z19-101.6-7	1.19	0.02	0.01	0.25	0.49	0.95	0.01	0.06	0.00	0.00	0.00	0.62	0.25	0.13	0.34	0.06	0.82
Z19-101.6-8	1.20	0.02	0.01	0.25	0.48	0.95	0.01	0.06	0.00	0.00	0.00	0.62	0.25	0.13	0.34	0.06	0.83
Z19-101.6-9	1.26	0.02	0.01	0.35	0.34	0.82	0.01	0.18	0.00	0.00	0.00	0.65	0.17	0.18	0.29	0.18	0.78
Z19-101.6-10	1.24	0.02	0.01	0.36	0.34	0.83	0.01	0.18	0.00	0.00	0.00	0.64	0.18	0.18	0.29	0.18	0.78
Z19-101.6-11	1.26	0.02	0.01	0.35	0.34	0.82	0.01	0.19	0.00	0.00	0.00	0.65	0.17	0.18	0.29	0.19	0.78
Z19-101.6-12	1.22	0.02	0.01	0.36	0.35	0.82	0.01	0.18	0.00	0.00	0.00	0.63	0.18	0.19	0.30	0.18	0.77
Z19-101.6-14	1.20	0.02	0.01	0.33	0.40	0.83	0.01	0.18	0.00	0.00	0.00	0.62	0.21	0.17	0.32	0.18	0.79
Z19-101.6-15	1.21	0.02	0.01	0.33	0.40	0.84	0.01	0.18	0.00	0.00	0.00	0.62	0.20	0.17	0.32	0.17	0.78
Z19-101.6-16	1.22	0.02	0.01	0.30	0.42	0.83	0.01	0.17	0.00	0.00	0.00	0.63	0.22	0.15	0.34	0.17	0.80

Z19-101.6-17	1.22	0.03	0.01	0.28	0.42	0.88	0.01	0.14	0.00	0.00	0.00	0.63	0.22	0.15	0.32	0.14	0.81
Z19-101.6-18	1.23	0.02	0.01	0.28	0.43	0.88	0.01	0.13	0.00	0.00	0.00	0.63	0.22	0.14	0.33	0.13	0.81
Z19-137.5-51	1.20	0.04	0.01	0.45	0.26	0.76	0.01	0.27	0.00	0.00	0.00	0.63	0.14	0.23	0.25	0.26	0.73
Z19-137.5-52	1.22	0.02	0.01	0.45	0.28	0.74	0.01	0.27	0.00	0.00	0.00	0.63	0.14	0.23	0.27	0.27	0.73
Z19-137.5-53	1.24	0.02	0.01	0.44	0.26	0.74	0.01	0.27	0.00	0.00	0.00	0.64	0.14	0.23	0.26	0.27	0.74
Z19-137.5-54	1.12	0.02	0.01	0.56	0.27	0.67	0.01	0.33	0.00	0.00	0.00	0.57	0.14	0.29	0.29	0.33	0.67
Z19-137.5-55	1.13	0.02	0.01	0.54	0.28	0.71	0.01	0.30	0.00	0.00	0.00	0.58	0.14	0.28	0.29	0.30	0.68
Z19-137.5-56	1.12	0.02	0.01	0.53	0.29	0.71	0.01	0.30	0.00	0.00	0.00	0.58	0.15	0.27	0.29	0.30	0.68
Z19-137.5-57	1.15	0.02	0.01	0.48	0.31	0.73	0.01	0.29	0.00	0.00	0.00	0.59	0.16	0.25	0.30	0.28	0.70
Z19-137.5-58	1.16	0.02	0.01	0.50	0.28	0.71	0.01	0.30	0.00	0.00	0.00	0.60	0.14	0.26	0.28	0.30	0.70
Z19-137.5-59	1.16	0.02	0.01	0.49	0.29	0.71	0.01	0.31	0.00	0.00	0.00	0.60	0.15	0.25	0.29	0.30	0.70
Z19-137.5-60	1.17	0.02	0.01	0.48	0.30	0.72	0.01	0.29	0.00	0.00	0.00	0.60	0.15	0.24	0.29	0.28	0.71
Z20-66.5-23	0.47	0.02	0.01	0.20	1.28	0.88	0.01	0.13	0.00	0.00	0.00	0.24	0.66	0.10	0.59	0.13	0.70
Z20-66.5-24	0.44	0.02	0.01	0.18	1.33	0.89	0.00	0.13	0.00	0.00	0.00	0.23	0.68	0.09	0.60	0.13	0.71
Z20-66.5-26	0.78	0.00	0.00	0.59	0.62	0.78	0.01	0.20	0.00	0.00	0.01	0.39	0.31	0.30	0.44	0.21	0.57
Z20-66.5-27	0.77	0.00	0.00	0.62	0.60	0.78	0.01	0.20	0.00	0.00	0.01	0.39	0.30	0.31	0.43	0.21	0.56
Z20-66.5-28	0.82	0.02	0.01	0.40	0.72	0.80	0.01	0.20	0.00	0.01	0.00	0.42	0.37	0.21	0.47	0.20	0.67
Z20-66.5-29	0.79	0.02	0.01	0.38	0.77	0.82	0.01	0.18	0.00	0.01	0.00	0.41	0.40	0.19	0.48	0.18	0.68
Z20-66.5-30	0.88	0.05	0.01	0.45	0.56	0.76	0.01	0.27	0.00	0.01	0.00	0.47	0.30	0.24	0.42	0.27	0.66
Z20-66.5-31	0.93	0.04	0.01	0.38	0.60	0.82	0.01	0.20	0.00	0.01	0.01	0.49	0.31	0.20	0.42	0.20	0.71
Z20-66.5-32	0.96	0.04	0.01	0.37	0.58	0.83	0.01	0.19	0.00	0.01	0.01	0.50	0.31	0.19	0.41	0.18	0.72
Z20-66.5-33	0.85	0.01	0.01	0.48	0.64	0.78	0.01	0.21	0.00	0.01	0.01	0.43	0.33	0.24	0.45	0.21	0.64
Z20-66.5-34	0.92	0.04	0.01	0.44	0.54	0.77	0.01	0.25	0.00	0.01	0.00	0.48	0.28	0.23	0.41	0.24	0.68
Z20-66.5-35	0.94	0.02	0.01	0.53	0.47	0.73	0.01	0.28	0.00	0.01	0.00	0.48	0.24	0.28	0.39	0.27	0.64
Z20-66.5-36	0.95	0.02	0.01	0.57	0.42	0.75	0.01	0.26	0.00	0.00	0.00	0.49	0.22	0.30	0.36	0.26	0.62
Z20-66.5-37	0.93	0.02	0.01	0.50	0.52	0.76	0.01	0.23	0.00	0.00	0.01	0.48	0.26	0.26	0.40	0.24	0.65
Z20-111-45	0.48	0.03	0.02	0.14	1.29	0.98	0.01	0.04	0.00	0.01	0.00	0.25	0.67	0.07	0.57	0.04	0.78
Z20-111-46	0.71	0.01	0.01	0.29	0.95	0.95	0.01	0.05	0.00	0.00	0.01	0.36	0.49	0.15	0.50	0.05	0.71

Z20-111-47	0.99	0.04	0.02	0.12	0.75	0.93	0.01	0.10	0.00	0.01	0.00	0.53	0.40	0.07	0.45	0.10	0.89
Z20-111-48	0.61	0.01	0.01	0.24	1.11	0.98	0.01	0.03	0.00	0.00	0.00	0.31	0.57	0.12	0.53	0.03	0.72
Z20-111-49	0.69	0.01	0.01	0.29	0.98	0.96	0.01	0.03	0.00	0.00	0.01	0.35	0.50	0.15	0.50	0.03	0.71
Z20-111-50	0.66	0.01	0.01	0.24	1.07	0.94	0.01	0.05	0.00	0.00	0.00	0.33	0.54	0.12	0.53	0.05	0.73

2. OLIVINE CHEMISTRY

Table 11-17: The initial EMPA oxide results of olivine.

Rock name	Analysis #	Mineral	SiO_2	TiO_2	Al_2O_3	Cr_2O_3	FeO	MnO	MgO	CoO	NiO	Total
FHZB	Z20-66.5-38	OL	40.02	0	0.01	0.01	15.03	0.18	44.91	0.05	0.32	100.56
FHZB	Z20-66.5-39	OL	40.09	0.01	0.01	0.01	14.66	0.22	44.98	0.04	0.34	100.39
FHZB	Z20-66.5-40	OL	36.84	0.07	0.37	0.55	23.48	0.17	37.02	0.03	0.3	101.87
FHZB	Z20-66.5-41	OL	40.25	0	0.02	0.02	15.2	0.2	44.66	0.03	0.33	100.74
FHZB	Z20-66.5-42	OL	40.07	0.02	0.01	0	15.35	0.23	44.64	0.03	0.33	100.71
FHZB	Z20-66.5-43	OL	40.13	0	0.02	0	15.58	0.22	44.91	0.02	0.32	101.22
FHZB	Z20-66.5-44	OL	37.42	0.02	0.12	0.2	18.2	0.21	39.95	0.02	0.33	97.21